

# University of Southampton Research Repository ePrints Soton

Copyright © and Moral Rights for this thesis are retained by the author and/or other copyright owners. A copy can be downloaded for personal non-commercial research or study, without prior permission or charge. This thesis cannot be reproduced or quoted extensively from without first obtaining permission in writing from the copyright holder/s. The content must not be changed in any way or sold commercially in any format or medium without the formal permission of the copyright holders.

When referring to this work, full bibliographic details including the author, title, awarding institution and date of the thesis must be given e.g.

AUTHOR (year of submission) "Full thesis title", University of Southampton, name of the University School or Department, PhD Thesis, pagination

### UNIVERSITY OF SOUTHAMPTON

### 

## Fluid-structure interactions of membrane wings in free-flight and in ground-effect

by

### Robert Bleischwitz



Thesis for the degree of Doctor of Philosophy

June 2016

#### UNIVERSITY OF SOUTHAMPTON

#### ABSTRACT

## FACULTY OF ENGINEERING AND THE ENVIRONMENT Aerodynamics and Flight Mechanics

Doctor of Philosophy

## FLUID-STRUCTURE INTERACTIONS OF MEMBRANE WINGS IN FREE-FLIGHT AND IN GROUND-EFFECT

by Robert Bleischwitz

Currently, there is a growing demand to improve the aerodynamic performance of Micro-Air-Vehicles for extended mission time, higher payload capacity and improved agility. Their wings have to operate within a challenging Reynolds number regime of Re =  $10^4 - 10^5$  which is known for its low energy content in the boundary layer, causing early flow separation and loss in lift production. Flexible wings, inspired from bats, could potentially exploit given flow separations by forming lift carrying shedding structures close to the upper wing surface. The aspect-ratio is one key parameter which modifies these vortex formations and their ability to couple with the membrane. However, vortex related lift production comes at a price of increased drag and limitation in aerodynamic efficiency. Membrane wings in ground-effect could combine ground-effect related efficiency enhancement with flexibility related stall improvements. Therefore, two separate wind tunnel experiments are conducted to understand the impact of aspect-ratio and ground-effect on the fluid-structure interaction of membrane wings. Multiple high-speed recordings involve lift, drag and pitch moment measurements with a load-cell, membrane deformation measurements with photogrammetry and digital image correlation (DIC) and flow measurements with planar/stereo particle image velocimetry (PIV). Next to time-averaged quantities, reduced order models are used to group predominant flow and membrane dynamics. Synchronised fluid-membrane coupling of flexible membrane wings allows to exploit separated flow conditions to provide further lift enhancement from vortical flow formations. An exemplary membrane wing at  $\alpha = 25^{\circ}$  shows similar vortex-shedding to a rigid flat-plate at  $\alpha = 15^{\circ}$ , but comes with 50 % more lift production. Higher aspect-ratios are found to exploit the benefits of wing flexibility to a larger extend, showing a gain in peak-lift of up to 60% for an aspect-ratio of 2 and 31% for an aspect-ratio of 1 (in reference to rigid flat-plates). Membrane wings extend their performance window in ground-effect conditions by delaying ground-effect induced premature flow separation by  $\Delta \alpha = 5^{\circ}$ . In addition, membrane wings in ground-effect are found to be up to 30% more efficiency than rigid flat-plates.

## Contents

D	eclar	ation (	of Authorship	ix
A	ckno	wledge	ements	x
N	omei	ıclatur	re	xiii
1	Inti	roduct	ion	1
	1.1	Overv	view	. 1
	1.2	Motiv	vation	. 2
	1.3	Resear	arch Objectives and Approach	. 4
	1.4	Thesis	s Outline	. 5
2	Lite	erature	e Survey	7
	2.1	Aeron	nechanics of Membrane Wings	. 7
		2.1.1	Membrane Wing Types	. 7
		2.1.2	Load Performance	. 8
		2.1.3	Membrane Motions	. 9
		2.1.4	Flow Development	. 10
		2.1.5	Flow-Structure Coupling	. 11
	2.2	Effect	s of Aspect-Ratio	. 12
	2.3	Groun	nd-Effect	. 14
3	Exp	erime	ental Setup and Method	17
	3.1	Wind	Tunnel	. 17
	3.2	Setup-	p-1: Aspect-ratio Experiment	. 20
		3.2.1	Setup Design	. 20
		3.2.2	Wing Design	. 20
		3.2.3	Load	. 23
		3.2.4	Deformation	. 26
			3.2.4.1 Photogrammetry	. 26
			3.2.4.2 Sinusoidal-Decomposition	. 28
	3.3	Setup-	p-2: Ground-effect Experiment	. 30
		3.3.1	Setup Design	. 30
		3.3.2	Wing Design	. 34
		3.3.3	Load	. 37
		3.3.4	Deformation	. 42
			3.3.4.1 Digital-Image-Correlation	. 42
			3.3.4.2 Proper-Orthogonal-Decomposition	. 43

vi CONTENTS

		3.3.5	Flow	45
			3.3.5.1 Particle-Image-Velocimetry: Streamwise-plane	. 46
			3.3.5.2 Particle-Image-Velocimetry: Spanwise-plane	. 48
			3.3.5.3 Proper-Orthogonal-Decomposition	. 50
4	r <sub>ff</sub>	et of	Aspect-ratio on Membrane Half-wings	<b>5</b> 3
4	4.1		lynamic Loads	
	4.1	4.1.1	Lift and Drag of Rigid Flat Plates and Membrane Wings	
		4.1.2	Aerodynamic Range and Power Efficiency	
		4.1.3	Pitching Moment	
	4.2		prane Deformations	
	1.2	4.2.1	Mean Membrane Deflection	
		4.2.2	Chordwise location of maximum camber	
		4.2.3	Instantaneous Membrane Dynamics	
		4.2.4	Fluctuation Magnitude along Chord and Wingspan	
		4.2.5	Modal-Analysis of Membrane Dynamics	
	т а			0.0
5			of Ground-Effect on Membrane Wings	69
	5.1		lynamic Loads	
		5.1.1	Lift and Drag Statistics of Rigid flat-plate and Membrane Wings .	
		5.1.2	Aerodynamic Efficiency	
		5.1.3	Lift Dynamics of Membrane Wings	. 75
		5.1.4	Statics and Dynamics of Pitching moment in Rigid flat-plate and Membrane wings	. 76
	5.2	Memb	orane Deformations	
		5.2.1	Statistics	<b>7</b> 8
		5.2.2	Instantaneous Membrane Dynamics	. 80
		5.2.3	Modal-Analysis of Membrane Dynamics	. 81
	5.3	Flow	Development: On top of the membrane wing	. 85
		5.3.1	Flow Statistics	. 85
		5.3.2	Spatial Flow Structures	. 90
		5.3.3	Spectral Content of the Flow	. 95
	5.4	Flow	Development: cross-stream plane	. 98
		5.4.1	Flow Statistics	. 98
		5.4.2	Spatial Flow Structures	. 101
		5.4.3	Spectral Flow Content	. 103
	5.5	Aerod	lynamic Coupling	. 105
		5.5.1	Load-Membrane	
		5.5.2	Membrane-Flow	. 109
		5.5.3	Load-Membrane-Flow	
		5.5.4	Cycle-averaging	. 117
6	Dis	cussio	n and Recommendations	<b>121</b>
	6.1	Static	Camber and Wing Dynamic	. 121
	6.2		Structure Coupling	
	6.3		Stability	
	6.4	Effect	s of Aspect-Ratio	125

CONTENTS	vii

	-Effect	
Appendix A	Wing-In-Ground UAV	139
Appendix B	List of publications	143
Appendix C	Curriculum Vitae	145

### Declaration of Authorship

I, Robert Bleischwitz, declare that the thesis entitled *Fluid-structure interactions of membrane wings in free-flight and in ground-effect* and the work presented in the thesis are both my own, and have been generated by me as the result of my own original research. I confirm that:

- this work was done wholly or mainly while in candidature for a research degree at this University;
- where any part of this thesis has previously been submitted for a degree or any other qualification at this University or any other institution, this has been clearly stated;
- where I have consulted the published work of others, this is always clearly attributed;
- where I have quoted from the work of others, the source is always given. With the exception of such quotations, this thesis is entirely my own work;
- I have acknowledged all main sources of help;
- where the thesis is based on work done by myself jointly with others, I have made clear exactly what was done by others and what I have contributed myself;
- parts of this work have been published as: (Bleischwitz et al., 2016, 2015a,b, 2014)

Signed:	 	 	 
0			
Data			

### Acknowledgements

I would like to thank both my supervisors, Prof. Bharathram Ganapathisubramani and Dr. Roeland de Kat for their enthusiastic, sufficient and timely advice for this study. You both gave me supporting freedom, inspiration and space for new ideas. In addition, I thank you for giving me the chance to present and discuss my research through conferences in different countries all over the world. I also really appreciate your devotion and spirit to research, which was very motivating and helped me to tackle challenging questions.

I would like to thank all our technicians for their great effort, help and advice during experiments.

I would like to thank all my student colleagues, Jacob, Adriano, Alex, Kuti, Rammah, Jaques, Zoe, Ana and the entire "BGROUP" for their individual support and the exchange of ideas.

The study work was financially supported by the Engineering and Physical Sciences Research Council (EPSRC, grant EP/J001465/1), and the European Office of Aerospace Research and Development (EOARD, grant FA8655-12-1-2046). Thank you for enabling this research.

I would like to thank my mum and dad for their love, peace of mind and interest in sometimes rather abstract things. I thank you for giving me support and strength in my hobbies from an early age, allowing me to flourish and to follow my dreams. Finally, I would like to thank Romana for your support and inspiration, even when you were far away.

## Nomenclature

$\alpha$	global angle-of-attack [°]	$\Delta C_L$	increment in lift coefficient
β	membrane contact angle $[\circ]$	$C_L/C_D$	aerodynamic range efficiency
$\gamma$	force angle lift $/ \text{ drag } [^{\circ}]$	$(C_L/C_D)'$	·
λ	POD eigenvalue		increment in aero. efficiency
Π	aeroelastic parameter $(\frac{Et}{qc})^{1/3}$	$C_{M/4}$	pitch coefficient at 1/4 chord
$\sigma$	standard deviation	E	spectral energy [dB]
$\phi$	cycle based phase of CCF $[\circ]$	h	height above ground
$\omega$	flow vorticity $[1/s]$	k	phase of cross-correlation
A	POD eigenvector	LAR	low aspect-ratio
AR	aspect-ratio (full span)	LE	leading-edge
a	POD coefficient	n	mode number
b	wing full span [m]	POD	proper orthogonal decompositio
c	chord length [m]	PSD	power spectral density [dB]
CCF	cross correlation function	q	dynamic pressure $\frac{1}{2}\rho U_{\infty}^2$ [N/m <sup>2</sup> ]
$C_D$	drag coefficient	Re	Reynolds number $\frac{U_{\infty}c}{\nu}$
$C_D'$	drag coefficient fluctuation	$s_{1,2}$	two signals for correlation
$\Delta C_D$	increment in drag coefficient	St	Strouhal number $\frac{fc}{U_{\infty}}$
$C_L$	lift coefficient	TE	trailing-edge
$C_L'$	lift coefficient fluctuation	$U_{\infty}$	freestream velocity $[m/s]$
Coordina	ate system of wing structure	Coordinate	system of flow
x	chordwise wing coordinate [m]	x	chordwise flow coordinate [m]
y	spanwise wing coordinate [m]	y	vertical flow coordinate [m]
z	camberwise wing coordinate [m]	z	spanwise flow coordinate [m]
		U	streamwise flow velocity $[m/s]$
		V	vertical flow velocity $[m/s]$
		W	spanwise flow velocity [m/s]

## List of Figures

1.1	Fundamental limitations in aerodynamic efficiency for moderate Reynolds number flow conditions ( $10^4 \le Re \le 10^5$ ) (McMasters and Henderson, 1979)	1
2.1	Membrane wing types: a.) Perimeter supported b.) Batten supported c.) Leading/trailing-edge supported with free root/tip	7
2.2	Lift and pitch behaviour of rigid and membrane wings (PR = perimeter-reinforced (Figure 2.1a), BR = batten-reinforced (Figure 2.1b)) (Albertani et al., 2007).	(
2.3	Instantanious membrane wing oscillations for two different angle-of-attack, showing a membrane mode 5 (five peaks) and a membrane mode 2 oscil-	
2.4	lation (Rojratsirikul et al., 2009).  Turbulent kinetic energy of the flow for (a) rigid flat-plate, (b) rigid mean-cambered, (c) flexible membrane wing (Gordnier and Attar, 2014).	10
2.5	Normalised membrane and flow oscillation frequencies, changing with freestream velocity and angle-of-attack (Rojratsirikul et al., 2009)	11
2.6	Impact of migration distance of bats on aspect-ratio and wing-loading. Filled circles represent migration distances of bats with >1000 km, empty circles between 200 and 1000 km. The axis show difference to average	
2.7	values. (Norberg and Rayner, 1987).  Time-averaged lift capability of rigid cambered-plate and membrane wings, modifying with aspect-ratio (two seperate studies of Pelletier and Mueller (2001) and Song et al. (2008)).	12 13
2.8	Change in flow circulation in and out of ground-effect (Yun et al., 2010).	14
2.9	Typical wing layout between conventional high altitude and ground-effect airplanes (Rozhdestvensky, 2006)	15
2.10	Moderate Reynolds number Wing-In-Ground vehicle with membrane wings. Further details can be found in Appendix A.	15
3.1	Wind tunnel dimensions	17
3.2	Contraction and test section design	19
3.3	Half wing mount concept	20
3.4	Leading and trailing-edge concept	21
3.5	Influence of clamped and free-to-rotate leading and trailing-edge attachment for $AR-2$	22
3.6	Exemplary time-series signal in $C_L(t), C_D(t)$ and $C_M(t)$ and load cell in-	
	tegration within mount	23

xvi LIST OF FIGURES

3.7	Repeatability test of the load cell with one rigid flat-plate wing $(AR-1)$ at an exemplary wind speed of 5 m/s. The wing normal force $F_N$ is illustrated for two individual runs over a variaty of angles-of-attack. Ultimately, the load results are found to lie within the company given accuracy of $\pm 0.15g$ , if the wind on/off measurements are conducted within a short time-period of 60 s	24
3.8	Uncertainty bounds of aerodynamic coefficients for rigid flat-plate and membrane wings of $AR$ -1, and 2	25
3.9	Resonance behaviour of setup (based on $PSD(F_{Lift})$ ), modifying for rigid flat-plate and membrane wing between $0^{\circ} \leq \alpha \leq 27.5^{\circ}$ . Resonance points of the setup and individual hardware (yellow shading) stay fix for different incidences and can be isolated. Black shaded regions show membrane wing related dominant oscillation frequencies in lift, which modify (and can be resolved) for different flow conditions.	26
3.10	(a) Photogrammetry setup, measuring wing deformations at four sections along span.(b) Exemplary membrane vibrations over mean (blue) and without mean (red), at one span position	27
3.11	Sinusodial modal decomposition of membrane vibrations. This decomposition allows access to distinct spatial modes in the membrane and their	
	temporal content (Exemplary case: $AR$ -2, mid-semispan, $\alpha = 25^{\circ}$ ) Wind tunnel test section with integrated sting and rolling road system Sting arm with front mounted wing. Adjustable in pitch-angle and verti-	30
0.14	cal height.	31
	Sting system with heave and pitch units	
	Rolling road add-ons  A rolling road system removes the boundary layer and ensures a uniform boundary layer profile with deviations of less than 2% from the free-stream velocity.	33 34
3.18	Sting system with illustrated perimeter reinforced wing layout for rigid flat plate and membrane wing	35
3.19	(a) Transparent rigid flat plate and (b,c) membrane wing with translucent section, allowing optical access for PIV measurements above and below	
3.20	the wing	36
3.21	%) of all measured wing samples.  Load-cell integration in sting nose	
3.22	Uncertainty bounds of aerodynamic coefficients for rigid flat-plate and membrane wings at free-flight ( $h/c=2$ ) and ground-effect conditions	
	(h/c = 0.1)	38

LIST OF FIGURES xvii

3.23	Resonance behaviour of the setup. Cases: No wing mounted, flat-plate mounted, membrane wing mounted. $U_{\infty}=8.4m/s$ , stall-conditions at $\alpha=25^{\circ}$ , free-flight. Flow induced load-shedding of rigid flat-plates can not be resolved due to relatively strong wind tunnel fan induced noise (blower-type related) and excitation of the wing frame eigenfrequency (EF). Wing frame eigenfrequencies were localised with external hammer-tests. However, membrane wing load dynamics (membrane/flow induced) can be resolved (68Hz + 138 Hz) and emerge out the setup background frequencies.	39
3.24	Resonance behaviour of setup (based on $PSD(F_{Lift})$ ), modifying for rigid flat-plate and membrane wing in angle-of-attack of $15^{\circ} \leq \alpha \leq 30^{\circ}$ . Resonance points of the setup (yellow shading) stay fix for different incidences and can be isolated. Black shaded regions show membrane wing related dominant oscillation frequencies in lift, which modify (drop) within stall conditions.	40
3.25	Digital image correlation (DIC) of membrane surface. Blue LED-light is used for illumination. The illustrated speckled membrane has a translucent streamwise section for later PIV measurements above and below the	40
3.26	wing	42
3.27	impact on the POD mode shapes and their energy content Planar PIV setup with two slightly overlapping side-by-side PIV cameras, capturing flow above/below wing + wake region. The laser plane is	45 46
3.28	aligned parallel to the freestream at quater-wingspan Stereo PIV setup, showing tip-vortex development in a freestream-normal plane, located one chord downstream of trailing-edge. An exemplary tip-vortex vector field is shown in relation to the sting position	49
3.29	Sensitivity analysis of POD on streamwise flow-plane with 1000 and 5000 samples (based on POD without mean). Spatial POD mode shapes (inten-	10
3.30	sity normalised contours, showing $\sqrt{(U_{POD}^{\prime 2} + V_{POD}^{\prime 2})}/U_{\infty}$ ) and their individual energy content are shown for the first five dominant POD modes. Exemplary case: Extreme ground-effect (h/c = 0.1) at $\alpha$ =15°. Ultimetly, the assamble size does not show any significant impact on the POD mode shapes and their energy content	51
0.00	samples (based on POD without mean). Spatial POD mode shapes (inten-	
	sity normalised contours, showing $\sqrt{(W_{POD}'^2 + V_{POD}'^2)}/U_{\infty}$ ) and their individual energy content are shown for the first five dominant POD modes. Exemplary case: Extreme ground-effect (h/c = 0.1) at $\alpha$ =15°. Ultimetly, the assamble size does not show any significant impact on the POD mode	
	shapes and their energy content	52

xviii LIST OF FIGURES

4.1	Influence of $AR$ on lift and drag coefficients of rigid flat plates and mem-	
	brane wings. Shaded regions represent the measured standard deviation $(\sigma)$ in the aerodynamic coefficients. Additionally, spectral $(PSD)$ infor-	
	mation of the membrane wing lift coefficient (top) indicate low Strouhal	
	numbers at onset of stall. The intensity of fluctuations is lower for lower $AR$ .	54
4.2	Hysteresis in lift for membrane wings around zero angle-of-attack, modi-	0-
	fying with aspect-ratio	55
4.3	Influence of $AR$ on aerodynamic range, $C_L/C_D$ , and power efficiency, $C_L^{3/2}/C_D$ , of rigid flat plates and membrane wings, including error-bars	
	that indicate uncertainty. $\dots$	56
4.4	Pitching moment coefficient $C_{M/4}$ (mean and std) and its spectra ( $PSD$ ) for rigid flat plate and membrane wings	57
4.5	Influence of $AR$ on chord-normal membrane mean deflection $\overline{z}_{max}/c$ along	01
1.0	the wingspan. Note that $AR$ -2 case exhibits larger tip deformations,	
	probably due to strong localised tip-vortex which breaks down at $\alpha > 25^{\circ}$ . The $AR$ -1 case shows U-shape deflections along the wingspan and	
	could reflect a movement of the tip-vortex to the wing root	59
4.6	Illustration of membrane mean deflection $\bar{z}_{max}/c$ along the wingspan are shown in absolute dimentions [mm]. Direct comparison of $AR$ -2 Fig-	
	ure $4.5a$ and $AR$ -1 Figure $4.5b$ wings. Both wings show little overlap in their absolute values, suggesting significant different flow conditions	
	between both aspect-ratios	59
4.7	Chordwise location of maximum camber $(\frac{1}{c} x_{\overline{z}_{max}})$ at four sections along the span, modifying with angle-of-attack and aspect-ratio. Lines represent	
	mean values, shading standard deviation.	60
4.8	Influence of $AR$ on spatio-temporal characteristics of membrane deformation (mid-semispan, $\alpha = 25^{\circ}$ ).	62
4.9	Instantaneous membrane vibrations $z'(x,t) = \frac{1}{c}(z(x,t) - \overline{z}(x))$ as a function of time for different aspect-ratios and angles of attack at mid-span. Note clear standing-wave characteristics of the membrane vibrations across all cases. Reduced vibration intensities for low $AR$ wings is accompanied with increasing chordwise mode numbers. A video for $\alpha = 30^{\circ}$ is available	
4.40	via: https://youtu.be/3piItqwoo_g	62
4.10	Fluctuation intensity along the chord (at mid-semispan position $50\%$ ) and along the wingspan with changing angle-of-attack and $AR$ .	64
	Contribution of first 10 spatial sinusoidal mode shapes $\sigma_n(\alpha)$ of chordwise membrane vibrations and their overall variation in spectral content with angle-of-attack at mid-semispan location. (a) Relative contribution of individual mode shapes $\sigma_n(\alpha)$ to the overall chordwise deformation of the membrane (normalisation with total energy content $ \sigma(\alpha)  = \sum_{n=1}^{\infty} \sigma_n$ ) for various angles of attack, aspect-ratio at the midspan of the wing. Also shown in the figure are the shapes of the first 6 modes. (b) Variation in peak spectral energy content $E(St)$ (eq.3.4) of the first 10 modes Dominant frequencies for various angles of attack in membrane motion	65
7.14	(red) and lift coefficient $C_L$ (blue) of a membrane wing with $AR$ -1	66
5.1	Lift and drag coefficient for rigid flat-plate and membrane wings, changing distance to ground at constant $\alpha$ .	70

LIST OF FIGURES xix

5.2	Lift and drag coefficient changing with height and angle-of-attack	72
5.3	Lift and drag increment in relation to values out of GE (where $h/c=2$ ).	73
5.4	Aerodynamic range efficiency changing with angle-of-attack and height-	
	over-ground	74
5.5	Variation of lift fluctuations (a) and its spectral content (b) with angle-	
	of-attack and height above ground	75
5.6	(a) Time-averaged pitching moment coefficient $C_{M/4}$ for rigid flat plate	
	and membrane wing in and out of ground-effect. (b) Fluctuations of	
	$\sigma(C_{M/4})$ around the mean is displayed for membrane wings in blue shad-	
	ing	77
5.7	(a) Exemplary time-averaged membrane mean surface deflection and fluc-	
	tuation intensity $(h/c=2, \alpha=25^{\circ})$ . (b) Cross-sections at mid-span for	
	mean camber modifying with $\alpha$ and $h/c$ . Note the steaper incline in	
	camber within ground-effect for the lower angle-of-attack	78
5.8	Variation of membrane maximum mean deflection and maximum stan-	
	dard deviation with angle-of-attack for four heights-over-ground	<b>7</b> 9
5.9	Time averaged (a), time variant (b) and spectral content (c) of membrane	
	oscillations for three different heights and a given incidence of $\alpha=15^\circ$	81
5.10	POD analysis on membrane fluctuations, showing spatial (a) and spectral	
	(b) contribution of POD modes at a fixed incidence of $\alpha = 15^{\circ}$ for different	
	heights above ground. POD contours show normalised amplitude peaks	
	in red/blue and their zero level in green color	82
5.11		
	(b) contribution of POD modes in free-flight conditions $(h/c=2)$ for three	
	different angles-of-attack $\alpha = [15, 20, 25]^{\circ}$ . An increase in angle-of-attack	
	in free-flight conditions is found to modify membrane dynamics similarly	
	as seen for a reduction in height-over-ground at a fixed (pre-stall) angle	
	(Figure 5.10). Note the shedding induced excitation of the wing frame	
	at $\alpha = 25^{\circ}$ in POD mode a2 (the outer wing frame oscillates vertically	0.0
<b>-</b> 10	up/down in counterbalance with the membrane center)	83
5.12	PIV-setup with flow in streamwise plane (Flow based coordinate system,	0 =
<b>-</b> 10	see also Section 3.3.5)	85
5.13	Freestream normalised velocity magnitude and streamlines for rigid flat-	
	plate and membrane wings at $\alpha = [10, 15, 25]^{\circ}$ , modifying with height-	0.0
F 1.4	over-ground $h/c = [2, 0.25, 0.1]$	86
5.14	Turbulent kinetic energy for rigid flat-plate and membrane wings at $\alpha = 10^{-15}$	00
F 1F	[ 10, 15, 25 ]°, modifying with height-over-ground $h/c = [2, 0.25, 0.1]$ .	88
5.15	Time-averaged vorticity for rigid flat-plate and membrane wings at $\alpha = 1.0 \cdot 15^{-10}$	00
F 10	[ 10, 15, 25 ]°, modifying with height-over-ground $h/c = [2, 0.25, 0.1]$ .	89
5.10	Instantaneous snapshot of horizontal $(U')$ , vertical $(V')$ velocity and vor-	
	ticity ( $\omega'$ ) fluctuations. Additionally, streamlines are illustrated, based on	
	velocity fluctuation components $(U', V')$ . Instantaneous membrane fluctuations are shown applified by factor of 7 for clarity. Effect of POD	
	tuations are shown amplified by factor of 7 for clarity. Effect of POD as filter technique on highly dynamic flow components and streamlines	
	(using the first five modes). Exemplary case: Extreme GE $(h/c = 0.1)$ at	
	(using the first five fields). Excliping case. Extreme GE ( $n/c=0.1$ ) at $\alpha=15$ °	90

xx LIST OF FIGURES

5.17	Fluctuation snapshot on averaged velocity fluctuations $\sqrt{(U'^2+V'^2)}$ (upper) and its POD reconstruction with two to five POD-modes. Decomposition with five-POD mode shapes (lowest contour plot) shows additionally streamlines for clear vortex identification. Exemplary case: Extreme GE $(h/c=0.1)$ at $\alpha=15$ °. Five POD-modes sufficient enough to repli-		
5.18	cate major flow features	•	91
5.19	at $\alpha = 15$ °		92
	$\sqrt{(U_{POD}^{\prime 2}+V_{POD}^{\prime 2})}/U_{\infty}$ . Comparison of rigid flat-plate and membrane wings at moderate angle-of-attack of $\alpha=15$ °, changing from free-flight $(h/c=2)$ into extreme GE $(h/c=0.1)$ . Rigid flat plates show mid-wing to TE located dynamics in vortex-shedding, moving downstream with GE (Video via: https://youtu.be/1UfPYYo8s5g). Membrane wings show with the descent into GE flow dynamics happening close to membranes		
F 20	surface (Video via: https://youtu.be/aD-jtUUiWOQ).		93
5.20	Five most energetic POD mode shapes of averaged velocity fluctuations $\sqrt{(U_{POD}^{\prime 2}+V_{POD}^{\prime 2})}/U_{\infty}$ . Comparison of rigid flat-plate and membrane wings in post-stall conditions of $\alpha=25$ °, changing from free-flight $(h/c=2)$ into extreme GE $(h/c=0.1)$ . Rigid flat plates show vortex-shedding happening downstream of TE (Video via: https://youtu.be/pJkT0pRF1Y4). Membrane wings show in free-stream conditions strong dynamics close to membrane surface (b), which remain but detach from the wing surfance within GE conditions (d) (Video via: https://youtu.be/KoA-W_MuQtQ).		94
5.21	Spectral content of flow fluctuations $V'$ for rigid flat-plate and membrane wings, illustrated at a selection of listener points $(L1,,L5)$ in the wake.		
5.22	Exemplary case at $\alpha=15$ ° and $h/c=0.1$	•	95
	and $h/c = 0.1$		96
5.23	Summary of vortex-shedding frequency, comparing rigid flat-plates and membrane wings at different angle-of-attack and height-over-ground. The dominant Strouhal number of rigid flat plates (red-points) matches well to literature based flat/cambered plates (blue-shaded $d/\sin\alpha$ rule, where		
5 24	$0.17 \le d \le 0.23$ , see Rojratsirikul et al. (2011))		97
0.24	nate system, see also Section 3.3.5)		98
5.25	Effect of angle-of-attack on tip-vortex velocity magnitude and its position to the projected wing frame. Comparison of rigid flat-plate and membrane wings at $\alpha = [10, 15, 25]^{\circ}$ in free-flight conditions $(h/c = 2)$		99
5.26	Effect of height-over-ground on tip-vortex velocity magnitude and its po-	•	00
	sition to the projected wing frame. Comparison of rigid flat-plate and membrane wings at $\alpha=15$ °		99

LIST OF FIGURES xxi

5.27	Effect of height-over-ground on time-averaged, axial tip-vortex vorticity	100
F 90	magnitude, measured at a fixed angle-of-attack of $\alpha = 15^{\circ}$ .	. 100
5.28	Normalized circulation of the tip-vortex for rigid flat-plate and membrane wings as function of angle-of-attack (upper plot) and height-over-ground	
	(lower plot)	101
5 20	Instantaneous snapshot of freestream-normalised velocity fluctuations $U'$	. 101
0.23	(out-of-plane), $V'$ (vertical), $W'$ (spanwise). Additionally, streamlines are	
	illustrated, based on in-plane velocity fluctuation components $(V', W')$ .	
	Effect of POD as filter technique on highly dynamic flow components	
	and streamlines (usage of 5-modes). Exemplary case: Membrane wing	
	at $\alpha = 15^{\circ}$ in extreme GE $(h/c = 0.1)$ conditions. Videos are available	
	for the original (https://youtu.be/v23WQJzmL2U) and the POD-filtered	
	flow (https://youtu.be/5rKJUogbgj8)	. 102
5.30	Spectral analysis of vertical flow oscillations $PSD(V')$ at listener points	
	L6,,L10. Comparison between rigid flat-plate and membrane wing in	
	free-flight $(h/c=2)$ at $\alpha=25^{\circ}$ and extreme ground-effect $(h/c=0.1)$ at	
	$\alpha = 15^{\circ}$ . Membrane wings (b,d) show very distinct dominant shedding	
	frequencies in the flow which match well with the dominant oscillation	
	frequencies of the membrane (green line), suggesting membrane dynamics induced modifications in vortex shedding and fluid-membrane coupling.	104
5 31	(a) Time series of $C_L$ , $C_D$ and instantaneous membrane deformation $(z')$	. 101
0.01	for $\alpha = 15^{\circ}$ at three different heights over ground. (b) Cross correlation	
	between force coefficients and membrane deformation (wing body based	
	coordinate system, see Section 3.3.4)	. 105
5.32	(a) Extension of Figure 5.31 with added force angle $\gamma(t) = \frac{1}{20} atan(\frac{C_D}{C_L})$	
	[°] as alternative value for instant aerodynamic performance (green line in	
	Figure 5.32a), indicating temporal thrust producing periods if $\gamma(t) < 0$ .	
	(b) Cross-correlation of force angle $\gamma$ to membrane deformations. The	
	correlation of the membrane to the performance parameter $\gamma$ appears	
	with CCF = 0.24 weak but measureable at cases with generally enhanced	
	fluid-structure coupling (Figure 5.32b, lower $\Rightarrow$ ground-effect enforced fluid-structure coupling). Membrane wings at $\alpha = 15^{\circ}$ at three different	
	heights over ground	107
5.33	(a) Time series of $C_{M/4}$ and instantaneous membrane deformation $(z')$	. 101
0.00	for $\alpha = 15^{\circ}$ at three different heights over ground. (b) Cross correlation	
	between $C_{M/4}$ and membrane deformation	. 108
5.34	Cross-correlation (CCF) between vertical membrane fluctuations at point	
	M(x/c = 0.4) and vertical flow fluctuation velocity $(V')$ at listener point	
	P. Instantaneous membrane fluctuations are shown amplified by factor	
	of 7 for clarity. Correlations are conducted for the streamwise (a) and the	
	spanwise (b) PIV-plane. Exemplary case is at $\alpha = 15^{\circ}$ within extreme	
	GE $(h/c = 0.1)$	110
5.35	Cross-correlation (CCF) between vertical membrane fluctuation at point	
	M (x/c=0.4) and vertical flow fluctuation velocity (V') at listener point	
	$(P_n)$ , changing with height-over-ground at a fixed angle $\alpha = 25^{\circ}$ . The contour plots base on zero time lag. Instantaneous membrane fluctuations	
	are shown amplified by factor of 7 for clarity	111

xxii LIST OF FIGURES

5.36	Load-membrane-flow interactions at $\alpha = 15^{\circ}$ in extreme GE of $h/c = 0.1$ . (a) Time-snapshots (t1, t2, t3) for vertical flow and membrane fluctuations during one cycle. Streamlines based on POD-filtered flow fluctuations. (b) Time-corresponding development in lift, drag and pitch moment fluctuations. (c) Spectral signature of load-membrane-flow dynamics and their (d) phase-relation between each other. Membrane dynamics show strong coupling with LE-vortex-shedding, allowing improvements in overall prings performance.	116
5.37	all wing performance	. 112
5.38	https://youtu.be/728DsVxNcL4 Load-membrane-flow interactions at $\alpha=25^\circ$ in extreme GE of $h/c=0.1$ . (a) Time-snapshots $(t1,\ t2,\ t3)$ for vertical flow and membrane fluctuations during one cycle. Streamlines based on POD-filtered flow fluctuations. (b) Time-corresponding development in lift, drag and pitch moment fluctuations. (c) Spectral signature of load-membrane-flow dynamics and their (d) phaseal relation between each other. With the descent into GE, flow and membrane dynamics get out of phase. The overall correlations reduces drastically, resulting in reduced coupling between lift, membrane and flow dynamics.	
5.39	Membrane based cycle-averaged load (left) and vertical flow dynamics from both streamwise/spanwise PIV experiments (right), illustrated for $h/c=0.1$ and $\alpha=15$ °. Vertical membrane and flow fluctuations are colored red for upwards and blue for downwards motions. A flow listener point L1 is placed in both PIV-planes for later tracking in Figure 5.40. A video is available via: https://youtu.be/KA6BZrtAb3o	
5.40	Membrane based cycle-averaged loads and flow dynamics at listener point L1 for either GE (plot (a), $h/c=0.1$ at $\alpha=15^{\circ}$ ) or high angles-of-attack induced coupling (plot (b), $h/c=2$ at $\alpha=25^{\circ}$ )	
6.1	Seperation between aerodynamic impact of static wing cambering and dynamic membrane oscillations. Comparison of (a) lift, (b) aerodynamic efficiency and (c) flow characteristics between a rigid flat-plate wing, a membrane wing and a rigid cambered-plate with the same membrane mean shape (current study combined with results of Gordnier and Attar (2014) and Rojratsirikul et al. (2009))	. 122
A.1 A.2 A.3 A 4	First prototype membrane wing WIG-UAV drawings  Membrane wing structure  Usage on different surfaces  Vehicle in flight	. 140

## List of Tables

3.1	Half wing dimensions	22
3.2	Uncertainty analysis of streamwise (planar) PIV results	17
3.3	Uncertainty analysis of spanwise (stereo) PIV results	5(
A.1	Data-sheet of WIG-UAV	11
A.2	Equipment list of WIG-UAV	11

### Chapter 1

### Introduction

### 1.1 Overview

Moderate Reynolds number flight (Re =  $10^4 - 10^5$ ) is known to require different wing designs which differ to typical high Reynolds number layouts. Moderate Reynolds number flow conditions come with a weak boundary layer and low energetic flow conditions, resulting in a low lift-to-drag ratio (Figure 1.1), problems with lift generation, and flow attachment (McMasters and Henderson, 1979; Lissaman, 1983).

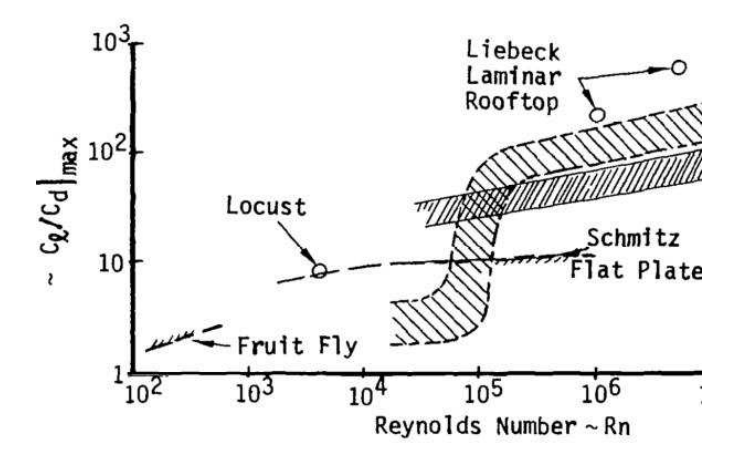


Figure 1.1: Fundamental limitations in aerodynamic efficiency for moderate Reynolds number flow conditions ( $10^4 \le Re \le 10^5$ ) (McMasters and Henderson, 1979).

Nature offers with membrane wings of bats and feathered wings of birds different solutions for enhancing the flight performance in this challenging moderate Reynolds number flow regime. The aerodynamic efficiency between the two wing types were found in favour to bird wings and their benefit was suggested to be linked with their need to cover longer migration distances and higher flight speeds (Muijres et al., 2012). On the other hand, membrane wings of bats are known for performance benefits in a cluttered

surrounding (Swartz et al., 2012) and show a high manoeuvrability with the ability of high turn-rates (Tian et al., 2006). In addition, thin and flexible membrane wings could offer options of a reduced wing mass, high impact resistance, low damage potential by impact on objects/persons, and easier foldability, making them specifically interesting for applications on MAV and their usage in densely populated cities (Shyy et al., 2005). Therefore, the current study focusses on bat-inspired membrane wings.

Based on thin, flexible membrane wings of bats, some criteria are found specifically important for enhancing the flight performance of MAVs in moderate Reynolds number flow conditions. First, the wings typically involve low-aspect-ratios (LAR), which allow the development of tip-vortices that entrain freestream fluid closer to the surface thereby promoting lift generation (Shields and Mohseni, 2013). Second, thin airfoils allow early leading-edge vortex formation, which can be used in combination with flexible airfoils to couple membrane and shedding dynamics, allowing retention of these (lift-producing) vortices closer to the wing surface (Muijres et al., 2008; Rojratsirikul et al., 2009).

Experimental studies on rigid flat-plates for MAVs highlights the influence of the aspectratio (AR) as the most affecting parameter for changes in the aerodynamics of LAR wings (AR-1 to 2). However, changes in aspect-ratio of flexible membrane wings could alter the surrounded flow which in turn could change the static cambering, membrane dynamics and the overall aerodynamic performance. Therefore, one key element of this study focusses on the implications of aspect-ratio changes in combination with flexible membrane wings.

Wings in moderate Reynolds number flow conditions are known for their strong limitations in aerodynamic efficiency (Figure 1.1). Membrane wings show improvements in the overall lifting performance by making use of static cambering and membrane dynamics, however, this often comes with additional drag penalties and efficiency constrains. Making use of ground-effect conditions could be one operation solution to extend the aerodynamic wing performance. A combination of flexible wings, used in ground-effect, could combine flexibility related lift, stall and gust reaction benefits with ground-effect related gains in lift and aerodynamic efficiency. As a result, MAVs with membrane wings in ground-effect might carry higher payloads, travel longer distances and could cope better with unsteady flow conditions. Therefore, the second part of this thesis concentrates on the elaboration of membrane wings in ground-effect conditions.

### 1.2 Motivation

The development of advanced MAVs has to cope with the major question: how to extend the mission range, flying time and vehicle stability in moderate Reynolds number flows? The flexibility of membrane wings in contrast to rigid wings offers an additional parameter to change the flow and thus the aerodynamics in a beneficial way. Previous

studies compared membrane wings with similar (mean cambered) rigid wings and found that the vibrations in the membrane energise the boundary layer over the airfoil, resulting in smaller recirculating areas and delayed flow separation regions (Gordnier, 2009; Rojratsirikul et al., 2009). The vibrations in the membrane promote an early leading-edge vortex roll-up which account for strengthened low pressure regions over the wing top surface. As a result, it is possible to improve post-stall aerodynamics with the usage of membrane wings.

The inherent flexibility of membrane wings allows to stimulate chordwise as well as spanwise deformations. Changes in aspect ratio result in the modification of the surrounded flow which in turn changes the deflection of the membrane. This phenomena of flow-structure interaction is found to be most distinct for aspect ratios between AR-1.0 and AR-2.0, where tip vortices start to gain influence over large regions of the wing (Torres and Mueller, 2004; Mizoguchi and Itoh, 2013). Previous membrane wing studies (Song et al., 2008) focused mainly on the influence of aspect-ratio on static lift and drag coefficients, whereas dynamic effects have not been considered in detail. Other studies focused on the dynamics of membrane wing motions, however restricted to one specific aspect ratio (Galvao et al., 2006; Rojratsirikul et al., 2011; Hubner and Hicks, 2011; Attar et al., 2012; Albertani et al., 2007; Hu et al., 2008). Detailed knowledge of the effect of aspect-ratio to membrane motions, changes in the flow and aerodynamic performance is essential to understand the flexibility modified performance envelope of low-aspect-ratio membrane wings.

It is known that MAVs, equipped with membrane wings, are able to improve their maximum lift production and stall characteristics by allowing static cambering and the development of vortical (low-pressure) shedding structures close to the upper wing surface (Tregidgo et al., 2011, 2012). However, the added gain in lift production is accompanied with an increase in drag, resulting in a strong limitation of the aerodynamic efficiency. Improvements in the aerodynamic efficiency are of specific high value in moderate Reynolds number flows, where wings suffer from significant performance constrains in comparison to high Reynolds number flows (McMasters and Henderson, 1979), limiting fundamentally the range and flight time of MAVs (Mueller, 1999; Mueller and DeLaurier, 2003; Pines and Bohorquez, 2006; Grasmeyer and Keennon, 2000).

During the decade of 1960s, Russian engineers developed a variety of large scale Wing In Ground (WIG) effect vehicles (Udalov and Belyaev, 1999; Komissarov and Gordon, 2010). The main aim focused on the radar invisibility and amphibious qualities. Further high Reynolds number wind tunnel tests showed significant improvements in aerodynamic efficiency and improved payload capacity of wings in the vicinity of the ground (Yun et al., 2010). However, very few studies are available on ground-effect based gains at moderate Reynolds number that we can utilise to design MAVs in ground-effect. Those studies which exist focus purely on rigid wings (Rozhdestvensky, 2000; Pistolesi,

1937). To the current knowledge of the author there are no experimental (as well as computational) studies to date that have explored the performance of moderate Reynolds number membrane wings in the vicinity of the ground. Wind tunnel test could be of high value to understand the flow-structure-ground interaction of membrane wings with the ultimate aim to apply the idea on MAVs with improved gust capabilities, combined with enlarged range and power efficiency by flying close to the ground.

### 1.3 Research Objectives and Approach

The first part of this work focusses on the influence of aspect-ratio on the aeromechanics of rectangular, simple leading/trailing-edge supported membrane wings in free-flight conditions. The following open questions are addressed in the first part of this thesis:

- What are effects of changes in aspect-ratio on the aerodynamic performance of membrane wings and how do these changes compare with thin rigid flat-plate wings?
- How does the pitch stability of membrane wings change with aspect-ratio and how does it compare with thin rigid flat-plate wings?
- How do membrane spatial and temporal oscillations modify with aspect-ratio?
- How do membrane oscillations correlate with dynamics in aerodynamic loads?

These open questions are examined by conducting wind tunnel experiments with time-resolved force and moment measurements by a load cell from which time-averaged and time-resolved aerodynamic properties (lift, drag, and pitch moment) are determined. Rigid flat-plate and membrane wings are compared for three different aspect-ratios (AR-1.0, 1.5, and 2.0) at a moderate Reynolds number of Re = 67,500. High-speed photogrammetry is applied separately to capture static and dynamic chordwise membrane motions at four different wingspan positions.

The second part of this thesis considers the influence of ground-effect on rigid flatplate and perimeter-reinforced membrane wings at similar moderate Reynolds numbers conditions. The following open questions are tackled:

- Could MAVs with rigid flat-plate wings at moderate Reynolds number benefit from a higher aerodynamic efficiency by flying in ground-effect?
- Does a membrane wing provide even superior aerodynamic performance in groundeffect and if so why?

- How does pitch and height stability change with ground-effect and how does it affect both wing types?
- What are the differences in the flow features for rigid flat-plate and flexible wings in ground-effect?
- How do flow, membrane and load dynamics change in close proximity to the ground?

In order to answer these questions, the aerodynamic performance of rigid flat-plate and perimeter-reinforced membrane wings is compared at a moderate Reynolds number (Re = 56,000) for different heights-over-ground and angles-of-attack. Load cell measurements, digital image correlation (DIC) and particle image velocimetry (PIV) are applied in high-speed to resolve time-synchronised lift, drag and pitch oscillations simultaneously with membrane and flow dynamics. PIV acquisition is conducted parallel and normal to the free-stream direction, showing flow-structure interactions above/below the wing at quarter-span and in a cross-flow-plane placed one chord downstream of the trailingedge. Time-resolved loads are used to extract mean values in lift, drag and pitch moment coefficients, their average fluctuation intensity and spectral content. Similarly, timeresolved membrane deformations are used to calculate mean deflection, fluctuation intensity, spectral content, whereas proper orthogonal decomposition (POD) is conducted to determine the spatiotemporal evolution of the membrane motions. Time-resolved flow results are used for time-averaged flow statistics and flow dynamics (POD-based). Selective cases involve time-synchronised load, membrane and flow measurements which reveal underlying coupling physics between each other.

#### 1.4 Thesis Outline

The thesis outline starts in Chapter 2 with a literature survey which covers the fundamental aeromechanics of membrane wings, effects of aspect-ratio and ground-effect. Chapter 3 illustrates the experimental facility as well as measurement and analysis techniques that were used for the two different experiments to examine the effects of aspect-ratio and ground-effect. Chapter 4 focusses on the effect of aspect-ratio and its impact on aerodynamic loads and membrane deformations. Most of the work in this chapter has been published as a journal article (Bleischwitz et al., 2015b). Chapter 5 focusses on the impact of ground-effect on the loads, membrane motions and flow structures. The aspects related to the loads and membrane motions has been published as a journal article (Bleischwitz et al., 2016). This chapter also presents results that show correlations between loads, membrane and flow dynamics. Finally, Chapter 6 discusses the key results and provides ideas for future work. The Appendix A includes details about a Wing-In-Ground UAV with membrane wings, the development of which led to the exploration of different concepts presented in this thesis.

### Chapter 2

### Literature Survey

### 2.1 Aeromechanics of Membrane Wings

### 2.1.1 Membrane Wing Types

Typical membrane wings for MAVs consist of a rigid support structure which transfers aerodynamic loads from the membrane to the main (center) body. The aerodynamics of membrane wings are largely effected by the attachment method of the membrane and the general layout of the wing frame. Figure 2.1 shows the three most common membrane wing configurations of perimeter (Tregidgo et al., 2011; Rojratsirikul et al., 2010b; Albertani et al., 2007), batten (Hu et al., 2008; Waszak and Jenkins, 2001; Timpe et al., 2013; Albertani et al., 2007), and leading/trailing-edge supported wing designs (Song et al., 2008; Galvao et al., 2006; Arbos-Torrent et al., 2013a).

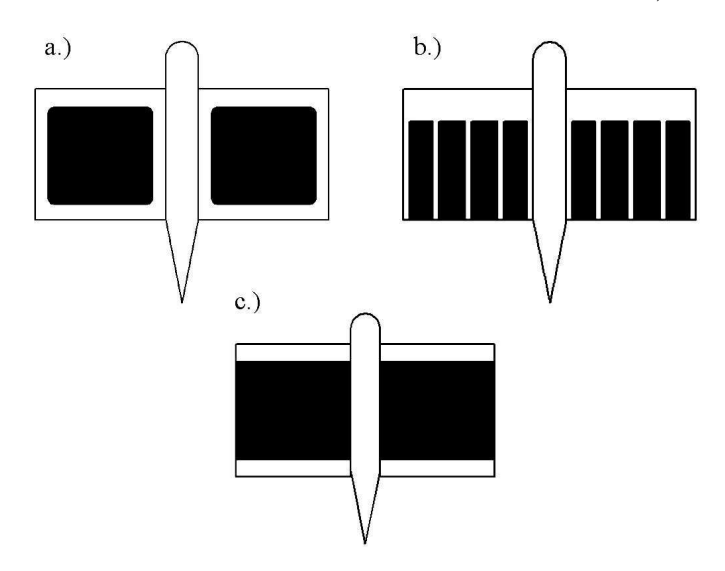


Figure 2.1: Membrane wing types: a.) Perimeter supported b.) Batten supported c.) Leading/trailing-edge supported with free root/tip

The wing structures depend on the attachment region of the membrane on leading-edge (LE), trailing-edge (TE), root, and tip and allow for varying degrees of adaptability. The perimeter support configuration (Figure 2.1a) allows large but wing tip constrained cambering. The batten support configuration (Figure 2.1b) allows the membrane to flex and reduce effective angle-of-attack for passive wash-out, reducing gust impact on the vehicle movement. The leading/trailing-edge support configuration (Figure 2.1c) allows the membrane to deflect along its full span, which gives this membrane configuration the ability to adapt to the flow to a high extent.

The aspect-ratio related experiment of this thesis considers leading/trailing-edge supported membrane half wings (Figure 2.1c) because they represent a simple and common attachment method for wings in MAVs, where the fuselage is located in the mid axis with wings attached to either side of the fuselage. In addition, this membrane wing type offers low attachment constrains, allowing to study large membrane deformations which are easier to resolve. The ground-effect related experiment of this thesis considers a perimeter-reinforced membrane wing design (Figure 2.1a) due to available reference studies and mounting issues.

#### 2.1.2 Load Performance

Figure 2.2 compares the aerodynamic lift and pitch coefficient between rigid and batten / perimeter-reinforced membrane wings. The billowing effect of perimeter-reinforced membrane wings was found to reach higher lift slopes (Figure 2.2a), higher lift coefficients and an improved pitch stability (Figure 2.2b). Batten-reinforced membrane wings have in contrast to perimeter-reinforced membrane wings a very similar lift slope to rigid wings. On the one hand, billowing of the membrane between the battens increases the lift slope by static cambering. On the other hand, adaptive washout reduces the effective angle-of-attack by lifting up the unsupported trailing edge between the battens, resulting in a reduction in the lift slope. Therefore, these two competing effects result in a lift slope that stays comparable to a rigid wing. Figure 2.2 does not include the aerodynamics of LE/TE supported wings with free root/tip and there is currently (to the authors knowledge) no literature available which references the aerodynamics of leading/trailingedge supported membrane wings (Figure 2.1c) to other membrane wing types. The results are seen as essential to validate the two different membrane wing types, which will be both individually considered within this thesis. Therefore, a part of this thesis will cover the aerodynamic effects between perimeter-reinforced (Figure 2.1a) and free root/tip (Figure 2.1c) membrane wings (see later in setup validation, Figure 3.20).

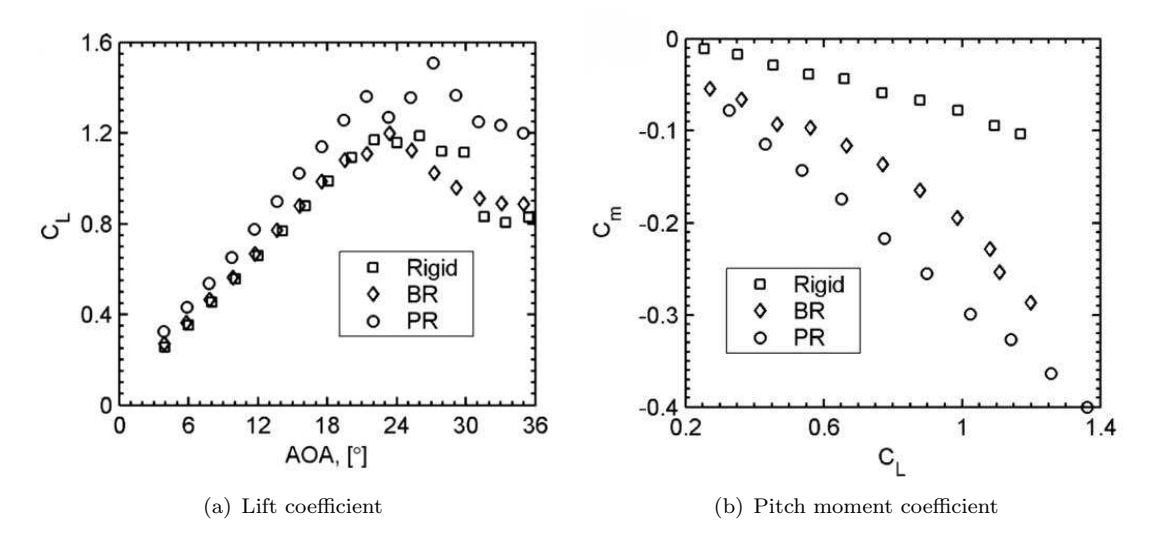


Figure 2.2: Lift and pitch behaviour of rigid and membrane wings (PR = perimeter-reinforced (Figure 2.1a), BR = batten-reinforced (Figure 2.1b)) (Albertani et al., 2007).

#### 2.1.3 Membrane Motions

The inherent flexibility of membrane wings allows to static camber with the incoming aerodynamic pressure. For typical MAV applications, membrane wings show up to 15 % (chord-related) static out-of-plane camber displacements (Song et al., 2008). This camber range of membrane wings appears relatively large in comparison to rigid cambered-plates, which were found to perform best for 6% to 9% camber (Null and Shkarayev, 2005). Membrane oscillations are known to appear above the mean camber (typically 1-10 % of mean displacement) and are suggested to be a key factor to enhance lift production even under large cambering and close-to-stall conditions (Gordnier and Attar, 2014; Rojratsirikul et al., 2010a). Figure 2.3 shows two examples of instantaneous membrane oscillations (wing structure with fixed LE/TE) which are excited due to boundary layer perturbations (at lower incidences) and/or leading-edge vortex shedding (at higher incidences).

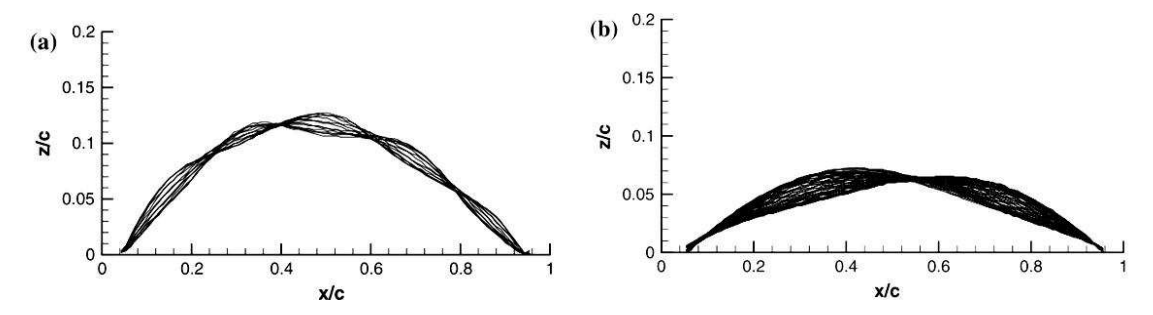


Figure 2.3: Instantanious membrane wing oscillations for two different angle-of-attack, showing a membrane mode 5 (five peaks) and a membrane mode 2 oscillation (Rojratsirikul et al., 2009).

The membrane motions base on the fundamental membrane eigen mode shapes and their harmonics. An exemplary mode—shape 1 represents the fundamental breathing—mode without any node (a single peak). Mode—2 reflects the first harmonic as a bending mode with one single node in the center of the chord (two peaks). Mode—3 is represented by two nodes as the second harmonic (three peaks), and so on.

Within low angles-of-attack around zero, membrane wings exhibit large membrane fluctuations (accompanied with low mode numbers) due to low aerodynamic loading (lack of membrane tension) and a bi-stable nature of flexible membranes (snap-through effect). For moderate angles-of-attack, membrane vibrations tend to reduce in amplitude and increase in mode number with increasing flow-induced tension of the membrane (Figure 2.3 left). Incidences in the vicinity of stall and post-stall reflect high fluctuation intensities and low mode numbers (Figure 2.3 right) which appear to be independent of membrane tension due to excitation with vortex-shedding.

### 2.1.4 Flow Development

The assessment of flow modification is important to understand the source of changes in the aerodynamic performance. Figure 2.4 shows results of an important study of Gordnier and Attar (2014) which compares the turbulent kinetic energy of the flow from rigid flat-plates, over rigid mean-cambered plates to membrane wings at three angles-of-attack. Rigid flat-plates (Figure 2.4, upper horizontal plots) show an early increase in flow dynamics with increasing angle-of-attack.

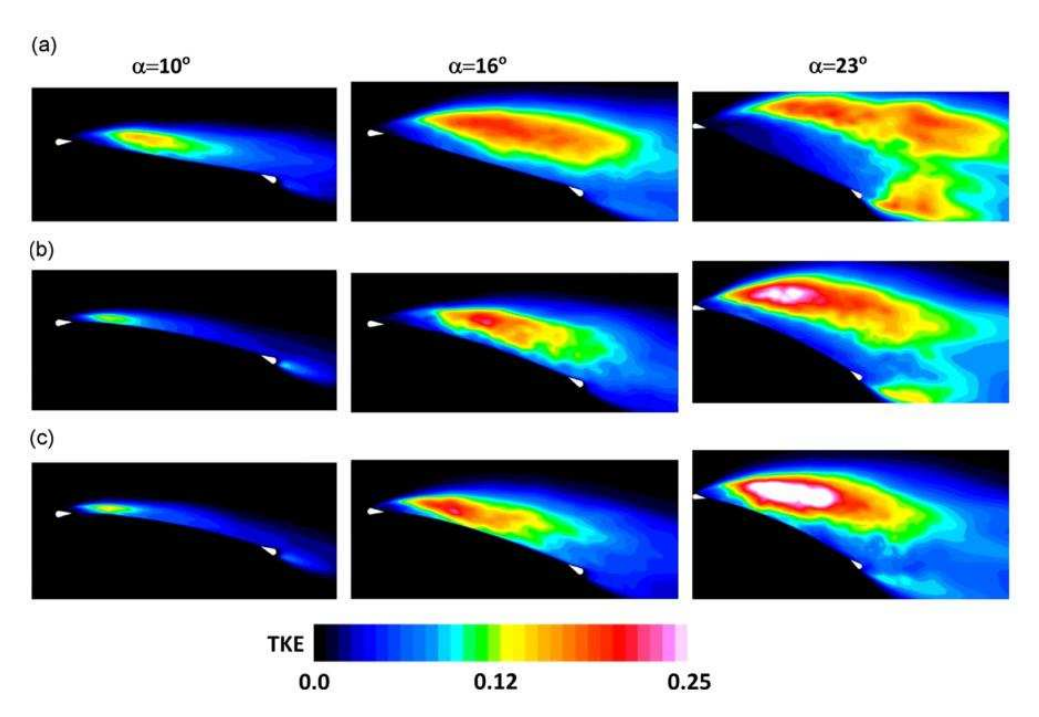


Figure 2.4: Turbulent kinetic energy of the flow for (a) rigid flat-plate, (b) rigid mean-cambered, (c) flexible membrane wing (Gordnier and Attar, 2014).

The shedding induced flow dynamics detach early from the upper wing surface and result in a sudden lift break-down. Rigid cambered-plates (based on membrane mean shape) show reduced flow separations and flow dynamics which appear slightly closer to the the leading-edge. Membrane wings (Figure 2.4, lower horizontal plots) show a concentration of the flow dynamics close to the upper wing surface. In addition, close-to-stall angles-of-attack ( $\alpha=23^{\circ}$ ) show drastically enhanced flow dynamics to both other wings. The results open the fundamental question how wing dynamics can change the flow conditions and what coupling mechanism are important for the illustrated modifications. The question extends further to understand the spatiotemporal flow-membrane-load interactions of flexible membrane wings with the ultimate aim to path the way into performance enhanced membrane wing MAVs with the ability to actively control the flow dynamics by the wing oscillations (active wings are not in focus of this pure passive membrane wing study).

### 2.1.5 Flow-Structure Coupling

Studies of Rojratsirikul et al. (2009), Gordnier and Attar (2014) and (Arce and Ukeiley, 2014) started to understand the coupling dynamics between the membrane and the flow. Figure 2.5 illustrates a key result of Rojratsirikul et al. (2009), showing normalised vibration frequencies of the flow and membrane dynamics for different angles-of-attack and freestream velocities. Membrane and flow frequencies are found to match for specific cases in wing stall conditions, suggesting strong fluid-membrane coupling. Fluid-membrane coupling seems to require a membrane oscillation frequencies which are of the order of the (wake) shedding frequency of the wing. In addition, the shedding structures and membrane dynamics seem to require a certain strength to couple. However, to validate and understand the global coupling mechanisms and their limitations in more detail, experimental studies would need to combine time-synchronised high-speed load, membrane and flow measurements, which are (up to this point) not existent within the current literature.

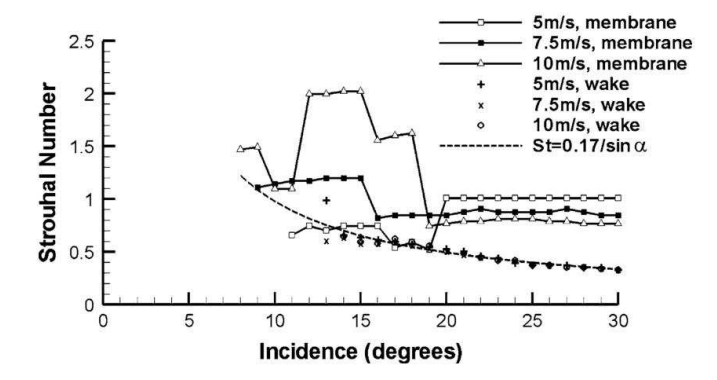


Figure 2.5: Normalised membrane and flow oscillation frequencies, changing with freestream velocity and angle-of-attack (Rojratsirikul et al., 2009).

## 2.2 Effects of Aspect-Ratio

The aspect-ratio is a key parameter for the wing performance at high as well as low Reynolds numbers. Bats typically fly within moderate Reynolds numbers of  $10,000 \le Re \le 100,000$  (Swartz et al., 2012; Neuweiler, 2000) and involve high as well as low aspect-ratios wings, which depend on their natural habitat. Figure 2.6 reflects that bats with larger aspect-ratios are often found for open air and long distance flights, whereas low aspect-ratios are used for slow, low distance flights in cluttered habitats (based on study of Norberg and Rayner (1987), with extension of Canals et al. (2011)).

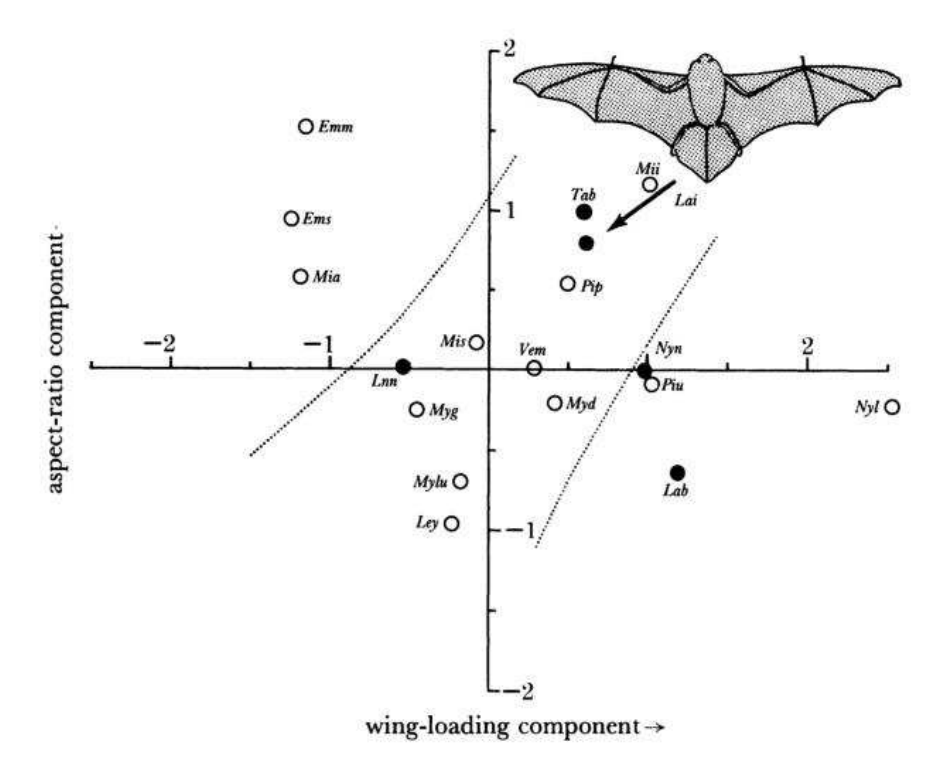


Figure 2.6: Impact of migration distance of bats on aspect-ratio and wing-loading. Filled circles represent migration distances of bats with >1000 km, empty circles between 200 and 1000 km. The axis show difference to average values. (Norberg and Rayner, 1987).

Experiments on simple rigid-flat or cambered-plates highlight the influence of AR as a parameter that significantly affects aerodynamics of LAR wings (AR-1 to 2) (Torres and Mueller, 2004; Okamoto and Azuma, 2011). The tip vortex strengthens with LAR wings and can cover almost 40% of the wing surface (Lian et al., 2003). However, the low pressure of tip vortices can only add additional lifting performance if it is located close to the wing top surface. The overall size, chordwise and spanwise position of the vortex systems depend strongly on the aspect-ratio and angle-of-attack (Mizoguchi and Itoh, 2013).

Figure 2.7a shows the impact of aspect-ratio changes on the lift production of rigid cambered-plates. Higher aspect-ratios show higher lift-slopes and involve sharper and

earlier stall angles. Lower aspect-ratios related gain in tip-vortex strength results in reduced lift slopes and a more horizontal stall characteristic.

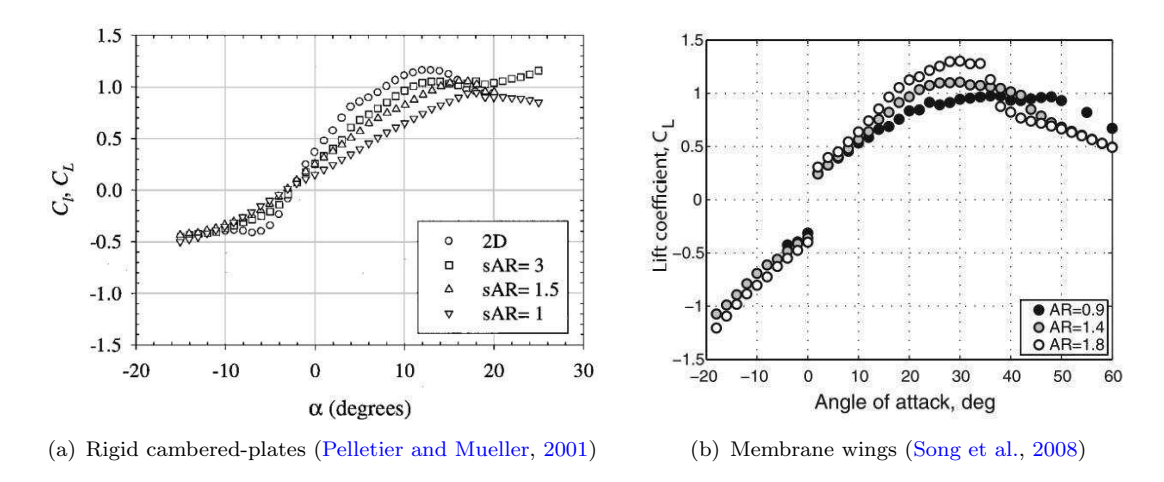


Figure 2.7: Time-averaged lift capability of rigid cambered-plate and membrane wings, modifying with aspect-ratio (two separate studies of Pelletier and Mueller (2001) and Song et al. (2008)).

The ability of membrane wings to interact with the flow raises the question how the aspect-ratio of membrane wings affects not only the membrane mean camber, but also membrane and load dynamics and the overall wing performance. Previous membrane wing studies focused mainly on static lift (Figure 2.7b) and drag coefficients and found similar downwash related effects for AR-changes compared with rigid flat-plates (Song et al., 2008). However, aspect-ratio effects were not in the main focus of this membrane wing study (nor their comparison to rigid flat-plates), which results in a lack of a complete dataset. In addition, membrane dynamics are only available for different membrane wing studies of a certain selected aspect-ratio, making it hard to interpret between the given AR-results. Nevertheless, an exemplary isolated experiment of Song et al. (2008) considered an AR-1.4 wing which exhibited stronger wing tip vibrations than a lower AR-0.9 wing of a different membrane wing study from Galvao et al. (2006). This result could be seen as an indication that membrane dynamics probably react to changing flow conditions, caused by the selection of different aspect-ratios.

In summary, previous aspect-ratio related experiments focused mainly on performance statistics of separately conducted rigid and membrane wing studies and did not consider modifications arising in membrane, load or even coupling dynamics. Additional experiments would be of high value to understand how and why aspect-ratio changes affect the global aerodynamic performance of membrane wings in comparison to their impact on rigid flat-plates.

## 2.3 Ground-Effect

Operating membrane wings close to a surface could be one option to gain efficiency whilst maintaining the stall characteristics and weight benefits of (passive) membrane wings. A wing is said to be in moderate ground-effect if its height from the ground is either lower than half of the wingspan h/b < 0.5 or below one chord length h/c < 1 (Yun et al., 2010), where the height-over-ground is measured from the trailing-edge of the airfoil and normalised with chord length.

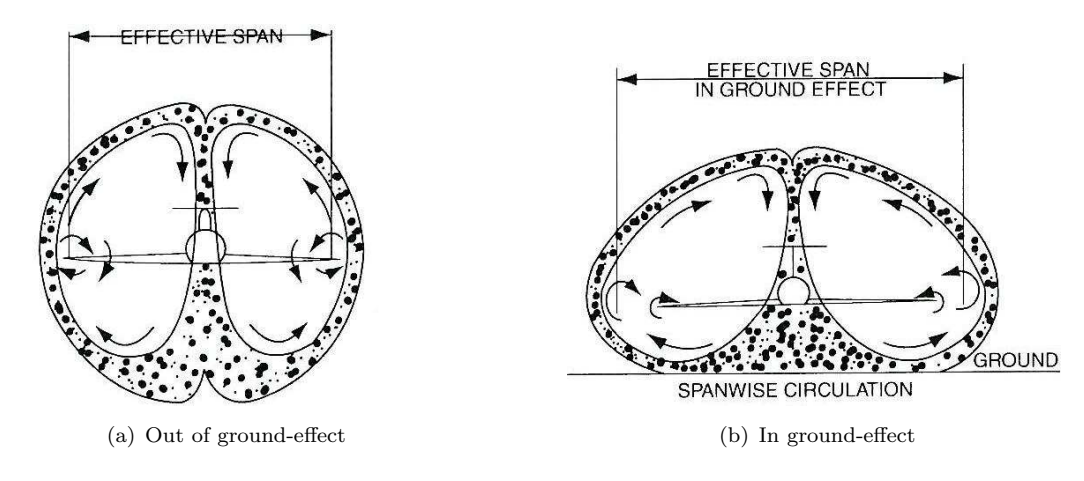


Figure 2.8: Change in flow circulation in and out of ground-effect (Yun et al., 2010).

Ground-effect of common thick airfoils relies on the increase in pressure below the wing which leads to a drop in velocity and results ultimately in a downwards movement of the stagnation point (Ahmed and Sharma, 2005). Extreme ground-effect is defined as h/c < 0.1, where air is forced to stagnate below the wing, causing a large pressure increase, called ram-pressure. As a result, the flow is diverted over the upper wing surface. A wing's effective aspect-ratio is virtually increased by going from free-flight (Figure 2.8a) into ground-effect conditions as the tip vortices are pushed outwards (Figure 2.8b). The interference of the tip vortices with the ground slows down their rotation, accompanied with a reduction in tip-vortex size and strength. As a result, the downwash angle and induced drag are found to decrease in ground-effect, allowing significant benefits in aerodynamic efficiency of up to 100% (Rozhdestvensky, 2006).

The vast majority of ground-effect research has focused on high Reynolds number flows  $Re > 10^5$  passing over thick and rigid wings (Qu et al., 2014, 2015) and their application on Formula-one aerodynamics (Zhang and Zerihan, 2003; Diasinos et al., 2012), trains (Moon et al., 2005) or large Wing-In-Ground (WIG) vehicles (Van Beek and Oskam, 1998; Carter, 1961; Lee et al., 2011). Figure 2.9 shows the concept of such a WIG vehicle in comparison to a conventional high altitude airplane design. A WIG plane (Figure 2.9b) involves typically a reduced aspect-ratio (for turning reason) in combination with end-plates to trap the airflow below the wings surface. A reduction in airfoil

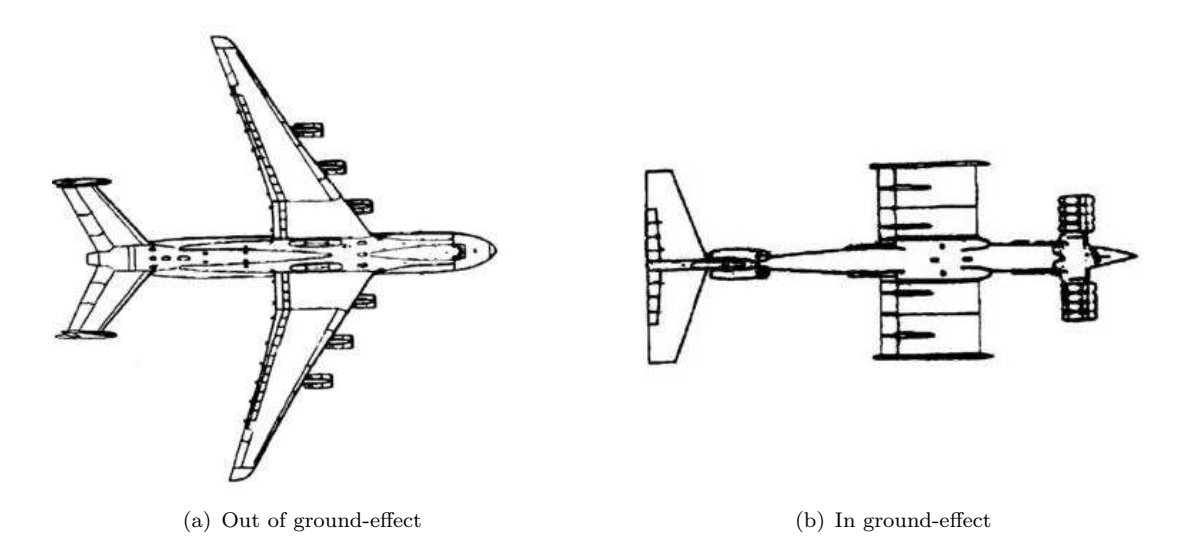


Figure 2.9: Typical wing layout between conventional high altitude and ground-effect airplanes (Rozhdestvensky, 2006).

thickness is found to benefit (lift producing) wings in ground-effect by reducing drag and lowering the risk of negative down-force caused by the Venturi effect (suction on lower concave surface) (Rad and Kazemi, 2001; Moon et al., 2005). An increase in wing camber is found to improve aerodynamic efficiency within ground proximity, but also shows a higher risk of flow separation on the suction side of the wing (Mosaad et al., 2011), which results in stronger limitations in flight incidences where high aerodynamic efficiency can be achieved.



Figure 2.10: Moderate Reynolds number Wing-In-Ground vehicle with membrane wings. Further details can be found in Appendix A.

Studies on Reynolds number influence reveal a reduction in lift coefficient and aerodynamic efficiency with lower Reynolds numbers, which appear even more severe for small ground clearances (Hsiun and Ghent, 1996; Mateescu et al., 2012). Most studies of rigid wings in ground-effect at low to medium Reynolds number date back to the early 20th century and focus on time-averaged aerodynamic performance (Raymond, 1921; Wieselsberger, 1921; Pistolesi, 1937). A recent computational study at Re = 15,000

concentrated more on the dynamics and found enlarged amplitudes in lift oscillation and tip-vortex-ground interactions within close proximity to the ground (Prasad and Damodaran, 2013).

The physics of flexible membrane wings in ground remain still totally unknown and could be important for the development of a membrane wing Wing-In-Ground MAV/UAV (Figure 2.10), aiming to combine improved vehicle range (ground-effect related), flow-structure tuning and smooth gust reaction (membrane related).

## Chapter 3

# Experimental Setup and Method

## 3.1 Wind Tunnel

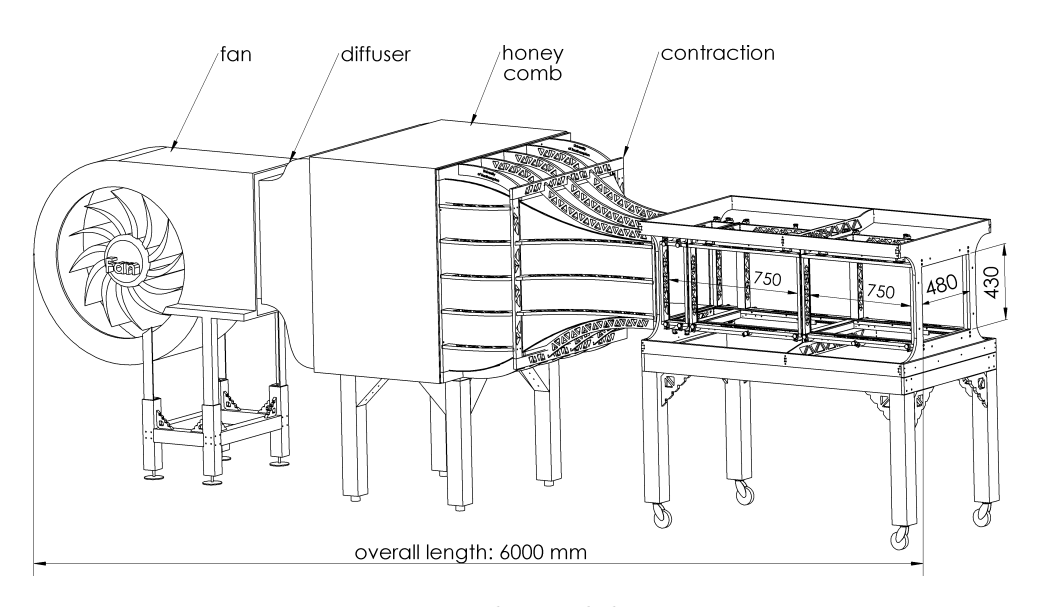


Figure 3.1: Wind tunnel dimensions

Wind tunnel experiments are conducted in an open-loop, low-speed blow-down wind tunnel at the University of Southampton (Figure 3.1). The author designed and built the contraction and test section within the first three months of his research period. The test section measures 43 cm width by 48 cm height with a free-stream turbulence intensity of less than 0.1%. The turbulence level was measured with hot-wire anemometry. The wind speed can be varied between 2 to 14 m/s. The wind speed is determined by measuring dynamic pressure with a pitot-static probe together with barometric pressure and ambient temperature, where the latter two are used to determine the air density  $\rho$ . The typical uncertainty in the free-stream velocity of the wind tunnel is  $\pm 0.1$  m/s and was verified throughout different experiments with flow-field (PIV) and hot-wire

measurements (next to pitot-tube recordings). The experiments were conducted for a chord related Reynolds number between  $56,000 \le Re \le 67,500$ .

The maximum blockage-ratio of all cases is measured no worse than 6% at the wing models, peaking with the highest angle-of-attack case at  $\alpha = 40^{\circ}$  (ground-effect setup, see Section 3.3).

In the following text, the constitutive parts of the wind tunnel are explained in more detail.

#### • Fan unit

A radial fan (recycled from an existing facility) delivers the air flow for the wind tunnel. The fan is raised in height such that the minimum test section height required for inserting the rolling road system for ground effect experiments can be achieved.

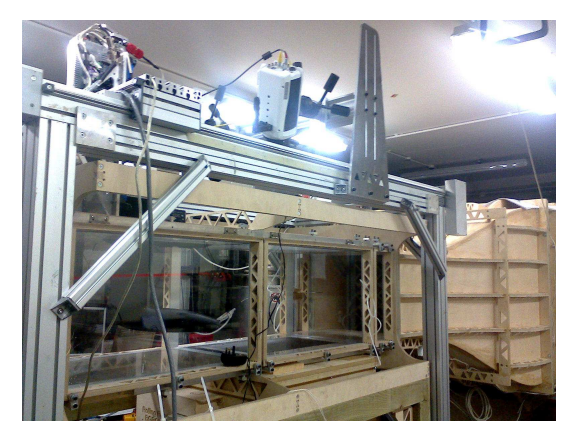
#### • Flow-conditioning section

The flow-conditioning section was also a part of an existing facility. This section consists of a honeycomb section as well as 3 screens of varying mesh dimensions to ensure a high quality airflow entering the contraction. The screens and the honeycomb are designed with common rules outlined in the literature (Mathew, 2006).

#### • Contraction

The contraction (Figure 3.2a) is based on a match-cubic polynomial that ensures the first and second derivation at the inlet and outlet to be zero thereby resulting in a continuous change in cross sectional area. The influence of three different transitions points was considered between the matched cubics (15%, 35% and 50%, based on large inlet dimension). The transition point was found to displayed a significant impact on the pressure drop along the inner surface of the duct and therefore is conducive to flow separation. The commercial software ANSYS-FLUENT was used to find the transition point with the lowest risk of flow separation in the contraction. The closer the transition point was placed to the large inlet of the duct, the lower appeared the risk of flow separation. This result corresponds to the theory that a smoother pressure drop can be reached with distributing it along a longer travelling way, resulting in a reduce gradient (Bell and Mehta, 1988). However, the manufacturing process of a contraction with a favourable 15% transition point is not trivial. The forces required to keep wooden plywood sheets attached to the highly curved curvature would be extremely high. Therefore, a compromise was made to manufacture a contraction with a transition point at 35%. In the literature, this transition point in combination with a contraction ratio of 1:6 was found to prevent flow separation in the boundary layer (Bell and Mehta, 1988).





(a) Contraction (b) Test section

Figure 3.2: Contraction and test section design

The contraction design was modelled with the use of CAD (Computer Aided Design). The focus was on a light structure, ensuring easier handling during assembly and later use. Plywood frames, 18mm thick were cut using a CNC (computer numeric cutting) and were used to support the inner sheet material. Both ends of the contraction were equipped with aluminium interfaces. These interfaces in combination with a sealing groove ensured an airtight intersection between the flow-conditioning/contraction section and the test section.

#### • Test section

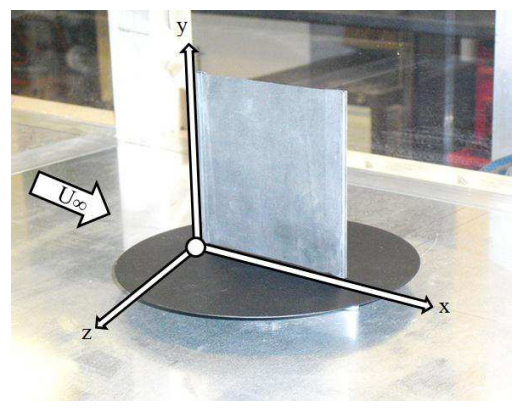
The test section design (Figure 3.2b) aimed to allow as much optical access for the later use of optical diagnostics. The side windows of size  $750\times430~mm^2$  (length×height) and the top windows of size  $750\times410~mm^2$  (length×width) are manufactured out of acrylic. The optical access for the vertical sections extends to the bottom of the wind tunnel to ensure full optical access for ground effect experiments. The inner part of the wind tunnel test section is made of aluminium bars which include a revolving groove with a silicon pipe sealing.

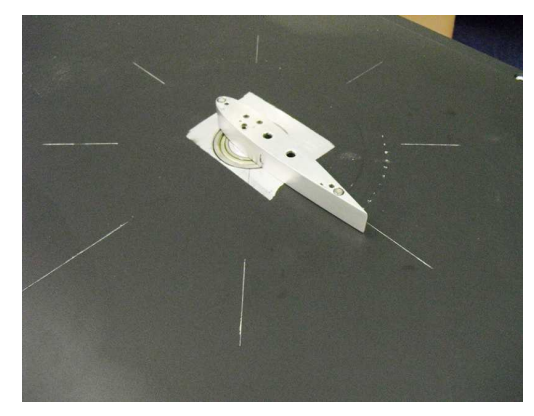
## 3.2 Setup-1: Aspect-ratio Experiment

The focus of this half-wing setup is to investigate the impact of aspect-ratio (AR) on the aeromechanics of membrane wings. Time-resolved wing forces and moments are captured with a load cell in a wind tunnel from which time-averaged and time-resolved aerodynamic properties (lift, drag, and pitch moment) are determined. Rigid flat-plate and membrane wings are compared for three different aspect-ratios (AR-1.0, 1.5, and 2.0) at a Reynolds number of Re = 67,500 (free-stream velocity 10 m/s). High-speed photogrammetry is applied separately (not load-synchronised) to capture static and dynamic chordwise membrane motions at four different wingspan positions.

#### 3.2.1 Setup Design

The half-wings (Figure 3.3a) are mounted on a rotating disc-system (Figure 3.3b) that rotates around the quarter-chord point. This system places the wing outside of the boundary layer of the wind tunnel wall, measured 10 - 15 mm within the streamwise location of the wing. This system consists of a 1 mm thin, 170 mm diameter aluminium disc and a 17 mm high, hollow streamlined body, which clamps the supports 15 mm deep and allows for inclusion of the load cell sensor (Figure 3.3b). The adjustment of the angle-of-attack is controlled by a highly geared stepper motor NEMA-17, which high gear ratio, in combination with a spring loaded shaft, enables a rotation without significant backlash and an uncertainty in positioning angle of  $\Delta \alpha \leq 0.05^{\circ}$ .





(a) Half wing mount with disc

(b) Streamline body below disc

Figure 3.3: Half wing mount concept

#### 3.2.2 Wing Design

The compliant membrane half-wings consist of latex sheet material with a thickness of t = 0.2 mm, a density of  $\rho = 1$  g/cm<sup>3</sup> and a linear approximated stiffness of about E = 1.5 MPa. This stiffness was measured in a separate experiment by applying a static

pretension ( $\sigma=0.05$  MPa) representing the membrane tension in the wind tunnel, followed by measuring the resulting strain. The resulting slope of the stress-strain curve was approximated by a linear fit. Significant J-curve behaviour of the membrane was only detected for higher pretensions. The aeroelastic parameter  $\Pi=(\text{Et/qc})^{1/3}$  (Smith and Shyy, 1996) was found to be  $\Pi=3.68$  for  $U_{\infty}=10$  m·s<sup>-1</sup>.

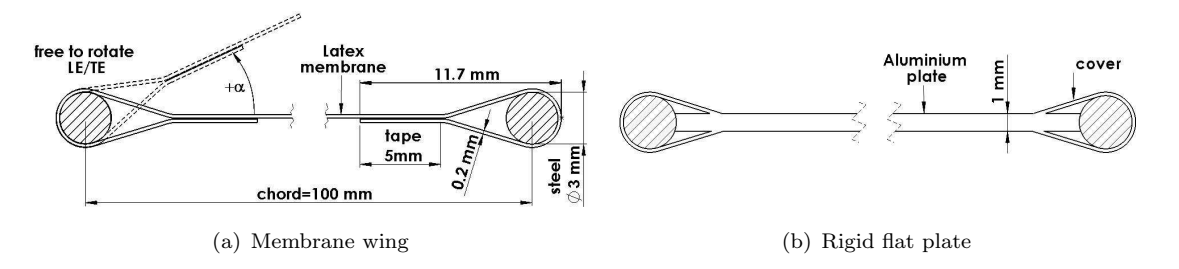


Figure 3.4: Leading and trailing-edge concept

The membrane was wrapped around 3 mm round steel-based LE/TE supports and attached to each other with a 5 mm wide and 0.05 mm thick double sided tape (Figure 3.4a). The present study uses a free-to-rotate attachment of the membrane on leading and trailing-edges which differs from clamped LE/TE versions used in previous studies (Song et al. (2008); Galvao et al. (2006)). Figure 3.5a displays lift and drag coefficient while figure 3.5b shows range and power efficiency with changing angle-of-attack for both attachment options. The results are shown for an AR-2 wing. AR-1.5 and AR-1 cases showed similar trends. At a fixed angle-of-attack between  $5^{\circ} \leq \alpha \leq 25^{\circ}$ , membrane wings with free-to-rotate LE/TE attachment exhibit a benefit of 30-35% in lift coefficient  $C_L$  compared with clamped LE/TE attachments. In addition, the maximum lift coefficient  $C_{L-max}$  rises by 30% and is delayed by 2.5° into higher angles of attack. The gain in lifting performance is likely related with increasing camber due to a higher freedom of movement with the free-to-rotate LE/TE attachment.

In addition, the free-to-rotate LE/TE adapts to changes of the local flow angle at the LE, resulting in a continuous chordwise cambering curve with rising angles of attack. In contrast, the clamped LE/TE show an inflectional chordwise deformation profile, with the inflection points located immediately next to the clamped ends. This inflectional profile leads to extremely unsteady chordwise membrane deformation, especially at high angles of attack (Rojratsirikul et al. (2009, 2010a); Albertani et al. (2007); Tregidgo et al. (2011)). The rise in lift for the free-to-rotate LE/TE is accompanied by increased drag of up to 15-45% between  $5^{\circ} \leq \alpha \leq 25^{\circ}$ . As a result, the clamped LE/TE show benefits of up to 23% in aerodynamic range efficiency  $C_L/C_D$  in comparison with the free-to-rotate attachment at low incidence of  $\alpha < 15^{\circ}$ , whereas the free-to-rotate LE/TE gains up to 17% over the clamped version at higher angles  $\alpha > 15^{\circ}$  (Figure 3.5b). Furthermore, a free-to-rotate attachment enables a power efficiency increase of 10% at moderate cruise angles of  $\alpha = 10^{\circ}$  and up to 44% at  $\alpha = 27.5^{\circ}$ .

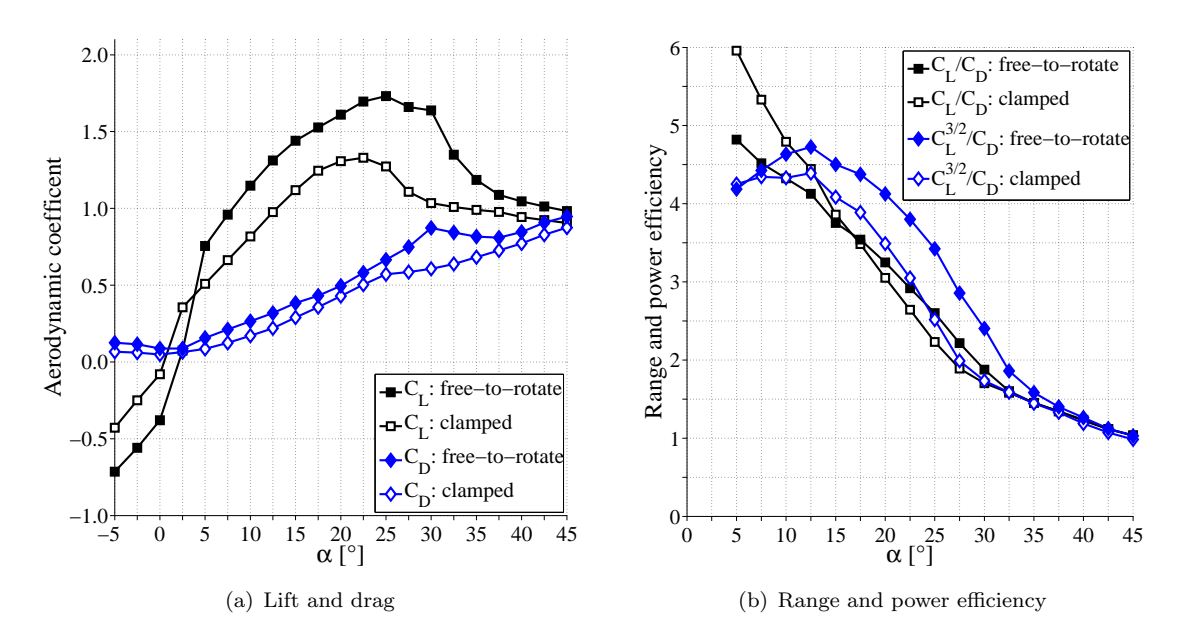


Figure 3.5: Influence of clamped and free-to-rotate leading and trailing-edge attachment for AR-2

The half wing design comes also with an unsupported wing tip, allowing a large degree of freedom to adapt to changes in tip-flow conditions. The aerodynamic effect of wing tip constrains are discussed with the introduction of perimeter-reinforced wings, shown in the second setup description (Section 3.3.2). All membranes are attached without pre-strain (nominally). The uncertainty on the membrane length was about 0.2 mm. To avoid ageing effects and account for repeatability of membrane production, all membrane wing results (forces, deformations) were performed on five membrane wing samples and averaged afterwards.

Layout	Wing aspect-ratio	Chord, mm	Half-wingspan, mm
	1.0	100	50
	1.5	100	75
	2.0	100	100

Table 3.1: Half wing dimensions

Rigid flat plate wings were manufactured by using 1 mm thick aluminium sheet material in combination with the same round LE/TE supports of the membrane wing setup (Figure 3.4b). Additionally, a LE/TE cover was used to obtain a similar transition surface at the supports as the membrane wing (Figure 3.4a).

All half-wings have a fixed chord length of c = 100 mm and different aspect-ratios (full span based) are obtained by changing the half – wingspan b/2 and consequently the wing area S (Table 3.1). The constant chord length was used to ensure comparable chordwise membrane deformation lengths with changing AR.

#### 3.2.3 Load

Lift and drag forces, as well as pitch moment data were measured by a six-axis load cell (ATI-Nano 17) with a maximum load capacity of 8 N. A sampling rate of 1 kHz and a sample length of 20 s was used. An exemplary time-series can be seen in Figure 3.6a, showing lift, drag and pitch coefficient oscillations. The uncertainty in the load cell is given from the company ATI as  $\pm 0.002$  N in forces and  $\pm 0.06$  Nmm in moments. The load-cell comes calibrated from the company (ISO 9001 standard). Adjustments of the load-cell calibration-matrix are not possible for the end-user. Nevertheless, the wide usage and acceptance of the ATI-system within the research community verifies the load-cell (calibration-system) as reliable and accurate within its maximum load specifications (Wahidi et al., 2014; Gardiner et al., 2011; Zhang et al., 2015; Colorado et al., 2012; Timpe et al., 2013).

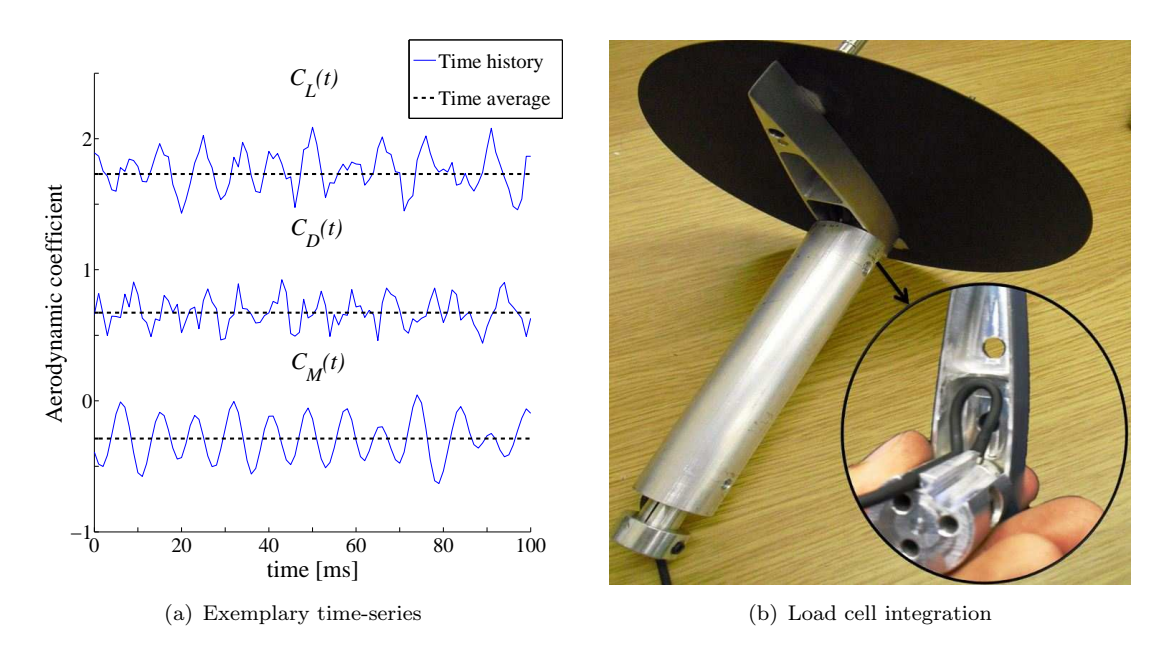
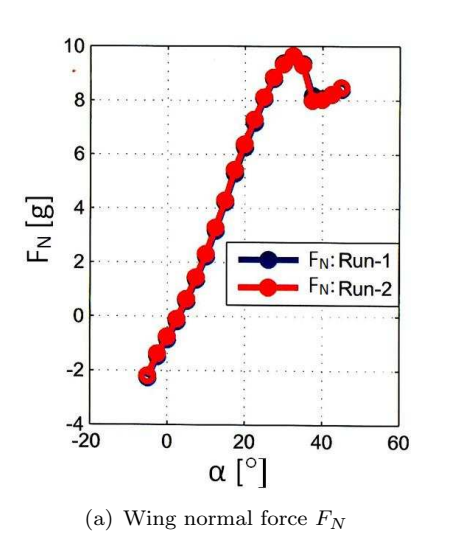


Figure 3.6: Exemplary time-series signal in  $C_L(t)$ ,  $C_D(t)$  and  $C_M(t)$  and load cell integration within mount

Nevertheless, extensive validation of the load-cell system showed that the company given load-cell accuracy holds only if the measurements were made within a overall time frame of 60 s due to effect of electrical drift (and or temperature related) of the load cell. In order to ensure reliable measurements, a wind-off tare point is obtained as a baseline just prior to the each measurement for all combinations of angle-of-attack. Figure 3.7 shows

an exemplary repeatability test of the wing force by measuring a rigid flat-plate wing (AR-1) through a selection of angles-of-attack of  $-5^{\circ} \leq \alpha \leq 45^{\circ}$ . The wing normal force  $F_N$  is measured and compared for two separate runs. The wind on/off measurements are conducted within the (from the author as optimal suggested) time frame of 60 s, which results in a load repeatability error of  $\pm 0.15$  g (Figure 3.7b). This overall load repeatability includes (minor) errors associated with angle-of-attack misalignment, free-stream velocity errors and load-cell drift (within the short period of 60 s).



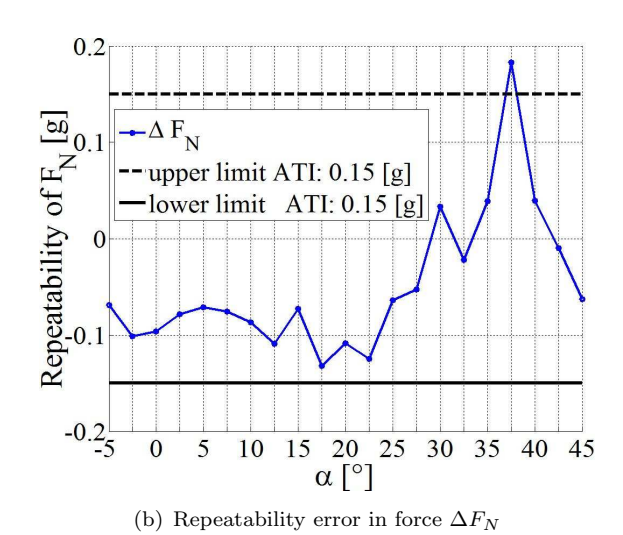


Figure 3.7: Repeatability test of the load cell with one rigid flat-plate wing (AR-1) at an exemplary wind speed of 5 m/s. The wing normal force  $F_N$  is illustrated for two individual runs over a variaty of angles-of-attack. Ultimately, the load results are found to lie within the company given accuracy of  $\pm 0.15g$ , if the wind on/off measurements are conducted within a short time-period of 60 s

A further error analysis focused on the final repeatability of different rigid flat-plate and membrane wing samples, based on their aerodynamic coefficients  $(C_L, C_D, C_M)$ . Associated manufacturing and attachment errors, temperature effects and errors of the pitot-meter pressure readings are included in the results. Figure 3.8 shows the mean values in the lift, drag and pitch moment coefficients, accompanied with their uncertainty bounds (errorbars with 68% confidence level). Rigid flat-plates and membrane wings are illustrated for AR-1 and AR-2. All wing samples show high consistency and a low error within their linear lifting region of  $5 \le \alpha \le 15^{\circ}$ . For example, membrane wings of AR-2 have an uncertainty in drag of less than 3% at  $\alpha = 5^{\circ}$  (Figure 3.8b) and this drops to below 1% for  $\alpha \ge 15^{\circ}$  whereas flat plates of the same AR show higher uncertainties due to lower drag forces with 5% at  $\alpha = 0^{\circ}$ , which drop to below 1% at  $\alpha \ge 15^{\circ}$ . However, membrane wings show a defined hysteresis (bistable) region around zero angle-of-attack, where the membrane can flip between a positive and negative camber, resulting in a large error. This effect is known and goes confirm with previous membrane wing studies (Song et al., 2008). In addition, membrane wing samples show larger errors in stall conditions,

probably due to unstable membrane motions and non-linear effects. In contrast, rigid flat-plate wings show no significant variations in the stall region.

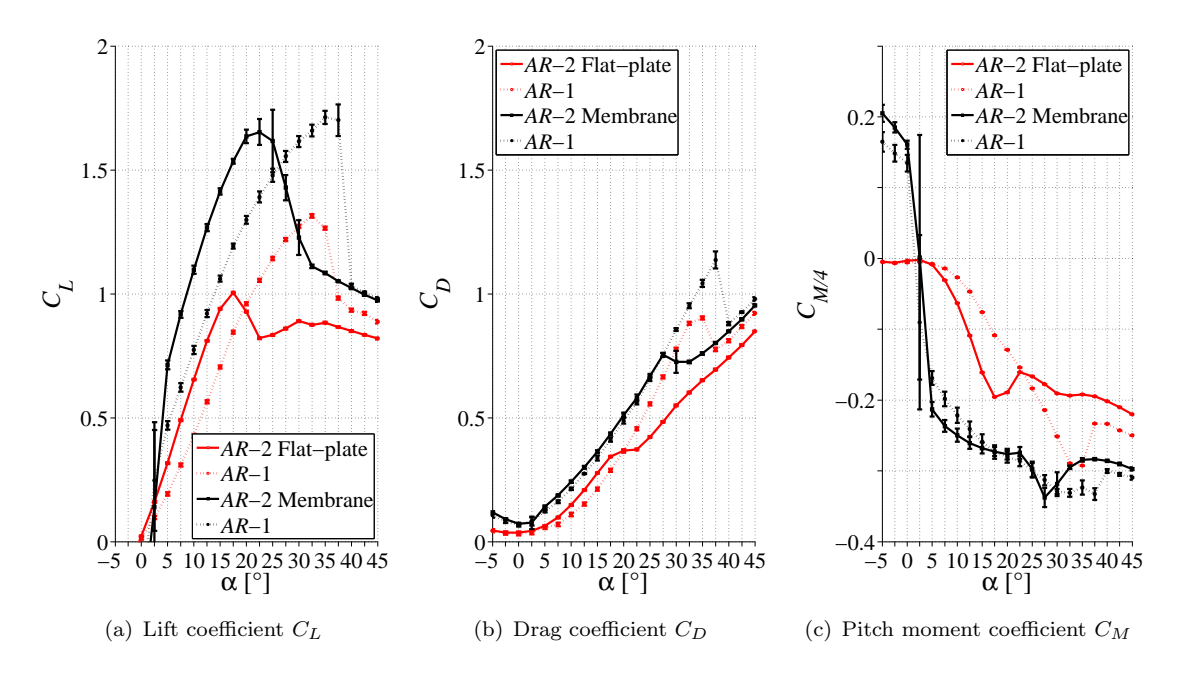


Figure 3.8: Uncertainty bounds of aerodynamic coefficients for rigid flat-plate and membrane wings of AR-1, and 2.

The force-transducer itself exhibited a very high natural frequency of around 5 kHz with an underdamped behaviour with damping ratio of  $\zeta = 0.47$  (measured with hammer-test). Figure 3.9 shows the resonance behaviour (lift related power-spectral-density (PSD)) of the setup for three different wing scenarios (no wing, flate-plate, membrane wing) and three different angles-of-attack ( $\alpha = 0^{\circ}$ ,  $\alpha = 22.5^{\circ}$ ,  $\alpha = 27.5^{\circ}$ ). The PSD bases on the fast-Fourier-transform (FFT) and illustrates the signal power intensity in the frequency space (Technologies, 1985). Wind on and wind off cases are illustrated for completeness. The excitation energy for the wind off cases are self-induced from the hardware (mainly stepper motor for pitch movements). The dominant setup eigen-frequency, mainly driven by the streamlined body/disc/support system (Figure 3.6b), was found to be 93 Hz with an energy between -40 to -50 dB (yellow shading in Figure 3.9). In addition, even the very low energetic excitation frequency of the stepper motor (for pitch motion) could be resolved with 40 Hz, showing -70 dB of energy with the wind tunnel switch off, and -55 dB for the wind tunnel switch on (yellow shading in Figure 3.9). The spectral content around these setup-eigenfrequencies was remarkably constant for all angles of attack and with significantly lower amplitude levels compared with membrane related force fluctuations (black shading in Figure 3.9). Clear changes in spectra of membrane wing force coefficients with changing angle-of-attack and aspect-ratios showed that the setup eigenfrequencies do not influence the results significantly and can be isolated. It is interesting to note that the wind tunnel design with a front mounted blower fan raises the overall background noise-level during its run from approximately -85 dB (wind off) to

-55 dB (wind on). This wind tunnel fan induced background noise is probably the major reason why vortex-shedding induced load oscillations of rigid wings (in stall conditions) can not be resolved in this study.

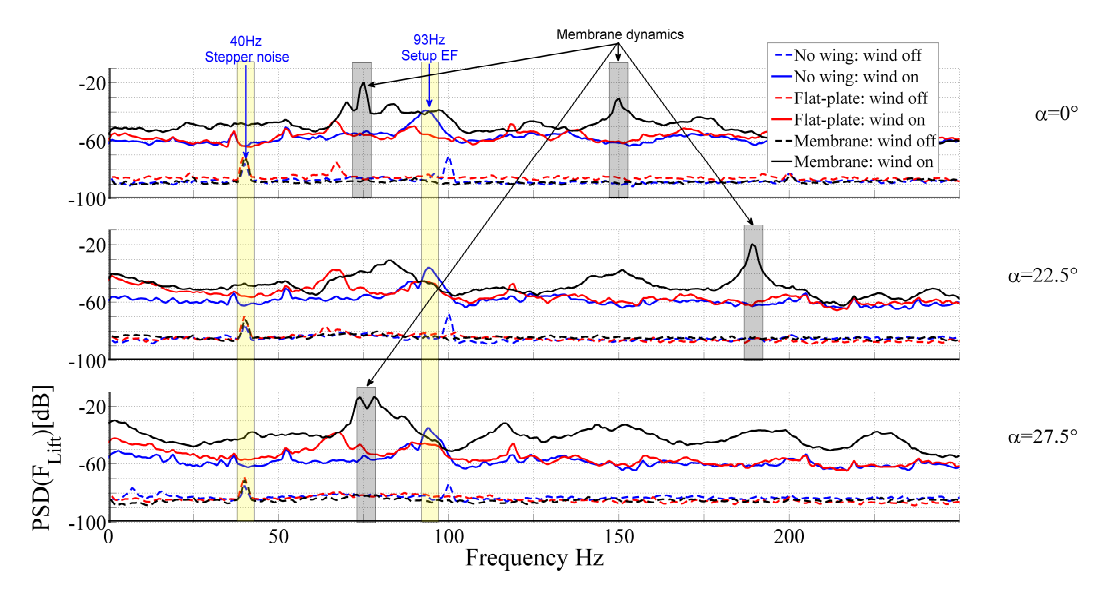


Figure 3.9: Resonance behaviour of setup (based on  $PSD(F_{Lift})$ ), modifying for rigid flat-plate and membrane wing between  $0^{\circ} \leq \alpha \leq 27.5^{\circ}$ . Resonance points of the setup and individual hardware (yellow shading) stay fix for different incidences and can be isolated. Black shaded regions show membrane wing related dominant oscillation frequencies in lift, which modify (and can be resolved) for different flow conditions.

Post-processing of the load measurements includes time-averaged statistics such as mean, standard-deviation (68%- confidence level) and power-spectral-density (PSD). The oscillation frequency f of the loads is normalised with the free-stream velocity  $U_{\infty}=10$  m/s and the chord length c=0.1 m. The resulting Strouhal number  $St=fc/U_{\infty}$  is commonly used to study and relate unsteady flow phenomenons such as leading-edge vortex-shedding and represents a measure of the inertial forces due to flow fluctuations to the inertial forces due to velocity changes within the flow field.

#### 3.2.4 Deformation

## 3.2.4.1 Photogrammetry

High-speed photogrammetry (Figure 3.10a) is used to measure instantaneous membrane deformations using a high-speed camera (Photron SA1) at sampling rate of 1 kHz and sampling time of 5 s. The chordwise measurements are performed along four different half-wingspan locations (y/(b/2) = 25, 50, 75, 95%). Membrane deformations are defined in a fixed wing body coordinate system, where x-coordinates measure along the chord between LE and TE, y-coordinates along the span and z-coordinates in camber direction.

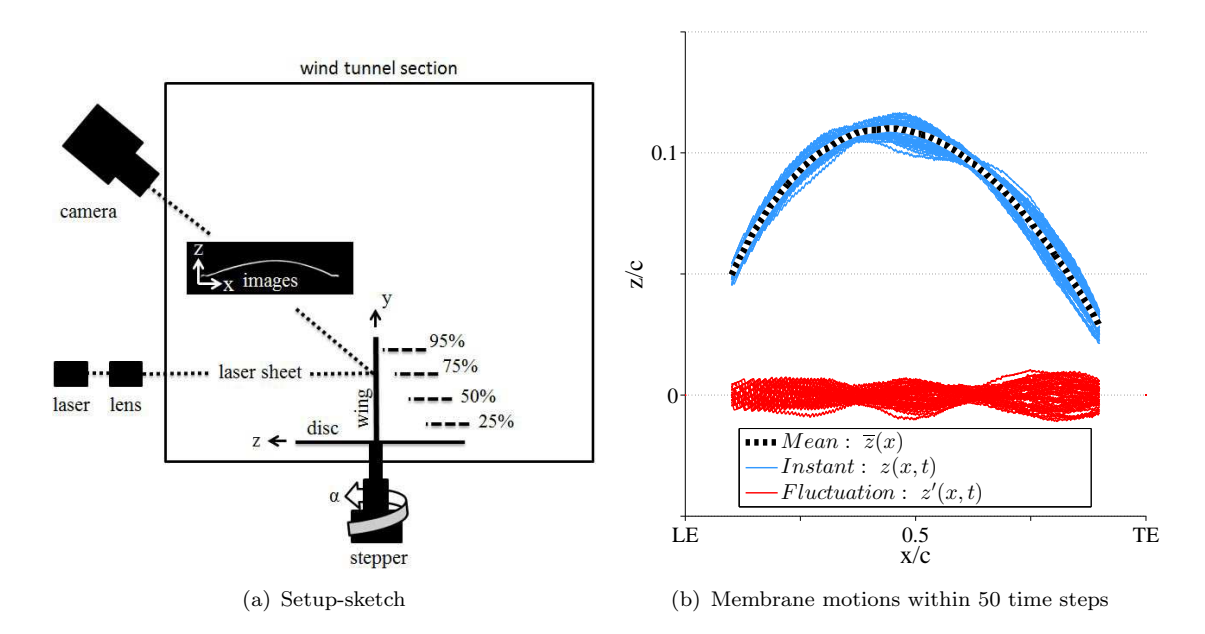


Figure 3.10: (a) Photogrammetry setup, measuring wing deformations at four sections along span.(b) Exemplary membrane vibrations over mean (blue) and without mean (red), at one span position

A class-3B CW laser (common powerful green laser pointer) was used in combination with a planar concave lens to generate a laser sheet in the horizontal x-z plane. The photogrammetry system had a resolution of 0.1 mm in z-displacement (cambering direction) with an overall measurement uncertainty of  $\pm 0.3$  mm. Displacements in the y-direction (along wingspan) were not captured.

The camera images were mapped into spatial coordinates using a mapping function, which is obtained using a calibration target. Figure 3.10b shows exemplary membrane vibrations over 50 time-steps for one wingspan section. The fluctuations of  $\sim 1$  mm amplitude identify a clear mode shape oscillation with three modal peaks. The angle-of-attack for these measurements was varied from  $\alpha = -5^{\circ}$  to  $+35^{\circ}$ , in steps of 2.5°.

Post-processing of the membrane motions includes time-averaged membrane mean deformations and averaged fluctuations, instantaneous membrane fluctuations and their spectral signature. Structural mode shapes of the membrane are studied and grouped with the help of a low order decomposition model which is discussed in the following section.

#### 3.2.4.2 Sinusoidal-Decomposition

In literature, time-averaged chordwise fluctuations are often considered for indicating changes in dominant structural mode shapes of the membrane (Rojratsirikul et al., 2009; Galvao et al., 2006; Tregidgo et al., 2011; Song et al., 2008). However, dominant mode shapes in the membrane are sometimes difficult to isolate due to an overlap of several modes shapes or a lack of fluid-structure tuning in these deformations. Their spectral content is ordinarily found by a fast-fourier-transform (FFT) of the chordwise camber point with the highest fluctuation intensity (standard deviation) or the time history of each chord position.

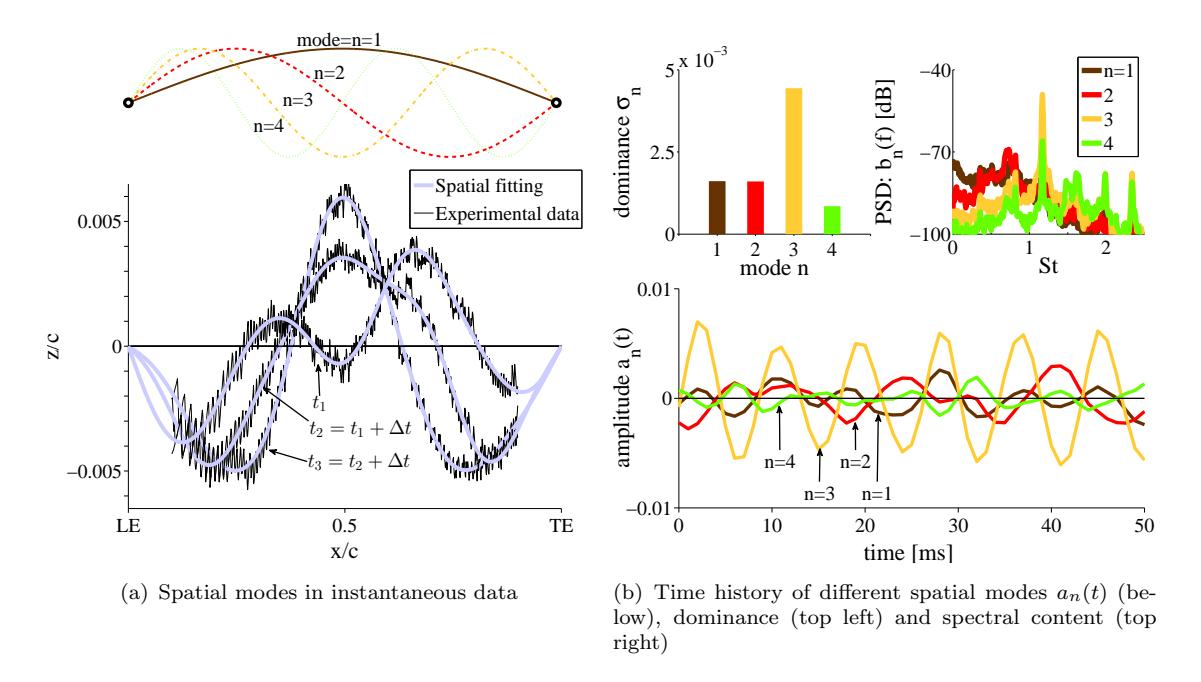


Figure 3.11: Sinusodial modal decomposition of membrane vibrations. This decomposition allows access to distinct spatial modes in the membrane and their temporal content (Exemplary case: AR-2, mid-semispan,  $\alpha = 25^{\circ}$ ).

Sinusoidal-decomposition is an alternative method, which is able to isolate the spacetime modal behaviour of the membrane oscillations. It provides information of the contribution of multiple mode shapes to the overall oscillation. In addition, it can capture the existence of lower mode shapes even with strong high frequency content.

In this method (eq.3.1), photogrammetry based instantaneous chordwise membrane fluctuations  $z'(x,t) = \frac{1}{c}(z-\overline{z})$  are decomposed into sinusoidal modes that extend from the LE(0,0) to the TE(1,0) at a given instant time point t using a least-squares approach (Wolberg, 2006).

$$\underbrace{\frac{z(x,t) - \overline{z}(x)}{c}}_{\text{Experiment}} \approx \underbrace{\sum_{n=1}^{N} a_n(t) sin(n\pi \frac{x}{c}) \ with : n = mode = 1, 2, 3, \dots}_{\text{Modal decomposition}}$$
(3.1)

Figure 3.11a illustrates exemplarily this decomposition process for three time steps. This chordwise fitting process results in amplitudes  $a_n(t)$  for each sinusoidal mode number n at a given time instant t. The sum of all these sinusoidal curves approximates the overall membrane deflection at a given time step t (eq.3.1). The most dominant mode is the mode shape that has the highest squared amplitude  $\sigma_n$  across all times (Figure 3.11b, upper left, eq. 3.2).

$$\sigma_n = \sqrt{\frac{1}{T} \sum_{t=0}^{T} a_n^2(t)} \tag{3.2}$$

Figure 3.11b illustrates an example that shows the time history of the amplitudes  $a_n(t)$  for the first four modes.

Spectra of mode: 
$$b_n(St) = PSD(a_n(t))$$
 (3.3)

Since, we get the amplitude of each mode shape as a function of time, the frequency content for each mode  $b_n(St)$  can be obtained by calculating the power spectral densities of those amplitudes  $a_n(t)$  (Figure 3.11b, upper right, eq.3.3).

Peak Spectral Energy: 
$$E(St) = max(b_n(St))$$
 (3.4)

The peak spectral energy E(St) (eq.3.4) is calculated by picking the highest frequency content  $b_n(St)$  of the decomposed mode selection for a given Strouhal-number and represents a reduced order (filtered) spectra of key membrane dynamics.

## 3.3 Setup-2: Ground-effect Experiment

The focus of this setup concentrates on understanding the fluid-structure interaction of rectangular perimeter-reinforced membrane full wings, going from free-flight conditions into ground-effect. A moderate Reynolds number of Re=56,000 (free-stream velocity  $8.4~\mathrm{m/s}$ ) is used. The aerodynamic performance of the membrane wings is compared with a rigid flat plate. Static and dynamic loads are measured using ATI-Nano 17 sensor, the wing displacements and flow characteristics were measured with non-intrusive high-speed camera systems. Time-resolved digital image correlation (DIC) is used to capture the surface deformation of the membrane wing and time-resolved particle image velocimetry (PIV) is used to measure the flow features. The experiments are carried out for relative ground clearances ranging from  $0.01 \le h/c \le 2$  (based on trailing-edge), where the height h/c=2 represents the center of the wind tunnel test section with free-stream flow conditions.

### 3.3.1 Setup Design

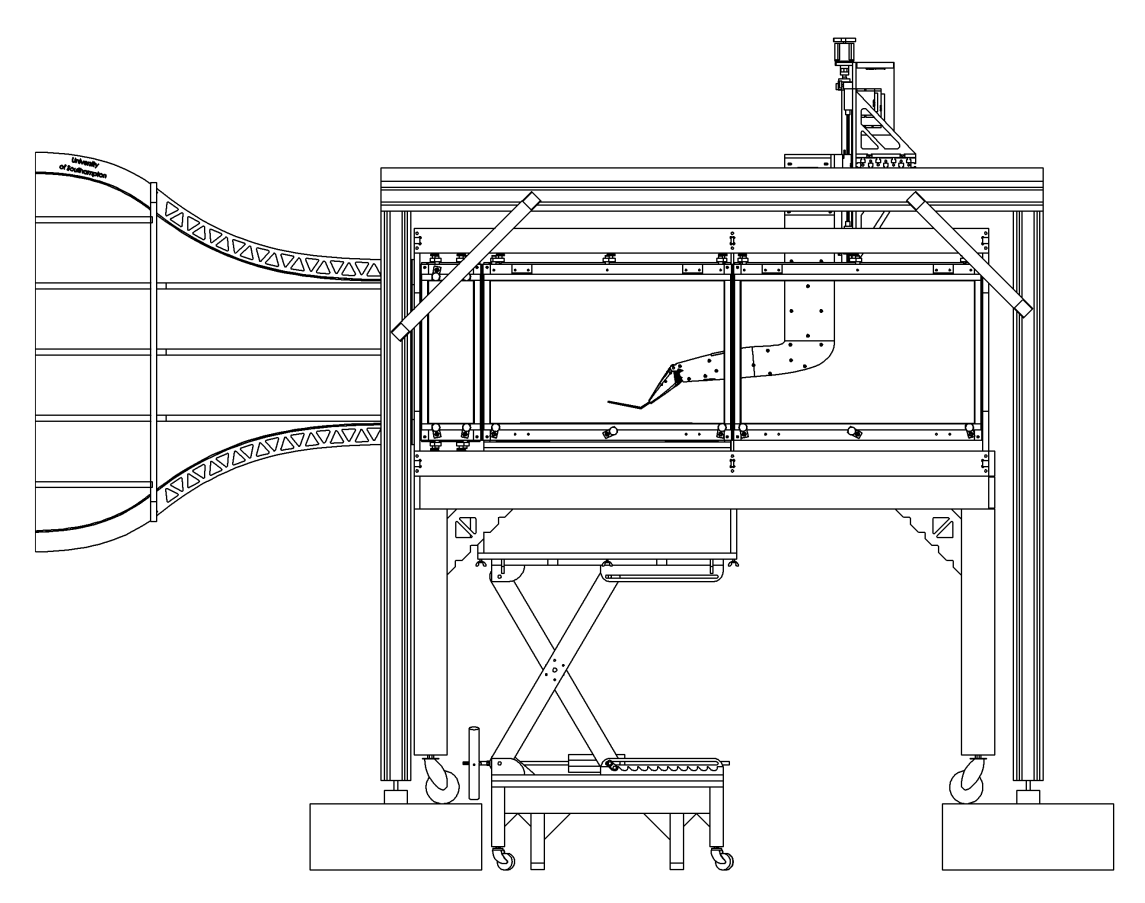


Figure 3.12: Wind tunnel test section with integrated sting and rolling road system

The key elements of the ground-effect setup include a rolling road and sting system which integrated into the wind tunnel test section (Figure 3.12). Both systems are discussed individually in the following section.

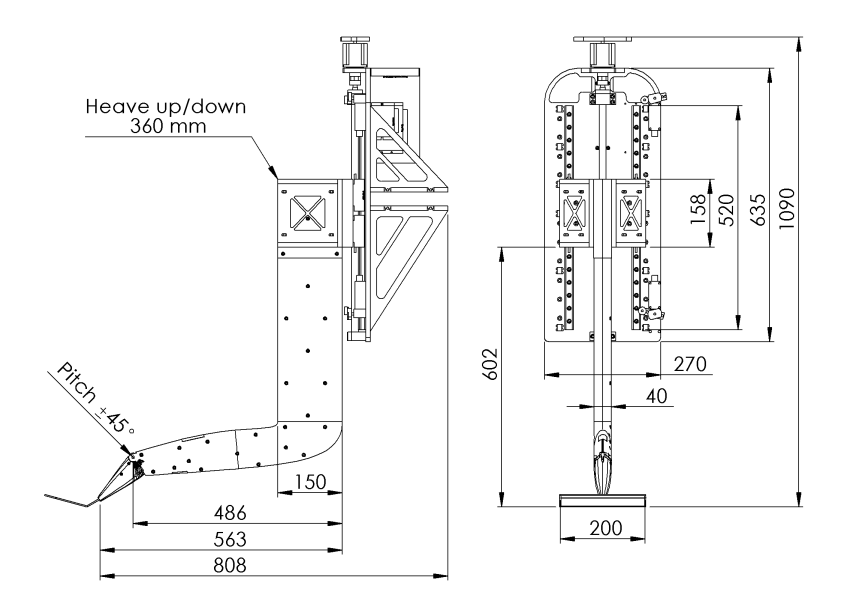
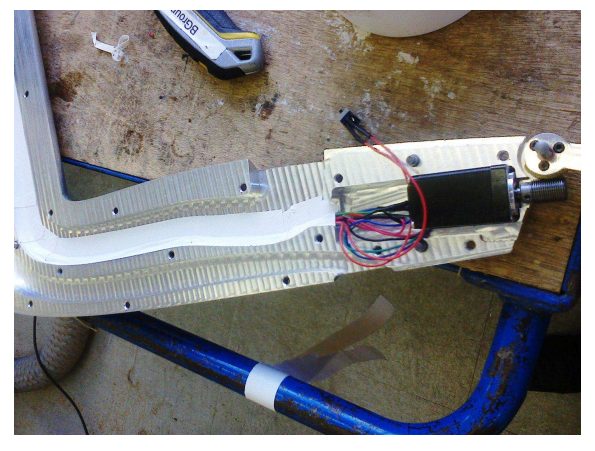


Figure 3.13: Sting arm with front mounted wing. Adjustable in pitch-angle and vertical height.

The perimeter full wing design and the wish to study flexible wings in ground-effect lead to the decision to use a robotic sting system, which was designed and build from the author during his study. Figure 3.13 shows the technical drawing of the sting system and its dimensions in mm. The system includes a traverse system with linear guides (and stepper motors) to change height-above-ground and 1:75-geared stepper motor to change angle-of-attack (spring-loaded worm-gear for backlash-free motions).







(b) Boxed sting with heave unit

Figure 3.14: Sting system with heave and pitch units

The vertical traverse system is decoupled with the sting system with rubber bobbins. The decoupling allowed to increase the signal-to-noise ratio between the sting eigen frequencies and flow/membrane induced load frequencies. The sting arm itself consists of two aluminium half's and was CNC machined from casted aluminium plates (casted aluminium allows to reduce machining induced warping). Figure 3.14a shows one open sting half with the integrated pitch stepper and two independent cable channels. The two, sting internal cable channels are designed to separate high-voltage cables from low-voltage signal cables for future electroactive membrane wing studies (not discussed in this study). For flow visualisation reasons, the sting was color coated in matt black with a scratch-proof two-component paint. Figure 3.14b shows the complete sting system within a custom designed transport box. The uncertainty of the sting mechanics is validated with < 0.1 mm in vertical positioning and  $< 0.1^{\circ}$  in angle-of-attack (both tested with a  $\frac{1}{100}$  mm accurate dial gauge).

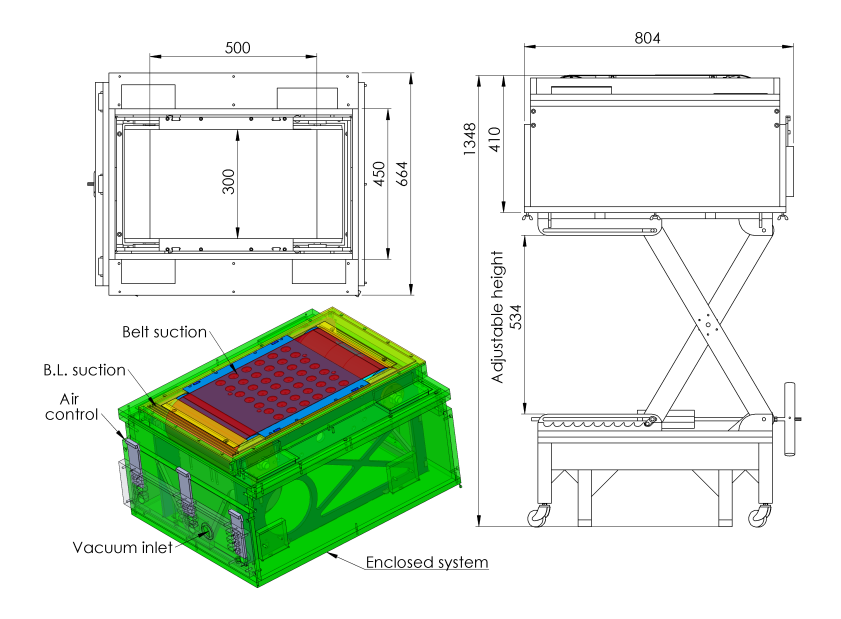


Figure 3.15: Rolling road design for ground-effect measurements. The system includes a boundary layer, belt and leackage suctioning system.

The measurement of wings within ground-effect involved a rolling road system (Figure 3.15), allowing correct boundary layer conditions. The main rolling-road structure was kindly given to us from previous experiments, but was highly modified and extended from the author. The major steel panels of the rolling-road were replaced with aluminium panels due to weight limitations to lift the rolling-road into the wind tunnel test section. In addition, the rolling-road was enclosed in a CNC-machined wooden box (Figure 3.16a) and equipped with boundary-layer (B.L.) suctioning, leakage and belt suctioning. Figure 3.16b shows the belt suctioning array of the rolling road in more detail (next to the sting system placed on top). Belt movements along the span are constrained with small ball-bearings which are in contact with the edges of the belt. The idea avoids the need for an active axis alignment system which is often used for large





(a) Casing with vacuum system valves

(b) Circular belt suctioning perforations

Figure 3.16: Rolling road add-ons

rolling-road systems. The wooden casing is decoupled to the rolling road with rubber bobbins and placed on a lifter system for vertical elevation into the wind tunnel test section. The custom lifter was successfully tested for a weight of up to 100 kg and comes with a 2nd-barrier safety system to reduce the drop risk by mechanical failure. The rolling road belt speed is modified with a 0 to 10 VDC analogue signal. The maximum belt speed reaches 30 m/s (however, max. 15 m/s is recommended due to vibrations).

Without the usage of the rolling road system (inserted, but system switched off), the velocity at the wind tunnel wall declines to 70% of the free-stream-velocity 1.5 mm ( h/c = 0.015) above the ground (Figure 3.17, black curve).

For correct boundary-layer conditions, the belt speed is matched to the free-stream velocity (8.4 m/s) and boundary layer suction is applied with air slots in front of the 300 mm wide belt, enabling a nearly uniform, vertical velocity-profile, reaching 98% of the free-stream-velocity 1.5 mm ( h/c = 0.015 ) above the ground in the mid-span position (Figure 3.17, blue curve). In addition, the boundary layer was measured offset by 100 mm in wing-span direction on either side of the wind tunnel center (Figure 3.17, green+red curve). The error-bars indicate that the spanwise velocity variations stay small and within the overall measurement uncertainty of  $\pm 0.1$  m/s.

A video that shows the development process of the sting and rolling road system can be found at https://youtu.be/7aE1\_ShQybc. A further video shows the ground-effect setup during wind tunnel measurements https://youtu.be/RAHejb3RHLI.

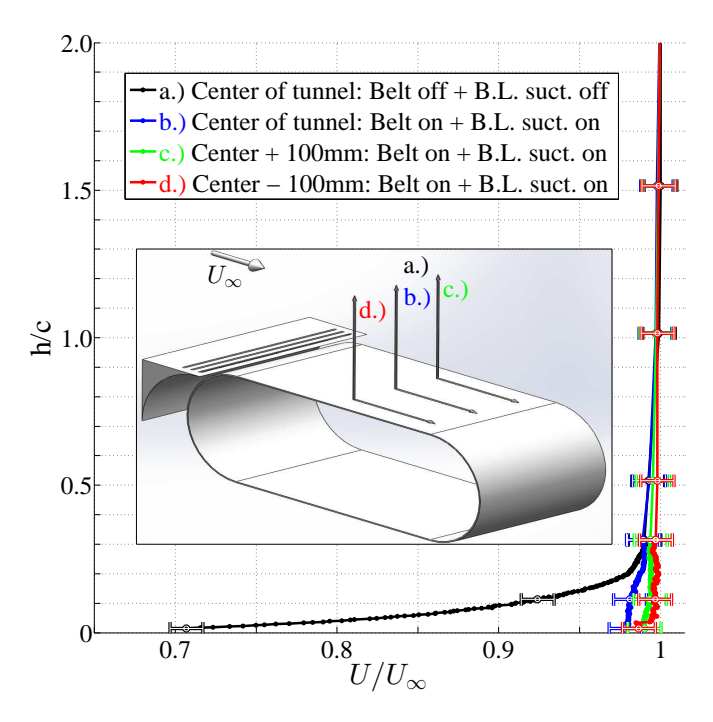


Figure 3.17: A rolling road system removes the boundary layer and ensures a uniform boundary layer profile with deviations of less than 2% from the free-stream velocity.

It should be mentioned that the illustrated ground-effect setup required a special measurement procedure to overcome gravity and membrane flexibility related problems. The horizontal wing arrangement of the ground-effect setup caused the flexible wings to camber down around their zero angle-of-attack ( $-5 \le \alpha \le 5^{\circ}$ ). This is different to the previous vertical AR-related setup (Section 4.1) and caused problems specifically in ground-effect due to physical wing-to-ground contact. The solution involved an initial pitch-up-angle of the wing of  $\alpha = +5^{\circ}$  (with wind tunnel switched on), causing the membrane to billow up (creating positive camber), followed by a pitch down movement to the actual (problematic) measurement angle within  $0 \le \alpha \le 5^{\circ}$  and its acquisition.

#### 3.3.2 Wing Design

The full wing models have a rectangular planform with a chord length of 100 mm and a wingspan of 200 mm, resulting in an aspect-ratio of AR = 2 (Figure 3.18). The wingspan to tunnel – width ratio for this span is 0.47, which is well below a maximum of 0.8 suggested by (Barlow et al., 1999) to avoid significant wall effects.

The rigid flat plate consist of a 1 mm thin aluminium plate which is surrounded by a 3 mm diameter perimeter steel frame. The transition between steel frame and the aluminium plate is aerodynamic covered to be comparable with the edge design of the membrane wing models (Figure 3.18, top left). The aluminium flat plate was replaced

with a similar thick transparent acrylic flat plate during flow measurements, giving optical access above and even below the wing (Figure 3.19a).

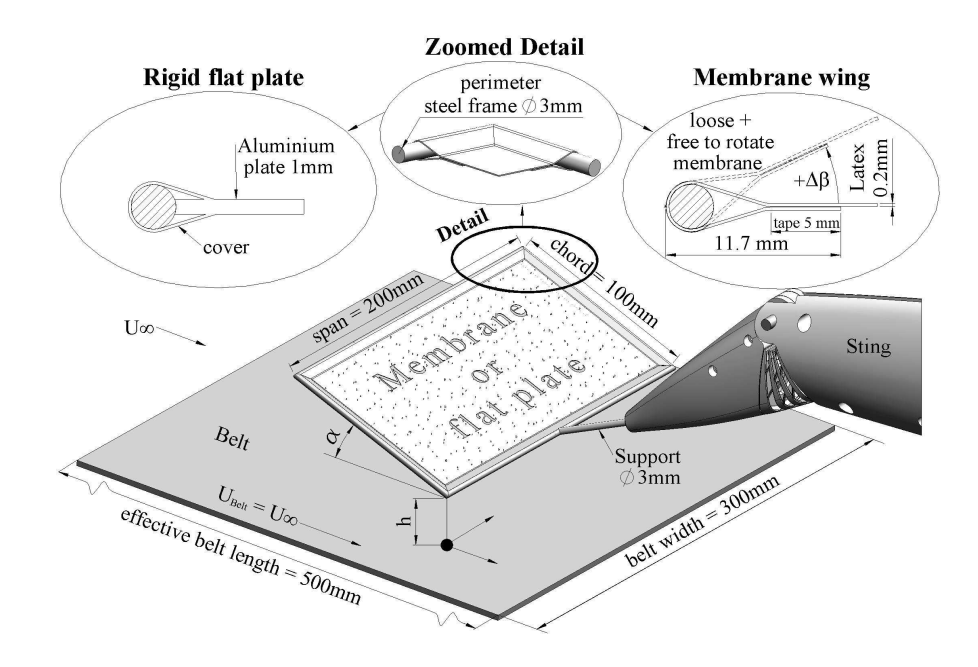


Figure 3.18: Sting system with illustrated perimeter reinforced wing layout for rigid flat plate and membrane wing

The perimeter reinforced membrane wing consists of a flexible latex membrane (Figure 3.19b,c) and a steel frame. PIV related experiments involve a membrane with a 10 mm wide translucent window at quarter-span to allow laser light to reach above and below the wing. The latex sheet material has a thickness of t = 0.2 mm, density of 1 g/cm<sup>3</sup> and a stiffness of E = 1.5 MPa. The aeroelastic parameter  $\Pi = (\text{Et/qc})^{1/3}$  (Smith and Shyy, 1996) is found to be  $\Pi = 4.27$  for  $U_{\infty} = 8.4 \text{ m·s}^{-1}$ . The membrane was wrapped around the 3 mm perimeter steel frame and attached to itself with a 5 mm wide and 0.05 mm thin double sided tape (Figure 3.18, top right).

The 3 mm supports were selected based on the findings of Arbos-Torrent et al. (2013b), who found that larger support diameters (5 mm instead of 3 mm) can act more like a bluff body and can promote (unwanted) larger separation bubbles, causing a steeper lift incline, accompanied with earlier and sharper stall conditions. In contrast, the smaller 3 mm support was found to maintain a smoother lifting behaviour beyond stall and encourages the dynamic response of membranes to a larger extent. In addition, sharp instead of round leading-edge shapes were found to excite the interference between the rigid wing support structure and the membrane, which coupling was not in focus of the current study.

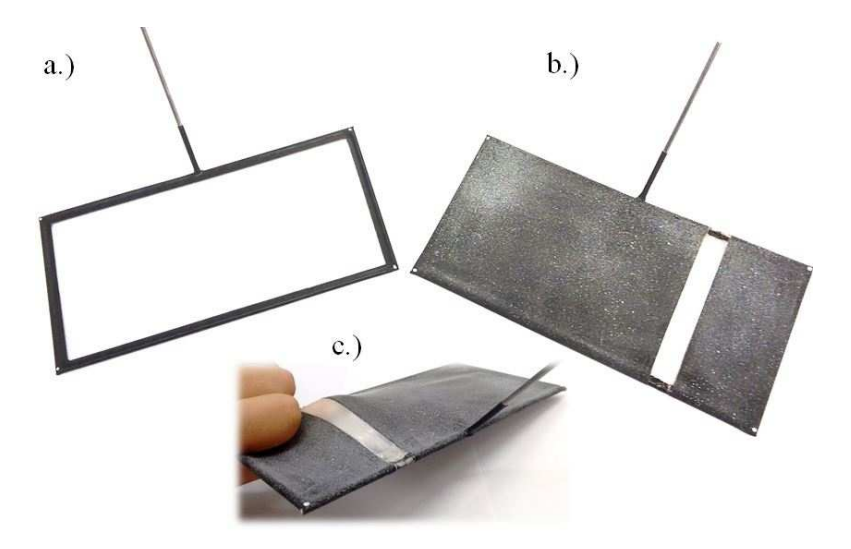


Figure 3.19: (a) Transparent rigid flat plate and (b,c) membrane wing with translucent section, allowing optical access for PIV measurements above and below the wing.

Assembly of the membrane wing is conducted using a custom made aluminium frame that supports the thin membrane in mid plane of the perimeter steel frame during assembly ensuring a maximum excess length of  $\epsilon/c < 0.01$  of the membrane and no pretension (nominally). The wrapped attachment method of the membrane allows to change contact angles  $\beta$  of the membrane on the outer perimeter steel frame (rotation around LE/TE and both wing tips, with slight constrains at the corners, see Figure 3.18).

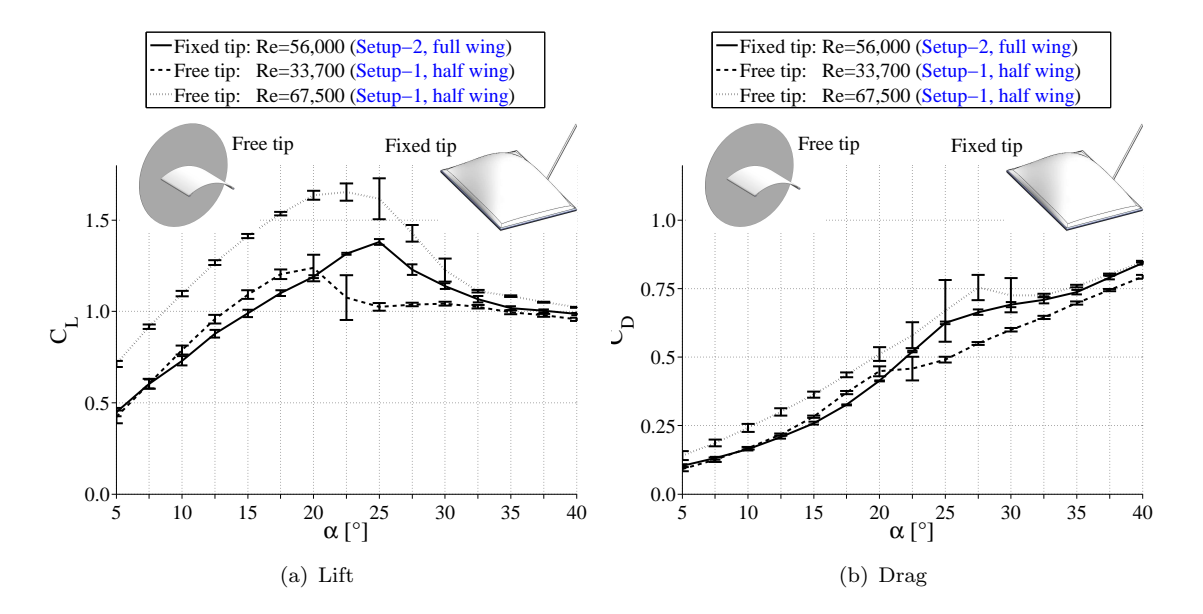


Figure 3.20: Aerodynamic effect of side (tip) support fixation on membrane wings. Comparison of half wing Setup-1 (Figure 3.3) and perimeter reinforced full wing Setup-2 (Figure 3.19). Errorbars show standard-deviation ( $1\sigma$ =68 %) of all measured wing samples.

The study on membrane half wings with unsupported wing tips (membrane free to billow up at wing-tip, Section 3.2.2) showed that the usage of free-to-rotate leading and trailing-edges allowed smoother shape adaption, resulting in higher stall angles and a gain in maximum lift. The given perimeter setup uses a similar free-to-rotate membrane attachment concept, however the membrane is additionally constrained at the wing tips. The aerodynamic comparison of a membrane wing with a free and fixed wing tip attachment (Figure 3.20) shows that the constrained perimeter wing-tip concept of the current study comes with a significant reduction in lift slope. Since the Reynolds number of the perimeter (fixed tip, full wing) study Re = 56,000 lies between the Reynolds numbers of the reference cases of Re = 33,700 and 67,500 (free tip, half wing), and the lift slope of the perimeter (fixed tip, full wing) study is shallower than both the reference studies (free tip, half wing), the difference can be attributed to the difference in free and fixed wing tip. For the perimeter wing-tip concept the membrane is more constrained and cannot freely billow up at the wing tips. As a result, the overall mean camber is restricted to grow, resulting in a lift penalty. The membrane with a fixed tip also exhibits a lower drag (most likely due to a reduction in induced drag).

#### 3.3.3 Load

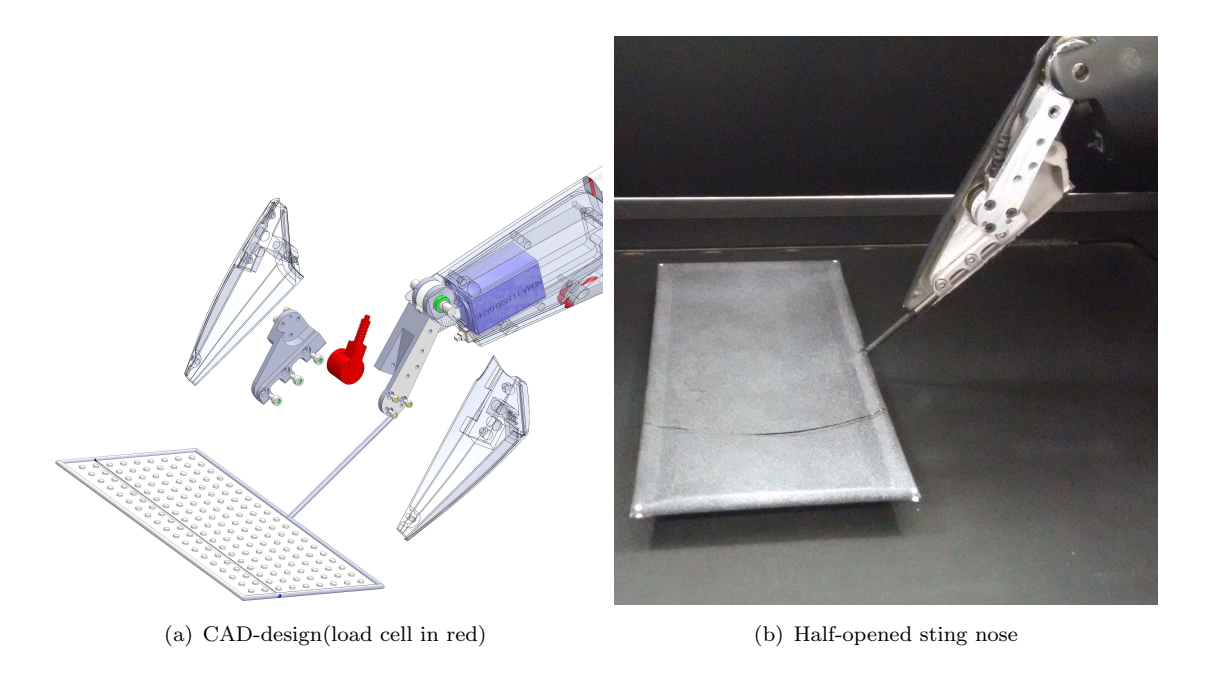


Figure 3.21: Load-cell integration in sting nose

All force and moment measurements are made for five different membrane wing samples and the mean loads and moments are computed from the resulting data. The attachment error has very little effect on the membrane dynamics as the force/moment spectra show almost identical dominant frequencies for a given angle-of-attack and height. The overall

standard deviation ( $1\sigma = 68\%$  confidence level) is computed by pooling the data from the five different samples.

Lift and drag forces are measured by a six-axis load cell (ATI-Nano 17), similar to the load cell used in Setup-1 (Section 3.2.3), but with a higher maximum load capacity of 25 N instead of 8 N. The decision for the larger 25 N load cell was necessary due to reaching overload limits with the 8 N load cell in maximum pitch moment. The load cell is integrated into a sting as shown in Figure 3.21. A sampling rate of 10 kHz and a sample length of 20 s was used. The uncertainty in the load cell is  $\pm$  0.006 N in forces and  $\pm$  0.03 [Nmm] in pitching moment. Calibration and drift compensation are conducted as previously described in Setup-1 (Section 3.2.3).

Figure 3.22 shows the mean values in the aerodynamic lift, drag and pitch moment coefficients, accompanied with their uncertainty bounds (errors come mainly from wing sample attachment and the load-cell, errorbars are shown with 68% confidence level). Rigid flat-plates and membrane wings are illustrated in free-flight (h/c = 2) and in one ground-effect case (h/c = 0.1) for brevity. All wings show a very consistent and small error, even in wing stall conditions. An exemplary membrane wing in free-flight conditions (h/c = 2) shows an uncertainty in drag of less than 3% at  $\alpha = 0^{\circ}$  and < 1% for  $\alpha \ge 15^{\circ}$ , whereas the flat plate shows a slightly higher uncertainty due to lower drag forces with 5% at  $\alpha = 0^{\circ}$  and < 1% for  $\alpha \ge 15^{\circ}$ . Ultimately, the error levels are found to be sufficient to compare the key parameters of the study (height-over-ground, angle-of-attack, flat-plate vs. membrane wing).

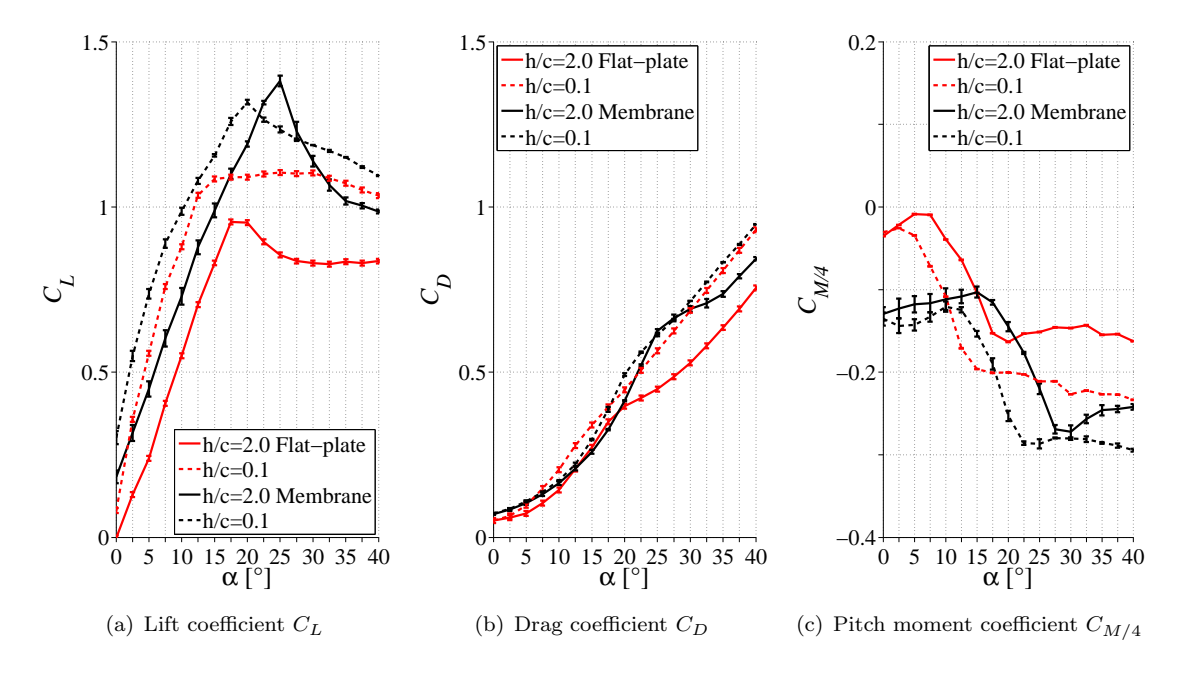


Figure 3.22: Uncertainty bounds of aerodynamic coefficients for rigid flat-plate and membrane wings at free-flight (h/c=2) and ground-effect conditions (h/c=0.1)

The dynamic behaviour of the experimental setup is separately validated to obtain the eigenfrequencies and damping characteristics of all its electro-mechanical components. The dynamics of all wing model structures are measured, avoiding resonance points for the measured wind/rolling road speed. As a result, the wind speed of 8.4 m/s was specifically selected for this setup as a result of resonance problems occurring by 10 m/s, which velocity was previously selected for the early aspect-ratio experiment on membrane half wings (Section 3.2). Although not illustrated here in detail, results showed that reduced Reynolds numbers shift the dynamic behaviour of membrane wings into lower angles-of-attack, resulting in lower mode shape orders (with lower frequencies) for a comparable angle-of-attack.

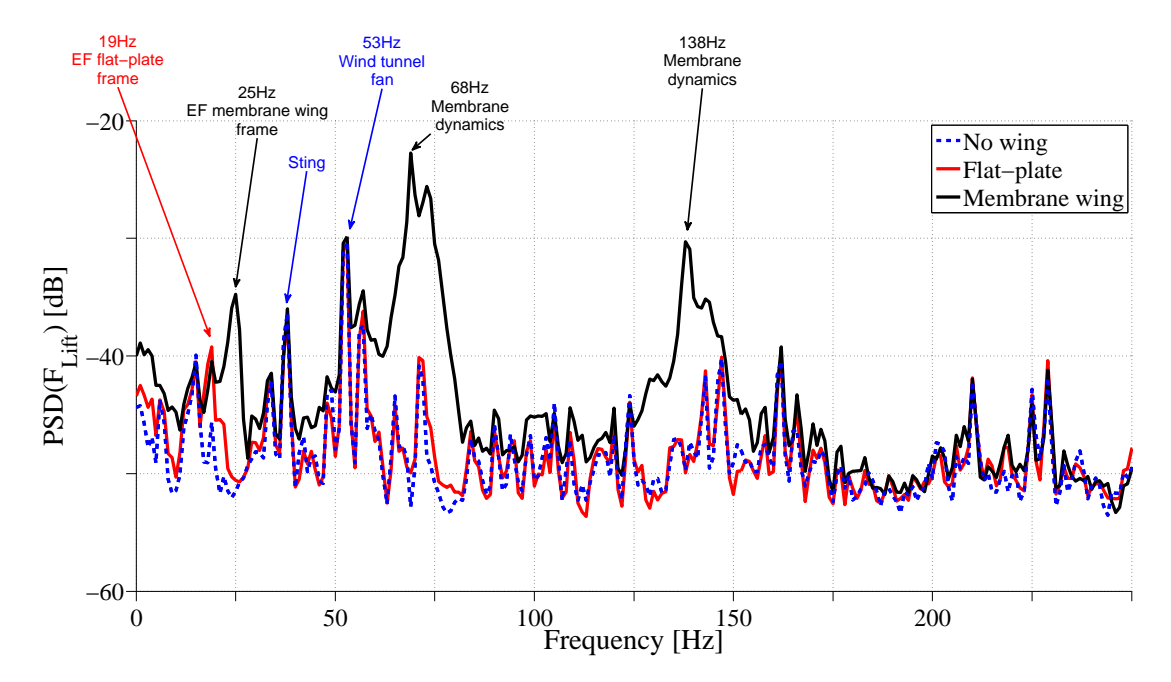


Figure 3.23: Resonance behaviour of the setup. Cases: No wing mounted, flat-plate mounted, membrane wing mounted.  $U_{\infty}=8.4m/s$ , stall-conditions at  $\alpha=25^{\circ}$ , free-flight. Flow induced load-shedding of rigid flat-plates can not be resolved due to relatively strong wind tunnel fan induced noise (blower-type related) and excitation of the wing frame eigenfrequency (EF). Wing frame eigenfrequencies were localised with external hammer-tests. However, membrane wing load dynamics (membrane/flow induced) can be resolved (68Hz + 138 Hz) and emerge out the setup background frequencies.

Figure 3.23 illustrates the lift based (load-cell acquired) resonance frequencies of the setup without any wing (blue-dotted line), a flat-plate (red-line) and a membrane wing (black-line) installed. The vibrations are excited due to all machinery equipment switched-on (rolling-road, wind tunnel fan, vacuum) and are measured with the wings in stall conditions ( $\alpha = 25^{\circ}$ ). The eigen frequencies of the wing frame (made of steel rods) are identified with an external hammer-test at 19 Hz for the flat-plate and 25 Hz for the membrane wing (again, steel frame related). Their excited energy level measures -40 dB to -35 dB. The sting eigen frequency was also identified with a hammer test and measures 33 Hz with an excitation of -35 dB. The wind tunnel blower-fan was found to

be an important noise producer and could be measured with up to -30dB at 52 Hz. As a result, the shedding frequencies of rigid flat-plates are often below this fan-based value and can not be resolved with the load-cell (but fortunately with the flow). In comparison, the load dynamics of membrane wings are strong enough and can be resolved at 68 Hz and 138 Hz by showing generally equal or higher energy levels of  $\geq$ -30 dB. It is even possible to use the membrane and the flow spectra to trace the origin of specific unclear load frequencies. This is one further benefit to use multiple measurement techniques.

Figure 3.24 shows the modifications of the resonance frequencies of the setup, involving rigid flate-plates and membrane wings and changes in angle-of-attack ( $15^{\circ} \leq \alpha \leq 30^{\circ}$ ). The spectral content of the rolling road/sting, wind tunnel fan and the attached wing appears remarkably constant for all angles-of-attack (yellow shading) and has mostly lower amplitude levels compared with membrane wing induced load fluctuations. Clear changes in the load spectra of membrane wings with modifying angle-of-attack show that the setup eigen frequencies do not significantly influence the results. Additionally, the modification of the load spectra of membrane wings correlates well with the frequencies in leading-edge vortex-shedding and membrane oscillation (modifying with angle-of-attack and height-over-ground), providing evidence to capture real flow/membrane induced load dynamics.

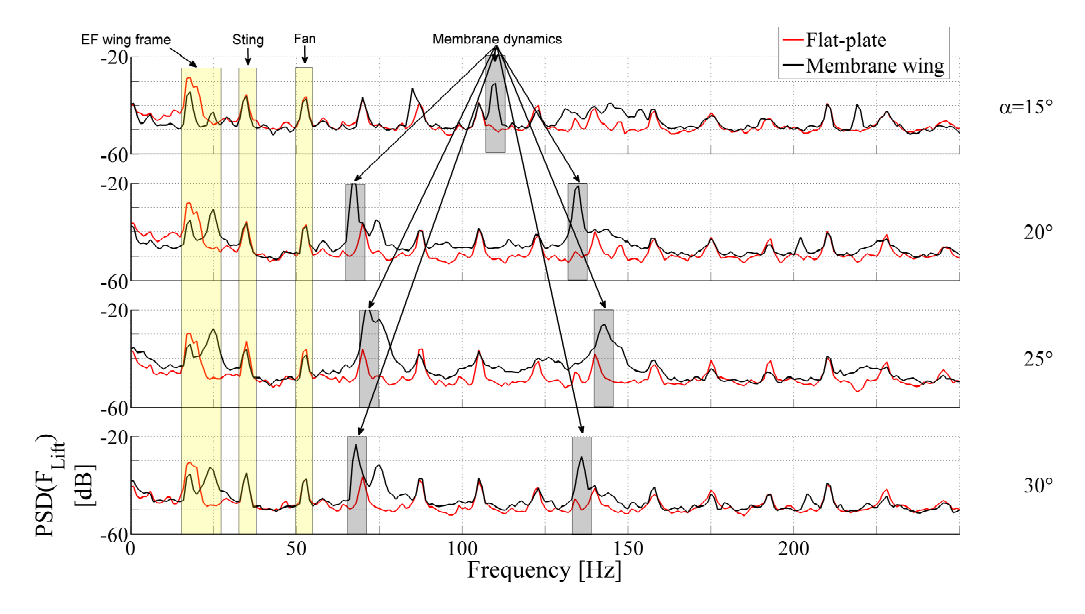


Figure 3.24: Resonance behaviour of setup (based on  $PSD(F_{Lift})$ ), modifying for rigid flat-plate and membrane wing in angle-of-attack of  $15^{\circ} \leq \alpha \leq 30^{\circ}$ . Resonance points of the setup (yellow shading) stay fix for different incidences and can be isolated. Black shaded regions show membrane wing related dominant oscillation frequencies in lift, which modify (drop) within stall conditions.

Post-processing of the load measurements includes time-averaged statistics such as mean, standard-deviation (68%- confidence level) and power-spectral-density (PSD, Technologies (1985)). The vibration frequency f is normalised with the (ground-effect setup

related) free-stream velocity  $U_{\infty} = 8.4 \ m/s$  and chord length  $c = 0.1 \ m$  to the Strouhal number  $St = fc/U_{\infty}$ . Time-synchronised load-membrane-flow acquisition allows to cross-correlate the load dynamics to the membrane and the flow dynamics. The correlation is of major importance to understand the coupling quality and phase leads/lags between the signal dynamics. The study uses the cross-correlation-function (CCF, see eq. 3.5) which normalises two signal amplitudes  $(s_1, s_2)$  with their individual standard-deviation  $(\sigma_{s_1}, \sigma_{s_2})$ . The MATLAB<sup>TM</sup> function crosscorr is used to conduct the correlation.

$$CCF(k) = \frac{\frac{1}{T} \sum_{t=1}^{T-k} (s_{1,t} - \overline{s_1})(s_{2,t+k} - \overline{s_2})}{\sigma_{s_1} \sigma_{s_2}} \quad with: \ k = 0, 1, 2, \dots$$
 (3.5)

It provides information about the overlap quality of the two signals (CCF = 1 = 100%) at zero phase difference (neglecting amplitude information) and their phase alignment (k) between each other. The time-shift k (eq. 3.5) between the two signals is modified to a phase shift  $\phi(k)$  in [°] which references to a 360° oscillation cycle of the acquisition frequency (eq. 3.6).

$$\phi(k) = k \frac{f_{dominant}}{f_{acquisition}} 360 [^{\circ}]$$
 (3.6)

The normalised phase shift  $\phi$  in  $[\circ]$  allows to compare cases of different dominant frequency (e.g. different frequencies in vortex-shedding) with a common base frequency (the acquisition frequency).

The load measurements were conducted for angles-of-attack ranging from  $0^{\circ} \le \alpha \le 40^{\circ}$  with a step size of 2.5° and heights-over-ground of h/c = [0.01, 0.02, 0.05, 0.1, 0.2, 0.3, 0.4, 0.5, 0.75, 1, 1.5, 2].

#### 3.3.4 Deformation

#### 3.3.4.1 Digital-Image-Correlation

Stereoscopic digital image correlation (DIC) is carried out to measure instantaneous membrane deformations using two high-speed cameras (Phantom V341, Figure 3.25) with 50 mm focal length lenses (Nikon AF Nikkor 50mm f/1.8D) with aperture set to f/8. The field of view is  $1312\times1000$  pixels, capturing the entire membrane wing surface. Volumetric calibration is conducted using a calibration plate (aluminium plate with dot-pattern) which was imaged at different positions within the measurement volume. The later volume reconstruction is conducted with the help of commercial software (LaVision). The black parts of the membrane are sprayed with a white random speckle pattern with  $\sim 3$  to 5 speckles per mm ( $\sim 2$  pixels per speckle).

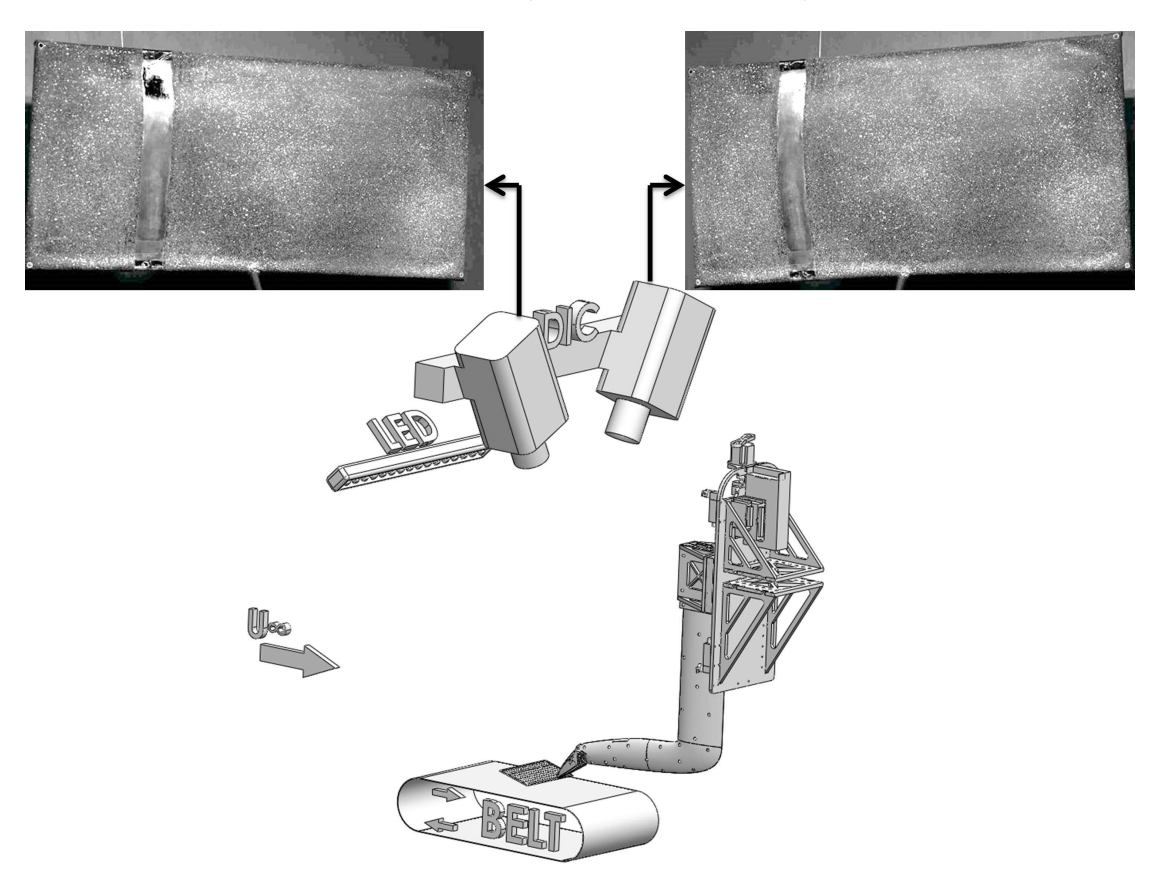


Figure 3.25: Digital image correlation (DIC) of membrane surface. Blue LED-light is used for illumination. The illustrated speckled membrane has a translucent streamwise section for later PIV measurements above and below the wing.

The patterns are illuminated with blue light emitting diodes (LEDs), which in combination with blue bandpass filters eliminates any interference from the green laser light during simultaneous DIC and PIV recordings. The light sheet window, a 10 mm wide translucent region in the membrane (Figure 3.25, upper), did not cause major problems

for the DIC measurements as the translucent surface even allowed DIC-correlation based on its natural texture.

High-speed images are captured at a sampling-rate of 800 Hz over a sampling-time of 10s for one of the five sample wings from the force/moment measurements. The sampling frequency allows to resolve dynamics in the membrane below 400 Hz. A total of 8000 images are obtained, spanning over 50 cycles of the most energetic modes.

Commercial software, LaVision StrainMaster, is used to obtain deformations from the stereo images. A subset size of  $89 \times 89$  pixels with a grid step of 15 pixels is chosen, resulting in an average spatial resolution of 0.03c. The uncertainty of the membrane deformation is estimated to be no worse than 0.1% of the chord length and is measured by recording two images in still position while comparing the displacement between them. The DIC-technique is widely used in experimental mechanics, allowing sub-pixel accuracy due to grey value interpolation schemes over the interrogation grid (Schreier et al., 2000). The results agree with previous studies that have applied DIC on membrane wings (Rojratsirikul et al., 2011; Galvao et al., 2006; Stanford et al., 2014).

Membrane deformations are defined in a fixed wing body coordinate system, where x-coordinates measure along the chord between LE and TE, y-coordinates along the span and z-coordinates in camber direction. Out-of-plane displacements of the membrane are referenced with respect to the plane coinciding with the wing's rigid frame. Final results include mean membrane deflections, instantaneous and time-averaged fluctuations and their spectral content (conducted at the surface point with the highest fluctuation intensity). The spatiotemporal relation of membrane dynamics is investigated with the proper-orthogonal-decomposition technique which will be described in detail in the following section.

The DIC measurements are conducted for a selection of angles-of-attack at  $\alpha = [5, 10, 15, 20, 22.5, 25, 35]^{\circ}$  and four heights-over-ground h/c = [2, 0.25, 0.1, 0.01].

#### 3.3.4.2 Proper-Orthogonal-Decomposition

Proper-orthogonal-decomposition (POD) is a statistical tool to analyse intrinsic structural properties with a reduced-order model. It has previously successfully been applied to membrane surface dynamics (Stanford et al., 2010; Buoso and Palacios, 2015; Shi et al., 2013) and is an alternative to the sinusoidal-decomposition, illustrated previously in Section 3.2.4.2. The complexity of membrane-vibrations requires a technique which is capable to identify and quantify two-dimensional spatial structures in membrane-surface-oscillations. The use of POD allows to capture those most energetic structural vibration mode shapes directly from time resolved image data (Han and Feeny, 2003; Lumley, 1967; Sirovich, 1987; Pinnau, 2008; Kostas et al., 2002). The POD modes of the membrane deformations are identified using the snapshot method.

Fluctuation components: 
$$Z = [z^1 z^2 ... z^N] = \begin{pmatrix} z_1^1 & z_1^2 & ... & z_1^N \\ z_2^1 & z_2^2 & ... & z_2^N \\ \vdots & \vdots & \vdots & \vdots \\ z_m^1 & z_m^2 & ... & z_m^N \end{pmatrix}$$
 (3.7)

The POD-process involves to align out of plane membrane fluctuations  $z_m$  for a given time step n into a single vertical vector  $z_m^n$  (eq. 3.7).

Eigenvalue problem : 
$$CA = \lambda^i A^i$$
 with :  $C = Z^T Z$  (3.8)

Those vectors are stacked into a Matrix Z for all time steps n = 1, ..., N. The fluctuation components Z (eq. 3.7) are forced into a stochastic process, producing an autocovariant matrix C (eq. 3.8).

POD coef. : 
$$ai = \frac{\sum_{n=1}^{N} A_n^i z^n}{||\sum_{n=1}^{N} A_n^i z^n||}$$
 with :  $i = 1, ..., N$  (3.9)

The eigenvalue problem is solved and POD coefficients are determined (eq.3.9).

Time series POD coef. : 
$$ai(t) = ai^T z^i$$
 (3.10)

The time-series of POD mode weights  $(a_i)$  are computed by projected every instantaneous membrane deformation in to their respective POD modes (eq. 3.10) and this data can be used to compute the frequency spectra of the mode weights  $a_i$  (power-spectral-density,  $PSD(a_i)$ ).

Energy contribution of POD coef. to total energy: 
$$\frac{\lambda^i}{\sum_{n=1}^N \lambda^n}$$
 (3.11)

Figure 3.26 shows the sensitivity analysis of POD for an exemplary membrane wing in stall conditions (h/c = 0.1 at  $\alpha$  =15°). The analysis is conducted on the membrane fluctuations (without mean) and considers 8000 images (full sample size), 4000 images and 1000 images. Membrane fluctuations with 1/4 or 1/8 of the number of acquired (8000) images are found to show the same mode shapes (Figure 3.26a) and energy

content (Figure 3.26b). Therefore, the POD modes are converged and confirm that the ensemble size is sufficient for this analysis on the membrane dynamics.

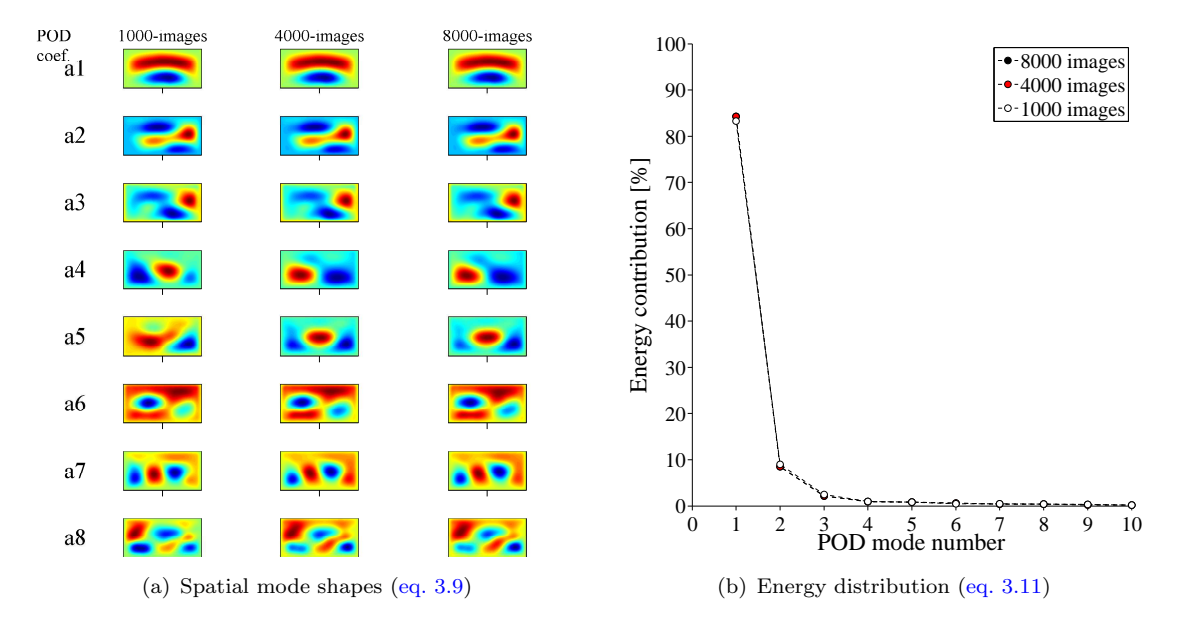


Figure 3.26: Sensitivity analysis of POD on membrane fluctuations with 1000, 4000 and 8000 samples (POD without mean). Spatial mode shapes (normalised contours) and their individual energy content are shown for the first eight dominant POD modes. Exemplary case: Extreme ground-effect (h/c = 0.1) at  $\alpha=15^{\circ}$ . Ultimetly, the assamble size does not show any significant impact on the POD mode shapes and their energy content.

#### 3.3.5 Flow

High-speed particle image velocimetry (PIV) is conducted by capturing frame pairs at 800 Hz, resolving dynamics in the flow up to 400 Hz. A double-cavity Nd: YLF laser (Litron LDY-300) with a wavelength of 527 nm is used. The flow is seeded with 1  $\mu m$  droplets generated using glycerine-water mixture in a typical atomiser. Previous studies with similar high-speed PIV and droplet sizes have shown that those particle are sufficient quick ( $\sim$ 30 kHz) to resolve the given (vortex-shedding dominated) flow scales (Timpe et al., 2013). The synchronisation between all cameras (DIC and PIV) and the laser is synchronised with a LaVision high-speed controller, which is triggered via Matlab. The commercial software LaVision Flowmaster is used for image acquisition and post-processing.

Flow measurements are conducted for one separate streamwise and spanwise PIV-plane. Each individual PIV-plane measurement is accompanied with time-synchronised membrane deformation (DIC) and load measurements, allowing to cycle-average both flow fields into a common cycle at a later stage. All flow related results are based on one representative wing sample. The flow based coordinate system (x, y, z) relates to (freestream-parallel, height-parallel, span-parallel) directions.

The following subsections will provide details of the PIV experiments carried out in the streamwise-chord-normal plane over the wing and the spanwise-chord-normal plane in the wake of the wing and will investigate the usage of proper-orthogonal-decomposition for flow field.

#### 3.3.5.1 Particle-Image-Velocimetry: Streamwise-plane

The first part of flow measurements is conducted at quarter-span in a streamwise wingnormal plane (Figure 3.27). The quarter-span position is chosen for these measurements as it has the least interference from the sting system while ensuring that we capture the representative flow dynamics that are correlated to the membrane deformations. Two Phantom V341 cameras (same type as used for DIC) are equipped with a set of two 105 mm focal length lenses (Sigma 105 mm f/2.8 EX DG Macro) with aperture set to f/2.8 (fully open). The applied laser-sheet was focused in level with the leading-edge and measured approximately 1 mm in thickness.

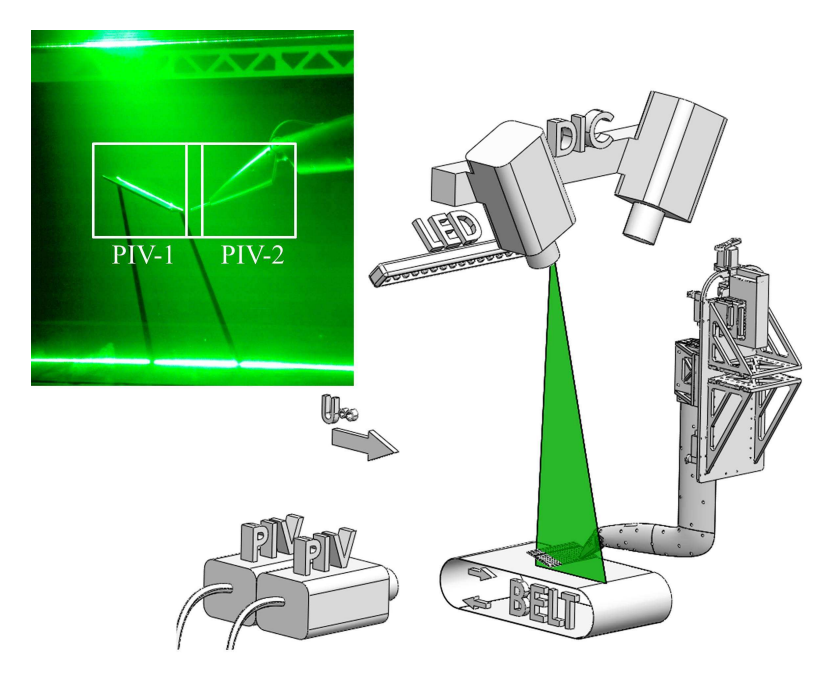


Figure 3.27: Planar PIV setup with two slightly overlapping side-by-side PIV cameras, capturing flow above/below wing + wake region. The laser plane is aligned parallel to the freestream at quater-wingspan.

Green bandpass filters are added on the PIV-lenses to increase the signal-to-noise ratio for the cameras by filtering out the background light from the (DIC-related) LEDs. The cameras are aligned perpendicular to the flow field in a side-by-side arrangement, allowing typical 2D flow measurements above/below the wing and in the near wake (Figure 3.27, upper left). A planar calibration plate of known grid spacing (acrylic plate with printed dot-pattern) is used to transfer pixel based displacements into millimetres. The calibration plate covers the full individual field-of-view of both side-by-side arranged

cameras (each spanning  $1616 \times 1088$  pixels, equal  $148 \text{ mm} \times 100 \text{ mm}$  (streamwise  $\times$  height)) and both cameras share a 36 mm wide overlapping region with common calibration points for the later vector-stitching process (Figure 3.27, upper left). The image-pair acquisition frequency is set to 800 Hz, acquiring 5000 images over a total time period of 6.25 s.

The time delay between image pairs is set to  $\Delta t = 50~\mu s$ , which results in a peak particle image displacement of about 5-7 pixels. Interrogation areas are set 64 x 64 pixels with 50 % overlap for a first pass and to  $16\times16$  pixels with 75 % overlap for the second pass. This results in a spatial resolution of 0.68 vectors/mm with a grid resolution of 1.6 % of chord. The resulting instantaneous vector fields of each of the two planar cameras are stitched using the 36 mm wide overlapping region (in which the vectors are averaged) to obtain a 26 cm×10 cm spanning vector field. The PIV-based freestream velocity is verified against a pitot tube system and they stay within 2 % of each other. The particle image correlation values in the flow reach 0.6 to 0.9 on the top side of the wing and reduce to 0.3 to 0.4 below the wing as the translucent latex window reduces the laser light intensity significantly. Nevertheless, it is possible to resolve the mean flow below the wings, which is of specific interest with the descent into ground-effect.

Description	Short	Uncertainty [%]
Horizontal mean velocity	$\overline{U}/U_{\infty}$	≤ 0.8
Vertical mean velocity	$\overline{V}/U_{\infty}$	$\leq 0.5$
Mean vorticity	$\overline{\omega}c/U_{\infty}$	≤ 0.3
Horizontal velocity fluctuation	$U'/U_{\infty}$	$\leq 2.3$
Vertical velocity fluctuation	$V'/U_{\infty}$	$\leq 2.3$
Vorticity fluctuation	$\omega' c/U_{\infty}$	$\leq 2.8$

Table 3.2: Uncertainty analysis of streamwise (planar) PIV results

Table 3.2 shows the results of an uncertainty validation of the given planar PIV study. The results depend on the individual measurement cases (wing type, angle-of-attack, height-over-ground) and are shown for a reference wing in stall (peak-lift) conditions (membrane wing, h/c = 2,  $\alpha = 25^{\circ}$ ). The uncertainties in the statistical quantities, such as time-averaged velocities and the vorticity (velocity-gradients), are calculated by the principles of Benedict and Gould (1996) and Kat (2012), considering 5000 vector fields. The technique relates fluctuation intensities (standard-deviation) of the flow-field with the acquired ensemble-size. The time-averaged vorticity is calculated by using a linear uncertainty-propagation of the velocity-gradients and relates to the peak vorticity in the shear layer, which was calculated as  $60 \frac{U_{\infty}}{c}$ . The uncertainties in the instantaneous velocity results are estimated by using the displacement uncertainties (subpixel accuracy

of 0.1 pixel, see Westerweel (1997)) in reference to the laser pulse-time separation. Similarly, the instantaneous vorticity is calculated by using a linear uncertainty-propagation of the velocity-gradients (relating instantaneous velocity uncertainties with the grid-spacing of the vector-field). It should be noted that the conducted analysis has to be seen as an estimate and indication of the uncertainty which may vary between different measurements (due to uncertainty in particle displacement, particle image density, calibration procedure, focusing errors, etc.).

Post-processing of the streamwise-PIV results involves flow statistics with time-averaged velocity fields (allowing to visualise separation bubbles), turbulent kinetic energy (measure for unsteady flow regions) and vorticity (measure of rotational part of the flow). A spectral analysis of vertical flow fluctuations reveals dominant shedding frequencies within the flow (shown as normalised Strouhal number) at selected listener points. Vertical flow oscillations are cross-correlated to membrane and load dynamics, revealing their coupling quality and phase. The reduced order model of POD is applied to investigate predominant flow structures above the wing surface and in the wake (discussed later in Section 3.3.5.3 in combination with spanwise flow-plane).

The streamwise-plane related PIV measurements are conducted for rigid flat-plate and membrane wings at a selection of angles-of-attack of  $\alpha = [10, 15, 25]^{\circ}$  for three heights-over-ground h/c = [2, 0.25, 0.1].

#### 3.3.5.2 Particle-Image-Velocimetry: Spanwise-plane

The second part of flow measurements is conducted in a freestream-normal plane, located one chord length downstream of the trailing-edge (Figure 3.28).

An exemplary instantaneous velocity vector field is illustrated within the upper right corner of Figure 3.28, showing the tip-vortex in relation to the wing root and sting position. The downstream position of the PIV-plane is selected to capture a fully developed tip-vortex structure of sufficient size and track its modification within ground-effect. The stereo-PIV setup involves two cameras which are aligned 45° to the laser plane, resulting in a 90° included angle between the cameras. The spanwise-PIV setup uses the same cameras, lens and filter systems as the streamwise-PIV setup (Section 3.3.5.1). However, each camera was additionally tilted with respect to the lens axis using Scheimpflug adapters and was focused at the centre of the PIV-measurement plane.

The stereo-PIV setup involves an aluminium two-level 3D calibration plate of known grid spacing and defined separation distance between the calibration planes. The applied laser-sheet thickness was enlarged to a width of approximately 3 mm to ensure that the number of later unmatched particles are no more than 50 % (Wieneke and Taylor, 2006). Apart from initial camera calibration, the stereo self-calibration technique was applied to account for misalignment between the calibration plate and the image plane.

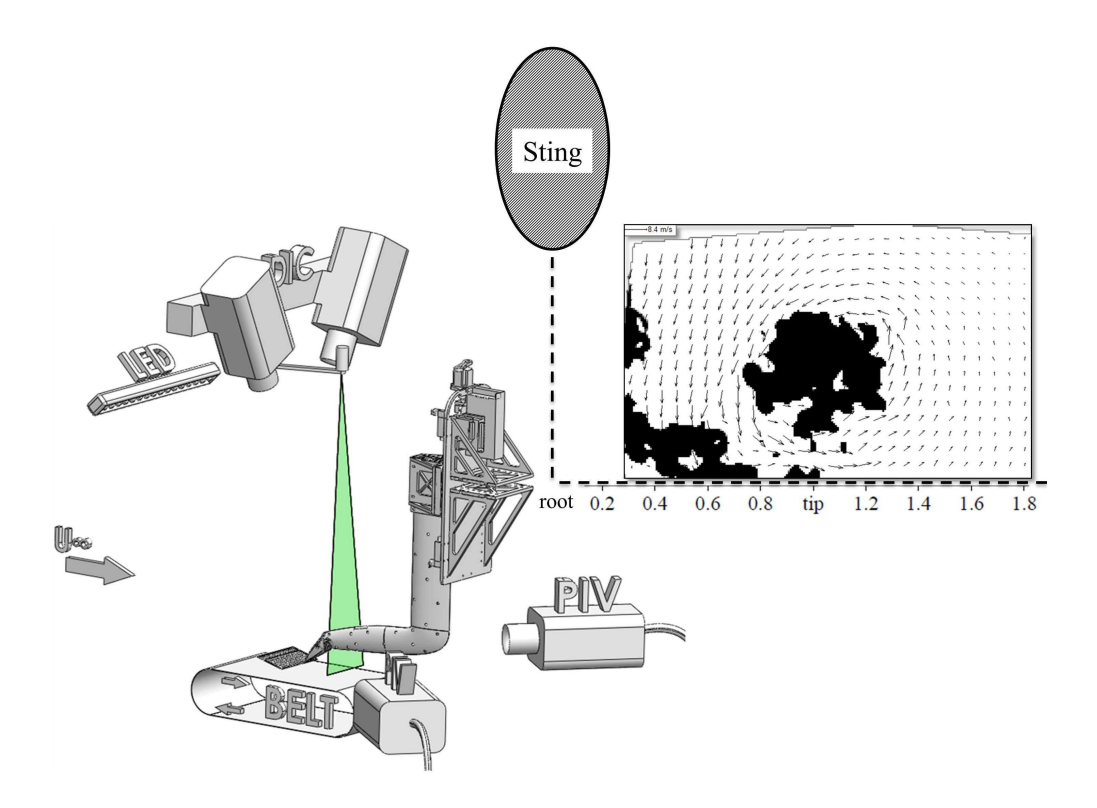


Figure 3.28: Stereo PIV setup, showing tip-vortex development in a freestream-normal plane, located one chord downstream of trailing-edge. An exemplary tip-vortex vector field is shown in relation to the sting position.

The image-pair acquisition frequency of 800 Hz allows a resolution of  $1616 \times 1088$  pixels for each camera, resulting in a laser-plane projected field-of-view of 170 mm×80 mm (span×height). A total of 5000 images are recorded over a time of 6.25 s. The time delay between image-pairs is set to  $\Delta t = 30 \mu s$ , resulting in a peak particle image displacement of about 4 pixels.

The images-pairs are mapped (using the upper calibration plate information) and processed into vector fields. Interrogation areas are set  $128 \times 128$  pixels with 75 % overlap for a first pass and to  $32 \times 32$  pixels with 75 % overlap for the second pass. This results in an in-plane spatial resolution of 0.43 vectors/mm and a grid resolution of 3 % in chord–lengths. The stereo-PIV based freestream velocity is validated against a pitot tube system and stays within 1 % of each other.

Table 3.3 shows the results of an uncertainty validation of the given stereo PIV study. The results depend on the individual measurement cases (wing type, angle-of-attack, height-over-ground) and are shown for a reference wing with strong leading-edge vortex shedding and a coherent tip-vortex (membrane wing, h/c = 2,  $\alpha = 25^{\circ}$ ). The uncertainty analysis for the stereo-PIV setup follows the same fundamental methodology as previously discussed with the planar PIV system (Section 3.3.5.1).

Description	Short	Uncertainty [%]
Out-of-plane mean velocity	$\overline{U}/U_{\infty}$	$\leq 0.3$
Vertical mean velocity	$\overline{V}/U_{\infty}$	$\leq 0.3$
Spanwise mean velocity	$\overline{W}/U_{\infty}$	≤ 0.3
Mean in-plane vorticity	$\overline{\omega}c/U_{\infty}$	≤ 0.2
Out-of-plane velocity fluctuation	$U'/U_{\infty}$	≤ 3.5
Vertical velocity fluctuation	$V'/U_{\infty}$	≤ 3.0
Spanwise velocity fluctuation	$W'/U_{\infty}$	≤ 3.0
In-plane vorticity fluctuation	$\omega' c/U_{\infty}$	≤ 2.6

Table 3.3: Uncertainty analysis of spanwise (stereo) PIV results

Post-processing of the spanwise-PIV results involves flow statistics with time-averaged velocity fields (showing tip-vortex size and location), vorticity (rotational component of the tip-vortex and its coherence) and circulation (flow-field integral of vorticity distribution). A spectral analysis of vertical flow fluctuations is conducted at several listener points in the flow and reveals dominant shedding frequencies close to the wing root which are correlated to the shedding results found in the streamwise-plane. The reduced order model of POD is applied to investigate shedding structures in the wake and will be discussed in the following section.

The spanwise-plane PIV measurements are conducted at a selection of angles-of-attack of  $\alpha = [10, 15, 25]^{\circ}$  at h/c = 2 and  $\alpha = 15^{\circ}$  for h/c = [0.25, 0.1].

#### 3.3.5.3 Proper-Orthogonal-Decomposition

Proper-orthogonal-decomposition (POD) can not only be useful to describe the membrane (Section 3.2.4.2) but also the flow dynamics. POD has previously successfully been applied to the flow field around membrane wings (Schmit et al., 2003; Lian et al., 2003) as it allows to group vortical structures of highest energy content. As a result, the overall flow dynamics can be reduced by smaller-scale vorticity carrying features and it is found useful to filter out the effects of these smaller scales in order to examine the interaction between the leading-edge vortex and the membrane. Therefore, POD analysis is applied on both streamwise- and spanwise PIV planes. The POD implementation on the flow structures is conducted in a similar way as seen in detail for the membrane dynamics (Section 3.3.4.2).

Figure 3.29 and Figure 3.30 show the sensitivity analysis of POD for both the streamwise and spanwise PIV-plane. It is shown that 1000 instead of 5000 PIV-images exhibit similar dominant POD-mode shapes of similar energy content. Therefore, the POD

modes of the flow (in both PIV-planes) are converged and confirm that the ensemble size of 5000 images is sufficient. It is interesting to note that the POD analysis on the flow requires significantly more mode numbers to converge (Figure 3.29c and Figure 3.30c) than needed for an analysis on the membrane dynamics (Figure 3.26b). The standing wave characteristic of membrane wings and their mass (eigen frequency) effects are likely to be responsible for their dominance in a single POD mode rather than multiple ones (as seen for the flow).

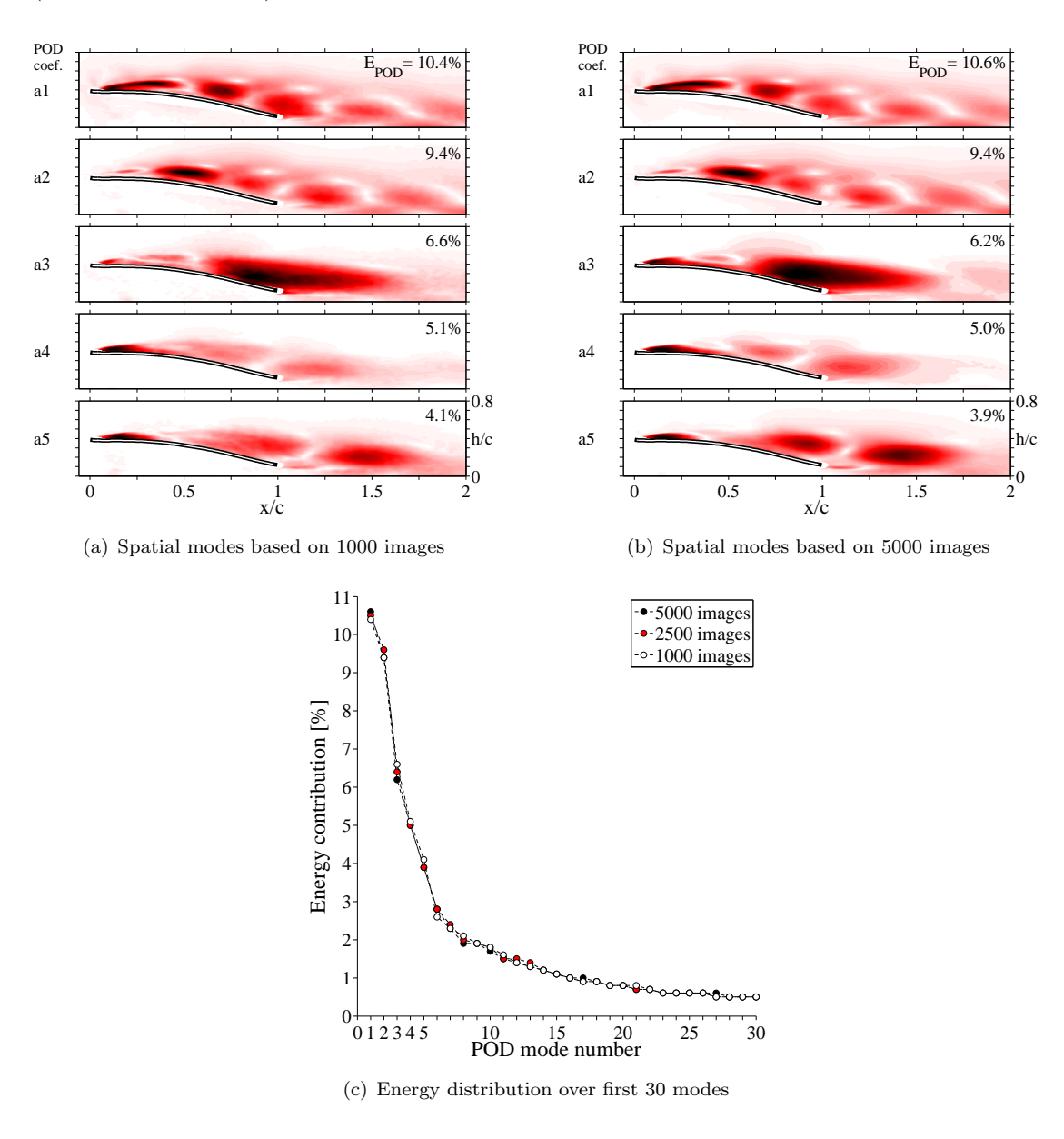


Figure 3.29: Sensitivity analysis of POD on streamwise flow-plane with 1000 and 5000 samples (based on POD without mean). Spatial POD mode shapes (intensity normalised contours, showing  $\sqrt{(U_{POD}^{\prime 2}+V_{POD}^{\prime 2})}/U_{\infty}$ ) and their individual energy content are shown for the first five dominant POD modes. Exemplary case: Extreme ground-effect (h/c = 0.1) at  $\alpha$  =15°. Ultimetly, the assamble size does not show any significant impact on the POD mode shapes and their energy content.

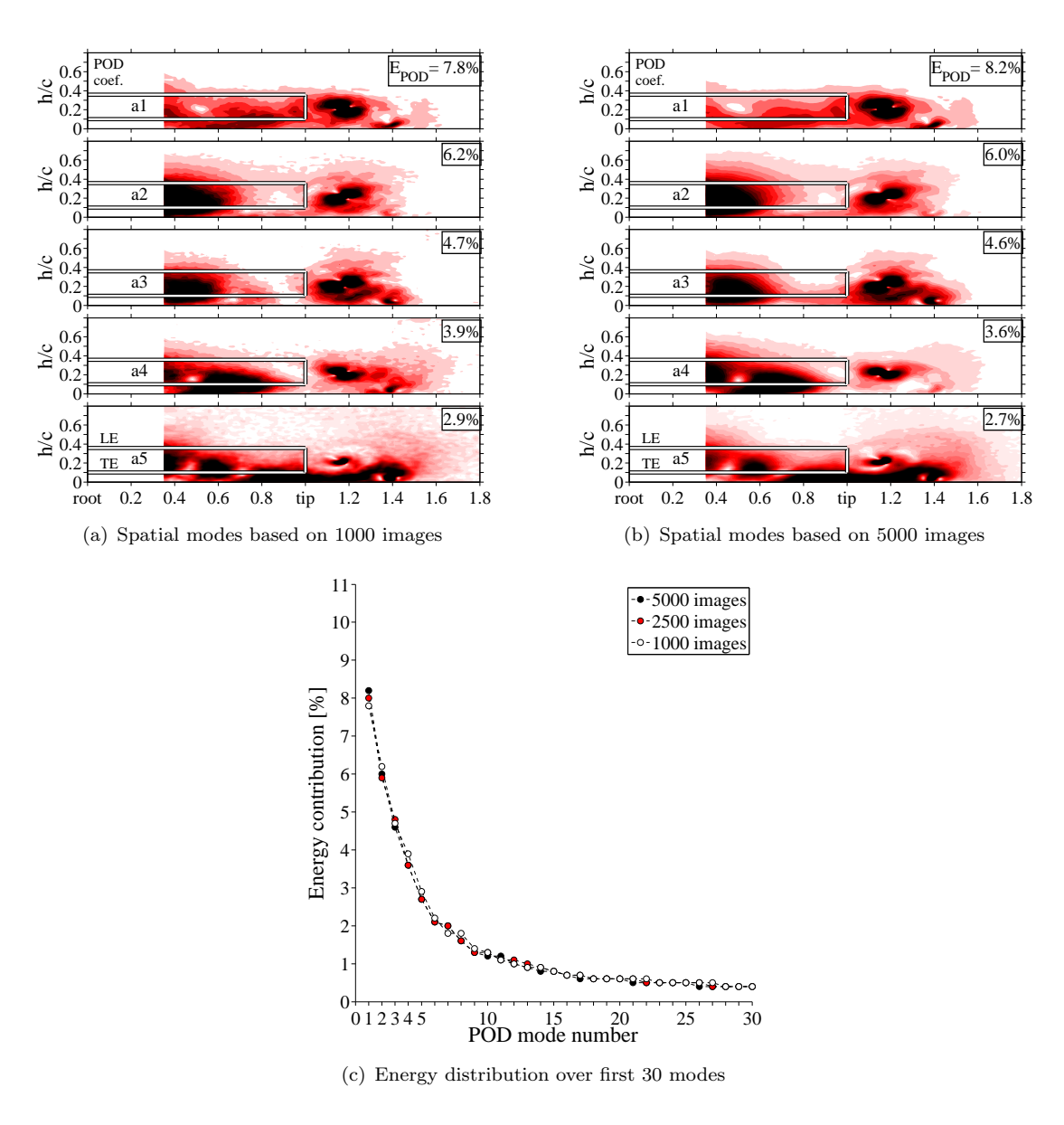


Figure 3.30: Sensitivity analysis of POD on spanwise flow-plane with 1000 and 5000 samples (based on POD without mean). Spatial POD mode shapes (intensity normalised contours, showing  $\sqrt{({W'}_{POD}^2 + {V'}_{POD}^2)}/U_{\infty}$ ) and their individual energy content are shown for the first five dominant POD modes. Exemplary case: Extreme ground-effect (h/c = 0.1) at  $\alpha$  =15°. Ultimetly, the assamble size does not show any significant impact on the POD mode shapes and their energy content.

# Chapter 4

# Effect of Aspect-ratio on Membrane Half-wings

# 4.1 Aerodynamic Loads

In this result section, the aerodynamic coefficients  $(C_L, C_D, C_{M/4})$  of membrane wings are compared with those of rigid flat plate wings. Modifications with aspect-ratio changes are in major focus. In addition to mean effects, lift, drag and pitch oscillations are also examined.

#### 4.1.1 Lift and Drag of Rigid Flat Plates and Membrane Wings

Figure 4.1 presents the influence of aspect-ratio (AR-1 and AR-2) on the aerodynamic lift and drag coefficients of rigid flat plate wings and membrane wings with increasing angleof-attack (note that sweeping towards increasing/decreasing angles can have hysteresis effect, see later in Figure 4.2). In addition to time-averaged lift and drag coefficients, the intensity of fluctuations of the coefficients ( $\sigma(C_L)$  and  $\sigma(C_D)$ , with 68% confidence level) is indicated by translucent regions. Furthermore, a waterfall chart at the top of the figure shows the power spectral density of the lift coefficient ( $PSD(C_L(t))$ ) across all angles of attack.

Membrane wings displayed a superior lift performance in comparison to rigid flat plates, which is expected. At ordinary cruise angles of MAVs of  $5^{\circ} \leq \alpha \leq 15^{\circ}$ , membrane wings showed a benefit of up to 50–57% in lift coefficient  $C_L$  in comparison with rigid flat plates for both AR-2 and AR-1, which is consistent with findings from other investigations (Galvao et al., 2006; Tregidgo et al., 2011; Song et al., 2008). This result is caused by the tendency of membrane wings to increase camber under loading, leading to a higher lift (Rojratsirikul et al., 2010b). The maximum lift coefficient of AR-2 membrane wings

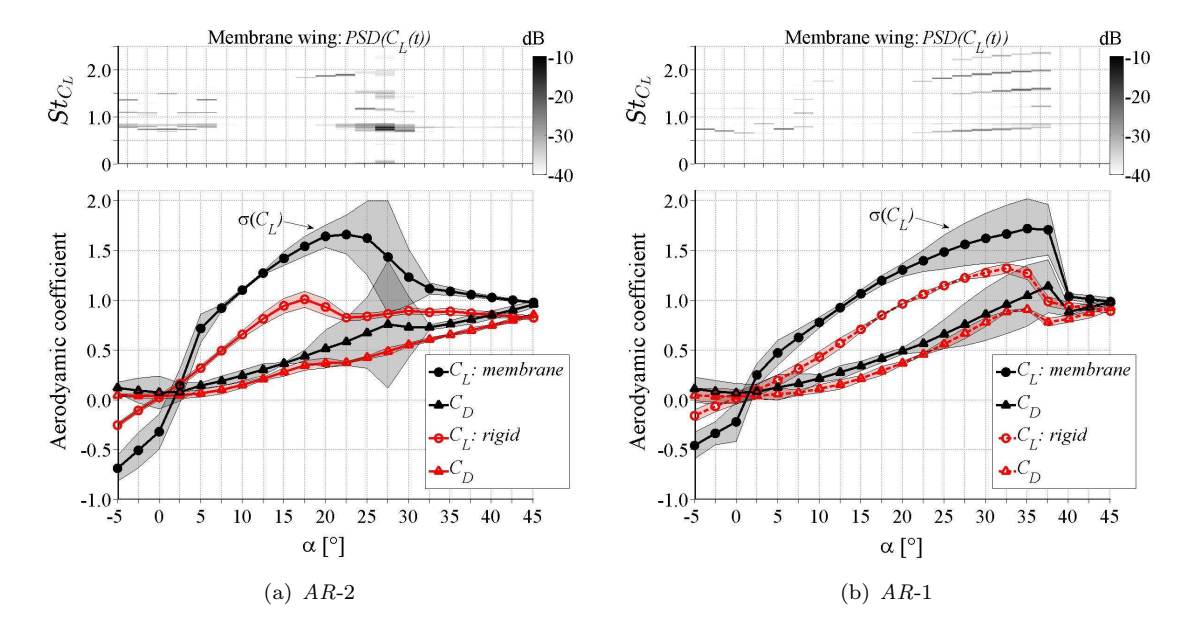


Figure 4.1: Influence of AR on lift and drag coefficients of rigid flat plates and membrane wings. Shaded regions represent the measured standard deviation  $(\sigma)$  in the aerodynamic coefficients. Additionally, spectral (PSD) information of the membrane wing lift coefficient (top) indicate low Strouhal numbers at onset of stall. The intensity of fluctuations is lower for lower AR.

increases by 60% from  $C_{L_{max}} = 1.0$  to  $C_{L_{max}} = 1.6$ , whereas the AR-1 wing still showed a gain of 31% from  $C_{L_{max}} = 1.3$  to  $C_{L_{max}} = 1.7$ . This benefit for the higher AR could be linked with its reduced downwash region (and therefore larger slope), which enables the wing to sustain high local angles of attack at the leading-edge, resulting in an increased camber in comparison with lower aspect-ratio membrane wings. This was supported by the comparison with overall camber deformations along the span, which are discussed later. The maximum stall angle of membrane wings  $\alpha(C_{L_{max}})$  was delayed by 5° in comparison with rigid flat plates. This delay can be explained by the flexible nature of membrane wings, which permit the excitation of boundary layer perturbations. These perturbations allow the flow to stay attached longer and promote vortex roll up with low pressure content to sustain the lift (negative pressure on upper wing surface) at high incidence (Rojratsirikul et al., 2009). At moderate incidence of  $5^{\circ} \le \alpha \le 15^{\circ}$ , the increase in lift was accompanied by an increase in (induced) drag of up to 43% for the AR-2 wing and 59% for the AR-1 case.

Further investigation of the lifting behaviour of rigid flat-plates and membrane wings around zero angle-of-attack reveals non-zero (bi-stable) lift values for the (inherent compliant) membrane wings which are able to snap-through their LE-TE related axis (zero bending-stiffness). The behaviour depends on the initial measurement direction (sweep towards inclining or declining angles-of-attack) and is illustrated in Figure 4.2 for all three aspect ratios. The size of the hysteresis zone is found to span between  $-5^{\circ} \leq \alpha \leq 5^{\circ}$  and is comparable with results from the literature (Song et al., 2008).

In addition, it appears that aspect-ratio changes do not have a significant effect on the shape and size of the hysteresis zone. Rigid flat-plates do not show hysteresis zones around zero angle-of-attack (not shown for brevity).

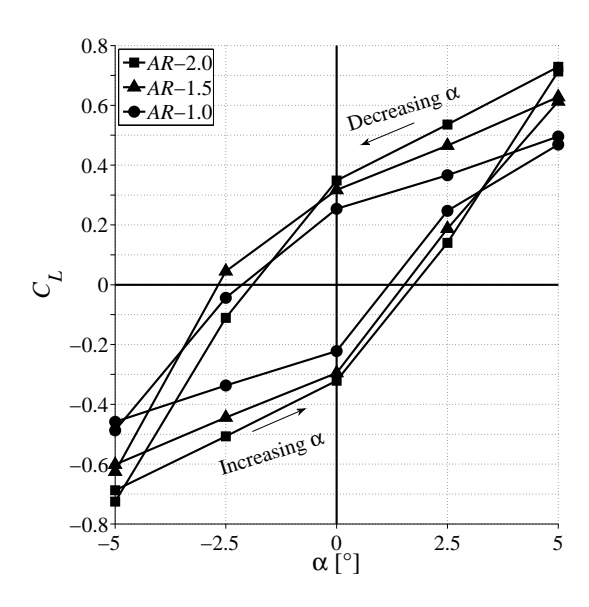


Figure 4.2: Hysteresis in lift for membrane wings around zero angle-of-attack, modifying with aspect-ratio

In addition to static results, the lift and drag of membrane wings show strong dynamics which change with angles of attack and aspect-ratio. Figure 4.1 indicates that membrane wings fluctuation intensity in lift and drag coefficient grows dramatically at the onset of stall, reaching  $\sigma_{max}=0.6$  at  $\alpha=27.5^{\circ}$  for the AR-2 and  $\sigma_{max}=0.2$  at  $\alpha=35^{\circ}$  for the AR-1 wings. This rise happens progressively for the AR-2 membrane wing with increasing angle-of-attack. Low fluctuation intensities can be observed between  $\alpha=7.5^{\circ}$  to  $15^{\circ}$  and at post-stall incidences. Rigid flat-plate wings also show dynamics in their aerodynamic coefficients at the onset of stall, however to a much smaller extent ( $\sim$  1-order of magnitude smaller). The strong excitation, encouraged by the membrane wing flexibility, is coupled with the unsteady flow over a stalled wing leading to a feedback loop between membrane wing deformation and the unsteady flow. This is manifested in the strong fluctuations in lift and drag forces.

Inspection of the spectral content of lift fluctuations of membrane wings (shown at the top of Figure 4.1) reveals the presence of strong frequencies at the onset of stall. The dominant frequency is the frequency with the highest amplitude peak of the PSD. The higher AR-2 (Figure 4.1a) shows an increase in dominant frequency of St=0.7 at  $\alpha=0^{\circ}$  up to St=1.9 at  $\alpha=20^{\circ}$ . This growth is probably linked with an increase in membrane tension with rising dynamic pressure and the higher structural response of the wing. At stall angles of  $\alpha=25^{\circ}$ , the structural response gets more energised and the dominant frequency drops back to St=0.7. Low frequency vortex-shedding excites the membrane structure at low mode shapes and results in energy content for low

frequencies (Gordnier, 2009). The lower AR-1 wing (Figure 4.1b) shows similar trends to the higher AR-2 wing, however with delay of the frequency-drop into higher angles of attack. At  $\alpha \geq 25^{\circ}$ , the AR-1 case shows energised higher dominant frequencies, which indicates that the membrane response is not driven by vortex-shedding as seen in AR-2.

### 4.1.2 Aerodynamic Range and Power Efficiency

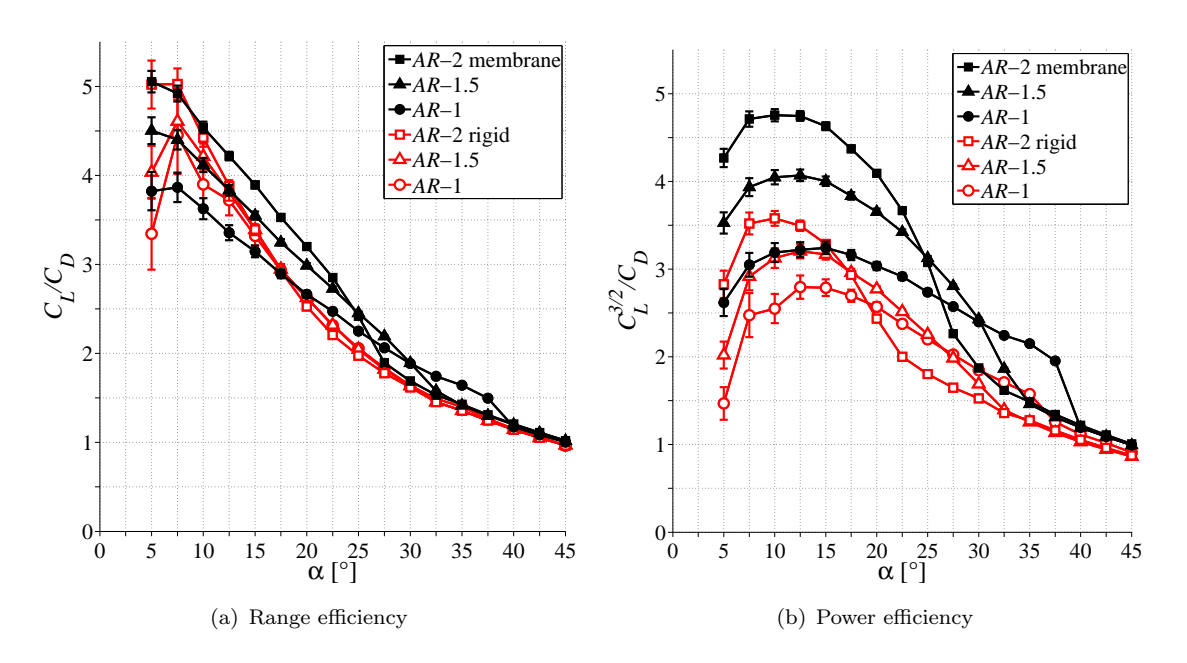


Figure 4.3: Influence of AR on aerodynamic range,  $C_L/C_D$ , and power efficiency,  $C_L^{3/2}/C_D$ , of rigid flat plates and membrane wings, including error-bars that indicate uncertainty.

Figure 4.3 displays the influence of AR on the aerodynamic range  $(C_L/C_D)$  and power efficiency  $(C_L^{3/2}/C_D)$  of rigid flat plates and membrane wings. In addition, the uncertainties in the mean values are displayed, which are based on the uncertainty in the load cell measurement. Generally, higher aspect-ratios classically result in higher aerodynamic range efficiencies  $(C_L/C_D)$ . Membrane wings are found to be largely comparable with rigid flat plates in terms of aerodynamic range, which is in agreement with previous studies (Galvao et al., 2006; Song et al., 2008). However, rigid flat plates show a trend in slightly higher range efficiency at low angles-of-attack of  $\alpha \leq 15^{\circ}$ , whereas membrane wings gain up to 15% at higher angles of  $\alpha \geq 15^{\circ}$  (Figure 4.3a). This is caused by the shape adaptability and flexibility of membrane wings, which enable benefits in efficiency especially at higher incidence due to longer flow attachment and promotion of vortex-shedding (Rojratsirikul et al., 2010a).

Membrane wings clearly show superiority in power efficiencies  $(C_L^{3/2}/C_D)$  in comparison with flat plates, due to their strong lift enhancement (Figure 4.3b). The power efficiency is a key factor in the endurance of MAVs. Membrane wings exhibit superior power

efficiencies over the entire range of angles of attack. They are able to extend the peak power efficiency  $(C_L^{3/2}/C_D)_{max}$  by 16% for AR-1 and up to 33% for the AR-2 wing. At higher angles of attack, membrane wings show even higher benefits (>60% for AR-2 at  $20^{\circ} \leq \alpha \leq 25^{\circ}$ ) compared with flat plates, which have large flow separations for these angles of attack. It is evident that the decision for the correct AR of a power efficient MAV depends on the angle-of-attack for cruise flight as well as the requirements for manoeuvrability.

#### 4.1.3 Pitching Moment

The pitching moment (about the quarter chord location) is found to oscillate strongly at angles of attack around  $-5^{\circ} \leq \alpha \leq +5^{\circ}$  and in the vicinity of stall, similar to the lift and drag coefficient. Figure 4.4 shows the variation of pitch moment coefficient about the quarter chord position  $C_{M/4}$  with angle-of-attack. Rigid flat plates and membrane wings with AR-1 and AR-2 are compared. In addition to time-averaged pitch moment variation with angle-of-attack, the variance in this coefficient  $\sigma(C_M)$  (68% confidence level) as well as its spectral content  $PSD(C_M(t))$  are investigated.

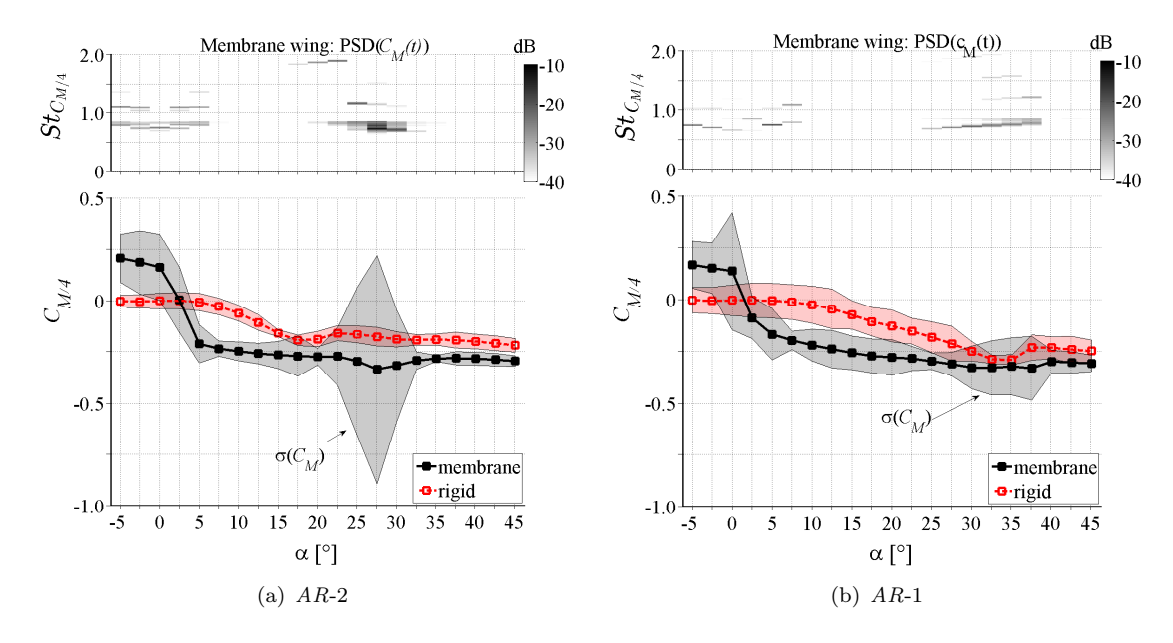


Figure 4.4: Pitching moment coefficient  $C_{M/4}$  (mean and std) and its spectra (PSD) for rigid flat plate and membrane wings.

Rigid flat plate wings and membrane wings both show fluctuations in pitching moment. However, the fluctuations for membrane wings reflect their flexibility and display a large variance. The higher AR-2 case (Figure 4.4a) exhibits significant variation in pitch moment  $\sigma(C_M)$  at high angles of attack, which can temporarily create positive pitch moment coefficients  $C_M$ . However, the dominant frequency of these pitch moment oscillations appears to be high  $(0.7 \le St \le 1.9)$  in relation to gust response frequencies of MAVs, which is in the range  $0.01 \le St \le 0.1$  (Ifju et al., 2002; Watkins et al., 2006).

In comparison, the lower AR-1 membrane wing (Figure 4.4b) seems to suppress strong vibrations in pitch effectively for these high angle incidences. The frequencies of AR-1 pitch oscillations tend to be similar for the AR-2 wing, however, the energy content is different. This indicates that the dominant oscillation frequency in the pitch moment is more related to chord than span variation, as the chord remains fixed in this experiment.

Furthermore, rigid flat plate wings indicate higher pitching moment slopes than membrane wings at moderate angles of attack  $10^{\circ} \leq \alpha \leq 15^{\circ}$  (Figure 4.4). Rigid flat-plate wings of AR-2 exhibit a distinct higher lift slope  $C_{M_{\alpha}} = -1.05 \frac{1}{rad}$  than membrane wings with  $C_{M_{\alpha}} = -0.25 \frac{1}{rad}$ . The AR-1 case still displays a benefit of  $C_{M_{\alpha}} = -0.56 \frac{1}{rad}$  for rigid wings in comparison with  $C_{M_{\alpha}} = -0.43 \frac{1}{rad}$  for membrane wings. The gain in static pitch stability  $C_{M_{\alpha}}$  of membrane wings increases for the given  $\alpha$ -range with lower aspect-ratios. This is in contrast with rigid flat plate wings where higher aspect-ratio perform better.

#### 4.2 Membrane Deformations

The results in this section focus on the influence of aspect-ratio on membrane deflection and dynamics. First, mean wing deflections are related to aerodynamic performance as discussed in the previous Section 4.1. Second, the pitch-stability related chordwise location of maximum camber is discussed. Third, instantaneous membrane vibrations are shown. Fourth, the time-series in membrane fluctuations are time-averaged and shown across the wingspan and chord. Five, spatial decomposition of the membrane vibrations illustrates dominant chordwise mode shapes and their spectral content. Finally, membrane dynamics are correlated to force dynamics.

### 4.2.1 Mean Membrane Deflection

The photogrammetry setup consists of a lightsheet in the x-z plane, which allows us to capture time-resolved vertical membrane motions z(x,y,t) along the chord at four semi–span locations (y/(b/2) = 25, 50, 75, 95%). Mean membrane deformations were obtained by averaging the instantaneous results of the high-speed photogrammetry measurements. Figure 4.5 shows the variation of the maximum chordwise membrane deformation  $z_{max}$  (this will serve as an indicator of the camber) at different wing span locations and at  $5^{\circ} \le \alpha \le 35^{\circ}$ . The line thickness in Figure 4.5 increases with angle-of-attack to clarify the drop in mean deflection at stall angles. The change in mean deflection can be correlated to the change of the mean lift forces. For the AR-2 case when  $\alpha > 25^{\circ}$ , the reduction in lift force (Figure 4.1a) is correlated with a reduction in maximum mean membrane deflection, especially towards the wing tip (Figure 4.5a). The AR-2 wing also shows that the membrane deformation displays a progressive increase in deflection from

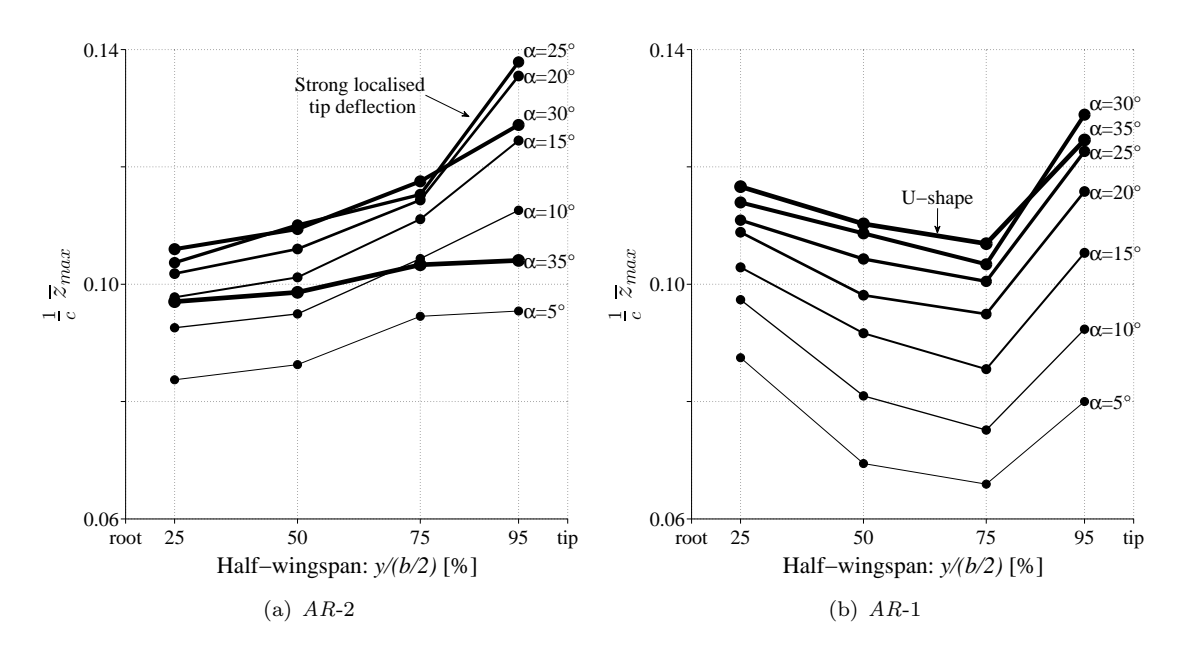


Figure 4.5: Influence of AR on chord-normal membrane mean deflection  $\overline{z}_{max}/c$  along the wingspan. Note that AR-2 case exhibits larger tip deformations, probably due to strong localised tip-vortex which breaks down at  $\alpha > 25^{\circ}$ . The AR-1 case shows U-shape deflections along the wingspan and could reflect a movement of the tip-vortex to the wing root.

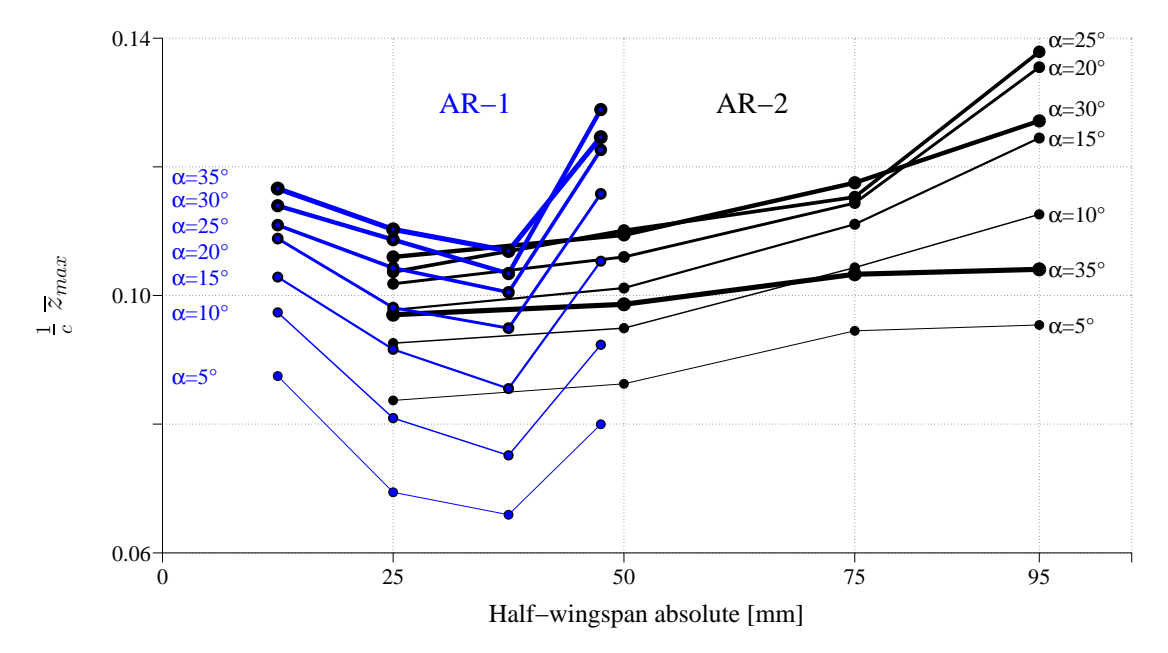


Figure 4.6: Illustration of membrane mean deflection  $\overline{z}_{max}/c$  along the wingspan are shown in absolute dimentions [mm]. Direct comparison of AR-2 Figure 4.5a and AR-1 Figure 4.5b wings. Both wings show little overlap in their absolute values, suggesting significant different flow conditions between both aspect-ratios.

the root to the wing tip with increasing angle-of-attack, which decreases in post-stall condition of  $\alpha \geq 25^{\circ}$ .

In comparison, the lower AR-1 case (Figure 4.5b) exhibits similar camber deflections at root and tip, while region between the root and tip exhibit lower deflections resulting in an overall U-shape deflection profile across the span. Figure 4.6 shows the membrane deflection of both aspect-ratios within one common absolute span coordinate system [mm]. Both aspect-ratios show little common features in their membrane deflection along the span. Different flow conditions (tip-vortex strengths) of both aspect-ratios might be the cause for this differences in the membrane mean deflection.

# 4.2.2 Chordwise location of maximum camber

The variation in the location of maximum camber can be used as an indicator for the pitching characteristics  $(C_{M/4})$  of flexible membrane wings and indicates pressure modifications along the chord (Gordnier and Attar, 2014). Figure 4.7 shows the chordwise variation in maximum camber position  $(\frac{1}{c} x_{\overline{z}_{max}})$  for four sections along the span, ranging from 25% to 95%-span and modifying with angle-of-attack and aspect-ratio. Time-averaged mean quantities are illustrated as lines whereas vibration intensities are shown with color-shading. The chord mid position is defined by  $\frac{1}{c} x_{\overline{z}_{max}} = 0.5$ . Higher values (>0.5) indicate a movement of maximum camber towards the trailing-edge, while low values (<0.5) show its propensity to be located towards the leading-edge.

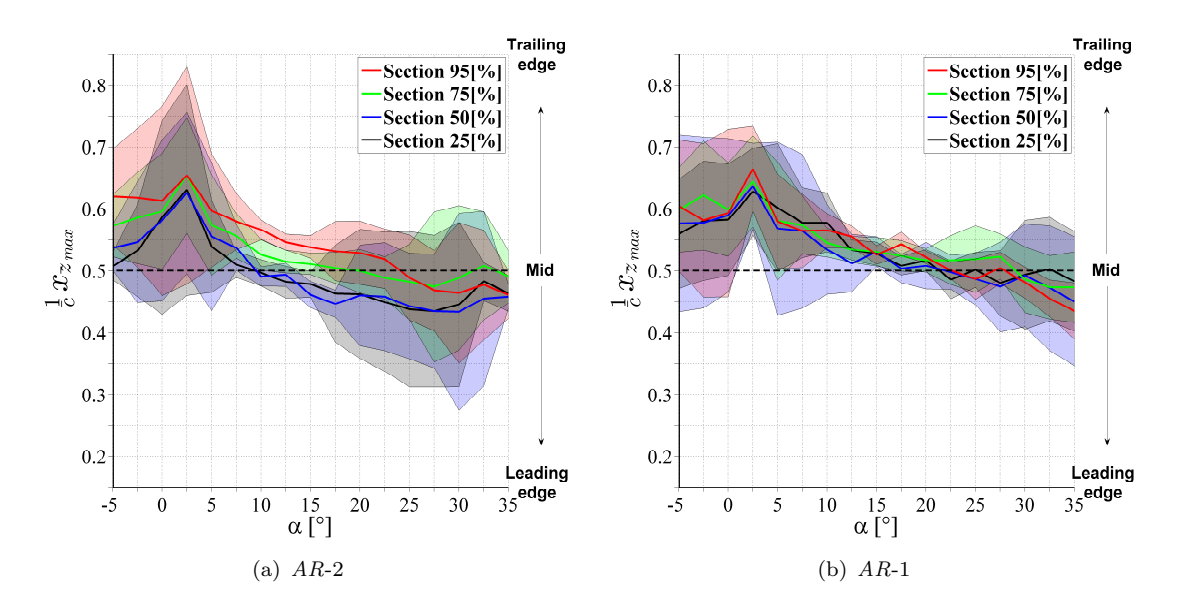


Figure 4.7: Chordwise location of maximum camber  $(\frac{1}{c} x_{\overline{z}_{max}})$  at four sections along the span, modifying with angle-of-attack and aspect-ratio. Lines represent mean values, shading standard deviation.

Similar to previous load-cell based pitch-moment results (Section 4.1.3), both aspectratios show a bi-stable hysteresis region around  $-5^{\circ} \leq \alpha \leq 5^{\circ}$  in which they are accompanied with a strong rearward camber position and strong (bi-stable related) camber fluctuations. The rearwards located maximum camber position (e.g. 13% out of mid towards TE for  $\alpha = 2.5^{\circ}$ ) indicates a trailing-edge localised suctioning effect which correlates well with the findings of a strong nose-down pitch moment of  $C_{M/4} = -0.25$ in Figure 4.4. For growing incidences between  $5^{\circ} \leq \alpha \leq 15^{\circ}$ , this rearwards located membrane wing camber (Figure 4.7) appears further reflected in a stronger (nose-down) pitch-moment in reference to rigid flat-plates (Figure 4.4).

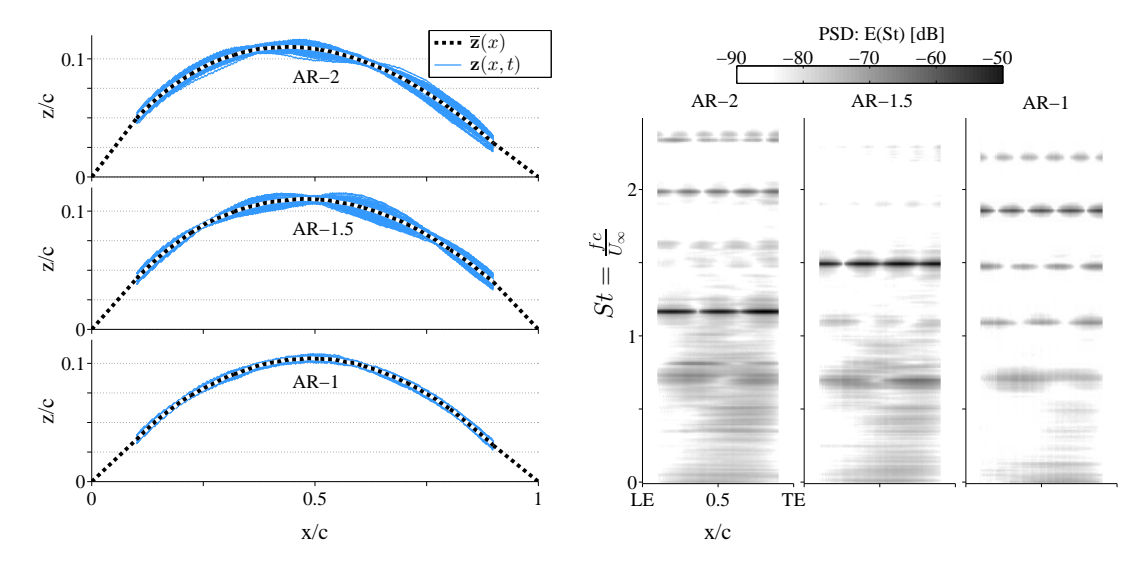
With further increasing angle-of-attack up to stall, the maximum camber point of membrane wings moves more and more towards their leading-edge, explaining their low (nearly horizontal) pitch moment slope (Figure 4.4). The vibration intensity reduces up to pre-stall conditions, suggesting an aerodynamically tensioned membrane with attached flow conditions. This behaviour goes confirm with findings in the literature (Arbos-Torrent et al., 2013a). Beyond stall conditions, the camber position close to the leading-edge tends to drop back to a mid-chord position and camber oscillations start to gain (shedding related) intensity. Lower aspect-ratios (Figure 4.7b) show generally a more rearward camber position and their movements towards the LE appear delayed with increasing angles-of-attack. The reason might base on the growing influence of the tip-vortex structures of low-aspect-ratio wings which might reduce the local angle-of-attack at the leading edge and therefore delay the impact of leading-edge vortex-shedding.

#### 4.2.3 Instantaneous Membrane Dynamics

Time-resolved photogrammetry allows to resolve time-dependent spatial and spectral membrane content, modifying with angle-of-attack and aspect-ratio. Figure 4.8 provides a view into a number of instantaneous chordwise membrane motions (Figure 4.8a) and their spectral content at every chordwise position (Figure 4.8b). A wingspan position of y/(b/2) = 50% and an angle-of-attack of  $\alpha = 25^{\circ}$  is selected for brevity.

AR-1 membrane wings show reduced vibration amplitudes in the membrane motion compared to the AR-2 case. Moreover, well-defined chordwise vibration modes can be observed in the membrane, which increase from spatial mode 3 to mode 5 with decreasing aspect-ratio, accompanied with an incline in frequency level.

Figure 4.9 illustrates the influence of AR and angle-of-attack on the temporal development of chordwise membrane vibration amplitudes  $z'(x,t) = \frac{1}{c}(z-\overline{z})$ . The midspan position y/(b/2) = 50% is considered. It can be seen that membrane deformation amplitudes can easily reach 10% of the membrane mean deflections for usual MAV flight incidence of  $\alpha = 10^{\circ}$  to 20°. However, the hysteresis zone at  $\alpha = \pm 5^{\circ}$  exhibits much



- crease in aspect-ratio.
- (a) Spatial instant z(x,t) and mean  $\overline{z}(x)$  chordwise (b) PSD of membrane vibrations at every chordwise lomembrane deflections. Note increase in chordwise mode cation. Note the increasing number of nodes as well innumber and reduced vibration amplitudes with de- creasing Strouhal numbers with decrease in aspect-ratio of membrane wings.

Figure 4.8: Influence of AR on spatio-temporal characteristics of membrane deformation (mid-semispan,  $\alpha = 25^{\circ}$ ).

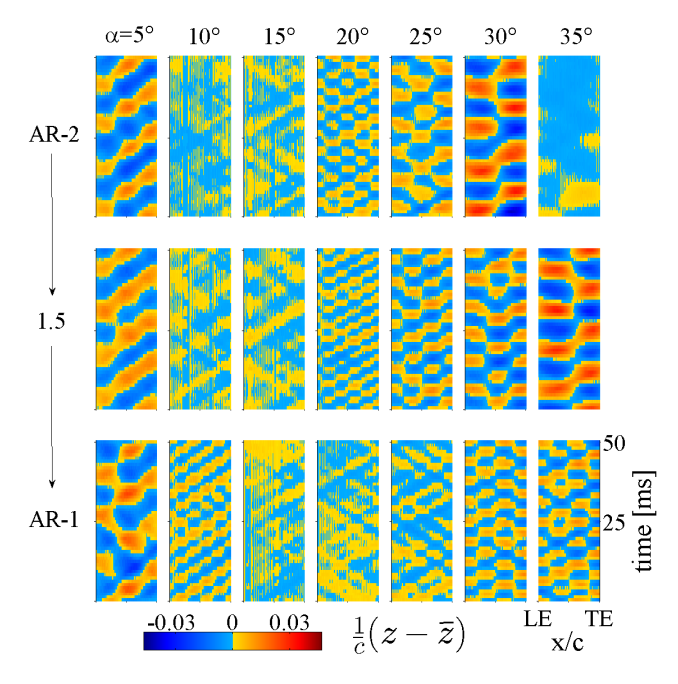


Figure 4.9: Instantaneous membrane vibrations  $z'(x,t) = \frac{1}{c}(z(x,t) - \overline{z}(x))$  as a function of time for different aspect-ratios and angles of attack at mid-span. Note clear standing-wave characteristics of the membrane vibrations across all cases. Reduced vibration intensities for low AR wings is accompanied with increasing chordwise mode numbers. A video for  $\alpha = 30^{\circ}$  is available via: https://youtu.be/3piItqwoo\_g

larger relative vibrations up to 30% due to the lack of membrane bending stiffness causing large, unstable camber deflections in combination with low membrane mean deflections. The high deformation amplitudes are accompanied by low mode shapes (or wavenumbers). High angles of attack show strong vibrations accompanied by a reduction in mode number in post-stall conditions. This result agrees with earlier membrane wing studies at a fixed aspect-ratio (Arbos-Torrent et al., 2013a; Rojratsirikul et al., 2011). Vibrations at those high incidences are shown to be a result of totally separated flow which contain strong and highly dynamic rolling-up vortices (Rojratsirikul et al., 2009). In contrast, incidence of  $\alpha = 10^{\circ}$  to  $15^{\circ}$  show very low fluctuation levels with difficulties in identifying clear dominant modes.

#### 4.2.4 Fluctuation Magnitude along Chord and Wingspan

Spatial distribution of membrane fluctuation magnitudes,  $z_{STD}$  (eq. 4.1), in both chordwise and spanwise direction were determined by taking the standard deviation of the vertical membrane motion z(x,t) at all surface points.

$$z_{STD}(x,y) = \sqrt{\frac{1}{T} \sum_{t=0}^{T} (z(x,y,t) - \overline{z}(x,y))^2}$$
 (4.1)

Figure 4.10 shows the influence of AR on chordwise (mid-semispan, Figure 4.10a) and spanwise (Figure 4.10b) membrane fluctuation magnitudes with changes in angle-of-attack. At a given angle-of-attack of  $15^{\circ} \leq \alpha \leq 30^{\circ}$ , lower aspect-ratios exhibit higher mode shapes with lower amplitude. For example, at  $\alpha = 30^{\circ}$ , the AR-2 wing exhibits mode-2, whereas AR-1.5 shows mode-3 and AR-1 displays mode-4. This could be related to an increased downwash region with decreasing AR, resulting in a declining local angle-of-attack at the leading-edge, which reduces cambering. As a result, the influence of vortex-shedding excitations may be suppressed at higher angles of attack.

Previous studies on membrane wings with an aspect-ratio of AR-1.4 indicate that membrane fluctuation magnitudes  $z_{STD}$  continue to rise from root to wing tip (Song et al., 2008), whereas the fluctuations was mostly a constant with slight increase at the mid of the semi-span for a lower aspect-ratio AR-0.9 (Galvao et al., 2006). However, these results are limited to a selected incidence of  $\alpha \sim 25^{\circ}$ . In the current study, the results in Figure 4.10b illustrate the influence of AR on fluctuation magnitude changes along the wingspan  $z_{STD_{max}}(y)$  with changing angles of attack. The fluctuation magnitude  $z_{STD_{max}}(y)$  bases on the highest standard deviation in membrane deformation along the chord for a given wingspan position y. The resulting contours are interpolated along the span and therefore have to be seen as qualitative due to the limited number of data points along the wingspan (y/(b/2) = 25, 50, 75, 95%).

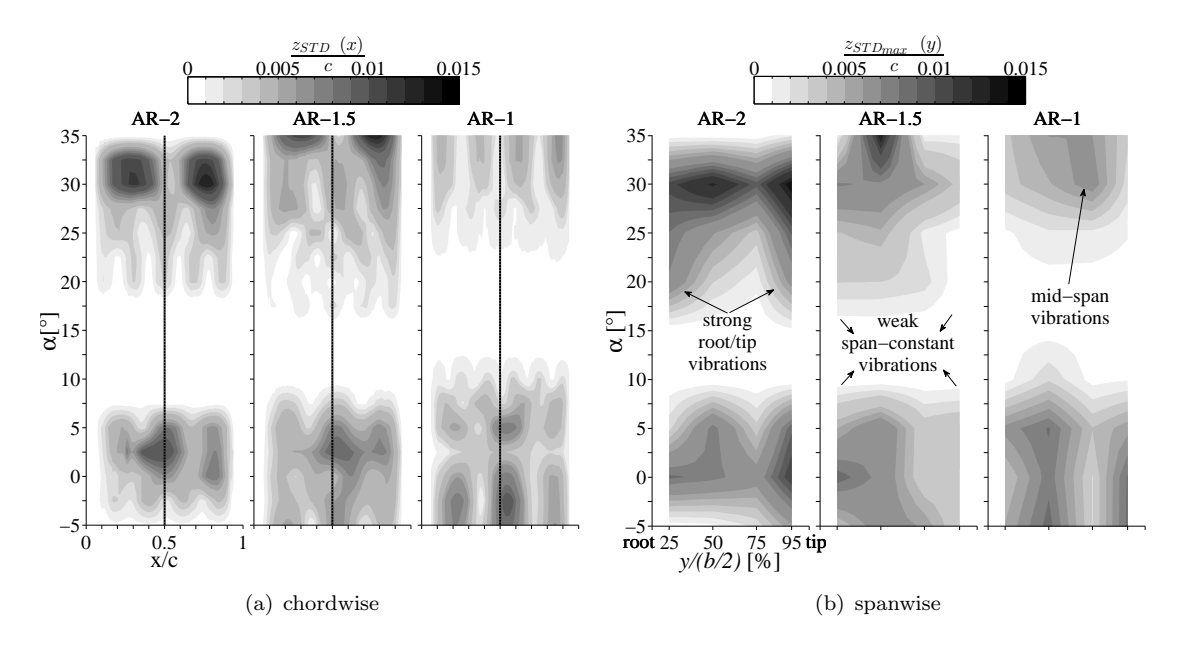


Figure 4.10: Fluctuation intensity along the chord (at mid-semispan position 50%) and along the wingspan with changing angle-of-attack and AR.

Because the membrane wing is only supported at the LE/TE, the unsupported root and wing tip of the membrane wing geometry show strong vibrations that increase in amplitude with increasing AR. The higher aspect-ratio AR-2 showed strong vibrations at wing tip and root, whose amplitude increases beyond  $\alpha \geq 20^{\circ}$ . The AR-1 wing shows dominant localised vibrations at mid half-span for  $\alpha \geq 20^{\circ}$ , which grow in magnitude with increasing angle-of-attack. Previous experiments with rigid flat plates show that the influence of the tip-vortex extends towards the root of the wing for lower aspect-ratio (Mizoguchi and Itoh, 2013). The vibrations towards mid half-span could be influenced by the tip-vortex. This change in membrane vibrations between AR-1 and AR-2 suggests the importance of the interaction between the flow field and the membrane.

Finally, it should be noted that the trends in chordwise and spanwise vibrations depend on the boundary conditions of the selected membrane wing structure. Unsupported membrane sections lead to non–uniform aerodynamic tensioning at the edges, resulting in more diverse vibrations and higher diversity in spectral signature (free LE/TE (Zhang et al., 2014), free TE (Attar et al., 2011)). However, it seems that all membrane wing structures share the main features such as correlation between tension and frequency at low incidence and excitation due to bluff body shedding at higher angles (free TE (Timpe et al., 2013), perimeter (Rojratsirikul et al., 2011)), free root/tip (Galvao et al., 2006)). The unsupported root section of the current half-wing setup has a small (< 0.5mm) gap to the wall.

This gap allows pressure exchange between lower and upper membrane surface, but due to its size this exchange is limited. However, changes in overall fluctuation magnitude  $z_{STD}$  at the near wall root region and the wing tip illustrate no significant differences in magnitude (Figure 4.10b).

# 4.2.5 Modal-Analysis of Membrane Dynamics

Applying the sinusoidal-decomposition technique (Section 3.2.4.2) on membrane vibrations reveals that chordwise membrane vibrations in high fluctuation regions can be described with 1 or 2 dominant sinusoidal modes with a fitting quality of  $R^2 \geq 0.8$  (where  $R^2 = 1$  is a perfect fit). Using 3 dominant modes, results in a quality of fit of  $R^2 \geq 0.9$ . The performance of fit using only a limited number of modes drops in regions of low vibration, because the dominance of individual modes is not apparent. Nevertheless, modes beyond the first 6 modes are found to make a negligible contribution.

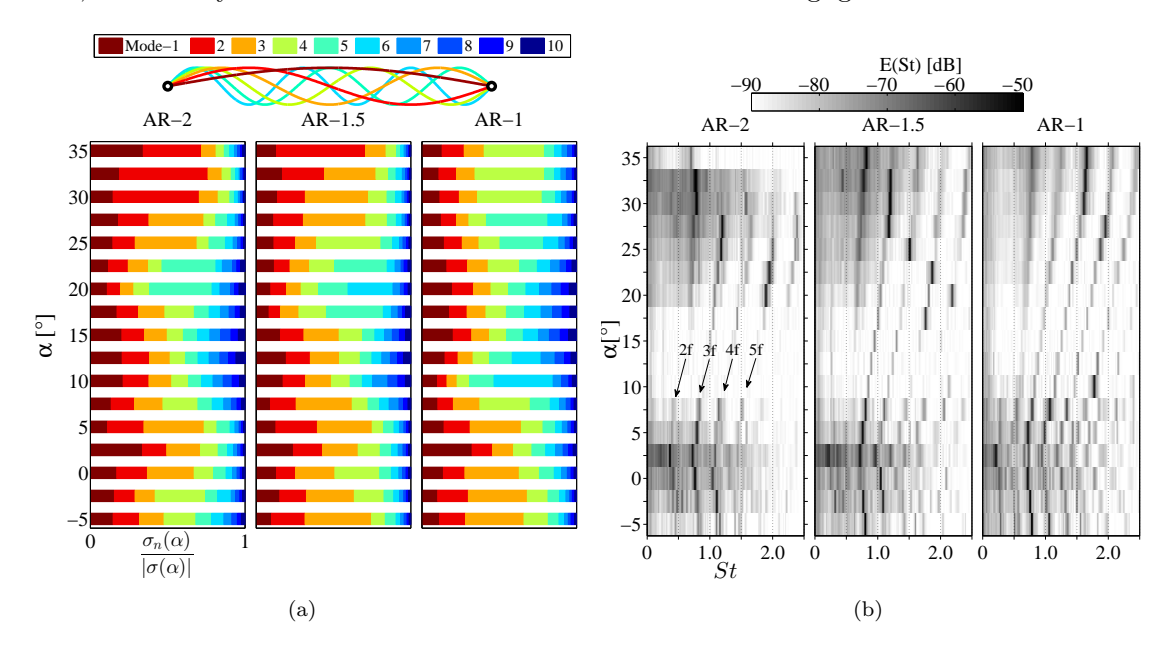


Figure 4.11: Contribution of first 10 spatial sinusoidal mode shapes  $\sigma_n(\alpha)$  of chordwise membrane vibrations and their overall variation in spectral content with angle-of-attack at mid-semispan location. (a) Relative contribution of individual mode shapes  $\sigma_n(\alpha)$  to the overall chordwise deformation of the membrane (normalisation with total energy content  $|\sigma(\alpha)| = \sum_{n=1}^{\infty} \sigma_n$ ) for various angles of attack, aspect-ratio at the midspan of the wing. Also shown in the figure are the shapes of the first 6 modes. (b) Variation in peak spectral energy content E(St) (eq.3.4) of the first 10 modes.

Figure 4.11a shows the relative contribution of individual sinusoidal-decomposed mode shapes  $\sigma_n(\alpha)$  (eq. 3.2) to the overall chordwise deformation of the membrane for various angles of attack and aspect-ratio at the midspan of the wing. Figure 4.11b shows the peak spectral energy content E(St) (eq.3.4) which bases on the 10 highest modes shapes. The spectral energy content is of major importance by mirroring the appearance and strength of (low-frequency) leading-edge vortex shedding (Rojratsirikul et al., 2009). In addition, the decomposition technique allows to filter the spectra by using a custom amount of

decomposed dominant mode shapes (reducing background-noise). This allows a clearer identification of dominant membrane vibration mode shapes with their spectral content. Regions of high vibration intensity (both at  $-5^{\circ} \leq \alpha \leq +5^{\circ}$  and  $\alpha$ -regions in the vicinity of stall) have low mode number (Figure 4.11a) and a lower dominant frequency (Figure 4.11b). At  $\alpha = 27.5^{\circ}$ , the AR-2 shows a transition region, where oscillations of mode-1, 2 and 3 appear to be strong, even though mode-3 is most developed. The corresponding frequencies are St = 0.4 (fundamental frequency, appears to be not well formed), 0.8 and 1.2. At  $\alpha = 30^{\circ}$ , stall has occurred and vortex-shedding has become a more dominant feature, resulting in mode-number 2 with lower dominant frequency. This mode shape trend is also found at infinite AR wings of free LE/TE (Arbos-Torrent et al., 2013a; Rojratsirikul et al., 2009) as well as perimeter reinforced membrane wings of the same AR-2 (Tregidgo et al., 2011), indicating that at these angles of attack chordwise mode number does not change with support structure for  $AR \geq 2$ . For the lower AR-1 at  $\alpha = 30^{\circ}$ , stall has not occurred (low influence of vortex-shedding), thus the membrane remains under tension due to increased lift, resulting in a higher mode shape 4 at St = 1.6. This trend of higher modes at lower AR is consistent with previous experiments (Galvao et al., 2006).

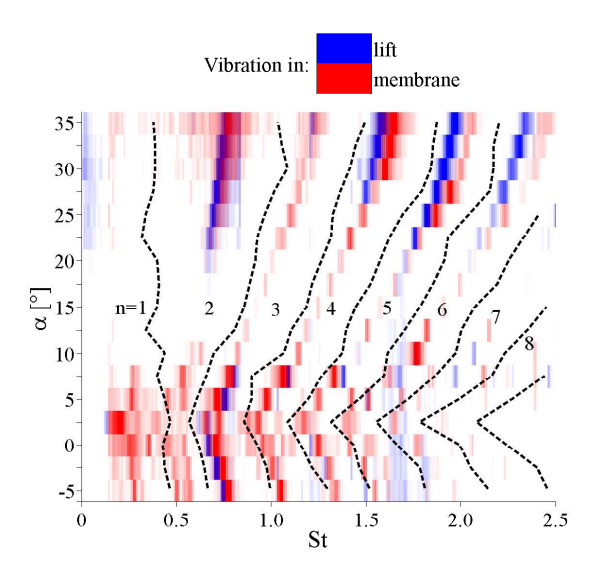


Figure 4.12: Dominant frequencies for various angles of attack in membrane motion (red) and lift coefficient  $C_L$  (blue) of a membrane wing with AR-1.

In order to synthesise the modal information and reconcile it with lift and drag fluctuations, a comparison of the spectral content of lift fluctuations and that of the membrane deformations is conducted. Figure 4.12 compares the spectra in lift coefficient (Figure 4.1b) and membrane oscillations (Figure 4.11b) for AR-1. Dominant frequencies in membrane vibrations are found to match well within  $\pm 5\%$  with the frequencies in lift coefficient  $C_L$ . In addition, the higher harmonic energy bands in lift fluctuation (blue, Figure 4.12) align well within the boundaries of the spatial mode shape changes in membrane motions (black dashed lines). These modal bands (n = [1, 2, ..., 8]) are

identified from the most energetic spatial mode number for a given frequency. This result illustrates the significant correlation between membrane motions and the dynamics in lifting forces. This observation is significant as it shows that almost all camber deformations appear to translate to force fluctuations. This is not obvious a priori since the deformation from different modes could cancel each other out and may not necessarily translate to force fluctuations. This observation is consistent across all aspect-ratios. It must be noted that this frequency information does not reveal any phase information and therefore one cannot conclude if changes in camber instantly translates to changes in forces. This lack of phase—information information is mainly caused by initially separate measurements of load and membrane dynamics. The problematic is addressed in the following experimental study on perimeter-reinforced membrane wings of Chapter 5, where time synchronised load/membrane/flow measurements will reveal time dependant coupling effects and phase—relations.

# Chapter 5

# Influence of Ground-Effect on Membrane Wings

# 5.1 Aerodynamic Loads

In this second, ground-effect related result chapter, the aerodynamic coefficients  $(C_L, C_D, C_{M/4})$  of membrane wings are compared with those of rigid flat plate wings, going from free-flight into ground-effect conditions. In addition to mean effects, lift, drag and pitch oscillations are also examined.

### 5.1.1 Lift and Drag Statistics of Rigid flat-plate and Membrane Wings

Figure 5.1 presents the influence of various ground heights h/c on the lift  $C_L$  and drag  $C_D$  coefficient of rigid flat plates and membrane wings. Firstly, both wings show lift enhancement for  $h/c \le 1$ , which matches previous results for higher (Yun et al., 2010) and lower (Rozhdestvensky, 2006) Reynolds numbers.

At low to moderate angles-of-attack of  $0^{\circ} \leq \alpha \leq 15^{\circ}$ , membrane wings show a significant benefit of up to 40% in total lift coefficient  $C_L$  in comparison to rigid flat plates. The membrane's benefit already exists for the initial unbounded flow environment at h/c = 2 and can mainly be related to flow induced cambering of the membrane, resulting in lift enhancing pressure modification on the suction-side of the wing, seen in previous rigid cambered wings (Pelletier and Mueller, 2000) and membrane wing studies (Visbal et al., 2009; Rojratsirikul et al., 2010a; Shyy et al., 2005; Gordnier and Attar, 2014).

In addition, this cambering effect of membrane wings results in a hysteresis (bi-stable) region around zero angle-of-attack which causes lift production at  $\alpha = 0^{\circ}$  (Figure 5.1b). As previously discussed in the setup design (Section 3.3.1), gravity related negative cambering (coming with negative lift trends) was overcome by placing the wing initially

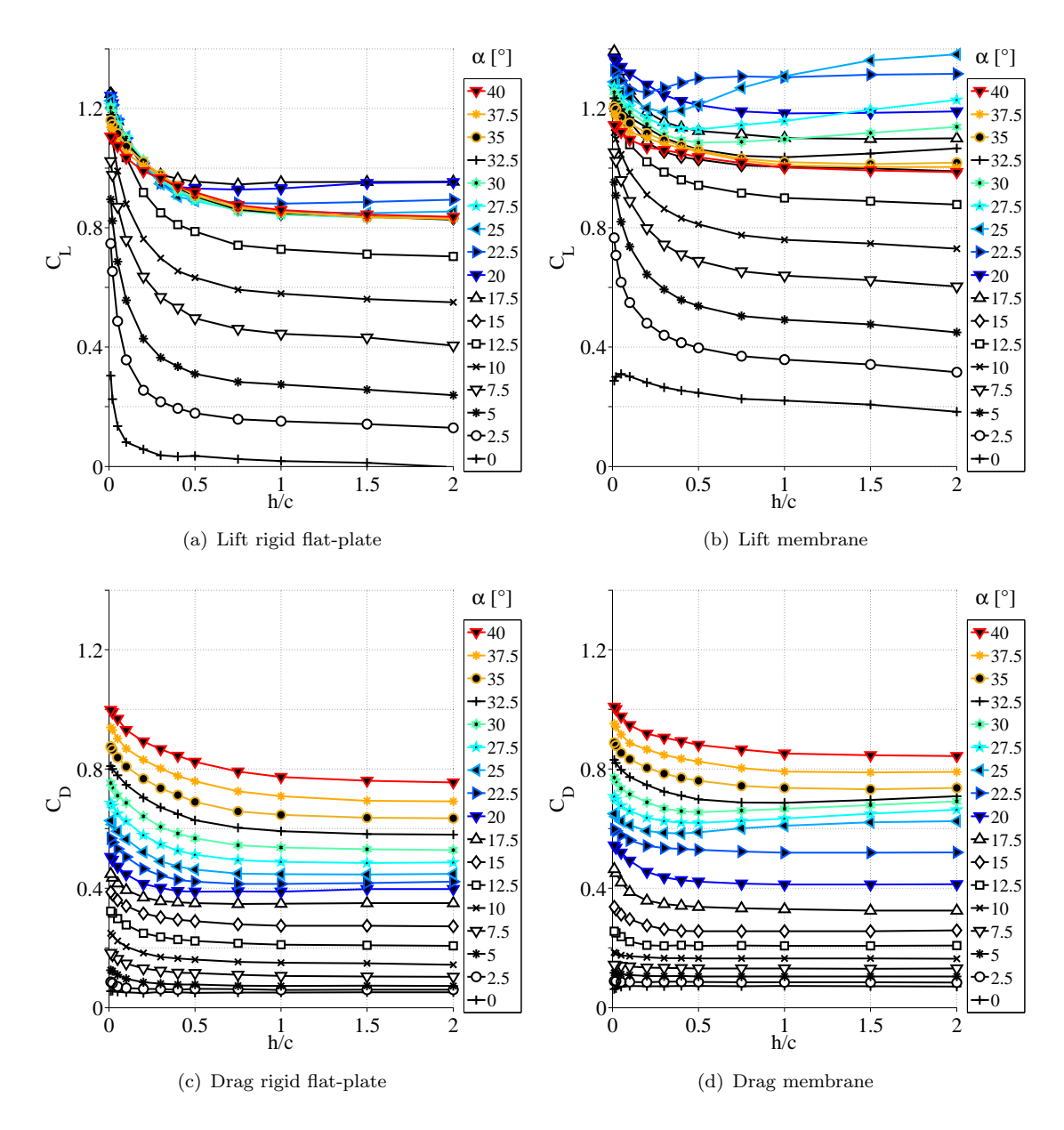


Figure 5.1: Lift and drag coefficient for rigid flat-plate and membrane wings, changing distance to ground at constant  $\alpha$ .

into positive and higher angles outside the hysteresis region ( $\alpha = 5^{\circ}$ ) before conducting the actual measurement within the hysteresis region of  $-5^{\circ} \le \alpha \le 5^{\circ}$  (always with wind on).

It should be mentioned that the slope  $dC_L/dh$  (Figure 5.1a) of rigid wings shows for most incidences a decreasing trend with height, allowing favourable stability characteristics in height. In other words, a reduction in height (due to a disturbance) results in a recovery due to gain in lift and vice versa. However, the slope appears slightly positive in the region of wing stall at  $17.5^{\circ} \leq \alpha \leq 25^{\circ}$ , resulting in instability in this region (loss of height is accompanied with lift loss). Membrane wings (Figure 5.1b) exhibit a similar unstable slope region in stall, however at higher angles-of-attack of  $22.5^{\circ} \leq \alpha \leq 35^{\circ}$  and

with significantly stronger positive slope and therefore more distinct unstable behaviour. The stability in height recovers for very close ground clearances of  $h/c \leq 0.1$ . A previous study (Rhodes and Sayers, 2009) explains the flow physics behind this phenomenon of slope modification within ground-effect using two different effects. The reduction in height into ground-effect  $(0.1 \leq h/c \leq 2)$  forces the incoming flow at the leading-edge to become parallel to the ground surface. As a result, the effective angle-of-attack is reduced, causing a drop in lift. Further descent into extreme ground-effect of  $h/c \leq 0.1$  causes the the ram-pressure below the wing to gain superiority, accompanied with an increase in lift.

The increase in lift within ground-effect comes at a price of higher drag (Figure 5.1c and Figure 5.1d). However, the rise in drag is less than the benefit in lift, especially at low angles-of-attack of  $\alpha \leq 5^{\circ}$  where the drag curve reveals almost no change in drag with decreasing height. The drag of membrane wings for  $22.5^{\circ} \leq \alpha \leq 35^{\circ}$  exhibits a decreasing trend with reducing height which correlates to a negative lift-slope (Figure 5.1b).

Figure 5.2 illustrates lift and drag coefficient contours for rigid and membrane wings. The scaling of the axis is semi-logarithmic (h/c-axis in log), enabling a better view into modifications in lift, appearing close to the ground. Small circular dots in the contours illustrate the measurement points. Additionally, the maximum lift at each height above ground,  $C_{L-max}$ , is reflected with vertical, dashed, white-black line.

The vicinity of the ground allows rigid flat plates (Figure 5.2a) to increase their maximum lift coefficient from  $C_{L-max}=0.96$  at h/c=2 to  $C_{L-max}=1.25$  at h/c=0.01. This growth comes with a modification in stall incidence, rising from  $\alpha=17.5^{\circ}$  at h/c=2 to  $\alpha=30^{\circ}$  at h/c=0.2, which could be from the reduction in effective angle-of-attack close to the ground. Lower heights of  $0.01 \le h/c \le 0.2$  result in a rapid decline of stall angles from  $\alpha=30^{\circ}$  to  $\alpha=15^{\circ}$ , which could be due to the strengthened adverse pressure gradient acting on the upper surface, enforcing earlier flow separation (Mateescu et al., 2012; Qu et al., 2014).

The stall starts to appear at the same angle of  $\alpha = 17.5^{\circ}$  when the wing is farther from the ground and it increases rapidly for h/c < 0.5. This post-stall lift behaviour could be a consequence of constricted air flow below the wing, allowing positive pressure induced lift enhancement in low ground clearances even when the flow may appear fully separated on the upper wing-surface (Qu et al., 2014; Carter, 1961).

The impact of such a separation of the flow seems to become more important for moderate to high incidences of  $\alpha > 17.5^{\circ}$ , causing the drag to increase more drastically within the descend into ground-effect.

As a result, the drag increases drastically for  $\alpha > 17.5^{\circ}$  and h/c < 0.5 due to large separation regions (Figure 5.2a,lower).

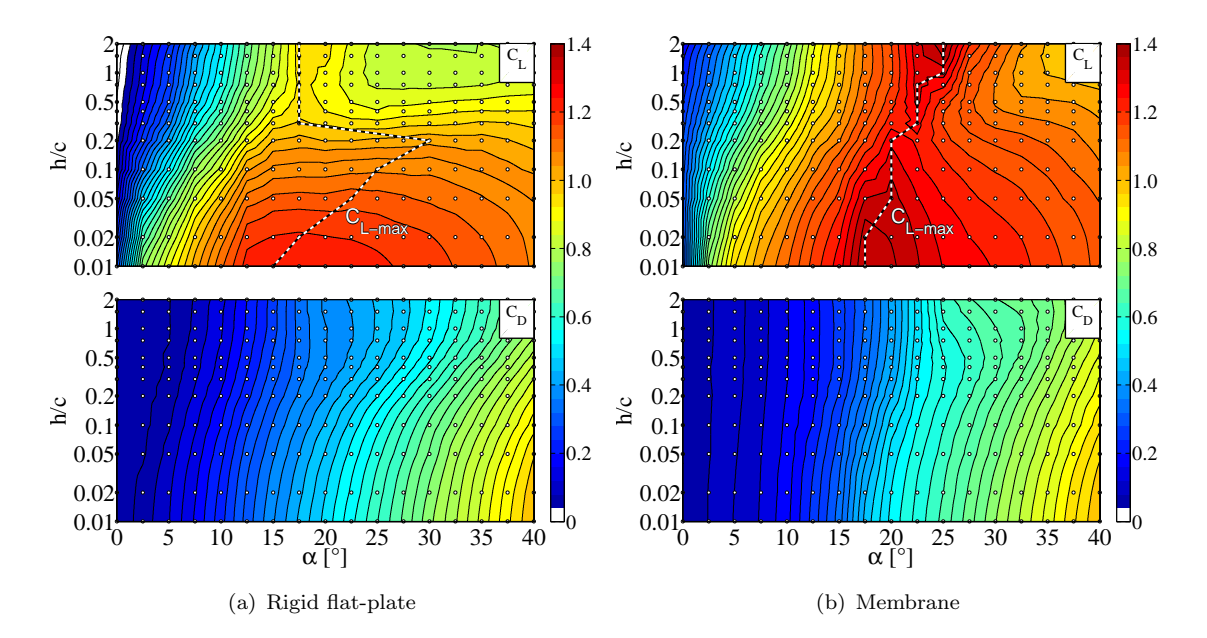


Figure 5.2: Lift and drag coefficient changing with height and angle-of-attack.

In comparison with rigid flat plates (Figure 5.2a, top), membrane wings (Figure 5.2b, top) show a 40% higher lift in an unbounded flow. In contrast to the rigid flat-plate, the membrane's maximum lift coefficient first reduces by 10% (from free-flight conditions) in moderate GE 0.2 < h/c < 2 before it increases again to the free-flight value for  $h/c \le 0.2$ . Such behaviour was also found for rigid cambered wings (Qu et al., 2014). The stall characteristics of membrane wings show a sharper drop in lift at low altitudes, which is found to be similar for cambered rigid wings (Pelletier and Mueller, 2000). Nevertheless, membrane wings show superior absolute stall angles of  $\alpha = 25^{\circ}$  in free-flight conditions (compared with  $\alpha = 17.5^{\circ}$  for flat plates). The stall-angle reduces steadily with lower heights and in close ground proximity, for  $15^{\circ} \le \alpha \le 17.5^{\circ}$ , coincides with the stall-angle of the rigid wings. The vicinity of the ground restricts the camber related benefits of  $C_{L-max}$  and  $\alpha_{stall}$  of the membrane wing.

The drag contours for membrane wings (Figure 5.2b, lower) exhibit less increase in drag than rigid flat plates (Figure 5.2a, lower), especially for higher incidences of  $\alpha > 17.5^{\circ}$ . This could be related to the inherent dynamics of membrane wings, allowing drag reduction due to longer flow attachment and reduction in wake-size (Gordnier and Attar, 2014; Arce and Ukeiley, 2014).

Figure 5.3 illustrates the lift and drag increment contours  $\Delta C_L$  and  $\Delta C_D$  (eq.5.1), which reference to the free flight conditions of h/c = 2.

$$\Delta C_L(\alpha, h/c) = C_L(\alpha, h/c) - C_L(\alpha, 2)$$

$$\Delta C_D(\alpha, h/c) = C_D(\alpha, h/c) - C_D(\alpha, 2)$$
(5.1)

The increments  $\Delta C_L$  and  $\Delta C_D$  provides more insight into lift and drag modifications in close ground proximity. Generally, rigid flat plates (Figure 5.3a, top) obtain the largest benefit in lift growth within ground-effect, ensuring a maximum gain of up to  $\Delta C_L = 0.6$  in comparison to  $\Delta C_L = 0.5$  for membrane wings (Figure 5.3b, top). However, rigid flat plates show also higher drag increments (Figure 5.3a, lower) than membrane wings (Figure 5.3b, lower) which may be caused due to lift-induced effects. Both wings show the steepest incline in lift increment  $\Delta C_L$  at low incidences of  $2.5^{\circ} \leq \alpha \leq 12.5^{\circ}$ .

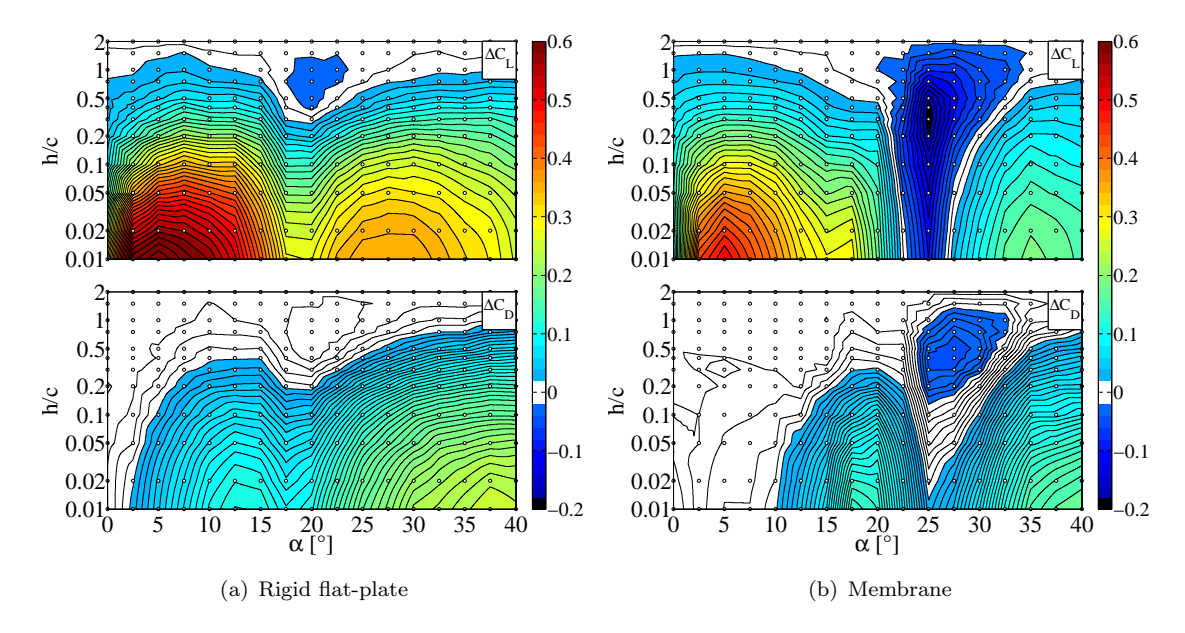


Figure 5.3: Lift and drag increment in relation to values out of GE (where h/c = 2).

At higher altitudes, membrane wings (Figure 5.3b, top) show a large region of so called "negative ground-effect" for  $20^{\circ} \leq \alpha \leq 35^{\circ}$ , which reduces in size in close ground-proximity to  $22.5^{\circ} \leq \alpha \leq 27.5^{\circ}$ . This region is comparable to previous studies on rigid cambered wings (Qu et al., 2014). It is found that the top surface does not contribute to lift generation at high incidences and that the main driving change in the flow physics on the way to GE is driven by a reduced angle-of-attack, causing a drop in lift increment  $\Delta C_L$ . Nevertheless, rigid flat plates show similar regions of negative GE (Figure 5.3a, top), however they appear less intense, more local and at lower incidence of  $17.5^{\circ} \leq \alpha \leq 22.5^{\circ}$  than membrane wings.

#### 5.1.2 Aerodynamic Efficiency

Lift and drag modifications can be combined in to a global aerodynamic range efficiency  $C_L/C_D$  parameter, which is illustrated for rigid flat-plate and membrane wings in Figure 5.4a and Figure 5.4b, respectively. Figure 5.4c shows differences in aerodynamic efficiency when rigid flat-plate wing results (Figure 5.4a) are subtracted from membrane

wing values (Figure 5.4b) at each incidence and height. For brevity, the angle-of-attack range displayed is from  $0^{\circ} \le \alpha \le 20^{\circ}$ .

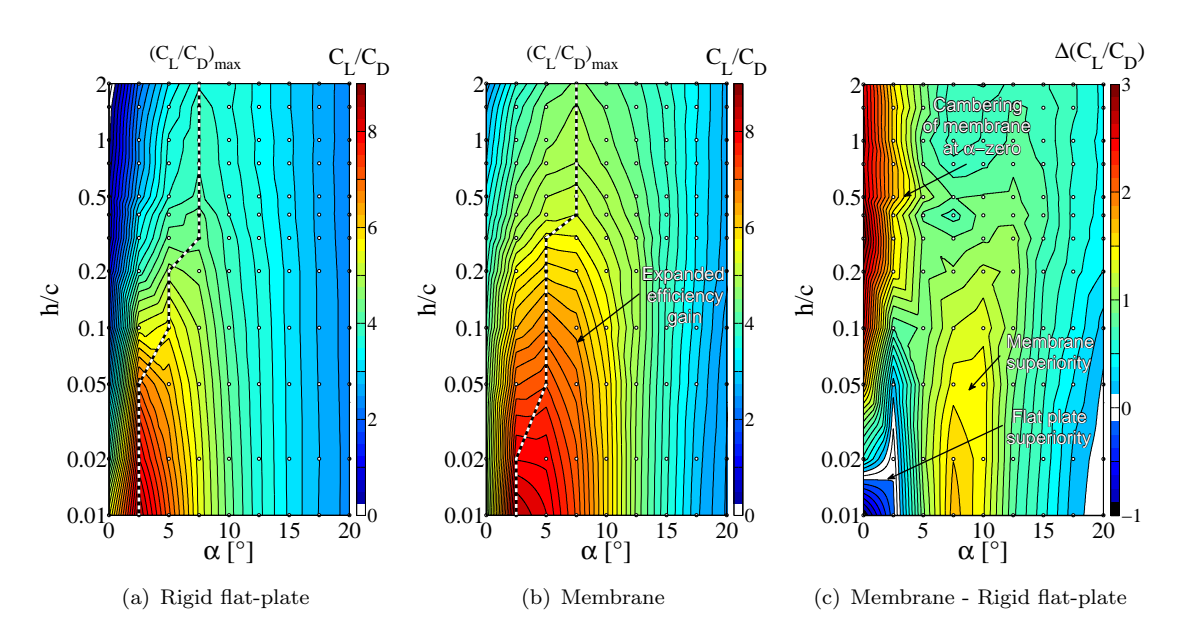


Figure 5.4: Aerodynamic range efficiency changing with angle-of-attack and height-over-ground

Both wings show a maximum aerodynamic efficiency  $(C_L/C_D)_{max}$  that is up to 50% more at h/c = 0.1 and over 100% more at h/c = 0.01, compared to free-flight conditions at h/c = 2. These values are similar to previous findings in higher Reynolds number studies Rozhdestvensky (2006). The highest aerodynamic efficiency can be gained for incidences ranging from  $2.5^{\circ} \le \alpha \le 7.5^{\circ}$ . At those low incidences, lowering the height causes no drastic modifications in drag (Figure 5.3,lower), whereas the lift enlarges progressively close to the ground (Figure 5.3, top). The most efficient angle-of-attack decreases for both wing types from  $\alpha = 7.5^{\circ}$  in free-flight conditions to  $\alpha = 2.5^{\circ}$  at close ground proximity of h/c = 0.01.

Direct comparison of rigid flat-plates and membrane wings reveals that the aerodynamic efficiency of membrane wings is mostly higher but with restrictions for low incidences of  $0^{\circ} \leq \alpha \leq 5^{\circ}$  and low ground-clearances of h/c < 0.05 (Figure 5.4c). Therefore, the superiority of membrane wings in GE can only be ensured if the angle-of-attack is chosen beyond  $\alpha \geq 5^{\circ}$ . The highest difference in efficiency  $\Delta(C_L/C_D)$  can be found at a ground distance of h/c < 0.1 and angles of  $5^{\circ} \leq \alpha \leq 10^{\circ}$ , providing with  $\Delta(C_L/C_D) = 1.7$  about 30% more than that of a flat plate under the same (angle, height) conditions.

The difference in angle-of-attack between peak-lift at  $\alpha=5^{\circ}$  (Figure 5.3b, top) and peak-drag at  $\alpha=17.5^{\circ}$  (Figure 5.3b,lower) results in progressive lift enhancement with negligible drag penalty. This is primarily responsible for aerodynamic superiority of membrane wings in GE for angles ranging  $5^{\circ} \leq \alpha \leq 17.5^{\circ}$ .

#### 5.1.3 Lift Dynamics of Membrane Wings

Figure 5.5 shows the fluctuation intensity of the lift coefficient  $\sigma(C_L)$  (Figure 5.5a) and its power spectral density  $PSD(C_L)$  (Figure 5.5b), changing with angle-of-attack and height-above-ground. The drop in dominant frequencies in near-stall conditions are labelled and marked in blue.

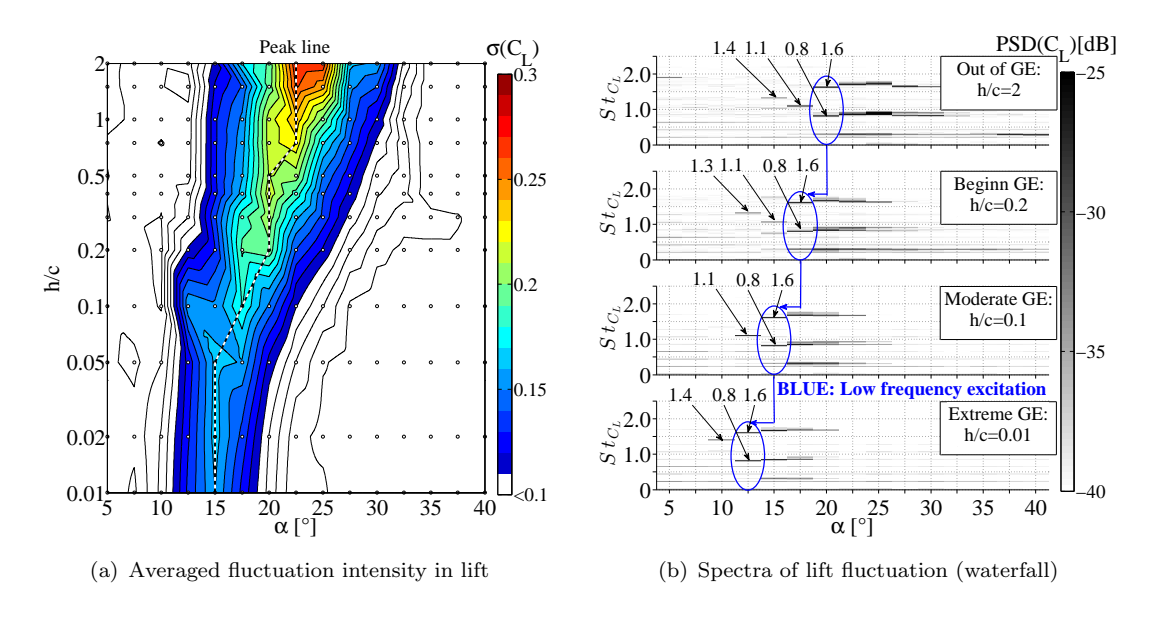


Figure 5.5: Variation of lift fluctuations (a) and its spectral content (b) with angle-of-attack and height above ground

For a given height (Figure 5.5a), lift fluctuations are found to peak close to wing stall, reaching  $\sigma_{max}=0.3$  at  $\alpha=22.5^{\circ}$  in free-flight conditions of h/c=2. This intensity halves in strength to  $\sigma_{max}=0.15$  and moves to  $\alpha=15^{\circ}$  in close proximity to the ground at h/c=0.01 (see dotted line in Figure 5.5a). This could be due to the weaker pressure fluctuations on the upper side of the wing surface when it is closer to the ground minimising the dynamics of the flow. Additionally, tip-vortices are known to reduce in size and vorticity in ground-effect (Han and Cho, 2005), which may also contribute to a global decrease in flow/structure/force dynamics of membrane wings. Nevertheless, at fixed moderate angles-of-attack, ranging from  $5^{\circ} \le \alpha \le 15^{\circ}$ , membrane wings show an increase in force fluctuations with decreasing ground height, which is perhaps to due to the premature onset of leading-edge flow separation, as found in previous studies (Prasad and Damodaran, 2013).

Inspection of the spectral content of lift fluctuations of membrane wings (Figure 5.5b) reveals that the frequencies at the onset of stall change with ground clearance. Free-flight conditions of h/c=2 and moderate angles of  $10^{\circ} \leq \alpha \leq 15^{\circ}$  exhibit high dominant frequencies of  $St_{C_L}=1.4$ , typically caused by a high membrane tension and driven by boundary layer perturbations (Rojratsirikul et al., 2009). Increasing the angle-of-attack to  $15^{\circ} \leq \alpha \leq 20^{\circ}$  causes a leading-edge vortex induced stairs-like drop into lower

dominant frequency levels from  $St_{C_L} = 1.4$  to 1.1 to 0.8. In the vicinity of stall-angles of  $\alpha \geq 20^{\circ}$  and beyond, dominant frequencies in lift remain at  $St_{C_L} = 0.8$  and its higher harmonics. The fluctuations for the stall region and beyond are most likely driven by the influence of leading-edge-vortex shedding.

Lowering the height from free-flight conditions (h/c=2) to extreme ground-effect (h/c=0.01) causes the dominant frequencies (blue encircled in Figure 5.5b) to shift to lower angles-of-attack (a shift of  $\Delta \alpha = 7.5^{\circ}$  is observed). This might be linked with the reduction in downwash-angle, caused by the close proximity of the ground (Vogt and Barber, 2012). At a fixed angle of  $\alpha = 15^{\circ}$ , membrane wings show a decrease in dominant frequency in lift from  $St_{CL} = 1.4$  to 0.8 with a decrease in height. Previous studies on rigid wings in ground-effect observed a reduction in vortex-shedding-frequency in the vicinity of the ground, which might explain the modification in lift dynamics due to coupling (Prasad and Damodaran, 2013). Further flow investigations in Section 5.3.3 will confirm this result and will discuss it in more detail.

# 5.1.4 Statics and Dynamics of Pitching moment in Rigid flat-plate and Membrane wings

The pitching moment is measured about the quarter chord position and its time-averaged value is shown in Figure 5.6a for rigid-flat plates and membrane wings in free-flight (h/c=2), moderate (h/c=0.1) and extreme (h/c=0.01) ground-effect conditions. Additionally, Figure 5.6b illustrates the fluctuations in pitching moment  $\sigma(C_M)$  of the membrane wings for different ground heights.

At a constant height, membrane wings exhibits a pitching moment slope that is near horizontal, likely due to the variable cambering of the membrane with angle-of-attack. This results in an inferior static stability performance of membrane wings compared to rigid wings (Figure 5.6a) for low angles-of-attack. The absolute value of the pitching moment appears more negative for a membrane wing, a behaviour known to be linked with changes in pressure distribution, and is comparable to previous results of rigid/membrane half wings seen in Section 4.1.3.

The reduction in height-over-ground translates the pitch curves down vertically. Earlier flow separation within ground-effect is acting similar to an increase in angle-of-attack in free-flight conditions. Therefore, an typical pitching moment of  $C_M = -0.1$ , measured at a rigid-flat plate in extreme ground-effect at  $\alpha = 5^{\circ}$ , is found again at  $\alpha = 15^{\circ}$  for free-flight conditions.

The flexibility of the membrane allows flow induced pitching moment fluctuations  $\sigma(C_M)$ , which change with angle-of-attack and height (Figure 5.6b). The fluctuations in pitching moment around  $\alpha = 0^{\circ}$  are large, primarily because the membrane is under very limited flow-induced tension, resulting in large membrane oscillations that directly affect

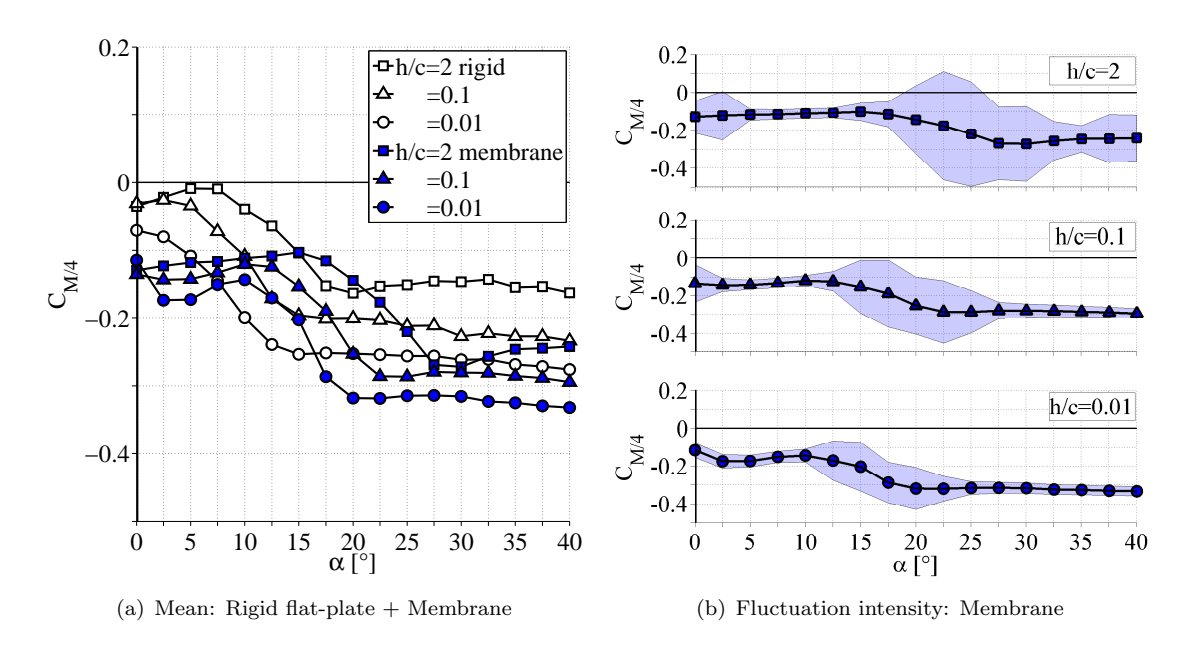


Figure 5.6: (a) Time-averaged pitching moment coefficient  $C_{M/4}$  for rigid flat plate and membrane wing in and out of ground-effect. (b) Fluctuations of  $\sigma(C_{M/4})$  around the mean is displayed for membrane wings in blue shading.

the dynamics of the pitching moment. At 5°, there is a balance between the flowinduced tension and gravity where there is decline in fluctuations with decreasing height above ground. The fluctuations reduce drastically at moderate angles-of-attack due to a gain in aerodynamic loading causing the membrane to stretch and stiffen (Figure 5.7). This region is also relatively unaffected by leading-edge vortex-shedding, avoiding significant membrane excitation. At angles-of-attack near stall, there is marked increase in fluctuations. This behaviour might happen due to growth influence of leading-edge vortex-shedding, which could excite the membrane and thereby affecting the pitching moment. Finally, variations in pitching moment reduces drastically in post-stall conditions, because the vortices that might shed from the leading-edge are no longer attached to the membrane surface and therefore do not influence the load distribution on the membrane in a significant way. This assumption will be confirmed to a later stage in Section 5.3.2, where POD-analysis of the flow fluctuations reveals dominating shedding structures and their vertical positioning to the upper wings surface. Further details of flow-membrane interaction, modifying with angle-of-attack at free-flight conditions can be found in the literature (Gordnier and Attar, 2014; Hu et al., 2008; Tregidgo et al., 2011; Rojratsirikul et al., 2009).

The descent into ground-effect causes the maximum in fluctuations to decrease. This could be due to the fact that the lift generation in ground-effect is dominated by the flow/pressure distribution on the lower wing surface. This could sufficiently reduce the dynamic influence of the upper wing surface. Further details will be discussed within the flow results in Section 5.3.

## 5.2 Membrane Deformations

The following section covers mean statistics and dynamics of membrane wing motions for different angles-of-attack and heights-over-ground.

#### 5.2.1 Statistics

Average out-of-plane membrane-deformation  $\bar{z}$  and fluctuations  $\sigma(z)$  are obtained by averaging the instantaneous surface results z(x,y,t) over the entire time series (Figure 5.7a). The flexibility of the membrane allows shape adaption with changes in angles-of-attack and height. Figure 5.7b shows the cambering of the membrane at mid-span for  $\alpha = 5^{\circ}$  and 15°. A reduction in height causes the membrane to increase its mean camber due to gain in positive pressure below the wing surface. The lower angle of  $\alpha = 5^{\circ}$  shows a higher relative increase in camber when the wing is closer to the ground compared to the higher angle of  $\alpha = 15^{\circ}$ . Lowering the height at  $\alpha = 5^{\circ}$  also causes the chord position of maximum camber to move towards the leading-edge, which is similar to the response to an increase in angle-of-attack.

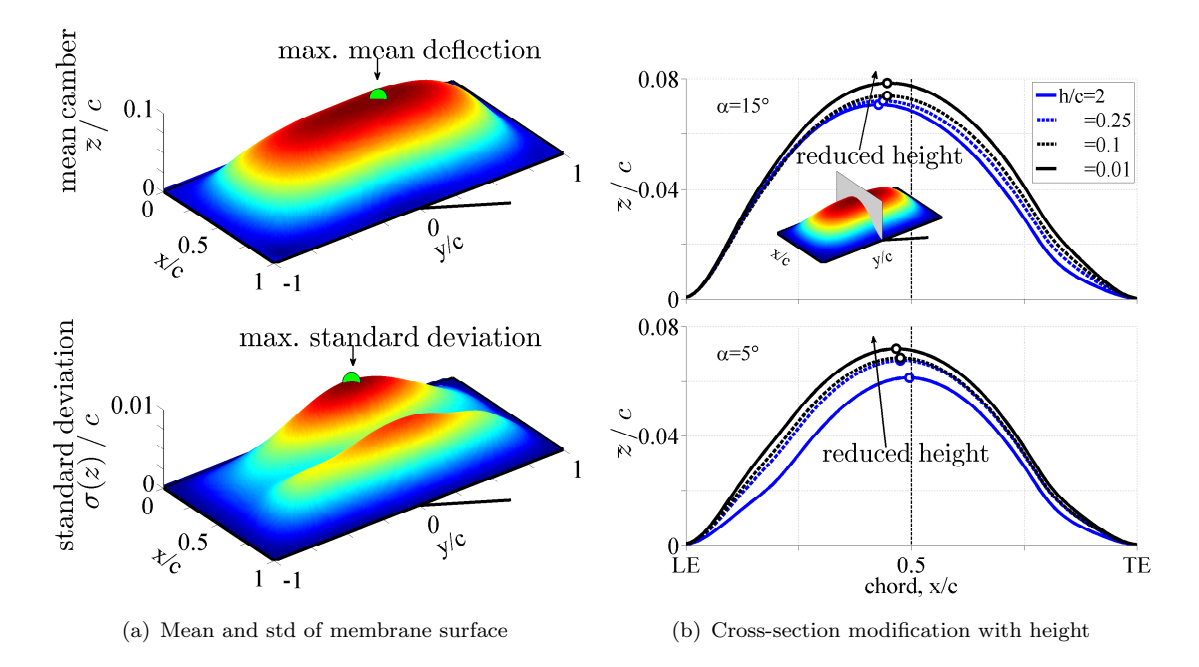


Figure 5.7: (a) Exemplary time-averaged membrane mean surface deflection and fluctuation intensity  $(h/c=2,\,\alpha=25^\circ)$ . (b) Cross-sections at mid-span for mean camber modifying with  $\alpha$  and h/c. Note the steaper incline in camber within ground-effect for the lower angle-of-attack.

Figure 5.8 shows the variation in maximum membrane mean deformation  $\bar{z}_{max}/c$  and fluctuation intensity  $\sigma(z)/c$  of the membrane surface, varying with ground clearance and angle-of-attack. The DIC-technique ensures a maximum deformation uncertainty of z/c = 0.001 (0.1% of chord, equal 0.1 mm). Membrane wings at h/c = 2 exhibit a steady

increase in maximum camber with angle-of-attack reaching 0.08c at  $25^{\circ}$  (Figure 5.8). This result compares well within previous findings of a wing of similar aeroelastic properties (Rojratsirikul et al., 2011). At these free-flight conditions, the maximum camber deflection is shown to peak with  $\alpha = 25^{\circ}$  at the same angle-of-attack found for maximum lifting capability (see Figure 5.1b). The membrane camber is found to decrease in post-stall conditions at h/c = 2, related to the loss in lift generation.

The vicinity of the ground forces the membrane to modify its camber in a way that is similar to changes in angle-of-attack in free-flight conditions (Figure 5.8). Low angles-of-attack ( $\alpha \approx 5^{\circ}$ ) show the highest increase in maximum camber (16%) between free-flight conditions at h/c=2 and extreme ground-effect at h/c=0.01. This result can also be correlated with earlier findings of predominant lift increase at low incidences (Figure 5.1b). Ground-effect was found to induce earlier stall, resulting in a drop in membrane camber in extreme ground-effect of  $h/c \leq 0.1$  at  $\alpha = 20^{\circ}$  and 22.5° (Figure 5.8). At even higher incidences of  $\alpha = 35^{\circ}$ , the membrane camber increases steadily with decreasing distance to the ground, suggesting predominant pressure build up on the lower surface of the wing and further lift enhancement despite a large stagnant-flow zone on the upper side of the wing. Ultimately, changing angle-of-attack in ground-effect causes smoother and more steady modifications in membrane displacement when compared to free-flight.

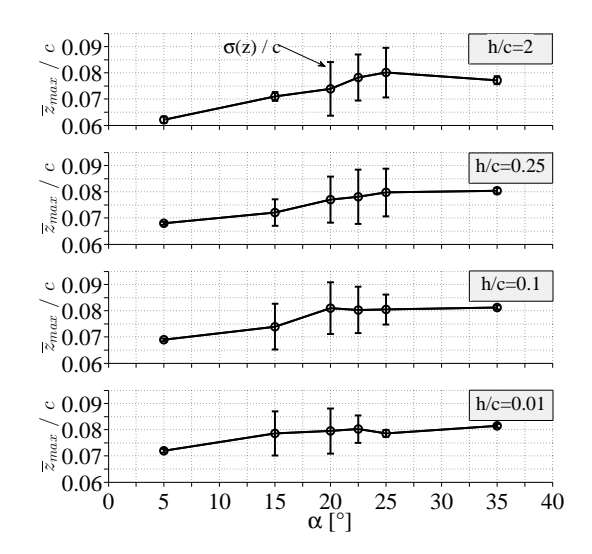


Figure 5.8: Variation of membrane maximum mean deflection and maximum standard deviation with angle-of-attack for four heights-over-ground.

The predominance of leading-edge vortex-shedding is known to significantly affect the amplitude of camber oscillations close to stall angles (Gordnier and Attar, 2014). This behaviour can clearly be seen in free-flight conditions of h/c=2 with a stall-angle of  $\alpha=25^{\circ}$  (Figure 5.8, top), where the fluctuation intensity  $\sigma(z)/c$  reaches nearly 10% of mean value. In comparison, low angles-of-attack around  $\alpha \sim 5^{\circ}$  do not exhibit any significant membrane vibrations at all, not even in ground-effect. This result will

be later found to be linked with mostly attached flow without any large leading-edge vortex-shedding which could trigger large oscillations in the membrane (Section 5.3.2). However, an increase in incidence to  $\alpha \sim 15^{\circ}$  shows a measurable impact in growing membrane fluctuations, gaining even more strength at lower ground clearances. It is suggested that this may be linked with the growing influence of the leading-edge vortex and its shedding, gaining strength with higher incidences or lower ground clearances. For very high angles-of-attack ( $\alpha \geq 25^{\circ}$ ), a steep drop in membrane fluctuations is observed when going from free-flight conditions into ground-effect (Figure 5.8). This phenomenon appears to be similar to that observed when incidence angles go from the stall to the post-stall regime at a constant height. This suggests that the dynamics of membrane wings in ground-effect might be predominately driven by flow modifications that are similar to those seen for angle-of-attack changes at a constant height. Further details of flow modifications will be discussed in Section 5.3.

### 5.2.2 Instantaneous Membrane Dynamics

Figure 5.9 displays spatial and temporal membrane-dynamics in the vicinity of the ground. Time-series of membrane fluctuations z'(t)/c, time-averaged membrane-vibrations  $\sigma/c$  and their spectral content PSD(z) are displayed at three heights of h/c = [0.1, 0.25, 0.25]2 ] at an angle of  $\alpha = 15^{\circ}$ . The power-spectra PSD(z) is evaluated at the point of maximum standard deviation of the membrane surface. At  $\alpha = 15^{\circ}$  and free-flight conditions, the membrane wings exhibits a dominant frequency at  $St_z = 1.3$  in membrane-vibrations, which is comparable to the findings in the force spectra of  $St_{C_L} = 1.4$  (Figure 5.5b). The membrane's high frequency (due to aerodynamic tensioning) accompanies a chord dominant mode shape of 4 peaks and relative low oscillation-amplitudes z'(t)/c, which are 5% of the membrane's average deformation (Figure 5.9). Reducing the height to h/c = 0.25 results in a drop into lower frequencies of  $St_z = 0.8$  and  $St_z = 1.1$  and a doubling of the oscillation amplitudes z'(t)/c, which reach up to 10% of the average displacement. Time-averaged fluctuations show a reduced chordwise-mode-shape (only 2 peaks along the chord). It must be noted that the peak near the leading-edge is weaker in strength and wider in spanwise distribution, compared with the one near the trailingedge. Rojratsirikul et al. (2011) found a similar behaviour, which could be linked with the interaction of tip vortices, which grow in diameter in downstream direction. Future study is required to find the flow physics behind this phenomenon. A further reduction in height to h/c = 0.1 increases the oscillation-amplitude to up to 18% of membrane's average displacement and yet maintains the low frequencies at around  $St_z = 0.7$  to 0.8 and the accompanying low order of the averaged (fluctuation) mode-shape with 2 peaks.

The moderate ground-effect case of h/c = 0.25 is of special interest, because it has two dominant frequencies at  $St_z = 0.7$  and  $St_z = 1$ . This suggests the existence of two dominant mode shapes of different spatial order (shape).

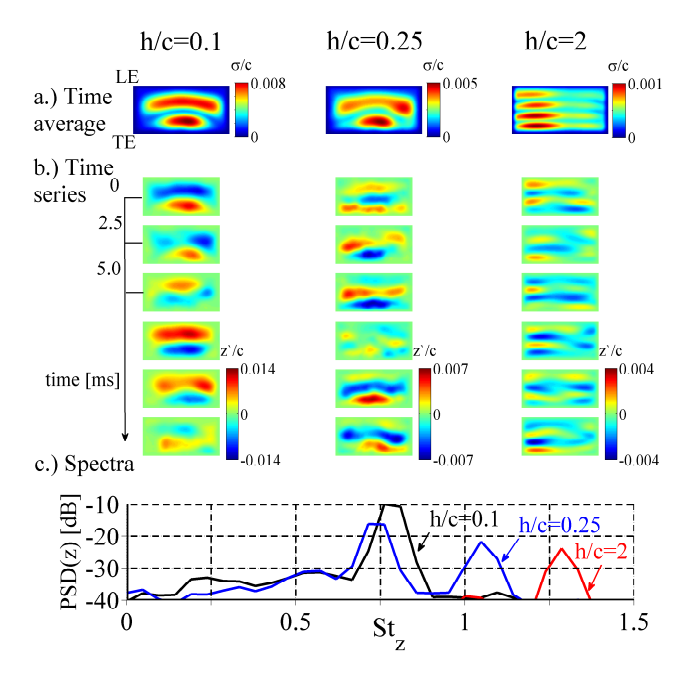
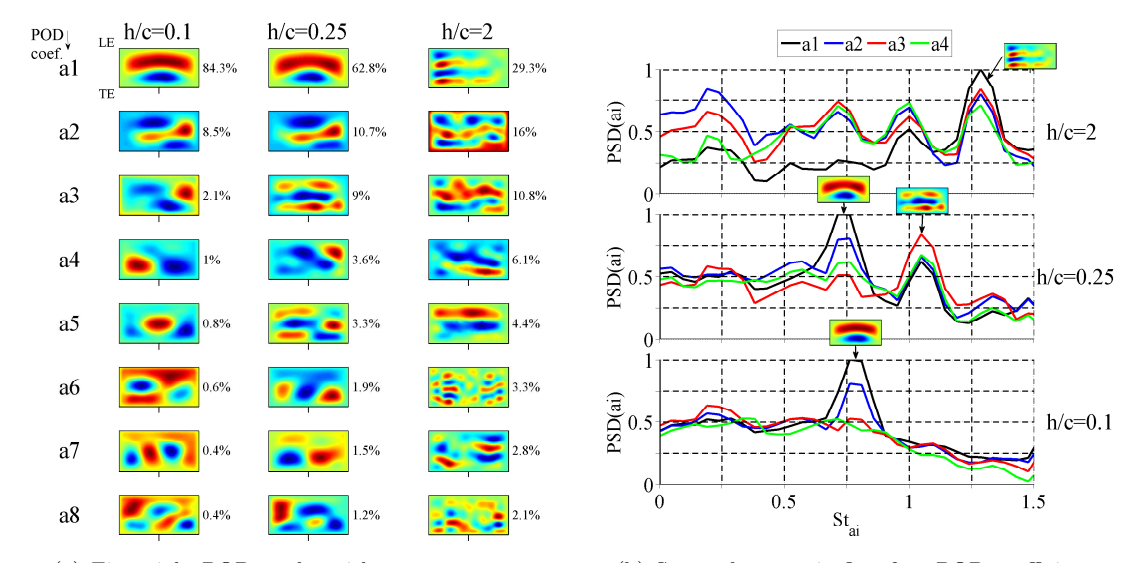


Figure 5.9: Time averaged (a), time variant (b) and spectral content (c) of membrane oscillations for three different heights and a given incidence of  $\alpha = 15^{\circ}$ 

# 5.2.3 Modal-Analysis of Membrane Dynamics

Proper-orthogonal-decomposition (POD) allows to decompose and grouped membrane surface dynamics in their underlying spatiotemporal development (see method in Section 3.3.4.2). Figure 5.10a shows the first eight POD mode shapes of membrane vibrations (excluded mean). These modes are in order of decreasing energy content as shown in the figure. Three heights h/c = [2, 0.25, 0.1] at a fixed angle-of-attack of  $\alpha = 15^{\circ}$  are selected for brevity.

In free-flight conditions (h/c=2), the vibration behaviour is mostly chordwise, with 29% of all energy captured in the 1<sup>st</sup> mode  $a_1$  (four chordwise extrema), 16% in the 2<sup>nd</sup> mode ( $a_2$ , three chordwise extrema) and nearly 11% in the 3<sup>rd</sup> mode ( $a_3$ , two chordwise extrema). Spanwise modes are visible but with very low energy content (<4%). This shows that the energy is distributed over these few modes. This energy distribution is consistent with the previous membrane wing study on membrane half wings, where the technique of sinusoidal decomposition was applied at a fixed span location (Section 4.2.5). The first POD coefficient  $a_1$  shows a dominant membrane vibration frequency of  $St_{a_1}=1.3$  (Figure 5.10b) which is comparable to the frequency found in the lift coefficient (Figure 5.5b). Higher modal coefficients,  $a_2$ ,  $a_3$ ,  $a_4$ , despite their lower spatial order, show strong excitation at the same frequency of  $St_{a_1}=1.3$ . This suggests that there is strong coupling between these mode shapes and that the spatial structures are essentially sub-harmonics of the fundamental mode shape.



- (a) First eight POD-modes with energy content
- (b) Spectral energy in first four POD coefficients

Figure 5.10: POD analysis on membrane fluctuations, showing spatial (a) and spectral (b) contribution of POD modes at a fixed incidence of  $\alpha=15^{\circ}$  for different heights above ground. POD contours show normalised amplitude peaks in red/blue and their zero level in green color.

Membrane vibrations are found to be strongly affected by the reduction in height. A reduction in height from h/c = 2 to h/c = 0.25 causes the most dominant mode shapes to change from four local extremes along the chord to just two. This will be shown to be linked with increasing influence of vortex-shedding when the membrane is in ground-effect (Section 5.3.2). In addition, the individual energy content appears less evenly distributed over different POD-coefficients, accumulating almost 63% in the first mode, 11% in the 2<sup>nd</sup> mode and 9% in the 3<sup>rd</sup> mode. Note that the mode shapes at h/c = 0.25 is different from those in h/c = 2. The increased vibration amplitude of the membrane allows us to clearly identify spanwise modes ( $\geq a_4$ ) of low energy levels (< 4%). Examining the spectral content of the first POD shapes (Figure 5.10b, mid) shows that at this height above ground (h/c = 0.25), two different frequencies appear to be dominant ( $St_{a1} = 0.8$  and  $St_{a3} = 1.1$ ). These frequencies are consistent with the frequencies observed in the force dynamics (Figure 5.5b).

A further reduction in altitude to h/c = 0.1 supports the trend of accumulation of energy in fewer modes (in this case 85% and 9% in the first two modes, respectively). The most dominant mode again has two chordwise nodes, known from the literature to be representative for a flow in near-stall conditions (Rojratsirikul et al., 2011). The spanwise modes carry very little energy ( $\leq 1\%$  to the total vibration energy in the membrane). The POD coefficient  $a_6$  at h/c = 0.1 illustrates a special case of a diagonal structure with a low energy content < 1%. The diagonal shape could be a result of alternating tip-vortex roll up or simply non-uniform boundary condition in membrane attachment. Further investigation is required to explain the source of these observed

POD-modes. An illustrative video can be found via: https://youtu.be/sgZTpHLgSYI, showing instantaneous membrane snapshots with their decomposed POD structures for a membrane wing at  $\alpha = 15^{\circ}$  in ground-effect conditions (h/c = 0.1).

Membrane vibrations are not only affected by the reduction in height-over-ground, but also by changes into higher angles-of-attack. Figure 5.11a shows modification of the POD mode shapes and their spectral content (Figure 5.11b), modifying from  $\alpha=15^\circ$  over  $\alpha=20^\circ$  to  $\alpha=25^\circ$  in free-flight conditions (h/c=2). Increasing angles-of-attack are found to reduce the dominant POD mode shapes from four chordwise peaks in a1 at  $\alpha=15^\circ$  (Figure 5.11a, right) to two chordwise peaks in a1 at  $\alpha=25^\circ$  (Figure 5.11a, left). This behaviour goes confirm with the literature of membrane wings in typical free-flight conditions (Rojratsirikul et al., 2009) and shows that stall induced modifications on membrane vibrations can either be achieved with inclining angles-of-attack in free-flight conditions (Figure 5.11a, from right to left) or the descent into ground-effect with a fixed (pre-stall) angle-of-attack (Figure 5.10a, from right to left). Later flow discussions within this thesis (Section 5.3.2) will reveal the comparability of underlying flow modifications between both height/angle-related options.

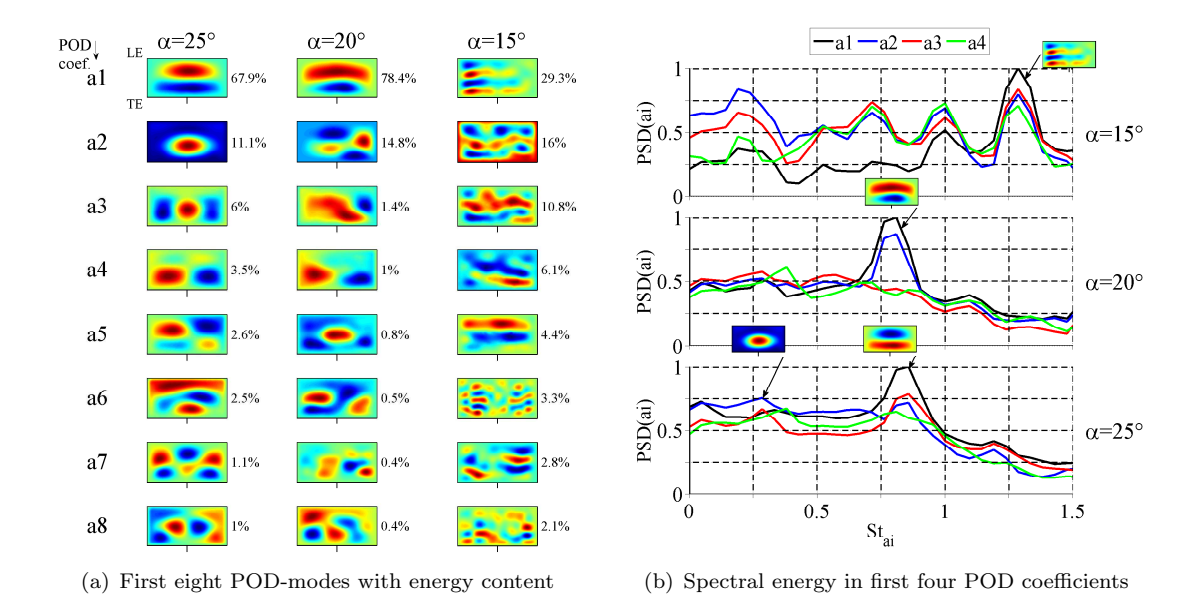


Figure 5.11: POD analysis on membrane fluctuations, showing spatial (a) and spectral (b) contribution of POD modes in free-flight conditions (h/c=2) for three different angles-of-attack  $\alpha=[15,20,25]^{\circ}$ . An increase in angle-of-attack in free-flight conditions is found to modify membrane dynamics similarly as seen for a reduction in height-over-ground at a fixed (pre-stall) angle (Figure 5.10). Note the shedding induced excitation of the wing frame at  $\alpha=25^{\circ}$  in POD mode a2 (the outer wing frame oscillates vertically up/down in counterbalance with the membrane center).

It is interesting to note that the membrane wing at  $\alpha = 25^{\circ}$  (Figure 5.11a, left) exhibits measurable excitation of its outer steel wing frame which can be detected within the second POD coefficient a2. Its dominant frequency of  $St_{a2} = 0.28$  (24 Hz) (Figure 5.11b,

lower, blue line) correlates well with the eigen frequency of the membrane wing structure (outer steel perimeter), which was previously measured with 25 Hz by an external hammer-test (Figure 3.23). Nevertheless, the excitation of the wing frame shows with an energy level of 10% little effect on the overall wing dynamics. The membrane dynamics appear mainly driven by the first POD coefficient a1 (68% energy contribution), which represents pure flow induced membrane eigen mode oscillations. This specific case illustrates the risk of structural excitation of the wing frame which could have an effect to alter the intended membrane dynamics. In addition, structural wing fatigue could be a problem for MAVs/UAVs. Further investigation is required to determine the effects.

Overall, the POD analysis has shown that the first two modes are sufficient to capture 90% of membrane deformation for either low values of h/c at moderate angles-of-attack of  $\alpha=15^{\circ}$  or high angles-of-attack in free-flight conditions, where the flow-dynamics are most likely be dominated by strong leading-edge vortices. In contrast, eight modes are required to capture 75% of membrane deformation in early pre-stall flow conditions, where membrane dynamics are more likely be driven by boundary layer perturbations than LE vortex-shedding. Ultimately, membrane mode shapes are shown to be different in ground-effect and the differences between ground-effect and free-flight at a fixed angle-of-attack are similar to differences observed across angles-of-attack in free-flight.

# 5.3 Flow Development: On top of the membrane wing

The following section presents flow statistics and flow dynamics of rigid and membrane wings for free-flight and ground-effect conditions. The flow is measured at quarter-span in a streamwise wing-normal plane (Figure 5.12).

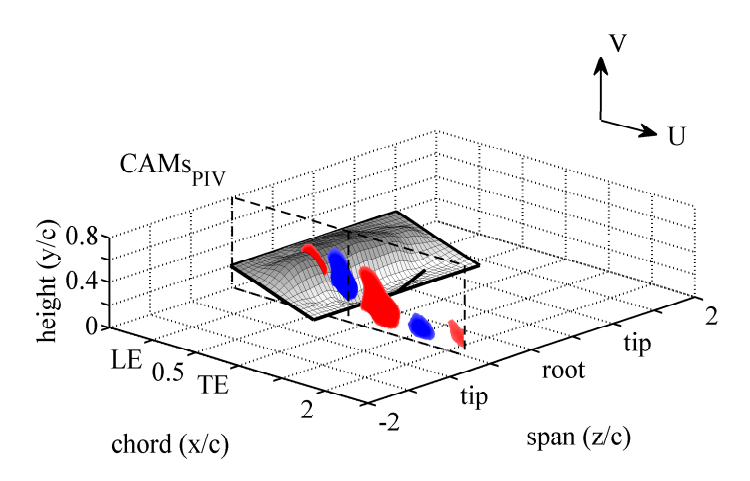


Figure 5.12: PIV-setup with flow in streamwise plane (Flow based coordinate system, see also Section 3.3.5)

## 5.3.1 Flow Statistics

Figure 5.13 shows contours of the time-averaged total kinetic energy  $(\sqrt{(U^2+V^2)}/U_{\infty})$  together with the mean streamline patterns. Rigid flat-plate and membrane wings are compared at three different angles-of-attack  $\alpha = [10, 15, 25]^{\circ}$ , going from free-flight (h/c=2) to moderate (h/c=0.25) and into extreme ground-effect conditions (h/c=0.1).

Both rigid and membrane wings show large separation regions that are induced by the adverse pressure gradient for increased angles-of-attack and reduced heights. The growth in flow separation within GE is related to a strong flow diversion over the upper wing surface, caused by the flow blockage on the lower side of the wing in GE (Qu et al., 2014). However, the ability to adapt to a mean camber (due to the effect of mean dynamic pressure) allows membrane wings to reduce the size of the separation region for both high  $\alpha$  or low height-above-ground. As a result, membrane wings show a separation region at  $\alpha = 25^{\circ}$  in free-flight conditions (Figure 5.13f, upper) which is similar in size to rigid wings at  $\alpha = 15^{\circ}$  (Figure 5.13c, upper). Similarly, membrane wings show a separation region at  $\alpha = 25^{\circ}$  in extreme GE (Figure 5.13f, lower) which is comparable in size to the separation region exhibited by rigid wings at the same incidence in free-flight conditions (Figure 5.13e, upper).

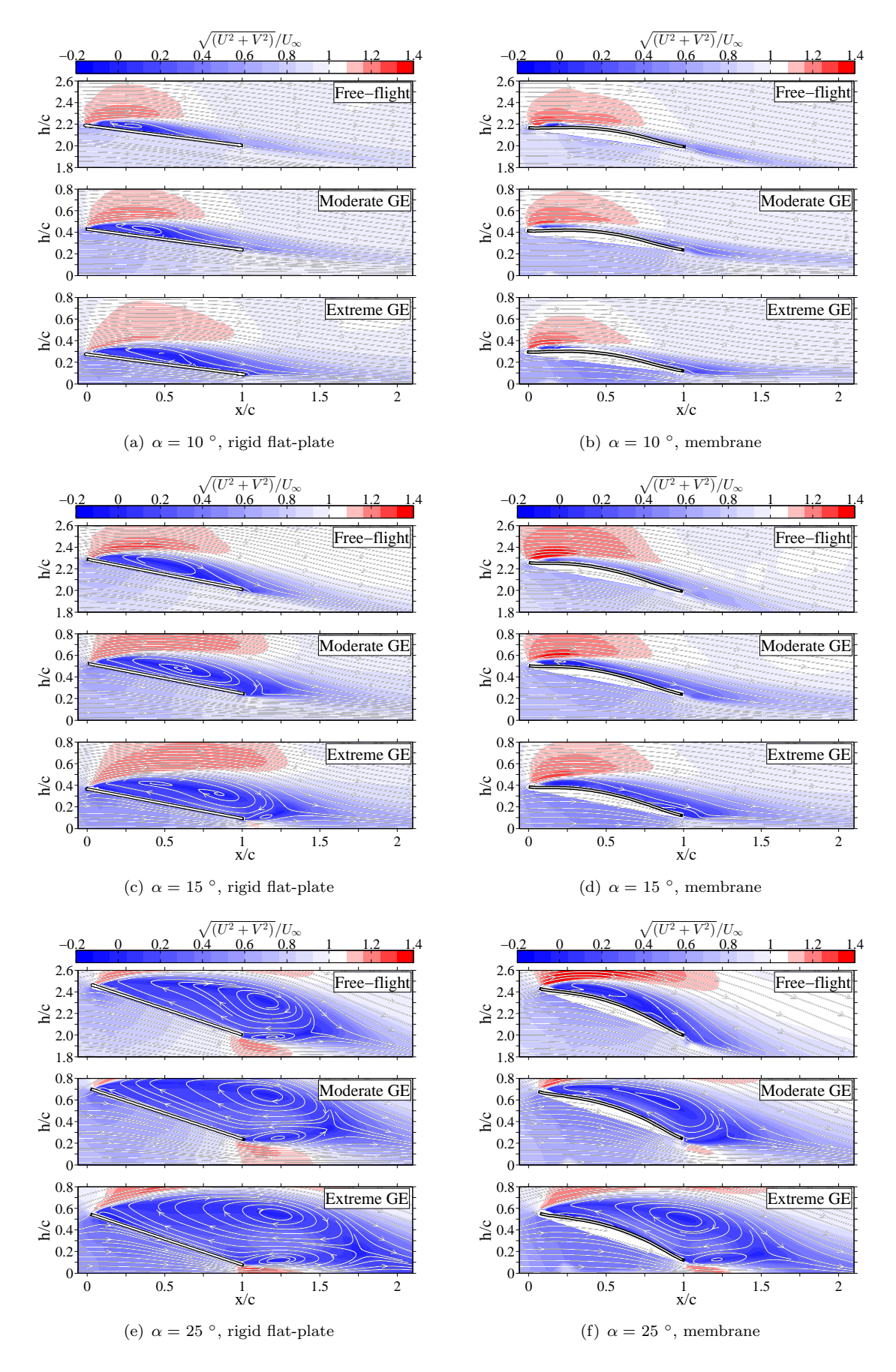


Figure 5.13: Freestream normalised velocity magnitude and streamlines for rigid flat-plate and membrane wings at  $\alpha = [10, 15, 25]^{\circ}$ , modifying with height-over-ground h/c = [2, 0.25, 0.1].

The descent into ground-effect shows for both wings a clear reduction in speed at the lower side of the wing, slowing down to 50% of the freestream value. This ram-effect in GE is well known from literature (Rozhdestvensky, 2006; Qu et al., 2014) and is accompanied with predominant lift generation at the lower side of the wing, reducing the aerodynamic impact of the upper wing surface. Membrane wings reflect the ram-effect by extending their maximum membrane camber with descent into GE, even while exhibiting fully separated flow conditions on the upper wing surface (Figure 5.8). Lower heights above ground are accompanied by downstream movement of the centroid of the separation bubble. This can be seen specifically for high angles-of-attack of  $\alpha=25^{\circ}$ . Rigid flat-plate wings (Figure 5.13e) exhibit separation bubbles whose centroid appears close to the trailing-edge or even farther downstream. In contrast, membrane wings (Figure 5.13f) show separation regions appearing close to the upper membrane surface. The chordwise or height location of the separation bubble becomes specifically important for fluid-structure interactions and resulting lift generation, discussed later in more detail (Section 5.3.2).

Figure 5.14 shows contours of turbulent kinetic energy  $\overline{(U'^2 + V'^2)}/U_\infty^2$  that highlights the regions of unsteady flow features. Again, rigid flat-plate and membrane wings are compared for three angles-of-attack and three heights-over-ground. Rigid flat-plate wings (Figure 5.14a,c,e) have generally strong velocity fluctuations close to the trailing-edge or even further downstream. In comparison, membrane wings exhibit strong velocity fluctuations close to the upper wing surface (Figure 5.14b,d,f). Interesting to note, the descent of membrane wings at  $\alpha = 25^{\circ}$  into ground-effect (Figure 5.14f) shows an increasing vertical movement of the highly energetic flow structures from the membrane surface, suggesting a fading influence in fluid-membrane coupling.

Figure 5.15 shows contours of the time-averaged vorticity  $\omega c/U_{\infty}$  of rigid flat-plate and membrane wings for different angles-of-attack and heights-over-ground. The figures show clear counter-rotating vortical structures at leading (clock-wise) and trailing-edges (anti clock-wise). The vorticity magnitude is in agreement with previous studies at comparable Reynolds numbers (Gordnier, 2009; Timpe et al., 2013). Both rigid flat-plate and membrane wings exhibit shedding of vorticity at the trailing edge along a line that is parallel to the ground. In comparison, wings in free-flight conditions exhibit the same shedding that is along the line joining the leading- and trailing-edges. This suggests strong TE-vortex interaction within GE and this is consistent with previous ground-effect studies on rigid wings (Prasad and Damodaran, 2013). Additionally, membrane wings are found to relocate the vorticity at the leading-edge. This is primarily due to introduction of small-scale vorticity in to the flow due to the vibrations of the membrane. As a result, membrane wings (Figure 5.15b,d,f) show more intense attached vorticity close to the LE than seen for rigid flat-plate wings (Figure 5.15a,c,e). Further exploration of fluid-membrane coupling will be discussed in Section 5.5.2.

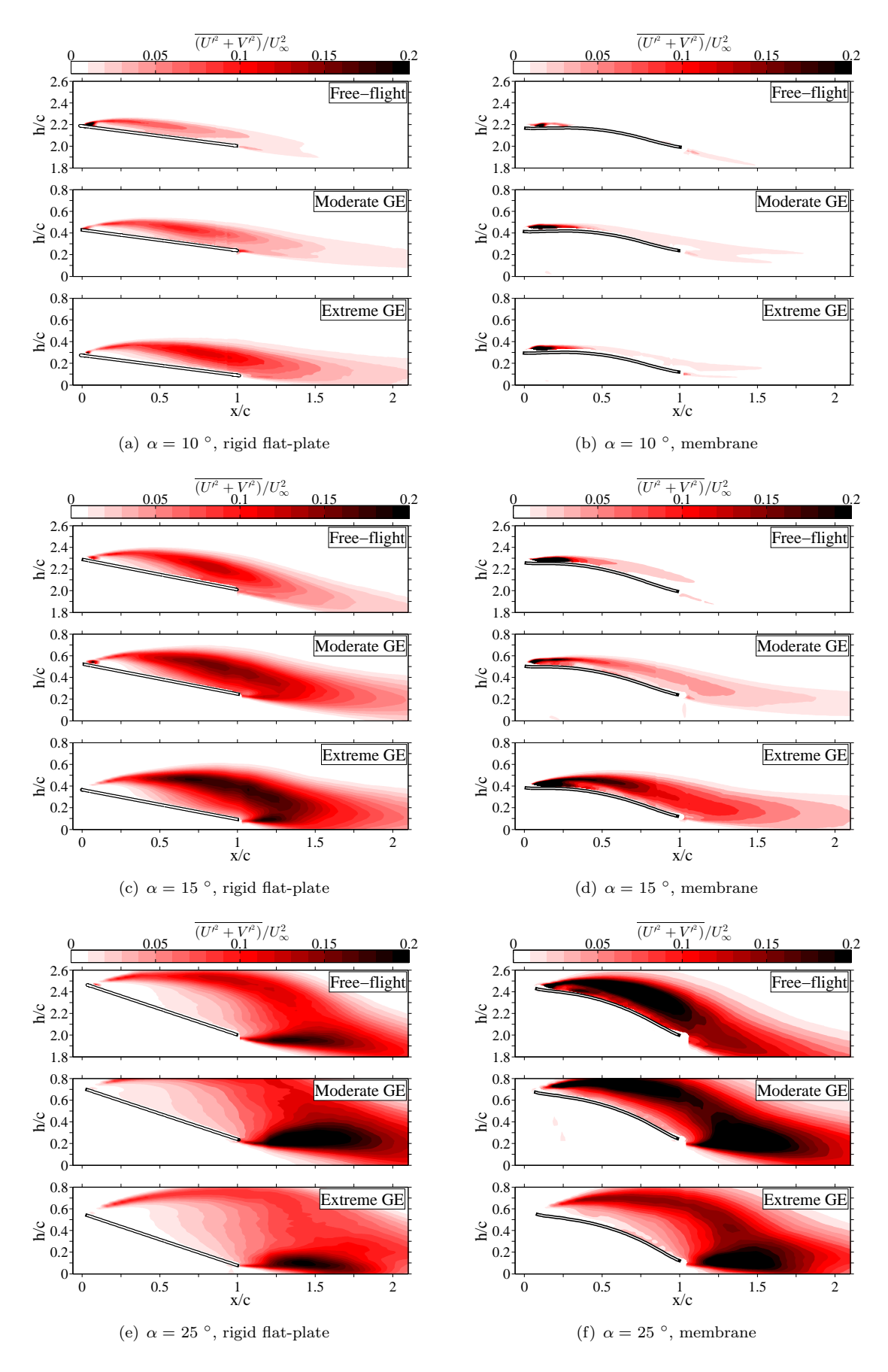


Figure 5.14: Turbulent kinetic energy for rigid flat-plate and membrane wings at  $\alpha = [10, 15, 25]^{\circ}$ , modifying with height-over-ground h/c = [2, 0.25, 0.1].

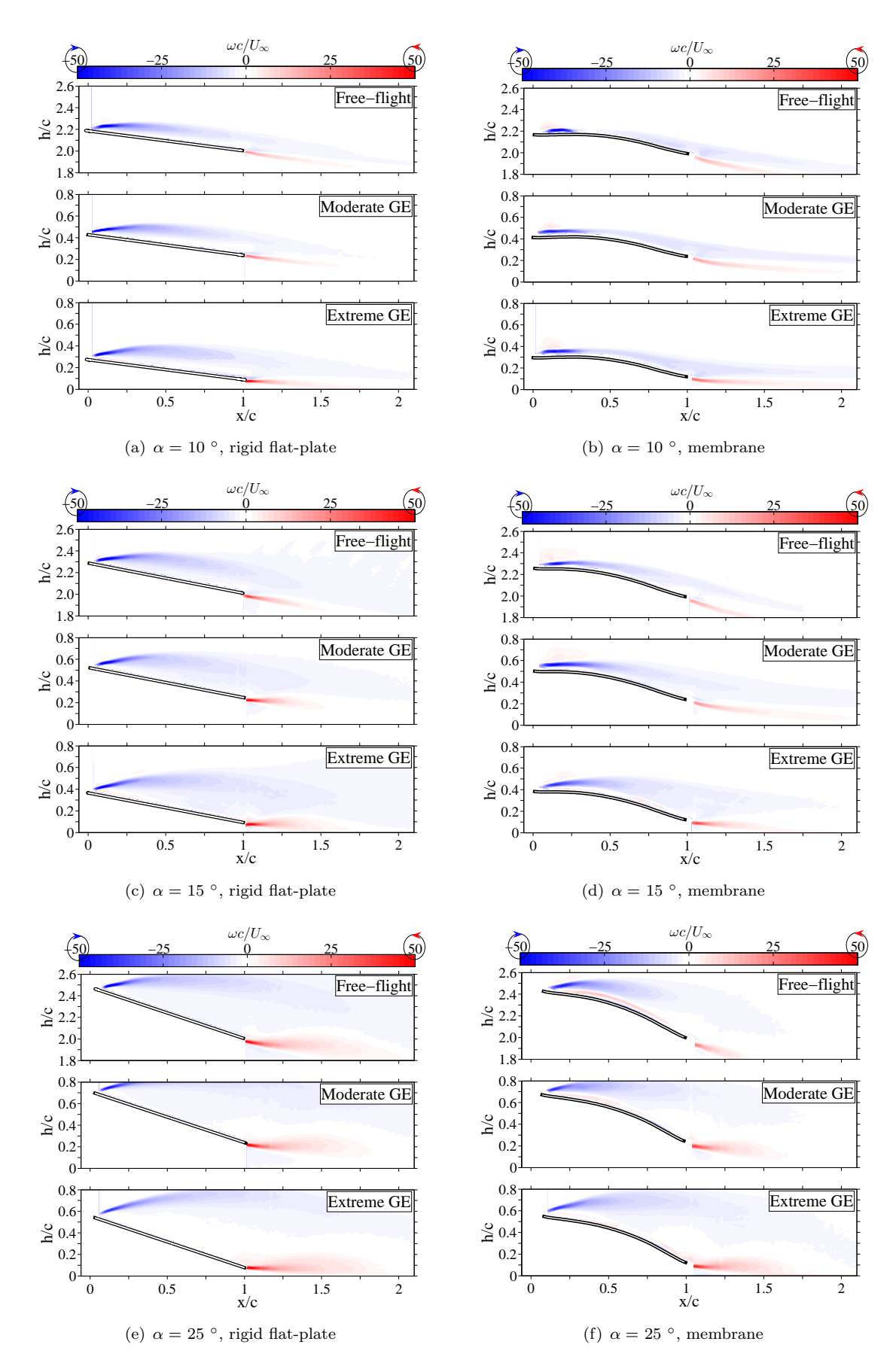


Figure 5.15: Time-averaged vorticity for rigid flat-plate and membrane wings at  $\alpha = [10, 15, 25]^{\circ}$ , modifying with height-over-ground h/c = [2, 0.25, 0.1].

## 5.3.2 Spatial Flow Structures

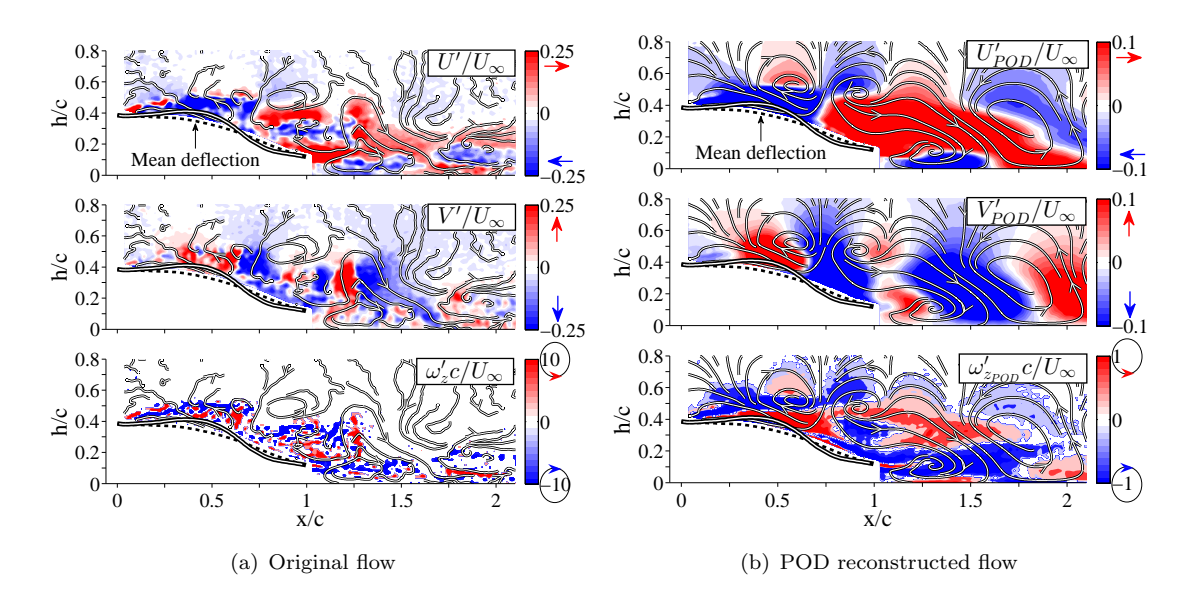


Figure 5.16: Instantaneous snapshot of horizontal (U'), vertical (V') velocity and vorticity  $(\omega')$  fluctuations. Additionally, streamlines are illustrated, based on velocity fluctuation components (U',V'). Instantaneous membrane fluctuations are shown amplified by factor of 7 for clarity. Effect of POD as filter technique on highly dynamic flow components and streamlines (using the first five modes). Exemplary case: Extreme GE (h/c=0.1) at  $\alpha=15$ °.

Proper orthogonal decomposition is a useful tool to examine and filter highly dynamic flow structures (technique see within setup by Section 3.3.5.3). Figure 5.16a explains the idea on an exemplary flow snapshot by showing the velocity components U' (upper), V' (mid) and vorticity  $\omega'$  (lower) together with the instantaneous streamline patterns (U',V'). Additionally, instantaneous membrane fluctuations are shown around their mean (dotted). Flow structures and streamlines are hard to identify at a given time-snapshot and come often without distinct coherent structures (Figure 5.16a). Figure 5.16b represents the same snapshot of the flow reconstructed using the first five most energetic POD modes. The POD reconstructed flow (Figure 5.16b) involves only  $\sim 35\%$ of the total flow fluctuation energy (Figure 5.17, lower) due a wide range of energetic scales in the flow (and a selection of only the first five POD-modes). As a result, the peak values of the POD-related color-bars are reduced accordingly to account for the energy loss and allow better illustration of the scale filtering ability of POD. The POD methodology reveals coherent leading-edge vortex-shedding with distinct streamlines (Figure 5.16b). It is interesting to note that the vertical flow fluctuations (Figure 5.16b, mid) seem to correlate well with vertical membrane motions.

Figure 5.17 shows an instantaneous snapshot of turbulent kinetic energy  $(\sqrt{(U'^2 + V'^2)})/U_{\infty}$  and the effect of POD-reconstruction by two to five POD-modes. The first two POD modes are able to capture 20% of the total fluctuation energy in the flow. In

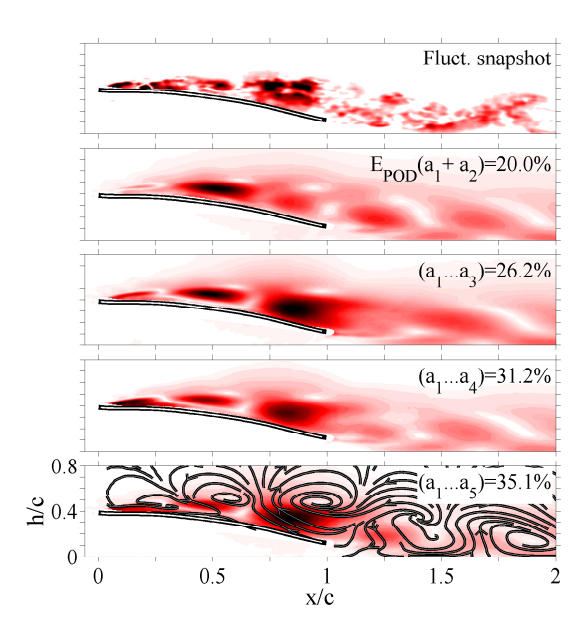


Figure 5.17: Fluctuation snapshot on averaged velocity fluctuations  $\sqrt{(U'^2+V'^2)}$  (upper) and its POD reconstruction with two to five POD-modes. Decomposition with five-POD mode shapes (lowest contour plot) shows additionally streamlines for clear vortex identification. Exemplary case: Extreme GE (h/c=0.1) at  $\alpha=15$ °. Five POD-modes sufficient enough to replicate major flow features.

comparison, over 80% of the fluctuations of the membrane for the same case (h/c=0.1,  $\alpha=15$ °) is contained in the first two POD modes (Section 5.2.3). This effect could be linked with the inertia and fundamental eigen frequency of the membrane, funnelling most energy into low order modes. Using up to five POD modes retains about 1/3 of the total energy in the flow-field fluctuations. In subsequent analysis we show that the a reduced-order model with five POD modes captures the necessary dynamics of the flow structures and is perhaps sufficient to explain various flow-membrane coupling observed in the current study.

Figure 5.18 compares a time-series of flow fluctuations to its POD-reconstruction based on five POD-modes. The usage of POD-filtering is found to allow easier localisation and interpretation of highly dynamic and convecting vortex structures. The reduced model enables us to select specific dominant energy scales of the flow by neglecting broader fluctuations that are of negligible importance (Lian et al., 2003; Kostas et al., 2002).

Figure 5.19 and Figure 5.20 show for  $\alpha = 15$  ° and 25 ° the five most energetic POD modes (a1,...,a5) of the velocity fluctuations ( $\sqrt{(U'^2 + V'^2)}/U_{\infty}$ ). Rigid flat-plate and membrane wings are compared, going from free-flight (h/c = 2) into extreme ground-effect (h/c = 0.1). Additionally, the energy contribution of individual POD coefficients ( $E_{POD}$ ) is illustrated on the top right corner of each contour plot. Contours in each individual subplot are normalised such that the peak value is 1. Both rigid flat-plate and membrane wings show coherent flow structures related to leading-edge vortex-shedding.

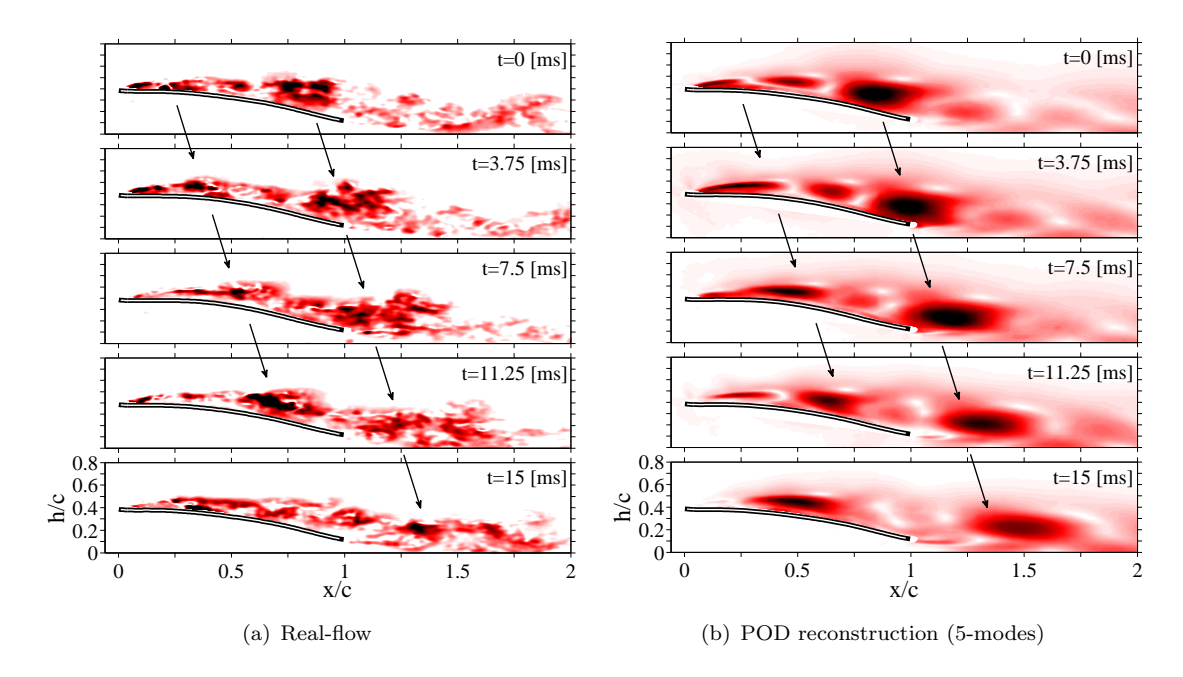


Figure 5.18: Timeseries of flow fluctuation snapshots  $\sqrt{(U'^2+V'^2)}/U_{\infty}$  and its POD reconstruction with five POD-modes. Convection of flow with time steps of three images or 3.75 [ms]. Exemplary case: Extreme GE (h/c=0.1) at  $\alpha=15$ °.

As previously suggested, the dynamics of rigid flat-plate wings in free-flight at  $\alpha = 15$ ° (Figure 5.19a) show comparable shedding structures to membrane wings at  $\alpha = 25$ ° (Figure 5.20b). This implies that membrane cambering and dynamic motions help to retain similar flow conditions at drastically higher angles-of-attack ( $\Delta \alpha = 10^{\circ}$ ), providing superior lifting capabilities to typical rigid flat-plate wings (up to 75%, see Figure 5.2a,b upper). Similarly, membrane wings benefit within ground-effect due to their ability to use growing separated flow dynamics to their own benefit, enlarging the overall performance window compared to rigid flat-plate wings.

The narrow performance window for rigid flat-plate wings  $(C_L/C_D \geq 5)$ , see Figure 5.4c) can be clearly related to the flow structures that are mainly located close to the trailing-edge or even further downstream (as identified by POD modes, see Figure 5.19a,c and Figure 5.20a,c). In contrast, membrane wings show mostly closely attached energetic regions of the flow which roll down the chord along the membrane (Figure 5.19b,d and Figure 5.20b). These energetic structures remain apparent under drastic adverse pressure gradients (GE induced, see Figure 5.20d), but are lifted up vertically from the membrane surface rather than moving downstream towards the TE as seen for rigid flatplate wings. This suggests that membrane oscillations still influence the flow structures passing over the wing, but the resulting energy entrainment is not sufficient to overcome the strong adverse pressure gradient. Nevertheless, membrane wing oscillations are found to actively enhance leading-edge vortex roll-up close to the moving wing surface.

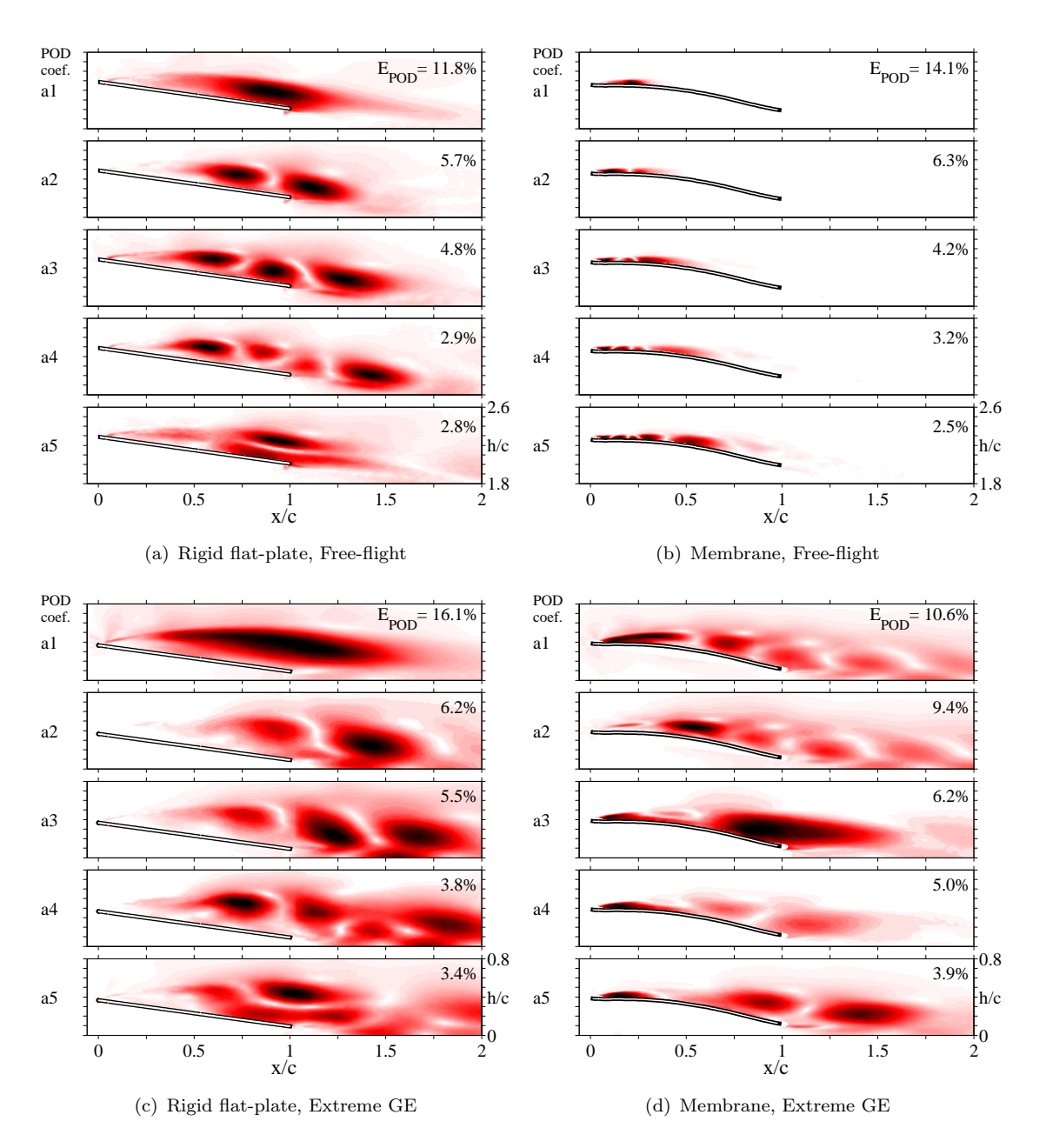


Figure 5.19: Five most energetic POD mode shapes of averaged velocity fluctuations  $\sqrt{(U_{POD}^{\prime 2}+V_{POD}^{\prime 2})}/U_{\infty}$ . Comparison of rigid flat-plate and membrane wings at moderate angle-of-attack of  $\alpha=15$ °, changing from free-flight (h/c=2) into extreme GE (h/c=0.1). Rigid flat plates show mid-wing to TE located dynamics in vortex-shedding, moving downstream with GE (Video via: https://youtu.be/1UfPYYo8s5g). Membrane wings show with the descent into GE flow dynamics happening close to membranes surface (Video via: https://youtu.be/aD-jtUUiWOQ).

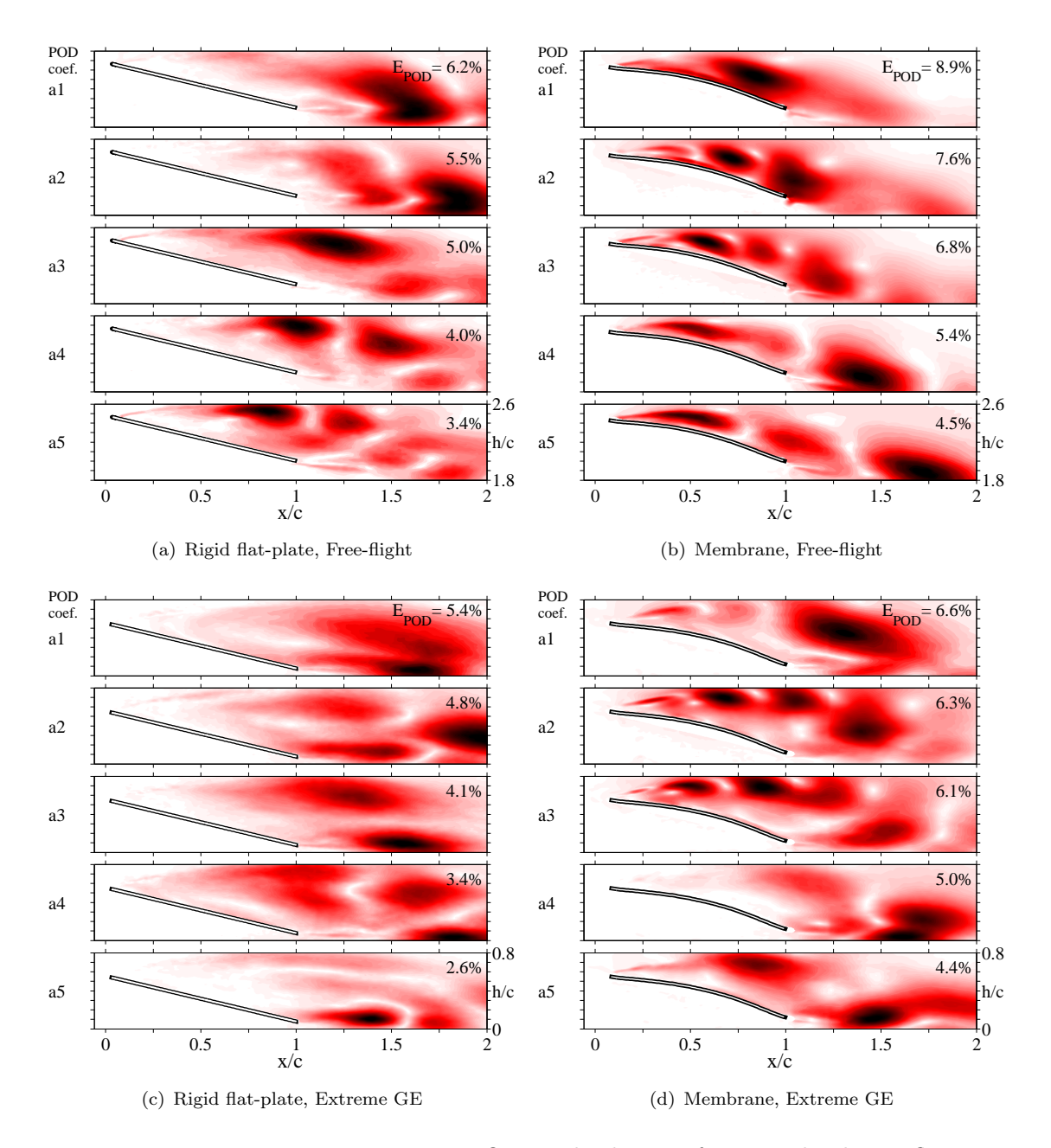


Figure 5.20: Five most energetic POD mode shapes of averaged velocity fluctuations  $\sqrt{(U_{POD}^{\prime 2}+V_{POD}^{\prime 2})}/U_{\infty}$ . Comparison of rigid flat-plate and membrane wings in post-stall conditions of  $\alpha=25$ °, changing from free-flight (h/c=2) into extreme GE (h/c=0.1). Rigid flat plates show vortex-shedding happening downstream of TE (Video via: https://youtu.be/pJkT0pRF1Y4). Membrane wings show in free-stream conditions strong dynamics close to membrane surface (b), which remain but detach from the wing surfance within GE conditions (d) (Video via: https://youtu.be/KoA-W\_MuQtQ).

For illustrative purpose, videos are available which show the convection of the POD mode shapes in time (based on first five POD modes). The contours show vertical velocity fluctuations together with streamline patterns:

- Rigid flat-plate,  $h/c=[2, 0.25, 0.1], \alpha=15$  ° https://youtu.be/1UfPYYo8s5g
- Membrane wing,  $h/c=[2, 0.25, 0.1], \alpha=15$  ° https://youtu.be/aD-jtUUiWOQ
- Membrane wing,  $h/c=[2, 0.25, 0.1], \alpha=25$  ° https://youtu.be/KoA-W\_MuQtQ

## 5.3.3 Spectral Content of the Flow

Figure 5.21 shows the spectral content of vertical flow fluctuations PSD(V') at a selection of flow-listener points L1,...,L5. Vertical flow dynamics are chosen as they are clearer in showing correlation to the membrane dynamics (compared to horizontal fluctuations that have more broadband information). The listener points are illustrated within the contour plots of averaged vertical velocity fluctuations  $\sigma(V)$ . Rigid flat-plate and membrane wings are compared for the case of  $\alpha = 15$  ° and h/c = 0.1.

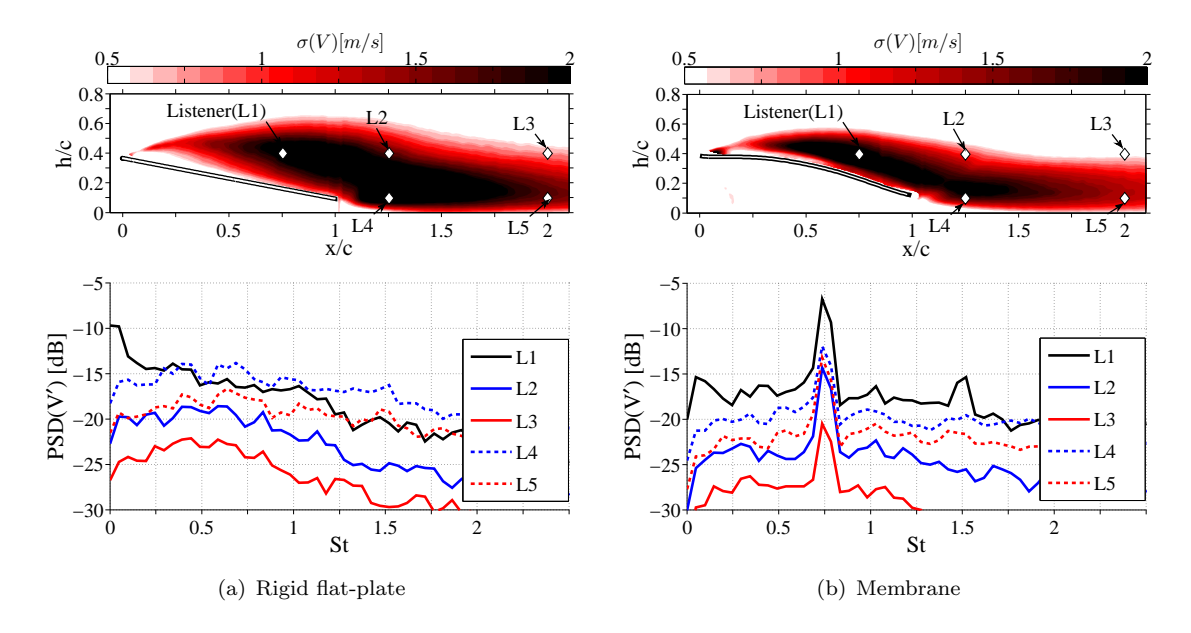


Figure 5.21: Spectral content of flow fluctuations V' for rigid flat-plate and membrane wings, illustrated at a selection of listener points (L1,...,L5) in the wake. Exemplary case at  $\alpha = 15$ ° and h/c = 0.1.

Both rigid flat-plate and membrane wings exhibit a flow with strong vortex-shedding for the given height and angle-of-attack (Figure 5.19c,d). However, the flow-spectra of rigid flat-plate wings (Figure 5.21a) makes identification of dominant spectral peaks challenging. Their spectral energy appears to be lower and spread over a broad range

of dynamic flow-scales, which goes to confirm the findings in previous studies (Timpe et al., 2013; Molkia and Breuerb, 2010). In comparison, membrane wings show a clear peak in dominant shedding frequency of St = 0.74, suggesting membrane induced flow structure amplifications which are discussed in detail later in this thesis (Section 5.5.2). The location of the listener point is not found to be crucial for the detection of major shedding frequencies. However, the energy values appear highest for listener points placed closer to the wings surface (L1) and immediately behind the trailing-edge (L4).

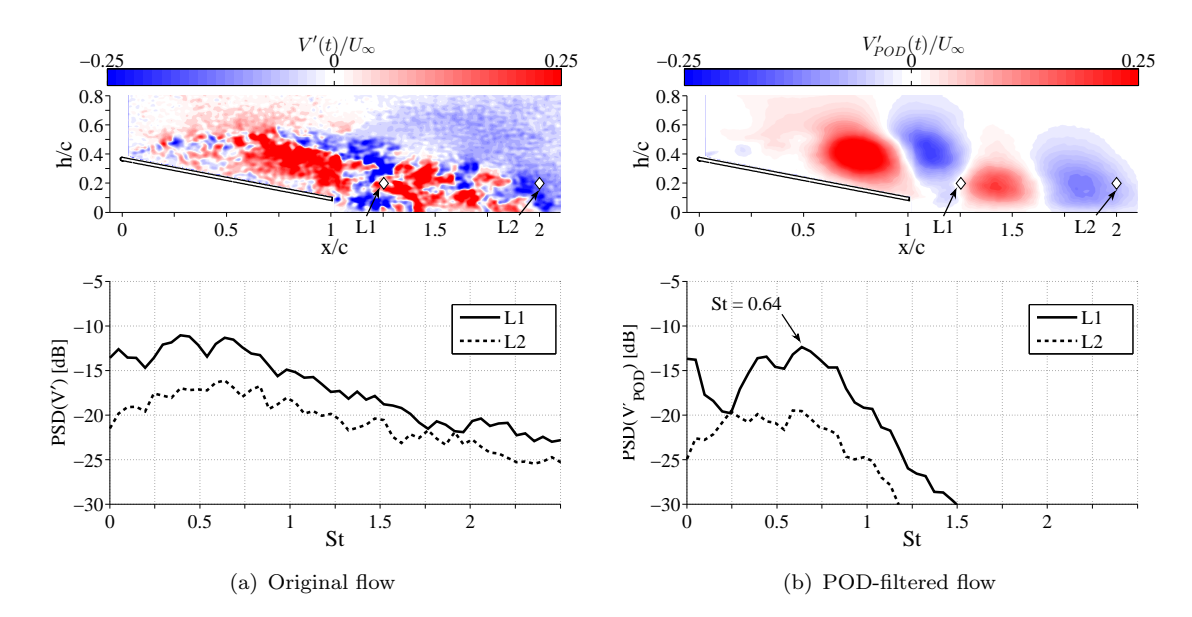


Figure 5.22: Usage of POD-filtering (using first five modes) to gain easier access to the vortex-shedding frequency in highly unsteady flow conditions. The contour plots show time-instant snapshots in vertical velocity fluctuations. The spectra bases on vertical flow fluctuations at the listener points L1(1.25, 0.2) and L2(2, 0.2). Exemplary case of a rigid wing at  $\alpha=15$  ° and h/c=0.1.

Since the frequency spectra is more broadband for rigid wings (Figure 5.21a), a POD-based filtering was first applied to the original flow signal, enabling identification of the dominant vortex-shedding frequency in the wake of the wing. Figure 5.22 shows an example of the original and POD-filtered spectra for a rigid wing at  $\alpha=15$  ° and h/c=0.1. As previously said, the original flow of wings (Figure 5.22a, upper) consists often of diverse flow scales with similar energy content in their spectra (Figure 5.22a, lower). The POD-filtered flow (Figure 5.22b, upper) removes unwanted background scales and enables to focus on the spectral content of the structures of interest (here leading-edge vortex). As a result, the interpretation of the spectra becomes easier and enables to resolve the dominant shedding frequency of the rigid wing with St=0.64 (Figure 5.22b, lower).

Figure 5.23 is a summary and illustrates the dominant vortex-shedding frequencies  $St_{wake}$  for rigid (red) and membrane (black) wings for different angles-of-attack (x-axis) and heights-above-ground (marker-shape). Generally, the wake shedding frequency of

rigid wings is found to match well with the observations of previous studies on flat/cambered plates, where the Strouhal number was found to be in the range  $0.17 \le St_{wake}sin\alpha \le 0.23$  (Rojratsirikul et al., 2011).

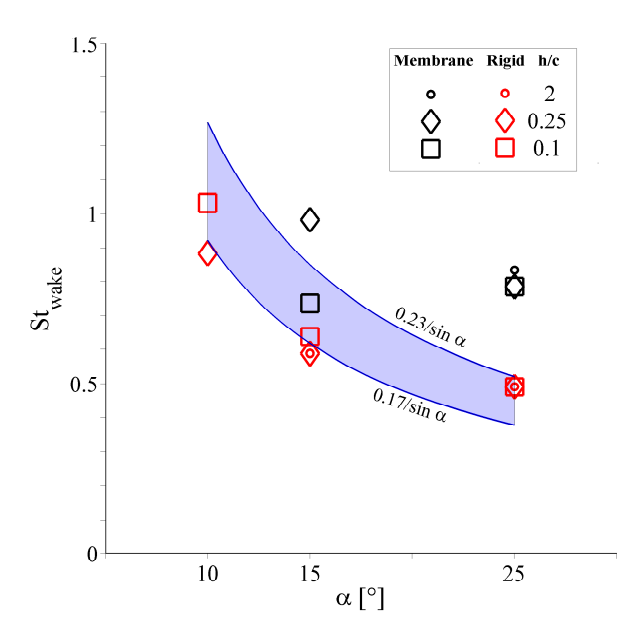


Figure 5.23: Summary of vortex-shedding frequency, comparing rigid flat-plates and membrane wings at different angle-of-attack and height-over-ground. The dominant Strouhal number of rigid flat plates (red-points) matches well to literature based flat/cambered plates (blue-shaded  $d/\sin\alpha$  rule, where  $0.17 \le d \le 0.23$ , see Rojratsirikul et al. (2011)).

The shedding frequencies of membrane wings (black markers) are significantly higher than the natural shedding frequencies of (flat/cambered) rigid wings, suggesting modifications of the flow dynamics due to fluid-structure coupling. Similar wing driven flow modifications are known from the literature by other membrane wing related studies (Timpe et al., 2013) or wings with active flow control (Miranda et al., 2005). Detailed spectral comparisons and coupling between the membrane and the flow will be further discussed in Section 5.5.2.

It should be mentioned that membrane wings at  $\alpha=10^{\circ}$  (all heights) and  $\alpha=15^{\circ}$  (free-flight) show attached flow conditions and therefore no dominant (or hardly resolvable) shedding frequencies (Figure 5.19b). As a result, those cases are discarded from the spectral summary in Figure 5.23.

# 5.4 Flow Development: cross-stream plane

The following section explains time-averaged and time-resolved flow features found in the cross-stream PIV-plane, located one chord downstream of the trailing edge (Figure 5.24).

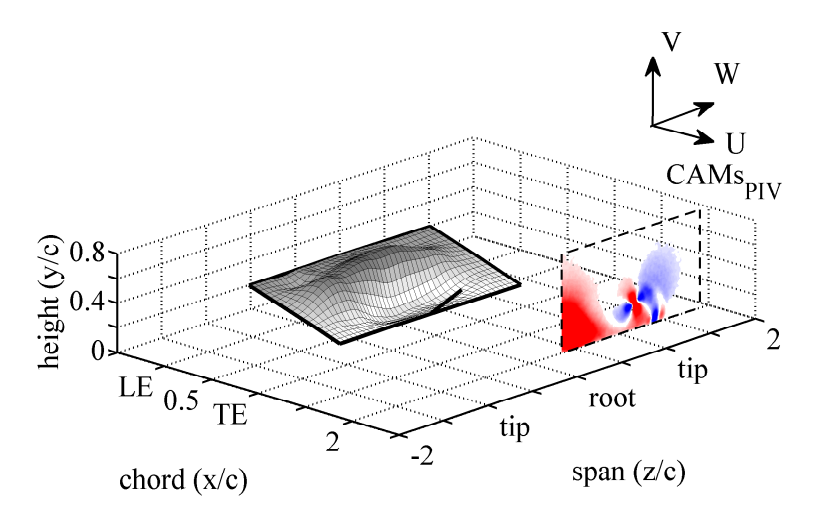


Figure 5.24: PIV-setup with flow investigation in spanwise plane (Flow based coordinate system, see also Section 3.3.5)

## 5.4.1 Flow Statistics

Figure 5.25 shows contours of the time-averaged in-plane absolute velocity ( $\sqrt{(W^2 + V^2)}/U_{\infty}$ ) together with the mean streamline patterns. Rigid flat-plate and membrane wings are compared at free-flight condition for different angle-of-attack from  $\alpha = [10, 15, 25]^{\circ}$ . The perimeter wing frame is shown projected into the cross-stream plane (only half-span visible), allowing to reference the tip-vortex size and its position in relation to the wing frame.

Both rigid flat-plate and membrane wings show an increase in averaged tip-vortex size with increasing angle-of-attack. Membrane wings (Figure 5.25b) show stronger tip-vortices than rigid flat-plate wings (Figure 5.25a), which is consistent with the higher lift produced by the membrane wings (Figure 5.2, upper). These results confirm to previous studies, comparing similar rigid flat-plate and membrane wings in free-flight conditions (Rojratsirikul et al., 2010b; Gordnier and Attar, 2014). For rigid flat-plate wings, the spanwise location of the centroid appears to move inwards (towards the root of the wing) with increasing angle-of-attack. This is consistent with the breakdown of the leading-edge vortex (Figure 5.20a,c) and its interaction with the tip-vortex that becomes more and more pronounced with increasing incidence. For membrane wings,

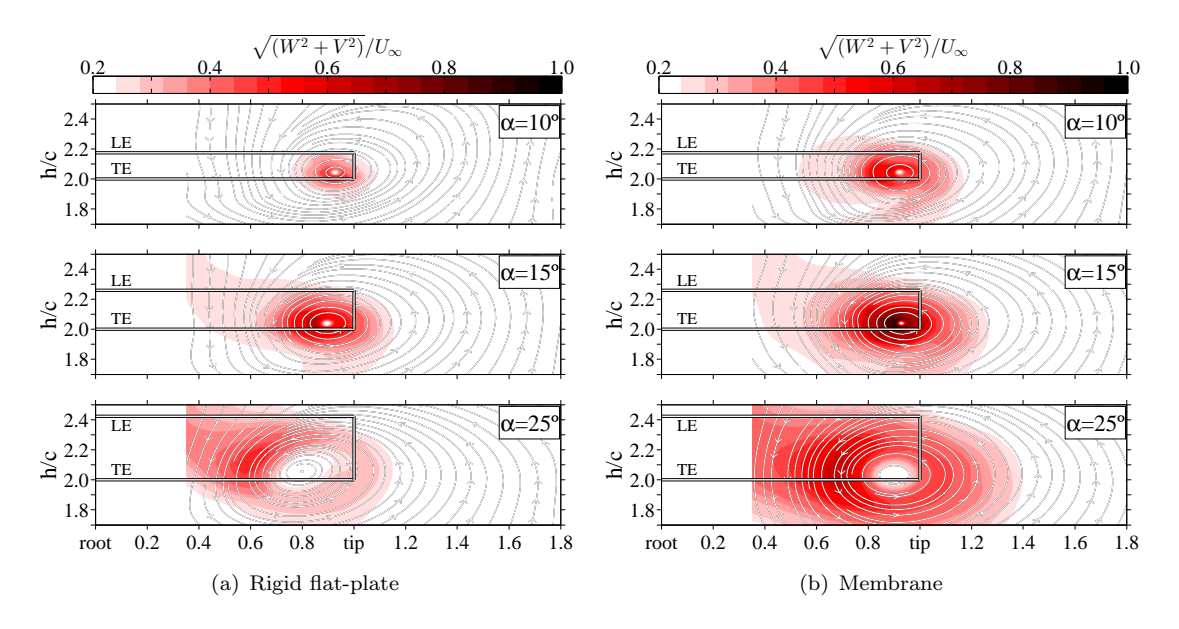


Figure 5.25: Effect of angle-of-attack on tip-vortex velocity magnitude and its position to the projected wing frame. Comparison of rigid flat-plate and membrane wings at  $\alpha = [10, 15, 25]^{\circ}$  in free-flight conditions (h/c = 2).

the horizontal centroid position appears to remain consistently at 0.9c for increasing  $\alpha$  indicating the stability of the tip-vortex.

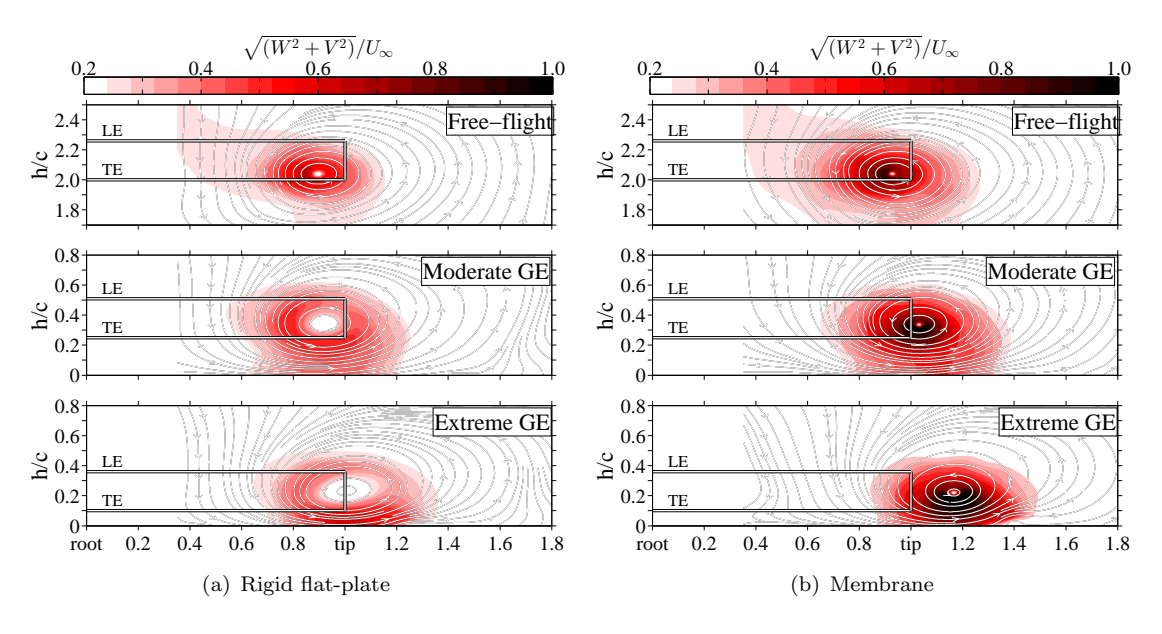


Figure 5.26: Effect of height-over-ground on tip-vortex velocity magnitude and its position to the projected wing frame. Comparison of rigid flat-plate and membrane wings at  $\alpha=15$  °.

Figure 5.26 shows the effect of height-over-ground on the time-averaged in-plane velocity magnitude  $(\sqrt{(W^2+V^2)}/U_{\infty})$ , changing from free-flight (h/c=2) to moderate (h/c=0.25) and into extreme ground-effect conditions (h/c=0.1). Rigid flat-plate (Figure 5.26a) and membrane (Figure 5.26b) wings are compared at  $\alpha=15^{\circ}$ . Both rigid

flat-plate and membrane wings show significant horizontal and vertical translation in the location of the tip-vortex with the descent into ground-effect. This translation results in improved aerodynamic efficiency by virtually extending the aspect-ratio of the wing (Figure 5.4a,b). Membrane wings show a tip-vortex located at 1.2c (for the extreme GE case, Figure 5.26b, lower), which is much larger than the impact observed in rigid flat-plate wings (Figure 5.26a, lower) where the tip-vortex only moves out to the spanwise edge of the wing at 1.0c. The effective push-out length can be correlated with the aerodynamic efficiency (Figure 5.4c), which showed substantial superiority of membrane wings to rigid flat-plate wings when they descent into GE. The vertical tip-vortex push-up effect is caused by the solid boundary of the ground, forcing the flow structures to move vertically upwards (in relation to the projected wing frame). Both rigid flat-plate and membrane wings exhibit similar push-up values across similar ground-effect cases.

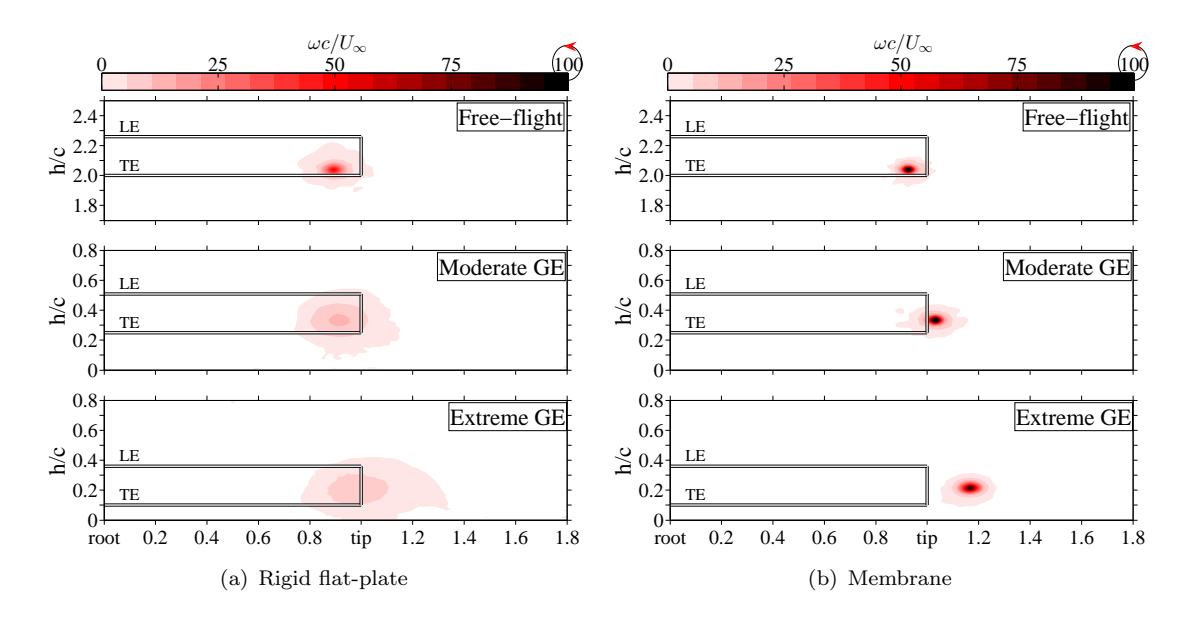


Figure 5.27: Effect of height-over-ground on time-averaged, axial tip-vortex vorticity magnitude, measured at a fixed angle-of-attack of  $\alpha = 15^{\circ}$ .

The enlarged tip-vortex strength of membrane wings can also be identified by considering the axial, time-averaged vorticity  $\omega c/U_{\infty}$  (Figure 5.27). For a fixed angle-of-attack of  $\alpha=15^{\circ}$ , rigid flat-plate wings show a reduced strength in vorticity and a clear tip-vortex break-down with the descent into ground-effect (Figure 5.27a). This vortex break-down with GE can also be achieved within free-flight conditions by increasing the angle-of-attack from stall into post-stall angles (not shown). In comparison, membrane wings show coherent tip-vortices with descent into ground-effect (Figure 5.27b), suggesting that the flow is closely attached to the wing surface over an extended portion of the wing. This suggestion can be confirmed by comparing previous streamwise POD flow dynamics. Rigid flat-plate wings show detached flow oscillations happening downstream of the TE (Figure 5.19c), whereas membrane wings illustrate flow dynamics happening close to the upper wing surface (Figure 5.19d).

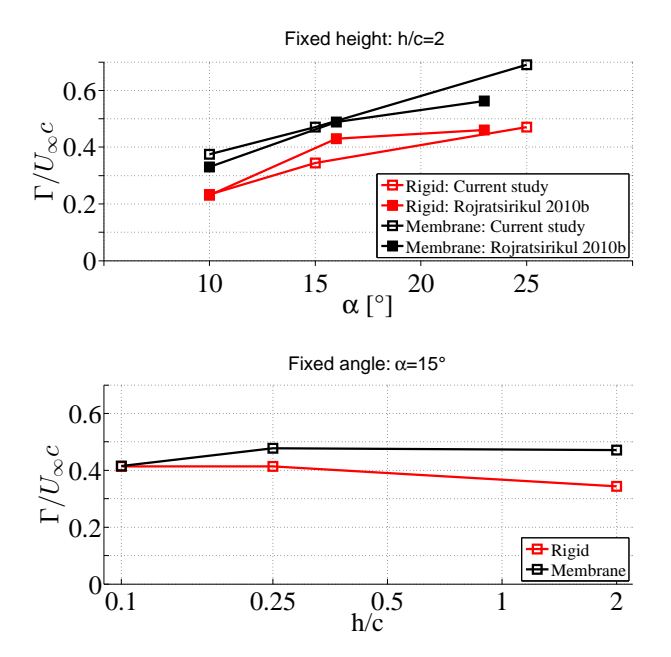


Figure 5.28: Normalized circulation of the tip-vortex for rigid flat-plate and membrane wings as function of angle-of-attack (upper plot) and height-overground (lower plot).

Figure 5.28 shows the magnitude of normalised circulation  $\Gamma/U_{\infty}c$  of the tip-vortex for rigid flat-plate and membrane wings, for various angles-of-attack and heights-over-ground. The circulation was calculated from the area integral of vorticity distribution. The circulations of rigid flat-plate and membrane wings are compared to other studies in the literature (Rojratsirikul et al., 2010b), showing a good match for both rigid flat-plate and membrane wings in free-flight conditions (Figure 5.28, upper). Ground-effect is found to affect the circulation much less than changes in angles-of-attack. This could be explained as the influence of two counteracting phenomena. The descent into ground-effect produces more lift, similar to an increase in  $\alpha$ . As a result, the circulation at the wing tips should increase with the descent into GE due to higher-pressure differences at the wing tips. However, ground-effect is also known to weaken the overall tip-vortex structure due to tip-vortex push-out and therefore extending virtually the aspect-ratio of the wing. As a result, the circulation stays relatively constant with the descent into GE (Figure 5.28, lower).

#### 5.4.2 Spatial Flow Structures

Figure 5.29a shows an example of an instantaneous snapshot of freestream-normalised velocity fluctuations in cross-stream (W', V') and streamwise (U') directions. The illustrated flow is for a membrane wing at  $\alpha = 15^{\circ}$  in extreme GE conditions (h/c = 0.1). The in-plane velocities (W') and (V') are also illustrated as streamline patterns. As previously discussed in the flow dynamics of the streamwise PIV plane (Section 5.3.2), the diversity of flow-scales and structures makes it difficult to observe the tip-vortices in

instantaneous snapshots. Therefore, POD is used as a filter in order to identify coherent flow structures and their dynamics (Figure 5.29b).

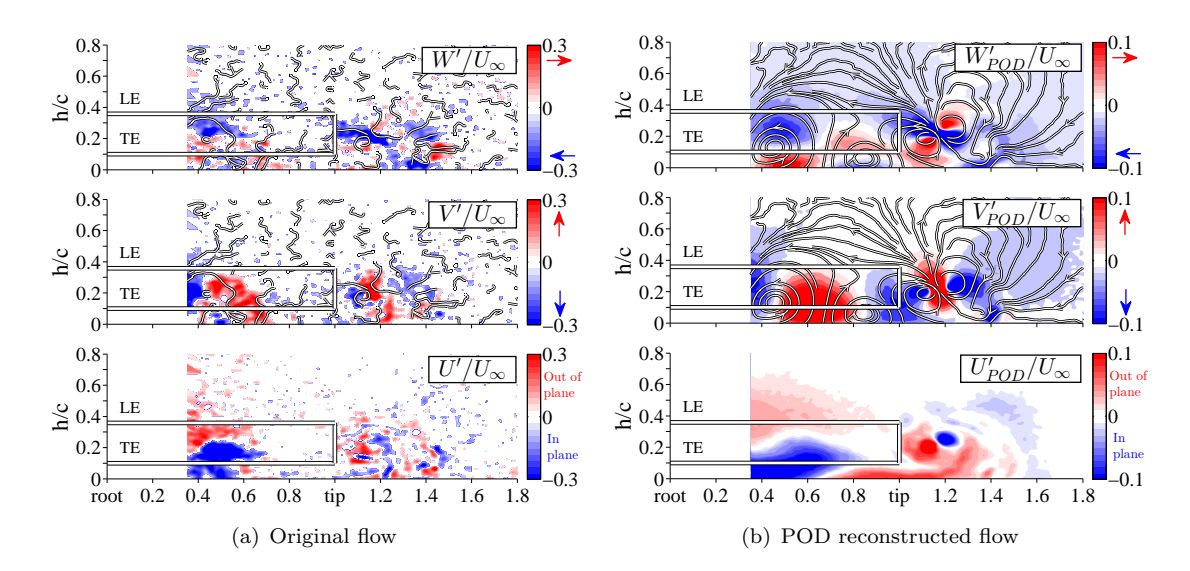


Figure 5.29: Instantaneous snapshot of freestream-normalised velocity fluctuations U' (out-of-plane), V' (vertical), W' (spanwise). Additionally, streamlines are illustrated, based on in-plane velocity fluctuation components (V',W'). Effect of POD as filter technique on highly dynamic flow components and streamlines (usage of 5-modes). Exemplary case: Membrane wing at  $\alpha=15^{\circ}$  in extreme GE (h/c=0.1) conditions. Videos are available for the original (https://youtu.be/v23WQJzmL2U) and the POD-filtered flow (https://youtu.be/5rKJUogbgj8).

The decomposition of dynamic flow structures reveals an important flow feature that occurs 0.4-0.8c away from the root. The streamlines shows a large vortex structure passing through the plane. The out-of-plane velocity component  $(U'_{POD})$  reveals the 3-dimensional spinning nature of the vortex, with flow passing downstream at h/c = 0.4 (red) and upstream at h/c = 0.1 (blue). This vortex structure is found to be a signature of LE-vortex that has shed and is passing through the cross-stream PIV-plane in the wake.

For illustrative purpose, videos are available which show the velocity components of the original and POD filtered flow (based on first five modes) together with streamline patterns. The illustrated video is for a membrane wing at  $\alpha=15^{\circ}$  in extreme GE conditions (h/c=0.1):

- Original flow: https://youtu.be/v23WQJzmL2U
- POD filtered flow: https://youtu.be/5rKJUogbgj8

## 5.4.3 Spectral Flow Content

High-speed flow measurements allowed to capture dominant flow frequencies within the cross-stream PIV-plane. Figure 5.30 shows the spectra in vertical flow oscillations at five listener points along the span (points L6,...,L10 are shown in the contour plots and are located in level with the trailing-edge). Rigid flat-plate and membrane wings are compared at  $\alpha=25^{\circ}$  in free-flight (Figure 5.30a,b) and at  $\alpha=15^{\circ}$  in extreme ground-effect conditions (Figure 5.30c,d). The illustrated height/angle-of-attack cases are selected for their strong presence of leading-edge vortex-shedding (capability to excite membrane dynamics).

Listener points located closer to the wing root (e.q. L6) are found to exhibit the highest signal-to-noise ratio, allowing to resolve the leading-edge shedding-frequency most effectively. This is a result of the tip-vortices which are able to constrain the spanwise expansion of LE vortex-shedding towards the wing root.

The dominant shedding frequencies in the wake (at L6) match well to the previously discussed flow spectra in the streamwise PIV-plane (Figure 5.23). As already mentioned, membrane wings show generally higher shedding frequencies to typical rigid flat/cambered plates. The reason might be explained by illustrating the dominant membrane vibrations frequencies as green lines in Figure 5.30b,d. The membrane dynamics are found to match specifically well with the wake shedding frequency for cases with peaklift (in-stall) conditions, where LE vortex-shedding appears predominantly close to the wing upper surface. LE vortex-shedding can either be reached with high angles-of-attack in free-flight conditions (Figure 5.30a,b) or reduced heights-over-ground at moderate incidences (Figure 5.30c,d). Ultimately, the results suggest that membrane wings come with the ability to imprint their structural membrane eigen frequencies into the flow spectra, if an energy entraining system is apparent to engage their membrane oscillations (here LE vortex-shedding). The result supports the idea to actively control the flow dynamics of membrane wings by modifying the dynamic characteristics of the membrane (e.g. with electro-active membrane wings (Hays et al., 2012; Curet et al., 2014; Buoso and Palacios, 2016)).

Thus far, a detailed examination of the flow-field has been presented and has been related to the statistical observations of the membrane deformation as well as the loads. However, the instantaneous coupling between the flow, the membrane and the loads has not been presented. The next chapter will attempt to characterise this coupling in detail as well the phase relationships between them.

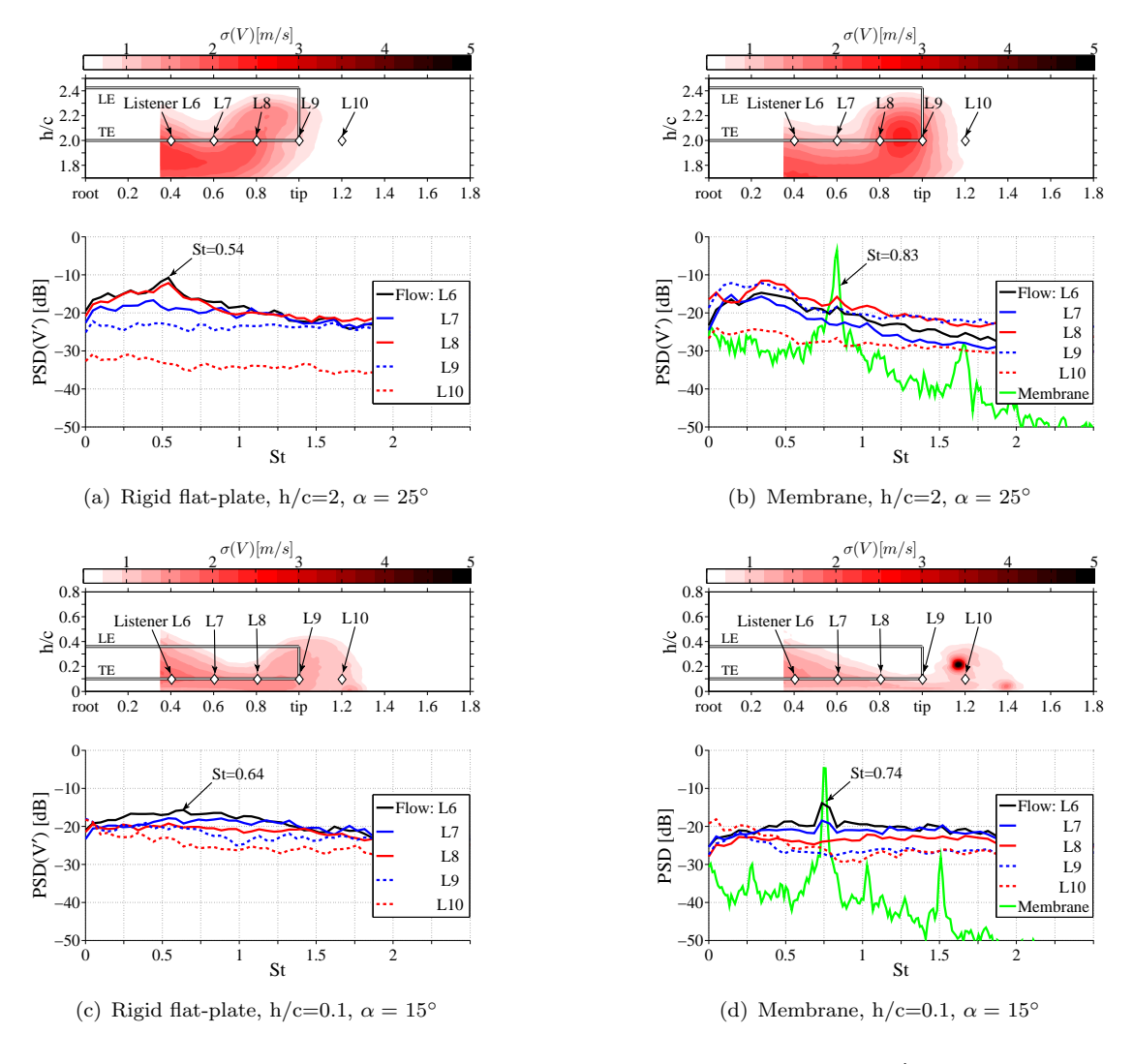


Figure 5.30: Spectral analysis of vertical flow oscillations PSD(V') at listener points L6,...,L10. Comparison between rigid flat-plate and membrane wing in free-flight (h/c=2) at  $\alpha=25^{\circ}$  and extreme ground-effect (h/c=0.1) at  $\alpha=15^{\circ}$ . Membrane wings (b,d) show very distinct dominant shedding frequencies in the flow which match well with the dominant oscillation frequencies of the membrane (green line), suggesting membrane dynamics induced modifications in vortex shedding and fluid-membrane coupling.

# 5.5 Aerodynamic Coupling

The first part of this chapter focusses on the coupling mechanics between the aerodynamic loads (lift, drag and pitch moment) and the membrane motions. The second part reveals the coupling between the membrane and the flow dynamics. The third part illustrates the coupling between the load, the membrane and the flow. Finally, time-synchronised load-membrane-flow acquisition allows to cycle-average the loads and both streamwise and cross-stream PIV planes by the phase information in membrane dynamics.

#### 5.5.1 Load-Membrane

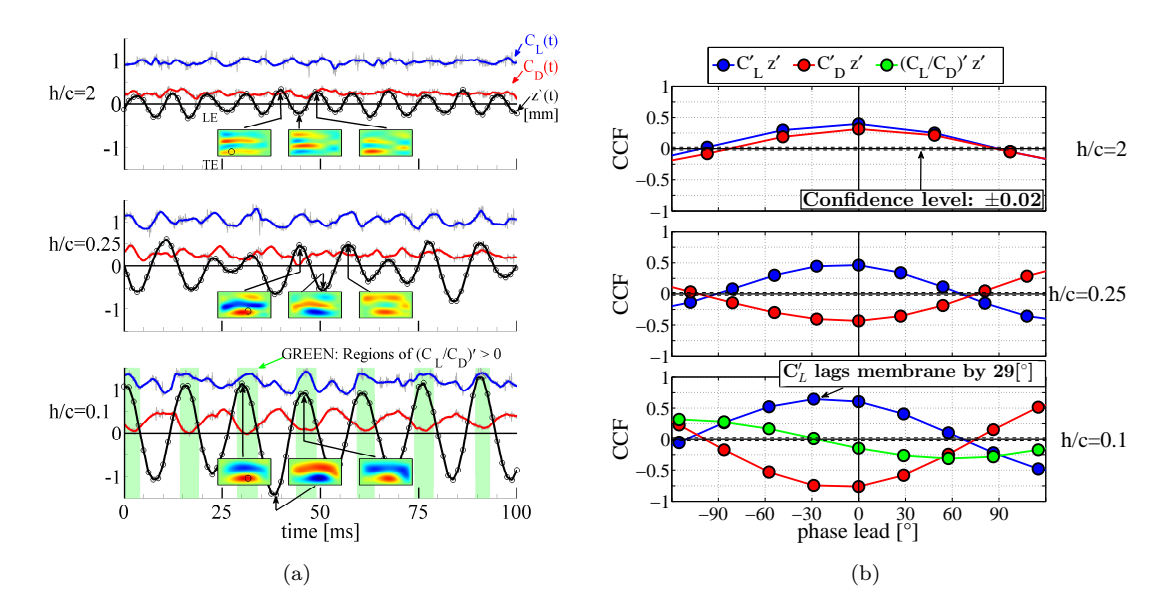


Figure 5.31: (a) Time series of  $C_L$ ,  $C_D$  and instantaneous membrane deformation (z') for  $\alpha = 15^{\circ}$  at three different heights over ground. (b) Cross correlation between force coefficients and membrane deformation (wing body based coordinate system, see Section 3.3.4).

Figure 5.31a shows a representative time-series of lift  $C_L(t)$ , drag  $C_D(t)$  and membrane vibrations z'(t) for heights h/c = [2, 0.25, 0.1] at an angle-of-attack of  $\alpha = 15^{\circ}$ . The membrane oscillation z'(t) is tracked on the membrane surface at the point of maximum vibration intensity. The location of this point changes with height-over-ground due to mode shape modifications, but is always located at the peak closest to the trailing-edge. The normalised, membrane based in-plane coordinates Figure 5.7 of that measurement point for the height h/c = [2, 0.25, 0.1] are given as (chord, span)= [(0.86, -0.49), (0.78, 0.14), (0.77, 0.14)] and are also illustrated within the first instantaneous membrane surface of Figure 5.31a. Smoothed lines in red (drag) and blue (lift) show down-sampled (with a low-pass filter) force results (gray lines show the unfiltered data) to match the sampling frequency of membrane deformations. Contours of instantaneous membrane

fluctuations z'(x, y, t) (wing body based coordinate system, see Section 3.3.4) are illustrated at three specific time steps of the given time series. Finally, the ground-effect case h/c = 0.1 shows additionally green vertical shadow regions, representing an instantaneous gain in aerodynamic efficiency  $C_L(t)/C_D(t)$  over its time-averaged mean value.

The illustrated cases (Figure 5.31a) allow detailed examination of modal information and their instantaneous contribution to lift, drag and range efficiency. The strong groundeffect case at h/c = 0.1 shows a very clear low frequency oscillation of two alternating chordwise motions in the membrane which suggest considerable influence of strong leading-edge vortex and near-stall flow conditions. It is found that the instantaneous maximum lift is produced when the membrane has a negative fluctuation close to the leading-edge (blue in membrane surface is a negative fluctuation relative to the average deformation) and a positive one near the trailing-edge (red). In other words, positive increase in lift is associated with an instantaneous rearward location of maximum positive camber. The drag is reduced within this region and can even become negative, producing thrust rather than drag (Figure 5.31a, lower). As a result, the aerodynamic efficiency (green vertical shading in Figure 5.31a is found to peak within these periods. The ability to produce thrust for short time-instances is suggested to be linked with strong membrane oscillations which are enhanced, triggered and synchronised with leading-edge vortex shedding, apparent in close-to-stall conditions. The given study shows two specific (height/angle-of-attack) cases with this promising properties: A membrane wing in free-flight conditions (h/c=2) at  $\alpha=25^{\circ}$  (at peak-lift) and a membrane wing in (stall-inducing) ground-effect conditions (h/c = 0.1) at  $\alpha = 15^{\circ}$  (Figure 5.31a, lower). Further within this study, both cases will be shown to provide lag-free coupling between membrane oscillations and flow shedding (Figure 5.36 and Figure 5.37) which are suggested to be key for thrust producing moments. The fundamental mechanism for this time-instant thrust periods could be explained by a recent study on flapping membrane wings (Jaworski and Gordnier, 2012), suggesting that an instantaneous pressure distribution focussed on the leading-edge (by a developing LE-vortex-core) allows for a forward tilted (thrust producing) resultant force. However, further studies are necessary to validate this idea on non-flapping passive membrane wings. A different explanation focusses on the current data-set and the rotational nature of the rolling-down leadingedge vortex. The vortex-rotation could reduce frictional drag due to enhanced upstream (recirculating) flow components. The high-speed flow recordings of the velocity magnitude confirm this (pulsing) recirculating flow by showing the vector-fields in a time-series (https://youtu.be/nKlWFL48c\_0). Nevertheless, future experiments are necessary to gain access to the fundamental physics behind this (thrust-producing) phenomenon.

A direct comparison of the normalised cross-correlation function (CCF, see eq. 3.5) between forces  $(C'_L, C'_D)$  and membrane (z') fluctuations reveals a nearly instantaneous response in forces to changes in membrane deformations (Figure 5.31b). The illustrated

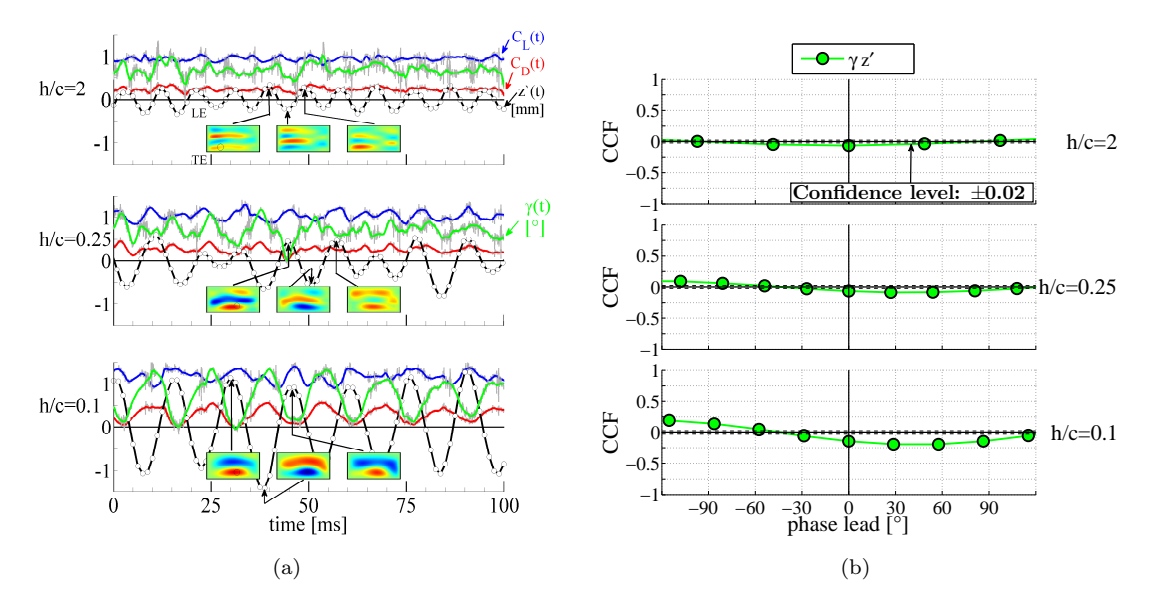


Figure 5.32: (a) Extension of Figure 5.31 with added force angle  $\gamma(t)=\frac{1}{20}atan(\frac{C_D}{C_L})$  [°] as alternative value for instant aerodynamic performance (green line in Figure 5.32a), indicating temporal thrust producing periods if  $\gamma(t)<0$ . (b) Cross-correlation of force angle  $\gamma$  to membrane deformations. The correlation of the membrane to the performance parameter  $\gamma$  appears with CCF = 0.24 weak but measureable at cases with generally enhanced fluid-structure coupling (Figure 5.32b, lower  $\Rightarrow$  ground-effect enforced fluid-structure coupling). Membrane wings at  $\alpha=15^{\circ}$  at three different heights over ground.

phase period  $\phi$  in [°] (eq. 3.6) is relative to the dominant vibration frequency of the membrane, which is measured as [108, 60, 64] Hz for h/c = [2, 0.25, 0.1]. For the highly energetic vibrations in ground-effect (h/c = 0.1), the lift and drag fluctuations are found to correlated (CCF = +0.70 and -0.75) with a maximum phase lag to the membrane of 29° (lift = positively correlated, drag = negatively correlated). The fluctuation in the  $(C_L/C_D)'$ -ratio is found to lead the membrane fluctuation by 58° (negative correlated). However, the correlation value is limited to CCF = -0.3. It should be mentioned that a high correlation value between the membrane and the aerodynamic efficiency does not necessarily mean a better gain in aerodynamic efficiency. However, if the correlation value is high, it could be possible to modulate and so modify membrane oscillations in the future (e.g. with electroactive membrane wings) with the aim to shift the overall mean efficiency upwards.

For h/c = 0.25 and h/c = 2, membrane deformations (Figure 5.31a) are coupled with higher frequencies and lower vibration-amplitudes. The correlation between lift, drag and membrane-fluctuations remains without significant lag but correlation reduces to 0.4 (Figure 5.31b). The time-instant gain in instantaneous aerodynamic efficiency appears further reduced to CCF  $\leq 0.1$  and is therefore discarded from the cases h/c = 0.25 and h/c = 2. Ultimately, the illustrated correlation technique in combination with the aerodynamic efficiency has to be seen with care due to  $C_L(t)/C_D(t)$ -periods with values

close to infinity (division by drag values close to zero) and the resulting necessity to filter and smooth the  $C_L(t)/C_D(t)$ -signal before correlation.

Therefore, Figure 5.32 shows an alternative way to validate aerodynamic performance modifications without the risk to reach nearly infinity values (drag often close to zero). Instantaneous aerodynamic performance benefits are illustrated with green lines in Figure 5.32a and base on the force angle between the lift and the drag vector ( $\gamma(t)$ )  $\frac{1}{20}atan(\frac{C_D}{C_L})$  in [°]). The angle  $\gamma$  in Figure 5.32a is shown reduced by a factor of 20 for illustrative reasons and can vary (without the scaling) between  $-7^{\circ} \le \gamma \le +40^{\circ}$  within the total recording period. The force angle has benefits by showing continuous performance trends without the (previously mentioned) risk to move  $C_L/C_D$ -values to infinity. A measured force-angle of  $\gamma < 0$  represents a period of thrust instead of drag by pointing its resulting lift-drag vector in an upstream direction. As previously suggested in Figure 5.31, cases with large fluid-membrane coupling show tendencies of regular thrust generation (Figure 5.32a, lower). In addition, it is found that the force-angle method (Figure 5.31b) shows no noticeable differences in their correlation values to the previous  $C_L(t)/C_D(t)$ -consideration in Figure 5.31. As a result, it can be said that the initial filtering and smoothing of some close-to-infinity  $C_L(t)/C_D(t)$ -values does not significantly affect the resulting correlation values.

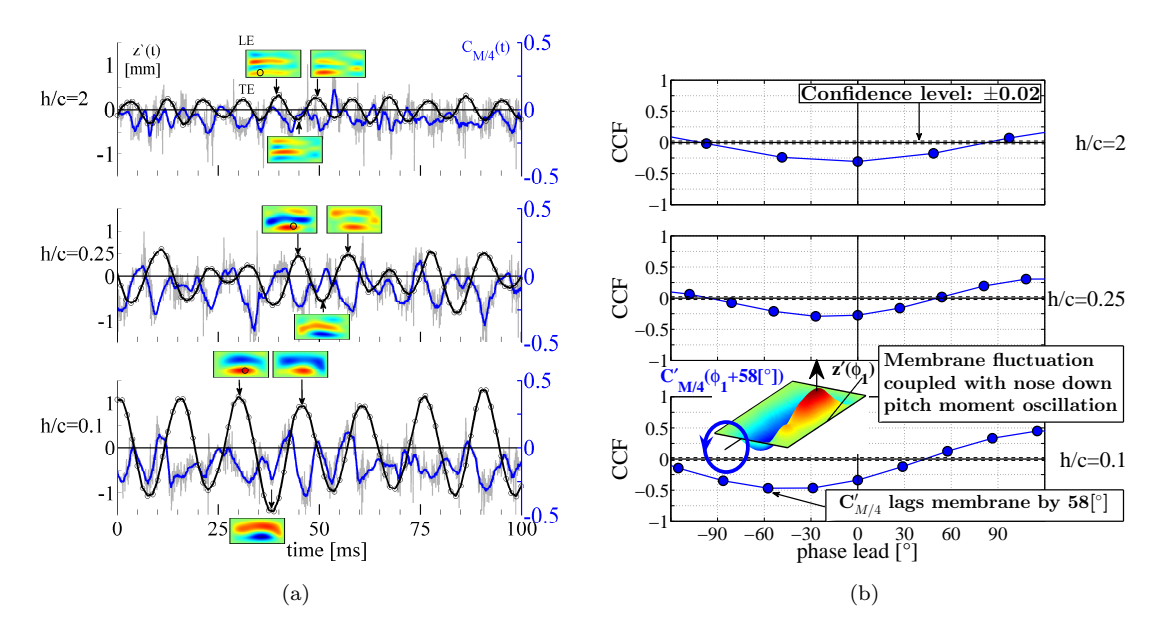


Figure 5.33: (a) Time series of  $C_{M/4}$  and instantaneous membrane deformation (z') for  $\alpha = 15^{\circ}$  at three different heights over ground. (b) Cross correlation between  $C_{M/4}$  and membrane deformation.

Figure 5.33 shows the correlation between the pitch-moment and membrane deformations. Figure 5.33a shows a time-series of the pitching moment  $C_{M/4}(t)$  (blue-line) and membrane vibrations z'(t) (black-line) for three different heights-over-ground (h/c = [2, 0.25, 0.1]) at an angle-of-attack of  $\alpha = 15^{\circ}$ . Figure 5.33b shows the cross-correlation between two time-series shown in Figure 5.33a.

At h/c = 0.1, the normalised cross-correlation value of -0.5 indicates that there is a relatively good match between membrane and pitching moment signal (Figure 5.33b). The nose-down pitching moment at the quarter-chord point  $(C_{M/4})$  lags the trailing-edge orientated positive membrane deflection +z' by 58° (as shown in the 3D-surface sketch in Figure 5.33b). For higher values of h/c, the correlation value reduces to -0.3, indicating a weaker but still negative correlation between membrane deformation and pitching moment. The lag also seems to reduce, becoming closer to zero with increasing h/c. However, the measurement uncertainty plays a role in this trend and the data for higher h/c, where the membrane vibrations are not large, is critical. It should be mentioned that flow/membrane induced pitch oscillations can play a major role for coupling and lock-in effects with roll oscillations of low aspect-ratio MAV systems (Tregidgo et al., 2012).

#### 5.5.2 Membrane-Flow

A recent study on batten-reinforced membrane wings correlated membrane dynamics with simultaneously recorded flow dynamics (Timpe et al., 2013). Vibrations at the trailing-edge of batten-reinforced membrane wings (Figure 2.1b) were shown to correlate well to the flow dynamics close to the trailing-edge. This result opens the question of how perimeter reinforced membrane wings couple with the flow dynamics.

The upper contour plots of Figure 5.34 show the cross-correlation, at zero time-lag, between the vertical membrane fluctuations at a listener point (M), placed 0.4c downstream of the leading-edge, and the vertical flow fluctuations (V') at listener points P1,P2,P3 for the streamwise (Figure 5.34a) and P3,P4,P6 for the cross-stream PIV-plane (Figure 5.34b). One representative case is selected for brevity at  $\alpha=15^{\circ}$  and h/c=0.1. Instantaneous membrane fluctuations are shown amplified by factor of 7 for clarity (Figure 5.34a). The lower line plots of Figure 5.34 show the normalised cross-correlation function (CCF) between the membrane and flow listener points.

Perimeter reinforced membrane wings show with CCF > 0.75 (Figure 5.34a, lower) similar flow-membrane coupling as found for batten-reinforced (BR) membrane wings (Timpe et al., 2013). However, perimeter-reinforced membrane wings show extended coupling due to the membrane vibrations occurring all along the chord length between leading- and trailing-edge (with two chordwise peaks), rather than only concentrating close to the unsupported trailing-edge. Therefore, a leading-edge localised upwards camber movement comes with a nearly instantaneous vertically upwards directed flow and vice versa (Figure 5.34a, lower). The vertically directed flow structures originate at the leading-edge and are shed due to the vertical motion of the membrane. Thus, perimeter reinforced membrane wings show strong correlations close to the leading-edge, initiating and promoting vortex-shedding from the beginning. The free-to-rotate membrane attachment likely helps the exploitation of coupling dynamics (Figure 3.5).

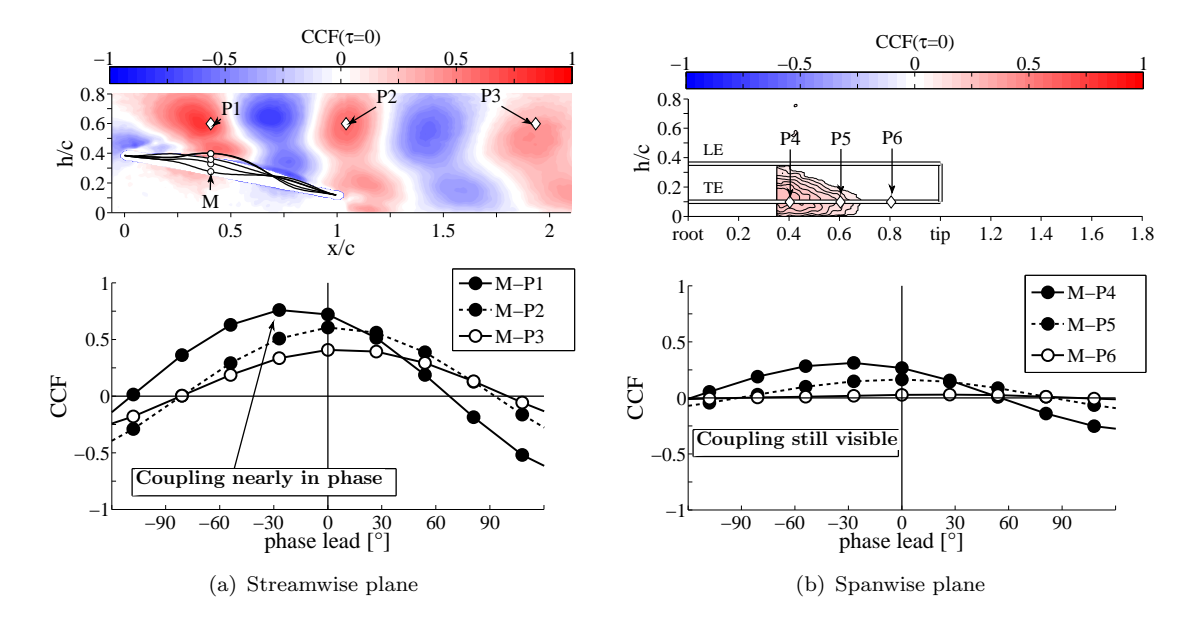


Figure 5.34: Cross-correlation (CCF) between vertical membrane fluctuations at point M (x/c = 0.4) and vertical flow fluctuation velocity (V') at listener point P. Instantaneous membrane fluctuations are shown amplified by factor of 7 for clarity. Correlations are conducted for the streamwise (a) and the spanwise (b) PIV-plane. Exemplary case is at  $\alpha = 15^{\circ}$  within extreme GE (h/c = 0.1).

Overall, the results suggest that constraining the trailing-edge of the membrane could provide more options for flow control. Further studies are required to understand the impact of chordwise vibration locations on flow interactions. It is important to mention that the vertical membrane fluctuations are often no more than 1% of the chord (roughly 1 mm) in peak regions (Figure 5.8) but can significantly influence the flow dynamics.

The relationship between the dynamics of the membrane oscillations and the vertical flow fluctuations one chord downstream the TE was also examined (Figure 5.34b). As previously discussed in Section 5.4.2, the spanwise position of the flow listener points (P4, P5, P6) appears crucial for the correlation quality of the LE-vortex and its shedding with the membrane (M). This correlation reaches a maximum of 0.45 for the flow listener point P4, located closest to the wing root.

The coupling between membrane and flow dynamics is found to change for different flow conditions, such as changes in angle-of-attack or height-over-ground. Figure 5.35 demonstrates this by moving a membrane wing at  $\alpha=25^{\circ}$  from free-flight (h/c=2) into GE conditions (h/c=0.25 and 0.1). The descent into the vicinity of the ground forces the flow to detach from the wing surface (Figure 5.35a, lower), resulting in a phase lead of the flow to the membrane with 60° phase-shift (Figure 5.35b, lower). Previously discussed force results show that this decoupling is accompanied with a loss in lift (Figure 5.3b, upper) and an increase in drag (Figure 5.3b, lower). Therefore, it is shown that direct (nearly lag-free) fluid-structure coupling of membrane wings, accompanied with lifting benefits, is only possible for specific flow conditions, at which

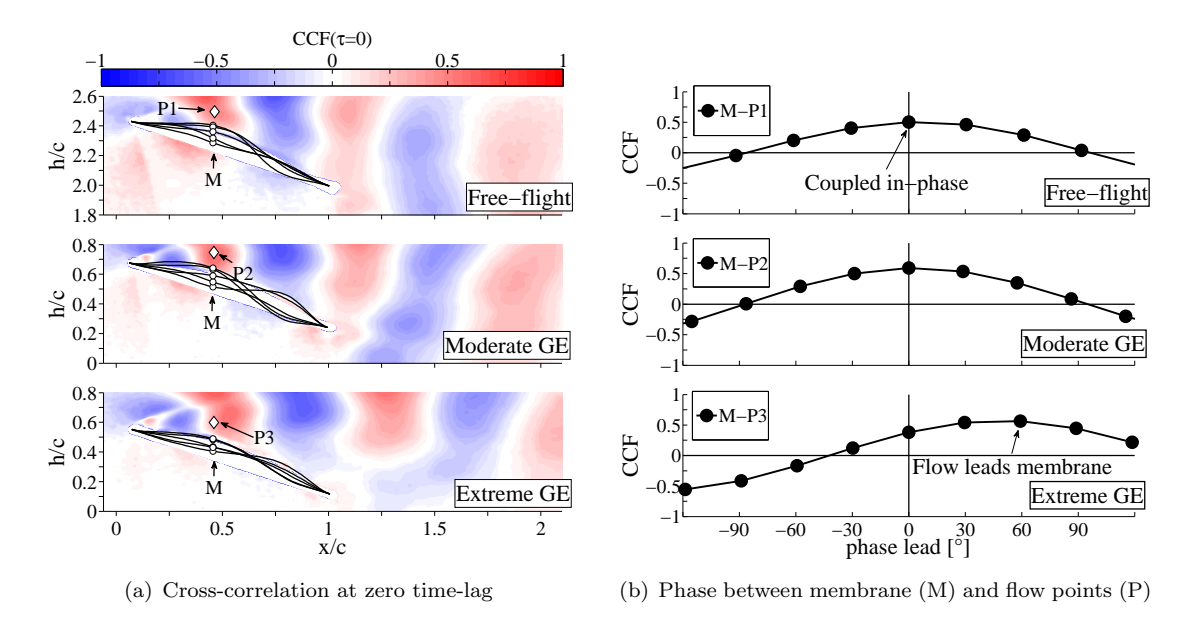


Figure 5.35: Cross-correlation (CCF) between vertical membrane fluctuation at point M (x/c=0.4) and vertical flow fluctuation velocity (V') at listener point ( $P_n$ ), changing with height-over-ground at a fixed angle  $\alpha = 25^{\circ}$ . The contour plots base on zero time lag. Instantaneous membrane fluctuations are shown amplified by factor of 7 for clarity.

the dominant eigen frequency of the membrane or its higher harmonics get close enough to the vortex-shedding frequency (for this study,  $\alpha=25^{\circ}$  for h/c=2 and  $\alpha=15^{\circ}$  for h/c=0.1 show this behaviour). Additionally, the adverse pressure gradient has to remain weak enough to enable close-to-surface energy transfer between the flow and the membrane surface. Ultimately, stimulated fluid-membrane coupling of membrane wings is found to result in enlarged performance windows compared with rigid flat-plate wings (Figure 5.4c).

#### 5.5.3 Load-Membrane-Flow

Figure 5.36 gives an extended overview into the coupling of aerodynamic loads, membrane oscillations and dynamic flow structures, measured at  $\alpha=15^{\circ}$  in extreme GE of h/c=0.1. Figure 5.36a shows free-stream normalised vertical flow fluctuations  $V'(t)/U_{\infty}$  for three snapshots (t1, t2, t3) over one membrane oscillation cycle at a Strouhal number of St=0.74. Also shown are streamlines computed from low-pass filtered velocity fields (using the first five POD modes). Finally, instantaneous membrane cross-sections (at the quarter-span PIV-plane) are illustrated by overlaying the time-averaged membrane shape (dotted-line) with the membrane fluctuation (where the fluctuation is amplified by a factor of 7 in order to display the vertical displacement of the membrane better.

At time-step  $t_1$  (Figure 5.36a, upper), the instantaneous positive vertical velocity close to the leading edge (red) appears to be accompanied with upward membrane deformation.

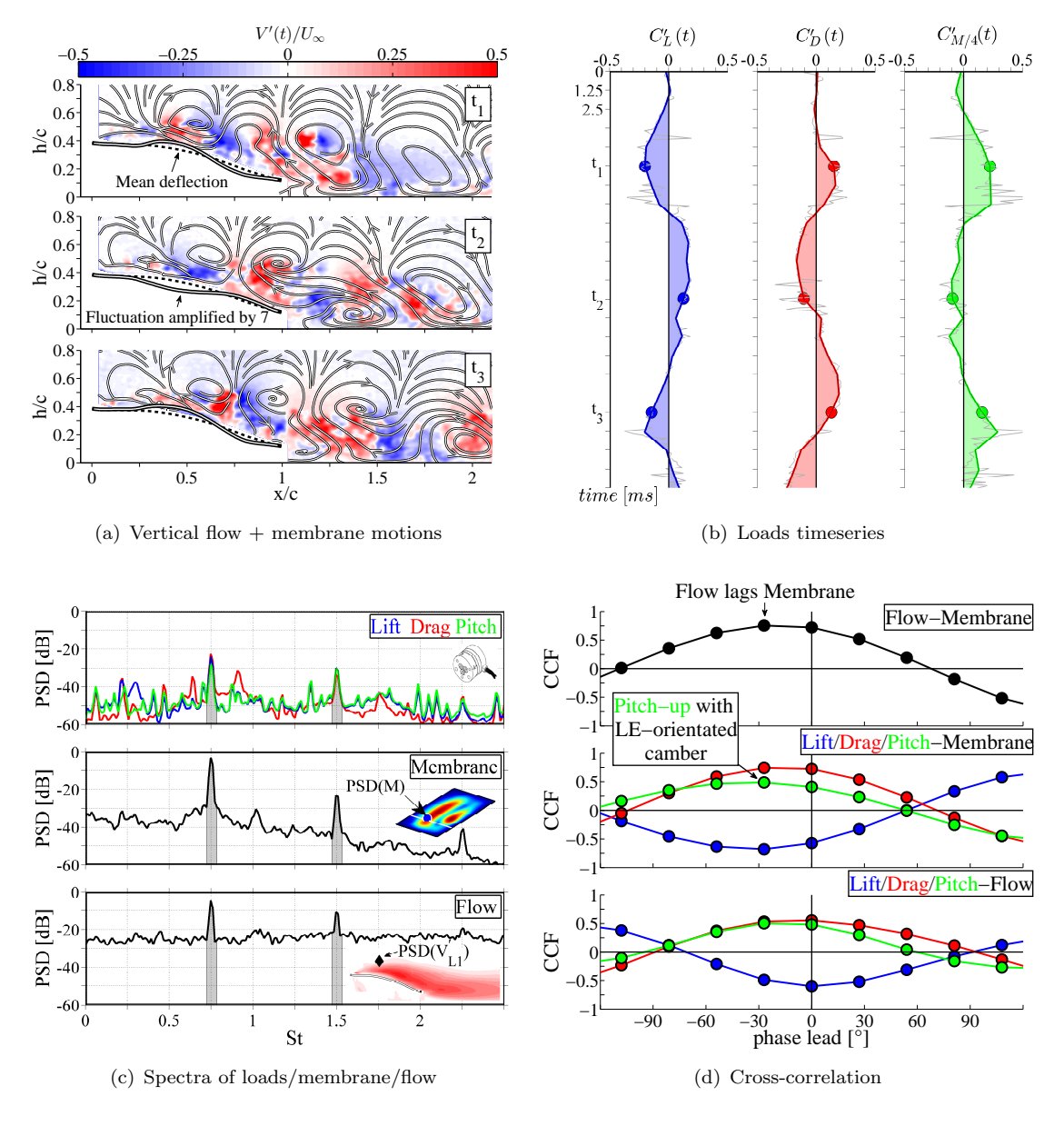


Figure 5.36: Load-membrane-flow interactions at  $\alpha=15^\circ$  in extreme GE of h/c=0.1. (a) Time-snapshots  $(t1,\ t2,\ t3)$  for vertical flow and membrane fluctuations during one cycle. Streamlines based on POD-filtered flow fluctuations. (b) Time-corresponding development in lift, drag and pitch moment fluctuations. (c) Spectral signature of load-membrane-flow dynamics and their (d) phase-relation between each other. Membrane dynamics show strong coupling with LE-vortex-shedding, allowing improvements in overall wing performance.

Half a membrane cycle further in time (Figure 5.36a, mid), the rolling down vortex structure has travelled down to the trailing-edge (core at x/c = 1) and results in an upwards deformation of the membrane close to the trailing-edge. This cycle repeats at time-step  $t_3$  (Figure 5.36a, lower), where the situation is the similar to that of time-step  $t_1$ .

Dynamics in flow/membrane oscillations are also transferred into aerodynamic load fluctuations, which are shown in Figure 5.36b. At time step  $t_1$ , the wing shows reduced total lift (blue-shaded), increased drag (red-shaded) and a pitch-up moment (green-shaded). This relation flips at a later stage  $t_2$ , showing gain in lift, decrease in drag and increasing pitch-down moment.

Figure 5.36c compares the spectra of all three load components, membrane deformation (at 40%-chord from leading-edge) and vertical velocity fluctuation (at listener point L1 as shown in the figure). The spectra reveals that the membrane motions, loads and flow are clearly linked. The membrane (Figure 5.36c, mid) exhibits dominant oscillation frequencies of St = 0.74 (1st harmonic), St = 1.48 (2nd harmonic) and St = 2.22 (3rd harmonic). The two most energetic membrane frequencies are also detected in the loads and the flow spectra, suggesting strong coupling of membrane dynamics with the flow and loads. The most dominant membrane oscillation frequency of St = 0.74 is significantly different from the typical natural shedding frequencies of (flat/cambered) rigid wings which is around St = 0.4 to 0.5 for the given case (Figure 5.23).

The cross-correlation between the flow and the membrane (Figure 5.36d, upper), the loads and the membrane (Figure 5.36d, mid) and the loads and the flow (Figure 5.36d, lower) underlines strong coupling between each other. The aerodynamic coefficients show a slight delay to membrane motions with a phase shift of  $\sim 30^{\circ}$ . This phase-shift is likely caused by membrane inertia effects, however, further studies are required to examine this in more detail.

Direct flow-to-membrane coupling can not only be initiated by moderate angles-of-attack ( $\alpha = 15^{\circ}$ ) in liaison with ground-effect (h/c = 0.1, Figure 5.36), but also in free-flight with high angles-of-attack (Figure 5.37).

Therefore, ground-effect acts only as a flow modifying parameter, and its results can also be accomplished with an increase in angle-of-attack in free-flight conditions, allowing to couple/decouple membranes-flow dynamics. Both options rely on *LE*-vortex shedding close to the membrane's upper surface, encouraging lift enhancing dynamics by entraining fluid to promote flow re-attachment in areas affected by adverse pressure gradient. However, ground-effect dynamics (Figure 5.36) show generally lower strength in comparison to free-flight dynamics (Figure 5.37), suggesting the increased importance of the lower (static) wing side in the vicinity of the ground, reducing the importance and the significance of flow dynamics occurring on the upper side of the wing. Therefore,

the flexibility of membrane wings can only be fully exploited outside of ground-effect conditions.

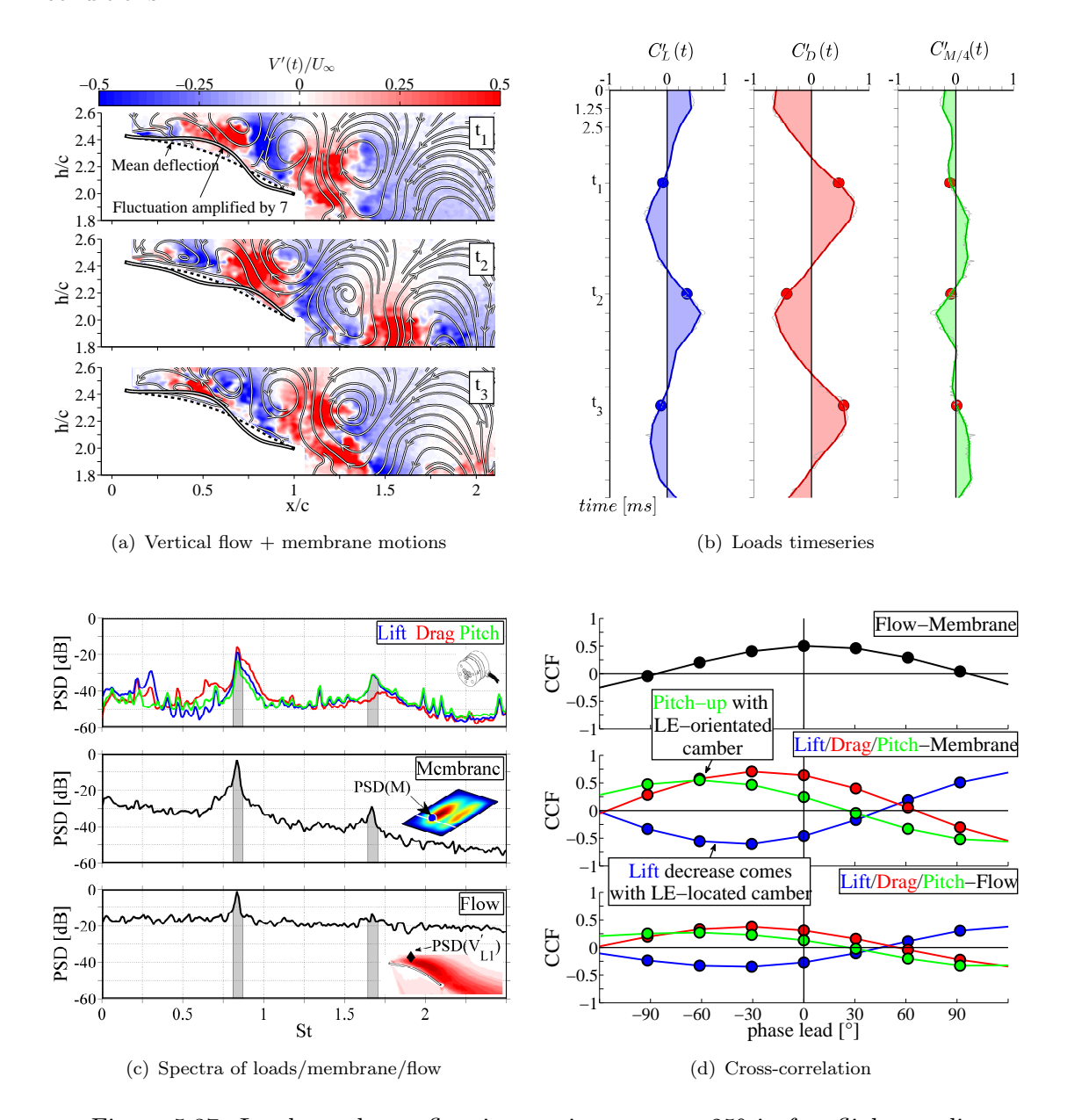


Figure 5.37: Load-membrane-flow interactions at  $\alpha=25^\circ$  in free-flight conditions of h/c=2. (a) Time-snapshots  $(t1,\,t2,\,t3)$  for vertical flow and membrane fluctuations during one cycle. Streamlines based on POD-filtered flow fluctuations. (b) Time-corresponding development in lift, drag and pitch moment fluctuations. (c) Spectral signature of load-membrane-flow dynamics and their (d) phaseal relation between each other. Membrane dynamics show strong coupling with LE-vortex-shedding, allowing improvements in overall wing performance. A video is available via: https://youtu.be/728DsVxNcL4

Fluid-membrane coupling has its limitations since lag-free coupling can not always been ensured. The descent from (highly coupled) free-flight conditions at  $\alpha=25^{\circ}$  into extreme GE (h/c=0.1) forces the flow to detach from the wing surface (Figure 5.38a).

As a result, the coupling between membrane dynamics and the flow reduces and results in a phase shift which is accompanied with declining correlation to load dynamics (Figure 5.38d, lower). The low correlation value and increasing phase-difference in load-to-membrane coupling reflects the low coherence in both signals, underlining a degrading overall wing performance (Figure 5.4b). It is important to mention that vortex-shedding, which appears vertically detached from the wing surface, remains still modified from the membrane eigen frequencies (Figure 5.38c, lower). This reflects the ability of flexible membrane wings to imprint their vibration frequencies further in to the flow.

For illustration, a video is available which shows load-membrane-flow interactions for an exemplary case at  $\alpha = 25^{\circ}$  in free-flight conditions: https://youtu.be/728DsVxNcL4

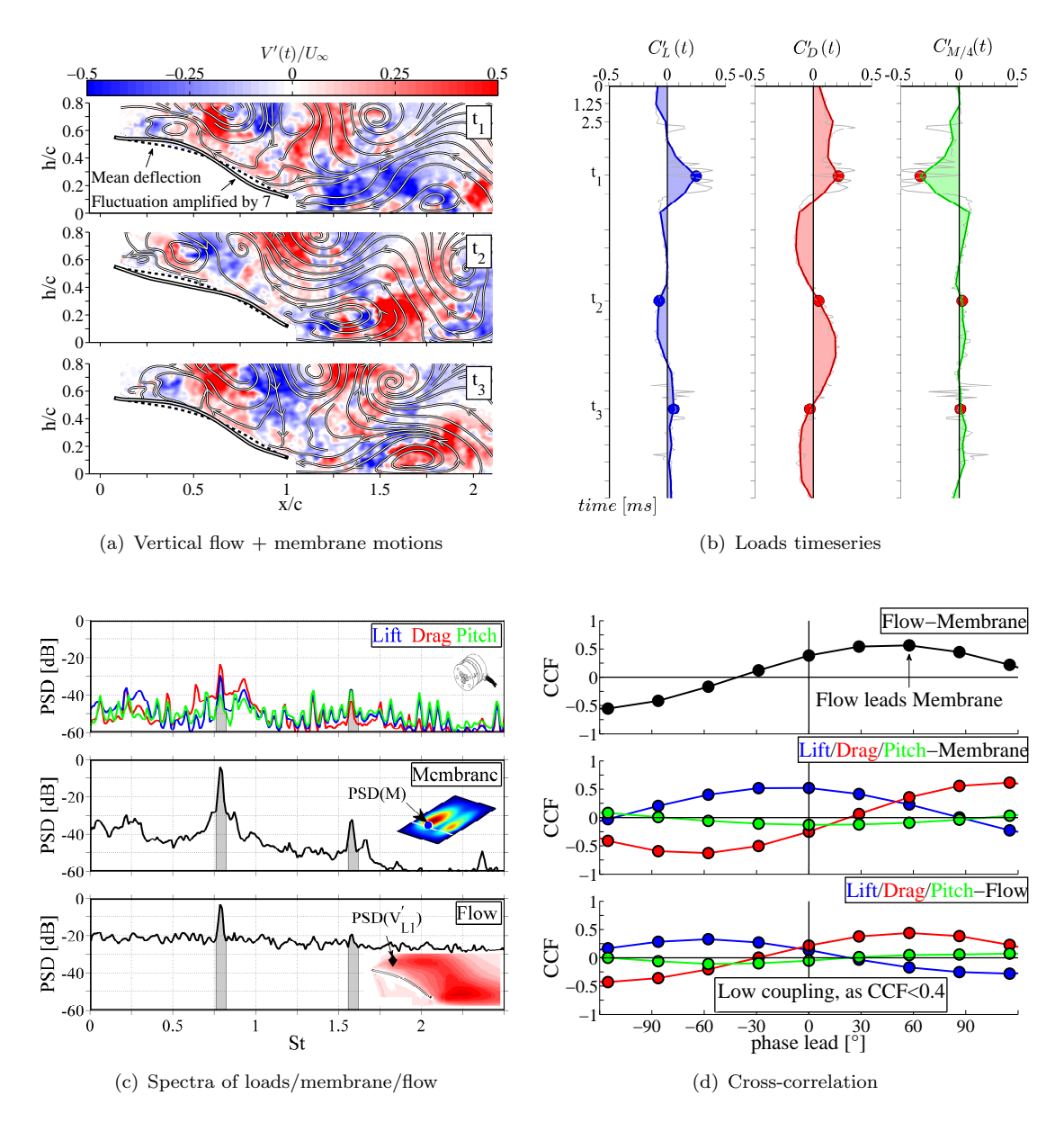


Figure 5.38: Load-membrane-flow interactions at  $\alpha=25^\circ$  in extreme GE of h/c=0.1. (a) Time-snapshots (t1, t2, t3) for vertical flow and membrane fluctuations during one cycle. Streamlines based on POD-filtered flow fluctuations. (b) Time-corresponding development in lift, drag and pitch moment fluctuations. (c) Spectral signature of load-membrane-flow dynamics and their (d) phaseal relation between each other. With the descent into GE, flow and membrane dynamics get out of phase. The overall correlations reduces drastically, resulting in reduced coupling between lift, membrane and flow dynamics.

## 5.5.4 Cycle-averaging

In this study, PIV measurements were carried out in one chordwise plane and one cross-stream plane. These measurements were conducted independently, however, were always accompanied with simultaneous DIC and load measurements. Membrane dynamics can be used as a reference to cycle-average both streamwise and cross-stream PIV planes. The membrane signal was specifically selected, providing the signal with the highest signal-to-noise ratio in comparison to load-cell and PIV acquisition. Similar techniques were previously conducted in other FSI-studies, involving flapping wings with multiple spanwise PIV-planes which were cycle averaged by the flapping motions of the wing (Suryadi et al., 2010). The average comprises of over 350 individual cycles during the (DIC, PIV) recording period of 6.25 s and measures 13 phase points per cycle.

Figure 5.39 shows cycle-averaged loads (Figure 5.39, left) and corresponding flow dynamics of both streamwise and cross-stream PIV measurement planes (Figure 5.39, right), which are computed by membrane oscillation of the same phase. The highlycoupled case at  $\alpha = 15^{\circ}$  in extreme GE h/c = 0.1 is shown for brevity (Figure 5.39). The cycle averaged loads show lift, drag and pitch moment fluctuations which are normalised such that the peak value is 1 (outer edges of shaded regions). In addition, the loads are shown averaged between both PIV experiments (mean line within shading). Vertical velocity fluctuations are shown with 60°-phase steps and are low-pass filtered using the first five POD-modes. Vertical upwards motions of the membrane and the flow-field is coloured in red, whereas downwards motions are shown in blue. Coherent LE-vortices are shed and convect downstream over the wing surface into the wake. LE-vortices are known to extend across the span and will only be spatial limited by the tip-vortices (Section 5.4.2). This assumption is supported by the literature (Gordnier and Attar, 2014), allowing us to correlate the vertical flow oscillations in both PIV planes at the listener point L1. The flow listener point L1 is placed in the streamwise plane at  $L1_{xy} = (chord, height, span) = (2, 0.2, -0.5)$  and the spanwise plane at  $L1_{zy} = (2, 0.2, 0.5)$ , resulting in a spatial separation of the points of one chord length in span.

Figure 5.39 shows at the beginning of the cycle at  $0^{\circ} \leq Phase \leq 60^{\circ}$  an instantaneous upwards velocity fluctuation (red) at the listener point L1 which correlates well between both PIV-planes and is accompanied with low lift, high drag and a pitch-up moment. The streamwise convection of LE-vortex structures to  $120^{\circ} \leq Phase \leq 240^{\circ}$  results into a downwards facing flow velocity (blue) at the listener points L1 for both PIV-planes which comes with increasing lift, reduced drag and inclining pitch-down moment. The results reveal the strong footprint of membrane oscillations in the flow which are detected and correlated even one chord downstream of the trailing-edge. An illustrative video is available via: https://youtu.be/KA6BZrtAb3o. In addition, the cycleaveraging of both PIV planes allows to extend the knowledge in LE-vortex-shedding

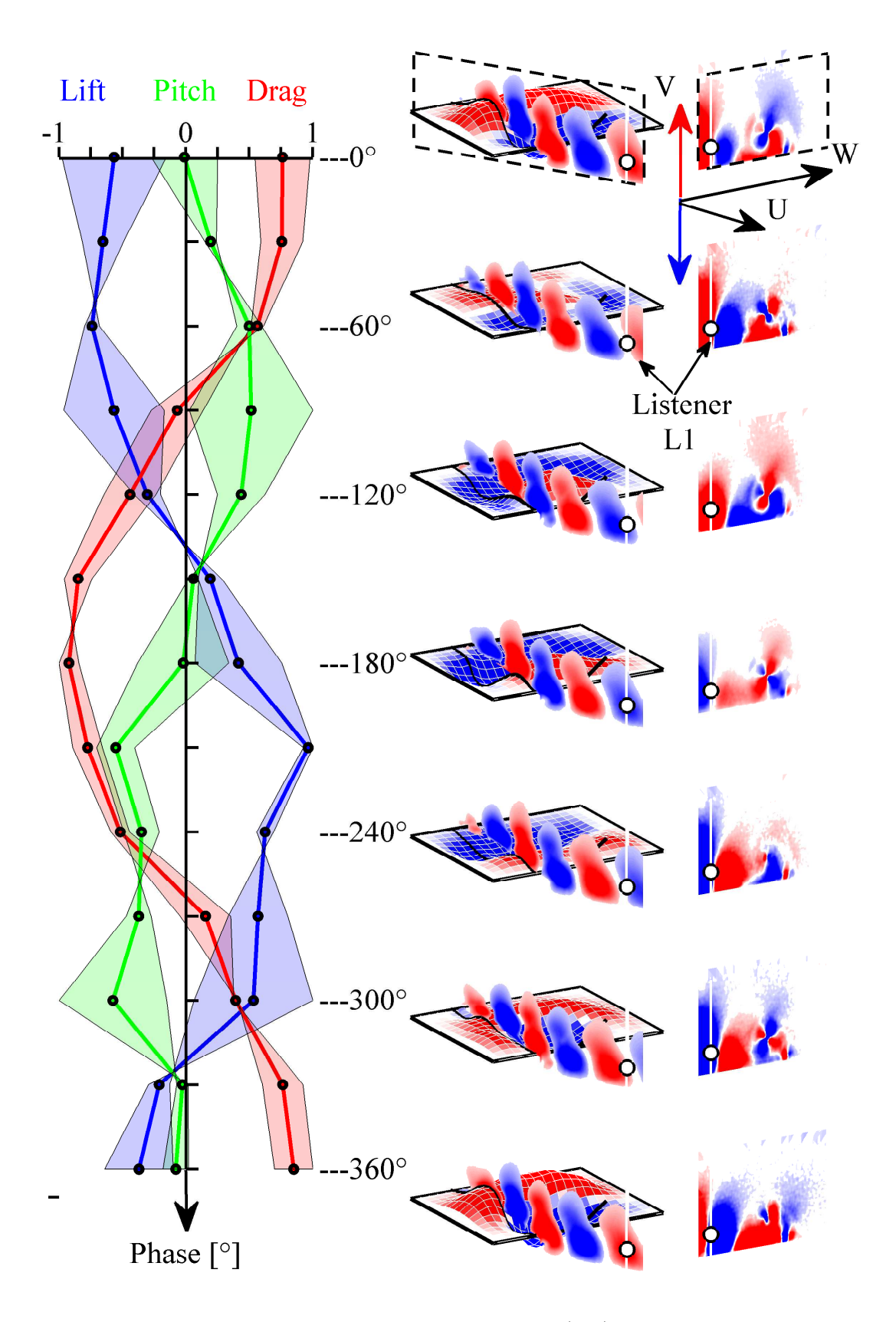


Figure 5.39: Membrane based cycle-averaged load (left) and vertical flow dynamics from both streamwise/spanwise PIV experiments (right), illustrated for h/c=0.1 and  $\alpha=15$ °. Vertical membrane and flow fluctuations are colored red for upwards and blue for downwards motions. A flow listener point L1 is placed in both PIV-planes for later tracking in Figure 5.40. A video is available via: https://youtu.be/KA6BZrtAb3o

along the span, providing a suitable option to conduct quasi-volumetric FSI-studies on flexible wings by exploiting the coherence of membrane oscillations as driving reference. Thus, quasi-volumetric flow-membrane interactions can be investigated without the need of Tomographic-PIV, which is known for its constrains in sufficient lighting and measurement depth (typical 10 mm, up to 100 mm as shown in Fukuchi (2012)).

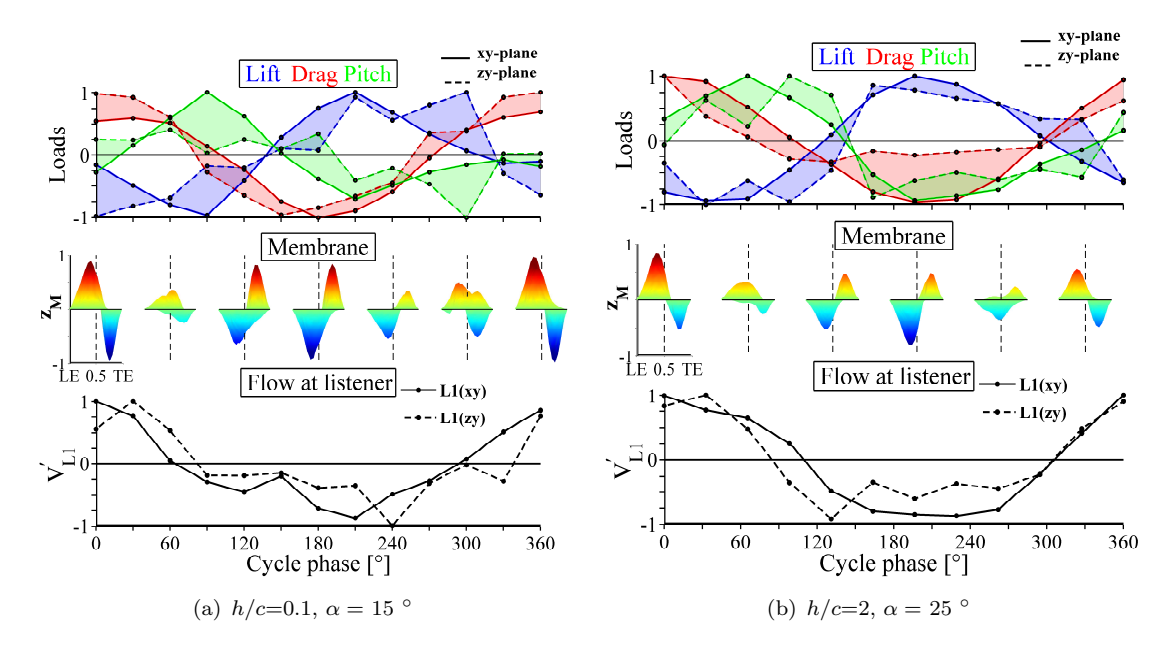


Figure 5.40: Membrane based cycle-averaged loads and flow dynamics at listener point L1 for either GE (plot (a), h/c = 0.1 at  $\alpha = 15^{\circ}$ ) or high angles-of-attack induced coupling (plot (b), h/c = 2 at  $\alpha = 25^{\circ}$ ).

Figure 5.40 shows cycle-averaged results of similar coupling scenarios, involving ground-effect (Figure 5.40a, see also Figure 5.39) as well as high angle-of-attack induced coupling (Figure 5.40b). The flow listener point for Figure 5.40b is defined as  $L1_{xy} = (2, 1.8, -0.5)$  (streamwise-plane) and  $L1_{zy} = (2, 1.8, 0.5)$  (spanwise-plane). Similar to Figure 5.39, all vertical-axis of either load, membrane and flow cycles are normalised such that the peak value is 1. Both streamwise (L1(xy)) and spanwise (L1(zy)) PIV-planes show comparable phase in vertical flow dynamics  $V'_{L1}$  at the listener point L1 (Figure 5.40, lower). In addition, the comparison of both GE (Figure 5.40a) and high angle-of-attack induced fluid-structure coupling (Figure 5.40b) underlines the similarity in their coupling conditions, suggesting GE as a pure flow modifying parameter which allows similar fluid-structure coupling as seen for free-flight conditions. The only difference relates to changing angles-of-attack which are necessary to trigger LE-vortex separation for different heights-over-ground. The ability to adapt to ground-effect related flow changes makes membrane wings a preferable option for high-performance WIG-MAVs.

## Chapter 6

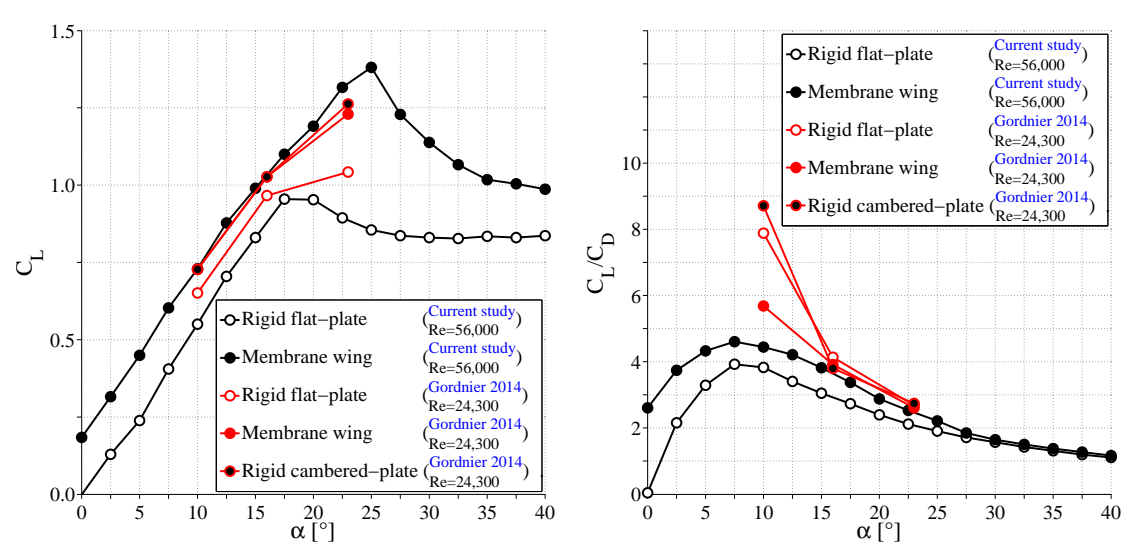
## Discussion and Recommendations

In a first experiment, moderate Reynolds number wind tunnel measurements were conducted at Re=67,500 using rectangular rigid flat-plate and membrane wings and a detailed investigation on the effects of aspect-ratio  $(AR-1,\ 1.5\ \text{and}\ 2)$  on the aerodynamic loads as well as membrane deformations was examined with high-speed recordings. Moderate Reynolds number related performance limitations of both rigid flat-plate and membrane wings lead to a second experiment to investigate their additional performance potential within ground-effect conditions. Therefore, the second experiment examines the influence of ground-effect on the aeromechanics of membrane and rigid flat-plate wings at Re=56,000 at a fixed aspect-ratio of AR-2. Time-synchronised high-speed recordings of load, membrane and flow dynamics are used to examine the coupling characteristics of flexible membrane wings not only in but also out of ground-effect conditions.

In the following sections, membrane wing results are discussed concerning their aerodynamic importance, opportunities due to fluid-structure coupling, pitch-stability modifications, impact of aspect-ratio and their usage in ground-effect conditions. Finally, research recommendations are given for future investigations.

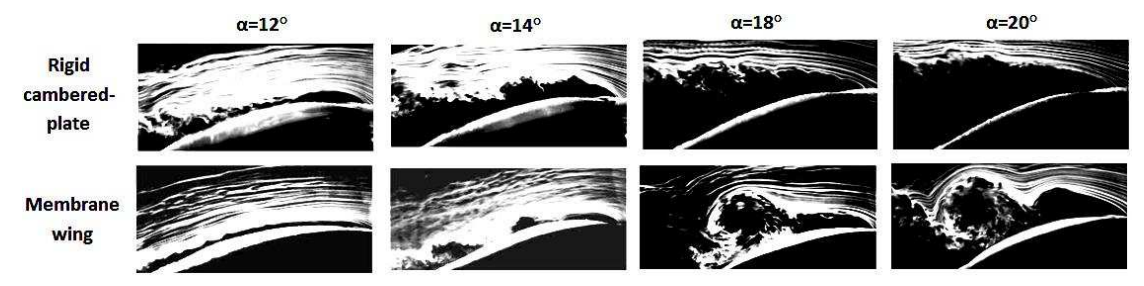
### 6.1 Static Camber and Wing Dynamic

The current study investigated the aerodynamics of rigid-flat plates and compared them with flexible membrane wings. However, membrane wings involve a static camber increase with inclining angle-of-attack and come with additional membrane oscillations relative to their static inflated wing camber. As a result, both individual parameters (mean-camber and oscillations) contribute to the aerodynamic performance modifications seen with flexible membrane wings over rigid flat-plates. Figure 6.1 tries to address and separate the individual aerodynamic impact of static membrane cambering and



(a) Lift performance: The lifting capability is predominantly driven by the mean camber. However, membrane vibrations help to gain additional lift in stall conditions.

(b) Aerodynamic efficiency: Lift encouraging vortical structures of membrane wings come with an equal or even higher increase in drag, which can even compensate cambering related gains in aerodynamic efficiency.



(c) Smoke-flow visualisation, extracted from Rojratsirikul et al. (2009), comparing a membrane wing with a similarly shaped rigid cambered-plate. Pure static cambering can be seen to retain flow attachment (and so performance) up to a certain point of angle-of-attack, where the flow detaches ( $\alpha \ge 14^{\circ}$ ). Beyond that point, membrane wings show further lift enhancement and drag increase due to vortical flow structures placed close to the wing surface.

Figure 6.1: Seperation between aerodynamic impact of static wing cambering and dynamic membrane oscillations. Comparison of (a) lift, (b) aerodynamic efficiency and (c) flow characteristics between a rigid flat-plate wing, a membrane wing and a rigid cambered-plate with the same membrane mean shape (current study combined with results of Gordnier and Attar (2014) and Rojratsirikul et al. (2009)).

membrane oscillations to integrate the results of this (flat-plate and membrane wing) study into the wider literature (Rojratsirikul et al., 2009; Gordnier and Attar, 2014).

Figure 6.1a shows the lift production of rigid-flat plates and membrane wings of the current study (black lines) in reference to rigid-flat-plates, rigid cambered-plates (based on membrane mean) and membrane wings (extracted from Gordnier and Attar (2014)). Despite different Reynolds numbers, the lift values are found to match well between the reference and the current study, reflecting a low Reynolds number dependency of the results. In addition, both studies show a gain in lift production of membrane wings to rigid flat-plates. However, rigid cambered-plates and membrane wings show comparable

lifting benefits to rigid-flat-plates at low to moderate angles-of-attack ( $\alpha \leq 15^{\circ}$ ). Their comparability is also reflected by similar (attached) flow conditions (see Figure 6.1c for  $\alpha = 12^{\circ}$ ). Therefore, the lifting capability (for  $\alpha \leq 15^{\circ}$ ) is shown (by Gordnier and Attar (2014)) to be predominantly driven by the static mean camber. At even higher angles-of-attack ( $\alpha > 15^{\circ}$ ), membrane wings show additional lift production to rigid (membrane mean) cambered plates due to encouraged (low-pressure) vortex-shedding happening close to the upper wing surface. Figure 6.1c shows between  $\alpha = 18^{\circ}$  and  $20^{\circ}$  clearly formed vortical shedding structures which only form in the presence of membrane wing dynamics. Those findings leave the question if the reduced wing vibrations for angles  $\alpha \leq 15^{\circ}$  (related to reduced LE vortex-shedding) are responsible for the lack of additional lift production and if actively enhanced membrane dynamics, which are not driven by vortex-shedding, could be used to enhance the overall lift performance at low to moderate angles-of-attack (e.g. with recently developed electro-active membrane wings of Buoso and Palacios (2016); Curet et al. (2014)).

Figure 6.1b shows the impact of static cambering and membrane oscillations on the aerodynamic efficiency. Generally, the aerodynamic efficiency is found to collapse for  $\alpha \geq 25^{\circ}$  for all wings. Within this post-stall region, the aerodynamic efficiency becomes independent on static cambering or any wing oscillations and the wings start to behave like a bluff body (consistent with Timpe et al. (2013)). For low to moderate angles-of-attack of  $\alpha \leq 25^{\circ}$ , results of Gordnier and Attar (2014) suggest that lift encouraging vortical structures of membrane wings are accompanied with significant drag penalties, which can be so severe that the drag penalties can even compensate (static) cambering related gains in aerodynamic efficiency (Figure 6.1b). As a result, next to the superior results for the rigid cambered-plate, even rigid-flat plates may involve higher aerodynamic efficiencies than membrane wings. However, the results are not universal and can not be confirmed with the results of the current study, showing generally (small) aerodynamic efficiency benefits of membrane wings over rigid flat-plates. Even a very recent study (Zhang et al., 2015) on batten-reinforced membrane and rigid (mean cambered) wings shows no clear indication whether membrane oscillations are of major benefit or drawback for the aerodynamic efficiency (efficiency margin are small, if they are available at all).

Ultimately, within close-to-stall conditions, membrane wing oscillations seem to act like a tool to exploit separated flow conditions by forming coherent shedding structure of lift producing nature. However, this type of lift production comes with strong drag penalties, limiting any aerodynamic efficiency gain. At low and moderate angles, membrane wings seem to be replaceable with cambered plates. The story could change with the ability to actively encourage membrane dynamics with electroactive membrane wings at low to moderate angles-of-attack.

#### 6.2 Fluid-Structure Coupling

As previously illustrated, membrane wings benefit not only from static wing cambering but can also exploit stall related vortex shedding for additional lift production. It is important to address the impact of membrane dynamics within close-to-stall conditions. An exemplary rigid flat plate at  $\alpha=15^{\circ}$  shows similar (shedding) flow dynamics as a membrane wing at  $\alpha=25^{\circ}$ . However, the membrane wing produces 50 % more lift than the rigid flat-plate wing due to (static camber + membrane motion) promoted flow attachment into higher angles-of-attack, causing ultimately a stronger downwards diverted flow to benefit overall lifting performance.

The perimeter reinforced membrane wing type (membrane constrained at LE/TE and both wing tips) is found to benefit specifically from its leading and trailing-edge constraints as these boundary conditions enable motions along the entire chord that enhance flow-membrane interaction. Additionally, membrane dynamics with large amplitudes appear close to the leading-edge, promoting the growth of leading-edge vortices and so their importance to the coupling dynamics. In contrast, other membrane wing types such as batten-reinforced membrane wings exhibit limited flow-structure coupling since the interaction is mostly localised near the free trailing-edge. Enhancing membrane-flow coupling along the entire chord is found to play a major role in improved lift performance in close-to-stall conditions.

For passive membrane wings, considered in this study, leading-edge vortex-shedding is necessary to drive and couple the membrane with the flow dynamics. The necessary shedding structures are typical triggered by high angles-of-attack in free-flight conditions. As a result, membrane motions can be strongly coupled and oscillate in-phase with the vertical flow motions. An exemplary instantaneous (low-pressure) vortex-structure placed close to the trailing-edge causes a rearward location of maximum camber which correlates to improvements in lift and drag reduction. The aerodynamic loads appear slightly delayed to the membrane dynamics, suggesting membrane inertia as possible reason.

Under extreme conditions with growing adverse pressure gradients, such as post-stall angles-of-attack, the phase difference between the flow and membrane increases signally an end to the direct flow-membrane coupling. Even under this extreme conditions, the dynamics of membrane motions can retain the development of leading-edge vortex-shedding, but the structures appear lifted up vertically from the membrane surface due to the strong adverse pressure gradient. This behaviour is rather different to rigid flat-plate wings which show a downstream movement of the shedding structures towards the trailing-edge and static recirculation zone on top of the wing surface, resulting in a sharp loss in their aerodynamic performance. Ultimately, the relatively static behaving recirculation bubble of rigid wings is suggested to be triggered from membrane oscillations to form sequential shedding structures of (lift) carrying low pressure content.

POD analysis is successfully applied on membrane and flow dynamics, allowing to group major and minor membrane/flow structures and enabling to filter important dynamics. In the vicinity of strong flow separation, most of the membrane vibration energy is concentrated in the first two POD modes ( $\geq 80\%$ ) of strongly chordwise oriented membrane fluctuations. At the same time, predominant leading-edge vortex-shedding can be well described by the first two to five POD modes, capturing  $\geq 30\%$  in total energy of the flow dynamics.

#### 6.3 Pitch Stability

The study reveals membrane wings high sensitivity of the pitch moment to changes in their chordwise position of maximum camber. At low and moderate angles-of-attack, membrane wings push the chordwise location of their maximum (static) camber towards the trailing-edge, resulting in a higher initial negative pitch-slope and a higher nosedown pitch moment (in comparison to rigid flat-plates). However, this behaviour could probably also be achieved with simple rigid cambered-plates. With inclining angles-of-attack, the chordwise location of maximum camber moves towards the leading-edge and results into a horizontal pitch moment slope which is similar to rigid flat-plates.

Membrane wings are found to show strong pitch moment oscillations around zero angle-of-attack (bi-stable snap-through region) and in stall conditions (shedding related dynamics). The oscillation amplitudes in pitch can be so severe that they can change their signs within the time-series. The pitch dynamics can be amplified by in-phase fluid-membrane coupling, showing resonance conditions with a nose-down pitch moment for a time-instant rearward located peak-camber and a pitch-up moment for a forward located peak-camber. However the typical resonance frequencies of > 50 Hz are probably to high to resonate MAV systems with membrane wings into (unwanted) pitch motions.

### 6.4 Effects of Aspect-Ratio

Low-aspect-ratio (LAR) wings allow independent of flat plates or membrane wings superior performance at high-angles-of attack. However, membrane wings are found to benefit from their static cambering to such an extend that their maximum lift coefficient can be extended by 31% at AR-1 and 60% at AR-2. The smaller gain for AR-1 seems to be driven by an increased downwash which reduces the wing camber. The use of membrane wings extend the maximum power efficiency by 16% for AR-1 and 33% at AR-2.

Higher aspect ratio membrane wings show inclining deformations along the span whereas lower aspect ratios exhibit a U-shape deflection. This finding could be related to a

modification of the tip vortex and its footprint, however further flow visualisation is needed for validation.

LAR wings suppress stall wherefore membrane motions are still driven by tensioning of the membrane with inclining incidence. This results in higher mode shapes and frequencies. Higher aspect-ratios are already exposed to stall conditions and excited from vortex shedding into low mode shapes and frequencies. However, this does not have to be a drawback and low order mode shapes could be used to couple with vortical shedding structures for improved lifting characteristics in stall conditions without the need for lift (and drag) encouraging tip-vortices.

#### 6.5 Ground-Effect

Both flat-plates and membrane wings show superior lift generation in ground-effect, while maintaining low drag at low to moderate angles-of-attack of  $2.5^{\circ} \le \alpha \le 7.5^{\circ}$ . Flow stagnation between the ground and the wing causes tip-vortex push-out, resulting in an increase in aerodynamic efficiency of up to 50% for heights measuring 10% in chord length from the trailing-edge to the ground and more than 100% for a height of 1% chord.

Ground-effect is found to modify the lift increment  $\Delta C_L$  differently for flat-plate and membrane wings, allowing uncambered flat-plate wings to benefit to a larger extent in their lift gain at low angles-of-attack. As a result, close to the ground (height at 1–5% chord), flat-plates show a slightly better aerodynamic performance at low incidences of  $\alpha \sim 2.5^{\circ}$ .

Nevertheless, in comparison to flat-plates, membrane wings show up to 30% increase in aerodynamic efficiency at larger angles-of-attack of  $\alpha \geq 7.5^{\circ}$  and heights of 1–10% chord length over ground. Flow enforced static shape-adaptability and dynamic membrane oscillations become an advantage when membrane wings are used in ground-effect, where the descent in height forces premature flow separation, accompanied with an early onset of leading-edge vortex-shedding and drag increase. Dynamic motions of membrane wings help to promote and use such vortex-shedding dynamics to maintain lift enhancing shedding structures close above the wing surface. The growing influence of leading-edge vortex-shedding in ground-effect is found to drop membrane mode shapes in a similar way as known for increased angle-of-attack from high-altitude studies. Flow-membrane coupling can be engaged with a membrane eigen frequency which is close to the vortex-shedding frequency of the flow. The exploitation of the dynamics of flexible wings is reduced within ground-effect, because the influence of the lower (more static) surface of the wing grows with respect to that of the upper surface (with more flow dynamics).

Ultimately, membrane wings ability to static camber with the incoming flow is found to improve the overall performance to rigid flat-plate MAVs at low to moderate angles-of-attack. However, similar gains could probably be achieved with rigid cambered-plates. Nevertheless, membrane wing oscillations offer the ability to couple with separated flow conditions (either high angle-of-attack or ground-effect induced) and encourage vortical shedding structures of (lift-encouraging) low pressure content to stay close to the upper wing surface.

#### 6.6 Recommendations

High-speed stereo-PIV measurement in the spanwise plane allows to extrude planar information into a 3D-volume. Planar PIV snapshots could be placed behind each other with a spacing based on the convecting freestream distance. The approach holds by assuming a fully developed vortex moving downstream of the trailing-edge and exhibiting no decay. The technique would help to visualise volumetric interaction of LE-vortex-shedding. A preliminary video is available via: <a href="https://youtu.be/Lo41Dg7nISM">https://youtu.be/Lo41Dg7nISM</a>, showing vortex shedding structures via the Q-criteria which are color coded with the vertical velocity fluctuations (red = upwards, blue = downwards).

It was shown that POD works as a powerful decomposition tool for grouping and visualising most energetic coherent flow structures. The usage of dynamic mode decomposition (DMD) could be a further step in grouping flow structures in a frequency rather than spatial space. A comparison between POD and DMD approaches could be conducted, proofing individual system benefits and drawbacks. A good overview about this topic can be found in (Bistrian and Navon, 2014).

It was shown that coupling between the flow and the membrane can only occur for a small range in close-to-stall conditions. In addition, the selection of the membrane material, wing shape and Reynolds number fixes the resulting coupling dynamics of passive membrane wings. Mechanical or electro-active cambering systems could extend and customise beneficial membrane motions on demand. Mechanical systems could involve to roll the membrane around the trailing-edge for static camber generation and around the leading-edge for dynamic oscillations. Electro-active wings could combine both static and dynamic cambering within one system.

Ultimately, a gain in aerodynamic performance has to be linked with an increase in lift and reduction in drag performance. Due to the dynamic engagement of the membrane with the flow, the key relies on the ability to manipulate those membrane/flow oscillations in such a way that positive lift and negative drag fluctuations are actively encouraged and negative lift and positive drag fluctuations are actively suppressed. One practical implementation could base on individual, span-parallel membrane actuation regions to engage and disengage certain membrane dynamics at different chord positions

at a given time-instant. This would also allow to generate travelling waves of unknown aerodynamic impact.

### References

- Ahmed, M. and Sharma, S. (2005). An investigation on the aerodynamics of a symmetrical airfoil in ground effect. *Experimental Thermal and Fluid Science*, 29(6):633–647.
- Albertani, R., Stanford, B., Hubner, J., and Ifju, P. (2007). Aerodynamic Coefficients and Deformation Measurements on Flexible Micro Air Vehicle Wings. *Experimental Mechanics*, 47:625–635.
- Arbos-Torrent, S., Palacios, R., and Ganapathisubramani, B. (2013a). Leading- and Trailing- Edge Effects on the Aeromechanics of Membrane Aerofoils. *Journal of Fluids and Structures*, 38:107–126.
- Arbos-Torrent, S., Palacios, R., and Ganapathisubramani, B. (2013b). Leading- and Trailing- Edge Effects on the Aeromechanics of Membrane Aerofoils. *Journal of Fluids* and *Structures*, 38:107–126.
- Arce, M. A. and Ukeiley, L. (2014). Fluid Structure Interactions in Low Aspect Ratio Membrane Wings. In 17th International Symposium on Applications of Laser Techniques to Fluid Mechanics, pages 1–15, Lisbon, Portugal.
- Attar, P., Gordnier, R. E., Johnston, J. W., Romberg, W. A., and Parthasarathy, R. N. (2011). Aeroelastic Analysis of Membrane Microair Vehicles Part I: Flutter and Limit Cycle Analysis for Fixed-Wing Configurations. *Journal of Vibration and Acoustics*, 133(2):1–8.
- Attar, P., Morris, B. J., Romberg, W. A., Johnston, J. W., and Parthasarathy, R. N. (2012). Experimental Characterization of Aerodynamic Behavior of Membrane Wings in Low-Reynolds-Number Flow. AIAA Journal, 50(7):1525–1537.
- Barlow, J. B., Rae, W. H., and Pope, A. (1999). Low-speed wind tunnel testing. Jhon Wiley & Sons, Canada.
- Bell, J. H. and Mehta, R. D. (1988). Contraction Design For Small Low-Speed Wind Tunnels. *Joint Institute For Aeronautics and Acoustics*, 84.
- Benedict, L. H. and Gould, R. D. (1996). Towards better uncertainty estimates for turbulence statistics. *Experiments in Fluids*, 22:129–136.

Bistrian, D. and Navon, I. (2014). Comparison of optimized Dynamic Mode Decomposition vs POD for the shallow water equations model reduction with large-time-step observations. *International Journal for Numerical Methods in Fluids*, (00):1–25.

- Bleischwitz, R., de Kat, R., and Ganapathisubramani, B. (2014). Effects of aspect ratio on fluid-structure interactions in membrane wings. In 52nd AIAA Aerospace Science and Technology Forum and Exposition, National Harbor, Maryland.
- Bleischwitz, R., de Kat, R., and Ganapathisubramani, B. (2015a). Aeromechanics of Membrane Wings in Ground-Effect. In 45th AIAA Fluid Dynamics Conference, pages 1–28, Dallas, Texas.
- Bleischwitz, R., de Kat, R., and Ganapathisubramani, B. (2015b). Aspect-Ratio Effects on Aeromechanics of Membrane Wings at Moderate Reynolds Numbers. *AIAA Journal*, 53(3):780–788.
- Bleischwitz, R., Kat, R. D., and Ganapathisubramani, B. (2016). Aeromechanics of membrane and rigid wings in and out of ground-effect at moderate Reynolds numbers. *Journal of Fluids and Structures*, 62:318–331.
- Buoso, S. and Palacios, R. (2015). Electro-aeromechanical modelling of actuated membrane wings. *Journal of Fluids and Structures*, 58:188–202.
- Buoso, S. and Palacios, R. (2016). Viscoelastic effects in the aeromechanics of actuated elastomeric membrane wings. *Journal of Fluids and Structures*, 63:40–56.
- Canals, M., Iriarte-diaz, J., and Grossi, B. (2011). Respiratory and Cardiovascular Adaptations of Bats and the Case of the Small Community of Bats in Chile. In *Biomechanics in Applications*, chapter 13, InTech, Rijeka, ISBN: 978-953-307-969-1.
- Carter, A. (1961). Effect of Ground Proximity on the Aerodynamic Characteristics of Aspect-Ratio-1 Airfoils With and With-out End Plates. *NASA technical note*, 970.
- Colorado, J., Barrientos, A., Rossi, C., and Breuer, K. S. (2012). Biomechanics of smart wings in a bat robot: morphing wings using SMA actuators. *Bioinspir. Biomim.* 7 (2012) 036006 (16pp).
- Curet, O. M., Carrere, A., Waldman, R., and Breuer, K. S. (2014). Aerodynamic Characterization of a Wing Membrane with Variable Compliance. AIAA Journal, 52(8):1749–1756.
- Diasinos, S., Barber, T. J., and Doig, G. (2012). Influence of wing span on the aero-dynamics of wings in ground effect. *Proceedings of the Institution of Mechanical Engineers*, Part G: Journal of Aerospace Engineering, 227(3):569–573.
- Fukuchi, Y. (2012). Influence of number of cameras and preprocessing for thick volume Tomographic PIV. In 16th Int. Symp. on Applications of Laser Techniques to Fluid Mechanics, Lisbon, Portugal.

Galvao, R., Israeli, E., Song, A., Tian, X., Bishop, K., Swartz, S., and Breuer, K. S. (2006). The Aerodynamics of Compliant Membrane Wings Modelled on Mammalian Flight Mechanics. In 36th AIAA Fluid Dynamics Conference and Exhibit, San Francisco, California.

- Gardiner, J. D., Dimitriadis, G., Codd, J. R., and Nudds, R. L. (2011). A potential role for bat tail membranes in flight control. *PloS one*, 6(3):e18214.
- Gordnier, R. E. (2009). High fidelity computational simulation of a membrane wing airfoil. *Journal of Fluids and Structures*, 25:897–917.
- Gordnier, R. E. and Attar, P. J. (2014). Impact of flexibility on the aerodynamics of an aspect ratio two membrane wing. *Journal of Fluids and Structures*, 45:138–152.
- Grasmeyer, J. M. and Keennon, M. T. (2000). Development of the Black Widow Micro Air Vehicle. In 39th AIAA Aerospace Sciences Meeting and Exhibit, number 0127, Reno, NV.
- Han, C. and Cho, J. (2005). Unsteady Trailing Vortex Evolution Behind a Wing in Ground Effect. *Journal of Aircraft*, 42(2):429–434.
- Han, S. and Feeny, B. (2003). Application of Proper Orthogonal Decomposition To Structural Vibration Analysis. Mechanical Systems and Signal Processing, 17(5):989– 1001.
- Hays, M. R., Morton, J., Dickinson, B., Chakravarty, U. K., and Oates, W. S. (2012). Aerodynamic control of micro air vehicle wings using electroactive membranes. *Journal of Intelligent Material Systems and Structures*.
- Hsiun, C.-m. and Ghent, C. (1996). Aerodynamic Characteristics of a Two-Dimensional Airfoil with Ground Effect. *Journal of Aircraft*, 33(2):386–392.
- Hu, H., Tamai, M., and Murphy, T. (2008). Flexible-Membrane Airfoils at Low Reynolds Numbers. *Journal of Aircraft*, 45(5):1767–1778.
- Hubner, J. and Hicks, T. (2011). Trailing-edge scalloping effect on flat-plate membrane wing performance. *Aerospace Science and Technology*, 15:670–680.
- Ifju, P. G., Jenkins, D. A., Ettinger, S., Lian, Y., and Shyy, W. (2002). Flexible-Wing-Based Micro Air Vehicles. In 40th AIAA Aerospace Sciences Meeting and Exhibition, number 0705, Reno, NV.
- Jaworski, J. W. and Gordnier, R. E. (2012). High-order simulations of low Reynolds number membrane airfoils under prescribed motion. *Journal of Fluids and Structures*, 31(1):49–66.
- Kat, R. D. E. (2012). Instantaneous planar pressure determination from particle image velocimetry. doctoral thesis, TU Delft.

Komissarov, S. and Gordon, Y. (2010). Soviet and Russian Ekranoplans. Midland Publishing.

- Kostas, J., Soria, J., and Chong, M. (2002). Particle image velocimetry measurements of a backward-facing step flow. *Experiments in Fluids*, 33(6):838–853.
- Lee, H. J., Kang, B. J., Park, J. H., Lee, C. M., Kang, K. J., and Kang, C. G. (2011). Development of Hoverwing Type WIG Craft WSH-500. In *OCEANS*, Yeosu. IEEE.
- Lian, Y., Shyy, W., Viieru, D., and Zhang, B. (2003). Membrane wing aerodynamics for micro air vehicles. *Progress in Aerospace Sciences*, 39:425–465.
- Lissaman, P. B. S. (1983). LOW-REYNOLDS-NUMBER AIRFOILS. Ann. Rev. Fluid Mech. 1983. 15:223-39.
- Lumley, J. L. (1967). The structure of inhomogeneous turbulent fows. Atmospheric turbulence and radio wave propagation, pages 166–178.
- Mateescu, D., Scholz, O., and Wang, C. (2012). Aerodynamics of Airfoils at Low Reynolds Numbers in the Proximity of the Ground. In 12th Pan-American Congress of Applied Mechanics, pages 2–7.
- Mathew, J. (2006). Design, Fabrication, and characterization of an anechoic wind tunnel facility. *PhD-Thesis*, University.
- McMasters, J. H. and Henderson, M. L. (1979). Low-Speed Single-Element Airfoil Synthesis. In Boeing Commercial Airplane Co.; Seattle, WA, U. S., editor, NASA. Langley Res. Center The Sci. and Technol. of Low Speed and Motorless Flight, Pt. 1; p 1-31;, pages 1–31, Seattle. NASA. Langley Res. Center The Sci. and Technol. of Low Speed and Motorless Flight, Pt. 1; p 1-31;.
- Miranda, S., Vlachos, P. P., Telionis, D. P., and Corporation, A. (2005). Flow Control of a Sharp-Edged Airfoil. *AIAA Journal*, 43(4):716–726.
- Mizoguchi, M. and Itoh, H. (2013). Effect of Aspect Ratio on Aerodynamic Characteristics at Low Reynolds Numbers. *AIAA Journal*, 51(7):1631–1639.
- Molkia, M. and Breuerb, K. (2010). Oscillatory motionsofaprestrained compliant membrane caused by fluid membrane interaction. *Journal of Fluids and Structures*, (26):339–358.
- Moon, Y. J., Oh, H.-J., and Seo, J.-H. (2005). Aerodynamic investigation of three-dimensional wings in ground effect for aero-levitation electric vehicle. *Aerospace Science and Technology*, 9(6):485–494.
- Mosaad, M. A., Gaafary, M. M., and Amin, I. A. (2011). Effect of Airfoil Camber on WIG Aerodynamic Efficiency. *Port Said Engineering Research Journal*, 1(1):1–9.

Mueller, T. J. (1999). Aerodynamic Measurements at Low Reynolds Numbers for Fixed Wing Micro-Air Vehicles. *Hessert Center for Aerospace Research*.

- Mueller, T. J. and DeLaurier, J. D. (2003). AERODYNAMICS OF SMALL VEHICLES. Annu. Rev. Fluid Mech., 35:89–111.
- Muijres, F. T., Johansson, L. C., Barfield, R., Wolf, M., Spedding, G. R., and Hedenström, a. (2008). Leading-edge vortex improves lift in slow-flying bats. *Science (New York, N.Y.)*, 319(5867):1250–3.
- Muijres, F. T., Johansson, L. C., Bowlin, M. S., Winter, Y., and Hedenstr??m, A. (2012). Comparing aerodynamic efficiency in birds and bats suggests better flight performance in birds. *PLoS ONE*, 7(5).
- Neuweiler, G. (2000). Biology of Bats. Zoological Institute, University of Munich.
- Norberg, U. M. and Rayner, J. M. V. (1987). Ecological Morphology and Flight in Bats (Mammalia; Chiroptera): Wing Adaptations, Flight Performance, Foraging Strategy and Echolocation. *Philiosophical Transactions of the Royal Society of London: Biological Sciences*, 316(1179):335–427.
- Null, W. and Shkarayev, S. (2005). Effect of Camber on the Aerodynamics of Adaptive-Wing Micro Air Vehicles. *Journal of Aircraft*, 42(6):1537–1542.
- Okamoto, M. and Azuma, a. (2011). Aerodynamic Characteristics at Low Reynolds Number for Wings of Various Planforms. *AIAA Journal*, 49(6):1135–1150.
- Pelletier, A. and Mueller, T. J. (2000). Low Reynolds Number Aerodynamics of Low-Aspect-Ratio, Thin/Flat/Cambered-Plate Wings. *Journal of Aircraft*, 37(5):825–832.
- Pelletier, A. and Mueller, T. J. (2001). Effect of Endplates on Two-Dimensional Airfoil Testing at Low Reynolds Number. *Journal of Aircraft*, 38(6).
- Pines, D. J. and Bohorquez, F. (2006). Challenges Facing Future Micro-Air-Vehicle Development. *Journal of Aircraft*, 43(2):290–305.
- Pinnau, R. (2008). Model Reduction via Proper Orthogonal Decomposition. In *Model Order Reduction: Theory, Research Aspects and Applications*, pages 95–109. Springer Berlin Heidelberg.
- Pistolesi, E. (1937). Ground effect theory and practice. *National Advisory Committee* for Aeronautics, 828.
- Prasad, R. and Damodaran, M. (2013). Computational Modeling of Steady and Unsteady Low Speed Wing in Ground Effect Aerodynamics. In 51st AIAA Sciences Meeting including the New Horizons Forum and Aerospace Exposition, Dallas, Texas.

Qu, Q., Jia, X., Wang, W., Liu, P., and Agarwal, R. K. (2014). Numerical Simulation of the Flowfield of an Airfoil in Dynamic Ground Effect. *Journal of Aircraft*, 51(5):1659–1662.

- Qu, Q., Wang, W., Liu, P., and Agarwal, R. K. (2015). Airfoil Aerodynamics in Ground Effect for Wide Range of Angles of Attack. *AIAA Journal*, pages 1–14.
- Rad, M. and Kazemi, F. J. (2001). Effect of Camber and Thickness on the Aerodynamic Properties of an Airfoil in Ground Proximity. *International Journal of Engineering*, 14(3):273–280.
- Raymond, A. E. (1921). Ground influence on airfoils. *National Advisory Committee for Aeronautics*, 67.
- Rhodes, S. C. and Sayers, A. T. (2009). Experimental Investigation: Stability Criteria of an Uncambered Airfoil in Ground Effect. *R & D Journal of the South African Institution of Mechanical Engineering*, 25:10–15.
- Rojratsirikul, P., Genc, M. S., Wang, Z., and Gursul, I. (2011). Flow-induced vibrations of low aspect ratio rectangular membrane wings. *Journal of Fluids and Structures*, 27:1296–1309.
- Rojratsirikul, P., Wang, Z., and Gursul, I. (2009). Unsteady fluid-structure interactions of membrane airfoils at low Reynolds numbers. *Experiments in Fluids*, 46:859–872.
- Rojratsirikul, P., Wang, Z., and Gursul, I. (2010a). Effect of pre-strain and excess length on unsteady fluid-structure interactions of membrane airfoils. *Journal of Fluids and Structures*, 26:359–376.
- Rojratsirikul, P., Wang, Z., and Gursul, I. (2010b). Unsteady Aerodynamics of Low Aspect Ratio Membrane Wings. In 48th AIAA Aerospace Sciences Meeting, number January, Orlando, Florida.
- Rozhdestvensky, K. V. (2000). Aerodynamics of a Lifting System in Extreme Ground Effect, volume ISBN: 978-. Springer, Berlin Heidelberg.
- Rozhdestvensky, K. V. (2006). Wing-in-ground effect vehicles. *Progress in Aerospace Sciences*, 42(3):211–283.
- Schmit, R. F., Glauser, M. N., and Gorton, S. A. (2003). Low Dimensional Tools for Flow-Structure Interaction Problems: Application to Micro Air Vehicles. In 41st AIAA Aerospace Science Exhibit Meeting and Exhibit, pages 1–9, Reno, NV.
- Schreier, H. W., Braasch, J. R., and Sutton, M. A. (2000). Systematic Errors in Digital Image Correlation caused by Intensity Interpolation. *Optical Engineering*, 39(November 2000):2915–2921.

Shi, S., New, T., and Liu, Y. (2013). Flapping dynamics of a low aspect-ratio energy-harvesting membrane immersed in a square cylinder wake. *Experimental Thermal and Fluid Science*, 46:151–161.

- Shields, M. and Mohseni, K. (2013). Roll Stall for Low-Aspect-Ratio Wings. *Journal of Aircraft*, 50(4):1060–1069.
- Shyy, W., Ifju, P., and Viieru, D. (2005). Membrane Wing-Based Micro Air Vehicles. *Applied Mechanics Reviews*, 58(7):283–301.
- Sirovich, L. (1987). Turbulence and the dynamics of coherent structures, I-III. Quarterly of Apploed Mathematics, 45(3):561–590.
- Smith, R. and Shyy, W. (1996). Computation of aerodynamic coefficients for a flexible membrane airfoil in turbulent flow: A comparison with classical theory. *Physics of Fluids*, 8(12):3346–3353.
- Song, A., Tian, X., Israeli, E., Galvao, R., Bishop, K., Swartz, S., and Breuer, K. (2008). Aeromechanics of Membrane Wings with Implications for Animal Flight. *AIAA Journal*, 46(8):2096–2106.
- Stanford, B., Ifju, P., and Albertani, R. (2014). Fixed Membrane Wings for Micro Air Vehicles: Experimental Characterization, Numerical Modeling, and Tailoring. *Bret Kennedy Stanford*, pages 1–53.
- Stanford, B., Lacore, D., Albertani, R., Parker, G., Walker, R., and Curtis, D. (2010). Proper Orthogonal Decomposition of Flexible Clap and Fling Motions via High-Speed Deformation Measurements. 48th AIAA Aerospace Sciences Meeting, pages 1–18.
- Suryadi, A., Ishii, T., and Obi, S. (2010). Stereo PIV measurement of a finite, flapping rigid plate in hovering condition. *Experiments in Fluids*, 49(2):447–460.
- Swartz, S., Iriarte-Diaz, J., Riskin, D., and Breuer, K. (2012). A bird? A plane? No, it s a bat: an introduction to the biomechanics of bat flight. In Gunnell, G. and Simmons, N., editors, *Evolutionary History of Bats: Fossils, Molecules and Morphology*, chapter 9, pages 317–351. Camebridge University Press, Camebridge, evolutiona edition.
- Technologies, A. (1985). The Fundamentals of Signal Analysis. Application Note 243. Technical report.
- Tian, X., Iriarte-Diaz, J., Middleton, K., Galvao, R., Israeli, E., Roemer, A., Sullivan, A., Song, A., Swartz, S., and Breuer, K. (2006). Direct measurements of the kinematics and dynamics of bat flight. *Institute of Physics Publishing*, 1(4):10–18.
- Timpe, A., Zhang, Z., Hubner, J., and Ukeiley, L. (2013). Passive flow control by membrane wings for aerodynamic benefit. *Experiments in Fluids*, 54(1471):1–23.

Torres, G. E. and Mueller, T. J. (2004). Low-Aspect-Ratio Wing Aerodynamics at Low Reynolds Numbers. *AIAA Journal*, 42(5):865–873.

- Tregidgo, L., Wang, Z., and Gursul, I. (2012). Frequency lock-in phenomenon for self-sustained roll oscillations of rectangular wings undergoing a forced periodic pitching motion. *Physics of Fluids*, 24(117101):1–18.
- Tregidgo, L., Wang, Z., Gursul, I., Kingdom, U., and Student, P. (2011). Fluid-Structure Interactions for a Low Aspect-Ratio Membrane Wing at Low Reynolds Numbers. In 41st AIAA Fluid Dynamics Conference and Exhibit, number June, Honolulu, Hawai.
- Udalov, K. G. and Belyaev, A. A. (1999). The Illustrated Story of Alexeev: Ekranoplanes, the caspian Sea Monster and Others. In *Avic-Press, ISBN: 9781857801460*, volume ISBN: 585-.
- Van Beek, C. and Oskam, B. (1998). Progress Report on Aerodynamic Analysis of a Surface Piercing Hydrofoil-Controlled Effect Seabus Configuration. In RTO AVT Symposium, volume 23, pages 23–1 to 23–18, Amsterdam. National Aerospace Laboratory.
- Visbal, M., Gordnier, R. E., and Galbraith, M. (2009). High-fidelity simulations of moving and flexible airfoils at low Reynolds numbers. *Experiments in Fluids*, 46:903–922.
- Vogt, J. and Barber, T. (2012). Ground effect phenomena about lift and downforce generating cambered aerofoils. *International Journal of Numerical Methods for Heat & Fluid Flow*, 22(2):153–174.
- Wahidi, R., Hubner, J. P., and Zhang, Z. (2014). 3-D measurements of separated flow over rigid plates with spanwise periodic cambering at low Reynolds number. *Journal of Fluids and Structures*, 49:263–282.
- Waszak, M. R. and Jenkins, L. N. (2001). Stability and Control Properties of an Aeroelastic Fixed Wing Micro Aerial Vehicle. In AIAA Atmospheric Flight Mechanics Conference, Montreal, Canada.
- Watkins, S., Milbank, J., Loxton, B. J., and Melbourne, W. H. (2006). Atmospheric Winds and Their Implications for Microair Vehicles. *AIAA Journal*, 44(11):2591–2600.
- Westerweel, J. (1997). Fundamentals of digital particle image velocimetry. *Meas. Sci. Technol.*, 8(1):1379–1392.
- Wieneke, B. and Taylor, S. (2006). Fat-sheet PIV with computation of full 3D-strain tensor using tomographic reconstruction. 13Th International Symposium on Applications of Laser Techniques To Fluid Mechanics, 13(Dracos 1996):26–29.
- Wieselsberger, C. (1921). Wing Resistance Near the Ground. Technical report, Zeitschrift für Flugtechnik und Motorluftschiffahrt.

Wolberg, J. (2006). Data Analysis Using the Method of Least Squares: Extracting the Most Information from Experiments. Springer, ISBN: 978-3540256748.

- Yun, L., Bliault, A., and Doo, J. (2010). WIG Craft and Ekranoplan: Ground Effect Craft Technology. In *Springer*, *ISBN:* 9781441900425.
- Zhang, X. and Zerihan, J. (2003). Off-Surface Aerodynamic Measurements of a Wing in Ground Effect. *Journal of Aircraft*, 40(4):716–725.
- Zhang, Z., Hopper, L., Wrist, A., Hubner, J. P., and Ukeiley, L. (2014). Nondimensional frequency scaling of aerodynamically-tensioned membranes. *Journal of Fluids and Structures*, 48:1–13.
- Zhang, Z., Martin, N., Wrist, A., and Hubner, J. P. (2015). Geometry and Prestrain Effects on the Aerodynamic Characteristics of Batten-Reinforced Membrane Wings. *Journal of Aircraft*, pages 1–15.

## Appendix A

# Wing-In-Ground UAV

One application of membrane wings in ground-effect could be a moderate Reynolds number Wing-In-Ground UAV (WIG-UAV), combining efficiency benefits due to ground-effect, enlarged payload capability and smooth gust reaction. An introduction video of the first prototype with flight tests on water can be found via: <a href="https://youtu.be/S9aTZleF9Js">https://youtu.be/S9aTZleF9Js</a>. The vibrations in the membrane can be seen here: <a href="https://youtu.be/YjDSfcTQZRc">https://youtu.be/YjDSfcTQZRc</a>.

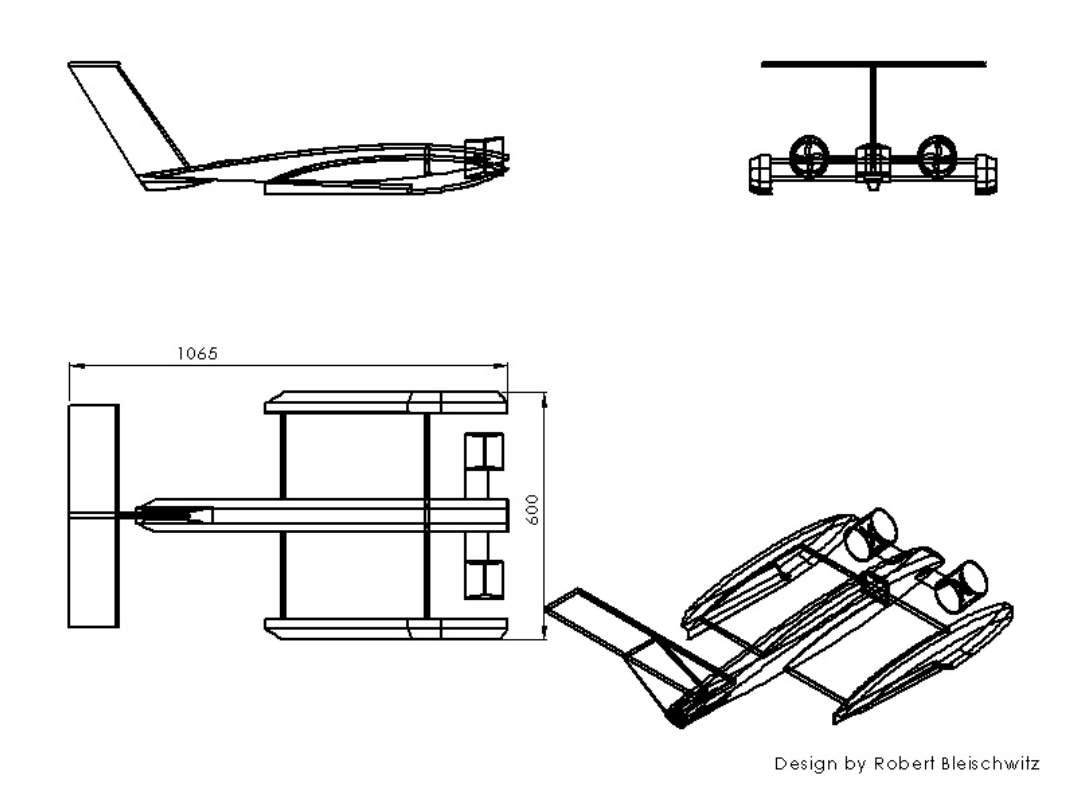


Figure A.1: First prototype membrane wing WIG-UAV drawings

The WIG-UAV consists of a balsa-carbon fibre sandwich material to ensure a light as well as strong structure for take-off and landing on rough surfaces. The first membrane WIG-UAV prototype (Figure A.1) was designed and built to gain experience with membrane wing UAV systems in ground-effect. Lift-off and flight above rough surfaces were studied in practical flight tests. The development of the WIG-UAV represents a project that worked in parallel with the wind tunnel experiments and can be seen as an amendment for qualitative progress in the main research topic of membrane wings in ground-effect. In future, it could be used as a start point for applying active membrane wings.

The overall dimensions are shown in Table A.1. The installed electronic equipment is shown in Table Table A.2.

The membrane wing consisted of a 0.2 mm thin latex sheet material which was also used for all wind tunnel measurements (Section 3.2.2). The membrane was attached on leading and trailing-edge with 4 mm diameter carbon fibre rods (Figure A.2). The angle-of-attack of the wing was fixed at 10°. The leading-edge was designed in a freely rotatable way to reduce the risk of flow separation at high angles-of-attack. Wind tunnel experiments proved the initial decision as beneficial (Figure 3.5).



Figure A.2: Membrane wing structure



Figure A.3: Usage on different surfaces

First flight-tests (Figure A.4) showed low aspect-ratio related roll instabilities, especially out of the ground-effect zone. The problem was temporary solved by making use of electrical gyroscopes for the stabilizing surfaces. The pitch stability was found to be adequate for free-flight conditions. However ground-effect flights required higher pitch stability margins which led to the use of gyroscopic feedback control. A test flight



Figure A.4: Vehicle in flight

Length	1065	mm
Width	600	mm
Height	320	mm
Weight	1600	g
Aspect-ratio main wing	1.4	-
Chord main wing	355	mm
Main wing area	14.9	$dm^2$
Tail wing area	6.1	$dm^2$
Angle-of-attack main wing	10	0
Maximum thrust	14	N

Table A.1: Data-sheet of WIG-UAV

with individually controlled fans for roll control was discarded as strong excited yawing motions started to develop.

Generally, the controllability of small Wing-In-Ground vehicles were found hard to ensure, especially in a gusty surrounding with GE limitations in roll and pitch angles. Active wings could be one option to gain drastic changes in lifting (or stabilizing) properties within a closed loop system by avoiding any mechanical stabilizer/flap units.

Thrust motors	HET 2W	Wemotec
Fan units	Mini Fan pro	Wemotec
Battery	Turnigy nano-tech 4000mAh 3S 40C	Hobbyking
Motor controller	YEP 80A (2-6S)	Hobbyking
Gyroscope and navigation	RX3S Orange RX 3-Axis	Hobbyking

Table A.2: Equipment list of WIG-UAV

## Appendix B

## List of publications

#### Journal articles

- Bleischwitz, R., de Kat, R., and Ganapathisubramani, B. (in preparation). On the load-membrane-flow interaction of flexible membrane wings in and out of ground-effect at moderate Reynolds numbers.
- Bleischwitz, R., de Kat, R., and Ganapathisubramani, B. (in preparation). Influence of ground-effect on the tipvortex development of rigid and membrane wings at moderate Reynolds numbers.
- Bleischwitz, R., de Kat, R., and Ganapathisubramani, B. (2016). Aeromechanics
  of membrane and rigid wings in and out of ground-effect at moderate Reynolds
  Numbers. *Journal of Fluids and Structures*, 62: 318-331. (URL)
- Bleischwitz, R., de Kat, R., and Ganapathisubramani, B. (2015). Aspect-ratio Effects on Aeromechanics of Membrane Wings at Moderate Reynolds Numbers. AIAA Journal, 53(3):780-788.(URL)

### Conference publications and contributions

- Bleischwitz, R., de Kat, R., and Ganapathisubramani, B. (due June 2016). Dynamics of Flexible Wings in and out of Ground Effect. 18th International Symposium on Applications of Laser and Imaging Techniques to Fluid Mechanics, Lisbon
- Bleischwitz, R., de Kat, R., and Ganapathisubramani, B. (2015). Fluid-structure
  Interaction of Membrane Wings in Ground Effect. In NIM-2015: Workshop
  on Non-intrusive Measurements for unsteady flows and aerodynamics, Poitiers.
  (URL)

- Bleischwitz, R., de Kat, R., and Ganapathisubramani, B. (2015). Aeromechanics of Membrane Wings in Ground-Effect. *In 45th AIAA Fluid Dynamics Conference*, Dallas, Texas. (URL)
- Bleischwitz, R., de Kat, R., and Ganapathisubramani, B. (2015). Fluid-structure Interaction of Rigid and Flexible Wings in Ground Effect. 68th Annual Meeting of the APS Division of Fluid Dynamics, Boston, Massachusetts. (URL)
- Bleischwitz, R., de Kat, R., and Ganapathisubramani, B. (2014). Influence of Ground Effect on Low Aspect Ratio Membrane Wings. 67th Annual Meeting of the APS Division of Fluid Dynamics, San Francisco, California. (URL)
- Bleischwitz, R., de Kat, R., and Ganapathisubramani, B. (2014). Effects of aspect ratio on fluid-structure interactions in membrane wings. *In 52nd AIAA Aerospace Science and Technology Forum and Exposition*, National Harbor, Maryland. (URL)

#### Public media (from 24.Feb.2016)

The media monitoring service of the University of Southampton showed more the 100 articles with worldwide coverage, reaching potential unique views of 268 million. A selection of media coverage is given as followed.

- EPSRC https://www.epsrc.ac.uk/newsevents/news/mavs/
- The Guardian https://www.theguardian.com/science/2016/feb/18/is-it-a-bird-is-it-a-bat-no-its-the-future-of-drone-technology
- New Scientist
   https://www.newscientist.com/article/2078239-bat-drone-uses-shape-shifting-wings-to-skim-over-water/
- News Discovery
   http://news.discovery.com/tech/robotics/new-wing-design-powers-crazy-bat-drones-160217.htm
- The Engineer

  https://www.theengineer.co.uk/bat-wing-membranes-inspire-developmentof-micro-air-vehicles/
- Daily-Mail

  http://www.dailymail.co.uk/sciencetech/article-3451243/Bat-drone-takesskies-Flying-machine-uses-shape-changing-wings-inspired-mammals.html

## Appendix C

## Curriculum Vitae

Robert Bleischwitz was born in the German city Dresden on 23 February 1987. He finished high school at "Lothar-von-Faber-Schule" in Nuremberg in 2005, at which he was awarded to the LGA-price as "Best graduate in technical department". His childhood interest in radio controlled high-speed boats and ground-effect vehicles lead him into the bachelor study in shipbuilding and maritime technology in Kiel, where he was elected for the "German National Merit Foundation (Deutsche Studienstiftung)". He continued in 2009 with a M.Sc.ETH degree in aerospace engineering at the Swiss Federal Institute of Technology (ETH) in Zurich, Switzerland. He specialised in aerodynamics, structural optimisation and composites and won the foreign exchange scholarship "ULDERUP-price". His Master-Thesis involved an optimization study on fluid-structure interactions of flexible, shape adaptable belt-rib wings. During his study, he conducted internships in shipbuilding (LINDENAU), composites (KRINGLAN) and aerospace (RUAG-SPACE) industry.

In June 2012, he started his doctoral study in experimental wind tunnel measurements on flexible membrane wings at the University of Southampton, UK. He was under supervision of Prof. B.Ganapathisubramani and Dr. R.de Kat as part of the Aerodynamicand-Flight-Mechanics group (AFM) at the faculty of engineering and environment. The results of this period are demonstrated in this thesis. He custom designed and build a wind tunnel and a variety of robotic equipment which he later used to conduct his study. He was responsible for several student projects on flexible wings. His major focus based on dynamic load, deformation (DIC) and flow measurement (PIV) on flexible membrane wings, used at moderate Reynolds numbers in UAVs and MAVs. An experimental ground-effect UAV with flexible membrane wings gained major interest in the public media, promoting the idea of flexible wings also outside the university.